UNIVERSIDADE FEDERAL DE MINAS GERAIS
Programa de Pós-Graduação em Engenharia Metalúrgica, Materiais e de Minas

Tese de Doutorado

"Oxidação de calcopirita: Investigação do mecanismo eletroquímico via difração de raios-X *ex situ e in situ* usando radiação síncrotron e quantificação do efeito galvânico da associação com pirita"

Autor: Daniel Majuste
Orientadora: Professora Virgínia S. T. Ciminelli
Co-orientador: Professor Kwadwo Osseo-Asare

Abril de 2011

UNIVERSIDADE FEDERAL DE MINAS GERAIS
Programa de Pós-Graduação em Engenharia Metalúrgica, Materiais e de Minas

Daniel Majuste

"Oxidação de calcopirita: Investigação do mecanismo eletroquímico via difração de raios-X *ex situ e in situ* usando radiação síncrotron e quantificação do efeito galvânico da associação com pirita"

"Chalcopyrite oxidation: Investigation of the electrochemical mechanism by applying *ex situ* and *in situ* synchrotron X-ray diffraction techniques and quantification of the galvanic effect of pyrite"

Tese de Doutorado apresentada ao Programa de Pós-Graduação
em Engenharia Metalúrgica, Materiais e de Minas
da Universidade Federal de Minas Gerais

Área de Concentração: Tecnologia Mineral
Orientadora: Professora Virgínia S. T. Ciminelli
Co-orientador: Professor Kwadwo Osseo-Asare, The Pennsylvania State University

Belo Horizonte
Escola de Engenharia da UFMG
2011

AGRADECIMENTOS

Agradeço aos meus pais Majuste e Vera pelo amor, exemplo, dedicação e, principalmente, por sempre acreditarem nos meus sonhos. Amo muito vocês!

Agradeço aos meus irmãos Rafa e Leco, e ao meu sobrinho João Gabriel, pela amizade e apoio constante ao longo desses anos.

Agradeço à minha namorada Ana Paula, meu amor, por perfumar todas as minhas manhãs, tardes e noites e, assim, tornar suave a realização dessa etapa.

Agradeço a todos os meus familiares e amigos de Montes Claros, Belo Horizonte e State College pelo carinho e apoio.

Agradeço imensamente à minha orientadora, Profª. Virgínia S. T. Ciminelli, pelo grande incentivo, suporte, confiança e amizade. Obrigado, Virgínia, pelos inúmeros conselhos e ensinamentos nesse período. Foi e será sempre uma honra poder trabalhar ao seu lado.

I would like to express my sincere gratitude to my co-adviser, Prof. K. Osseo-Asare, for providing me exceptional guidance and encouraging me, all the time, to push my research expectations to high levels. Thanks, Osseo, for everything!

Agradeço à Drª. Cláudia L. Caldeira e Profª. Maria Sylvia S. Dantas pelo conhecimento transmitido, excelente convivência, e por todo o apoio durante esses anos.

Agradeço à Ilda S. Batista e Christina Salvador pelo carinho, atenção e disponibilidade em me ajudar sempre. Vocês são muito especiais! Adoro vocês!

Agradeço aos colegas do Laboratório de Processamento Aquoso de Minerais e Materiais, Fernando, Graziele, Adélia, Gabriela, Clauson, Carolina, Douglas e Nílton, por tudo o que vivemos e aprendemos juntos. Esses 4 anos foram inesquecíveis e serão sempre lembrados com muita saudade. Também agradeço ao André N. O. Leite, aluno de iniciação científica, pela dedicação e companheirismo.

Agradeço a toda equipe do Laboratório de Análises Químicas, em especial, Prof. Júlio C. Silva, Profª. Roberta Froes e Izabella Costa Martins pelas análises realizadas.

Agradeço ao Prof. Dagoberto B. Santos (DEMET, UFMG), Prof. Paulo. R. G. Brandão (DEMIN, UFMG), Prof. Hélio A. Duarte (DQ, UFMG), Profª. Vanessa F. C. Lins (DEQ, UFMG) e Prof. Edwin A. Vilegas (DEMET, UFMG) pelo apoio e contribuições.

Agradeço ao Prof. Rogério M. Paniago (DF, UFMG) pela colaboração na elaboração de projeto e importante assistência na realização de medidas no Laboratório Nacional de Luz Síncrotron (LNLS), Campinas.

I'm grateful to Dr. Peter Eng (Consortium for Advanced Radiation Sources, University of Chicago) for the receptiveness to me and to the project, and for the valuable contributions during the measurements at the Argonne National Laboratory (ANL), Chicago.

I would like to thank Claire R. Fleeger and Andy J. Wall at Penn State University for the support on the construction work of the reaction cell used for measurements at ANL.

Agradeço a todos os funcionários do DEMET e CPGEM pela colaboração e convivência prazerosa, mas especialmente à Andréia B. Henriques, Laboratório de Difração de Raios-X; Patrícia M. T. Azevedo, Laboratório de Microscopia Eletrônica; Nelson A. Azevedo e Maria Aparecida Pacheco, Colegiado de Pós-graduação.

Agradeço ao Sr. Newton Urias Pinto por todos os serviços prestados nesses anos.

Agradeço ao Conselho Nacional de Desenvolvimento Científico e Tecnológico (CNPq) e ao INCT-ACQUA (Instituto Nacional de Ciência e Tecnologia em Recursos Minerais, Água e Biodiversidade), pelo suporte financeiro.

Agradeço a Deus que me guia e protege e que nesta data, com saúde e alegria, me permite agradeçer do fundo do meu coração a todas essas pessoas:

MUITO OBRIGADO!

OUTLINE

LIST OF TABLES

LIST OF FIGURES

LIST OF ABBREVIATIONS

Advanced Photon Source - Argonne National Laboratory (APS-ANL)

Atomic absorption spectrophotometry (AAS)

Brazilian Synchrotron Light Laboratory (LNLS)

Carbon paste electrode (CPE)

Critical potential (Ec)

Chalcopyrite-free pyrite electrode (PE)

Chronoamperometry (CA)

Cyclic voltammetry (CV)

Density functional theory (DFT)

Electrochemical impedance spectroscopy (EIS)

Electron probe microanalyses (EPMA)

Energy dispersive spectrometry (EDS)

Ex situ synchrotron small angle X-ray diffraction (S-SAXRD)

Flow method (FM)

Highest occupied molecular orbital (HOMO)

In situ synchrotron time-resolved X-ray diffraction (S-TRXRD)

Inductively coupled plasma mass spectrometry (ICP-MS)

Inductively coupled plasma optical emission spectrometry (ICP-OES)

Infrared spectroscopy (IR)

International Centre for Diffraction Data (ICDD)

Linear sweep voltammetry (LSV)

London Metal Exchange (LME)

Lowest unoccupied molecular orbital (LUMO)

Massive electrode (ME)

Mineral Liberation Analysis (MLA)

Mixed (chalcopyrite-pyrite) electrode (ME)

Mixed potential (EM)

Non-flow method (NFM)

Open circuit potential (OCP)

Pyrite-free chalcopyrite electrode (CE)

Raman spectroscopy (RS)

Rotating ring-disk electrode (RDE)

Saturated Calomel Electrode (SCE)

Scanning electron microscopy (SEM)

Silver/Silver chloride Electrode (Ag/AgCl)

Standard hydrogen electrode (SHE)

Stainless Steel Pseudo Reference Electrode (SSRE)

Synchrotron radiation (S)

Time-of-flight secondary ion mass spectrometry (TOF-SIMS)

X-ray absorption near edge structure spectroscopy (XANES)

X-ray absorption spectroscopy (XAS)

X-ray diffraction (XRD)

X-ray photoelectron spectroscopy (XPS)

RESUMO

A calcopirita ($CuFeS_2$) é o mineral de cobre mais abundante. A taxa de dissolução desse sulfeto em baixas temperaturas é lenta e tipicamente diminui com o tempo. A maioria dos estudos atribui essa cinética à formação de uma camada de produto insolúvel que impede o progresso da dissolução. Porém, o mecanismo de formação dessa camada, bem como sua natureza/efeito no processo não são completamente estabelecidos. Assim, o propósito desta tese foi investigar a taxa e mecanismos de dissolução de calcopirita em baixas temperaturas visando aumentar a extração de cobre a partir de minérios calcopiríticos de baixo teor. Os resultados dessa investigação incluem evidências experimentais originais de que a formação de sulfeto deficiente em metais nas condições de pré-onda anódica (*i.e.*, potenciais menores que o potencial crítico de $CuFeS_2$: 0.75-0.90 V *vs.* SHE) contribui para a taxa lenta de dissolução do mineral. Resultados obtidos por espectroscopia Raman e difração de raios-X (DRX) em baixo ângulo, com radiação síncrotron, demonstraram que a sua oxidação envolve a formação de camada de bornita (Cu_5FeS_4), produto este que diminui a taxa de oxidação de calcopirita à 0.70 e 0.80 V *vs.* SHE. Camadas de enxofre elementar (S_8) e covelita (CuS) também foram detectadas sobre eletrodos de $CuFeS_2$. Enquanto a formação de CuS impediu o progresso da reação, nenhuma evidência associando a formação de S_8 à diminuição da taxa de oxidação foi encontrada. Pela primeira vez, a transição *in situ* de $CuFeS_2$ para tais produtos foi investigada por DRX resolvido no tempo, com radiação síncrotron. À 25 °C, nenhum produto foi detectado durante o tempo de reação adotado (10 h). Por outro lado, o efeito significativo da temperatura na taxa de dissolução do mineral foi ilustrado. À 100 °C, observou-se a transição direta de $CuFeS_2$ para CuS em potencial de pré-onda anódica (*i.e.*, 0.75 V *vs.* SHE). Enxofre elementar fundido também foi detectado. Até então avaliado de forma qualitativa, o efeito galvânico de pirita (FeS_2) – fase presente em minérios de cobre – na taxa de oxidação de $CuFeS_2$ foi quantificado nesta tese. Quando associada à FeS_2, a densidade de corrente de dissolução de $CuFeS_2$ aumentou em até 2.6 e 2.2x, respectivamente, em soluções contendo 0.001 $mol.L^{-1}$ O_2 ou 0.05 $mol.L^{-1}$ Fe^{3+}, e em até 1.6x na presença de ambos os oxidantes. Portanto, o maior efeito de FeS_2 na taxa de oxidação de $CuFeS_2$ foi observada em condições de baixa oxidação. Resumindo, a aplicação original de métodos eletroquímicos e técnicas *ex situ* e *in situ* de DRX permitiu uma avaliação detalhada do mecanismo de oxidação de $CuFeS_2$, resultados essenciais ao desenvolvimento de processos de tratamento de minérios de cobre de baixo teor.

ABSTRACT

Chalcopyrite ($CuFeS_2$) is the most abundant copper mineral. The dissolution rate of this sulfide at low temperatures is slow and typically tends to decline with time. Most of the studies ascribe the slow kinetics to the formation of an insoluble layer, which prevents further mineral dissolution. However, the formation mechanism of this product layer and its nature/effects on the process are poorly understood. Thus, the purpose of this thesis was to investigate the rate and mechanisms of $CuFeS_2$ dissolution at low temperatures aiming at enhancing Cu extraction from low-grade, chalcopyrite ores. The findings of the present investigation provide experimental, original evidences that the formation of metal-deficient sulfides under anodic prewave conditions (*i.e.*, potentials lower than the critical potential of $CuFeS_2$: 0.75-0.90 V *vs.* SHE) contributes to the slow dissolution rate of this sulfide. Results by using Raman spectroscopy and *ex situ* synchrotron small angle X-ray diffraction (XRD) demonstrated that $CuFeS_2$ oxidation involves the formation of an intermediate bornite (Cu_5FeS_4) layer, which declined the $CuFeS_2$ oxidation rate at 0.70 and 0.80 V *vs.* SHE. Elemental sulfur (S_8) and covellite (CuS) were also detected at 0.80-1.00 and 0.80 V *vs.* SHE, respectively. While the presence of CuS led to hindered dissolution, no evidence to link the formation of S_8 to the diminution of $CuFeS_2$ oxidation rate was found. For the first time, the *in situ* transition of $CuFeS_2$ to the reaction products was also investigated by *in situ* synchrotron time-resolved XRD. At 25 °C, no reaction product was detected up to 10 h. On the other hand, the significant effect of temperature on the dissolution rate was illustrated. At 100 °C, a direct transition of $CuFeS_2$ to CuS at anodic prewave potential (*i.e.*, 0.75 V *vs.* SHE) takes place. Melted S_8 was also detected under these conditions. So far evaluated qualitatively, the effect of pyrite (FeS_2) – mineral phase often found in copper sulfide ores – on $CuFeS_2$ dissolution was quantified in this thesis. When associated to FeS_2, the dissolution current density of $CuFeS_2$ increased by a factor of approximately 2.6 and 2.2, respectively, in solutions containing 0.001 $mol.L^{-1}$ O_2 and 0.05 $mol.L^{-1}$ Fe^{3+}, and by 1.6 times in the presence of both oxidants. Therefore, more pronounced effect of pyrite on chalcopyrite oxidation rate was observed under the lower oxidizing conditions. In summary, this original application of electrochemical methods and *ex situ* and *in situ* synchrotron XRD techniques allowed a detailed discussion of the oxidation mechanism of $CuFeS_2$, which is essential to develop alternative processes for treating low-grade, copper ores.

Chapter 1 – Introduction

1.1. Copper: Economic value and main ore deposits

Copper (Cu) is the third most consumed metal in the world after iron and aluminum (USGS, 2010). Due to properties such as high ductility and malleability, high electrical and thermal conductivity, and resistance to corrosion, copper is found in diverse applications, either in the metallic form or alloys. Materials produced from copper are largely used in building wiring and construction, energy generation, telecommunications, transportation, consumer/general products, and high technology devices (ICSG, 2010).

In the nearby future, the global market may face a constant shortage of this important commodity. According to forecasts (CRU International, 2011), the worldwide demand for copper will overcome the supply from 2018. Among the main reasons for a decreasing production of copper is the drop in the metal content in the existent ore deposits.

Copper deposits are widely distributed in the world, but approximately 42% of the world mine production of copper comes from Chile and Peru (USGS, 2010). In Brazil, the main deposits are located in the states of Pará, Goiás, Bahia, and Ceará. Brazilian production of copper concentrates is relatively small, approximately 1.3% of the world production, level similar to that presented for the production of metallic copper (DNPM, 2010). This mineral commodity has as the main producers China, Chile, Japan and the United States (USGS, 2010).

Fig. 1.1 exhibits historic average prices of copper LME (London Metal Exchange), grade A (99.999%). It may be noticed that the average prices increased significantly in the period from 2003 to 2006, a trend that might be explained by the increasing copper demand especially from China, now the world's largest consumer of this metal (USGS, 2010). In the period 2008-2009, it may be observed that the price of Cu LME grade A has declined, according to the trend registered for the base metals, and especially for nickel and zinc. In 2010, the average price of this commodity increased again, returning to the higher level, registered in the period 2006-2008.

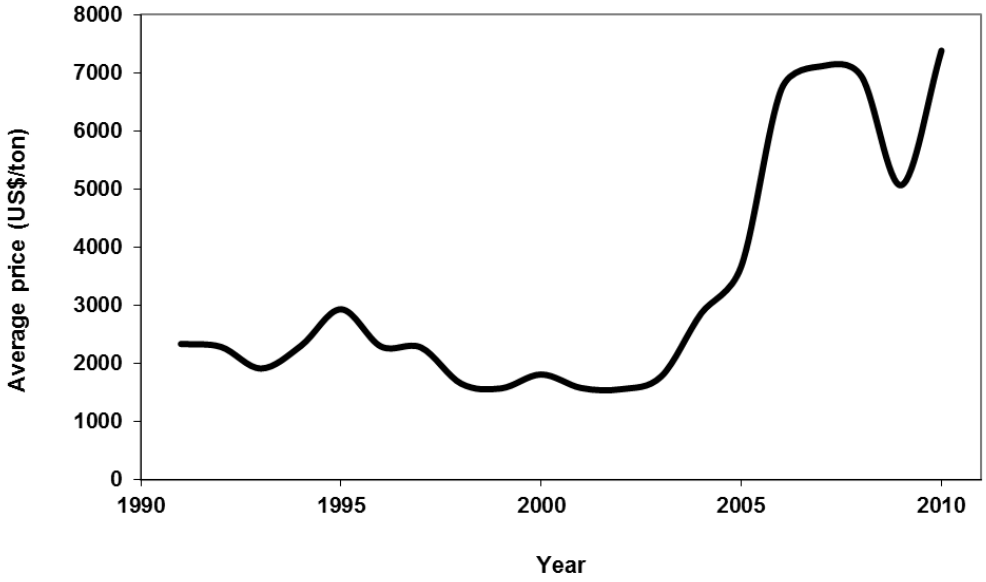

Figure 1.1. Copper LME, grade A: historic evolution of the average prices (1991-2010) (adapted of LME, 2010).

In nature, Cu is found in association with a range of elements in different structural forms and stoichiometric proportions, rarely in the pure state. Copper deposits, originated from volcanism, hydrothermal activity or weathering processes (Jensen and Bateman, 1981), are usually of large dimensions, but with low content. Typical deposits contain from 0.5% Cu (open mines) to 1-2% Cu (underground mines), and are classified in (1) primary or sulfide deposits, typically high-grade ores, found in the deeper zones of the earth crust; and (2) secondary or oxidized ores, with relatively lower Cu content, found in the superficial zones (Davenport *et al*., 2002).

For the sulfide deposits, chalcopyrite ($CuFeS_2$) is the most abundant copper mineral. This sulfide accounts for approximately 70% of the world's known copper deposits (Davenport *et al*., 2002). In the porphyry ores, the most extensive deposits, chalcopyrite is found in association to pyrite (FeS_2), with minor bornite (Cu_5FeS_4), molybdenite (MoS_2), and sphalerite (ZnS) content. These deposits are predominantly located in the west mountain region of South America, mostly in Chile and Peru; southwest of the United States; and west of Canada. In the sulfide ore deposits, mainly located in Canada, the United States, Spain, South Africa and Australia, chalcopyrite is associated to pyrrhotite ($Fe_{1.0\text{-}0.8}S$) and

pentlandite ($(Fe,Ni)_9S_8$) (Jensen and Bateman, 1981; Berry *et al.*, 1983; Habashi, 1993). Chalcopyrite also occurs in low-temperature hydrothermal deposits (associated with galena (PbS), ZnS and dolomite ($CaMg(CO_3)_2$)), and high-temperature deposits (associated with $Fe_{1.0-0.8}S$ and $(Fe,Ni)_9S_8$) (Berry *et al.*, 1983).

In the last decades, the processing of sulfide ores has been extensively investigated, mainly for treating chalcopyrite – the main copper source and the main constituent in low-grade ores. The future development of copper industry is, therefore, allied to the effectiveness of chalcopyrite dissolution.

1.1.1. Chalcopyrite oxidation mechanism

As will be discussed in this thesis, chalcopyrite does not dissolve significantly under heap bioleaching conditions and economically attractive processing at high pressures requires high-grade ores.

For low temperatures, the mineral leaching rate in acidic media is known to be extremely slow, and often tends to decline with time (Jones and Peters, 1976; Dutrizac, 1978, 1981; Muñoz *et al.*, 1979; Majima *et al.*, 1985; Hirato *et al.*, 1987a). In an attempt to overcome this constraint, a number of investigations have been conducted aimed at understanding the kinetics and mechanisms of dissolution of this sulfide. Most of the studies available in the literature ascribe the slow leaching rate of chalcopyrite to the formation of an insoluble layer, which prevents further mineral dissolution. Nonetheless, the nature of such product layer and the mechanisms by which it is formed and affects the dissolution reaction are subject of debate in the literature.

There are many uncertainties regarding the (i) nature of the product phases that form on chalcopyrite (particles or electrodes) from about 0.5 V to 1.5 V *vs.* the Standard Hydrogen Electrode (SHE), under atmospheric conditions, and the (ii) effects of these layers on the dissolution rate of chalcopyrite. Many efforts have been made to increase the kinetics of chalcopyrite in acidic solution and, then, to overcome the so-called hindered dissolution effect.

The efforts to improve the mineral leaching rate have mainly focused on the understanding on the kinetics and mechanisms of dissolution of this sulfide. Kinetics and mechanistic investigations have been conducted by different techniques at varied acidity, oxidizing and temperature conditions, and by using chalcopyrite samples from different sources. Many authors have investigated the nature and effects of the product phases (Jones and Peters, 1976; Linge, 1976; Dutrizac, 1978, 1989; Ammou-Chokroum *et al*., 1979; Biegler and Swift, 1979; Muñoz *et al*., 1979; Parker *et al*., 1981; Warren *et al*., 1982; Majima *et al*., 1985; Hirato *et al*., 1986, 1987a; Yin *et al*., 1995; England *et al*., 1999; Klauber *et al*., 2001; Arce and González, 2002; Elsherief, 2002; Farquhar *et al*., 2003; Lázaro and Nicol, 2003, 2006; Parker *et al*., 2003; Todd *et al*., 2003; Abraitis *et al*., 2004; Hiroyoshi *et al*., 2004; Mikhlin *et al*., 2004; Al-Harahsheh *et al*., 2006; Harmer *et al*., 2006; Nava and González, 2006; Viramontes-Gamboa *et al*., 2007; Córdoba *et al*., 2008b; Nava *et al*., 2008; Parker *et al*., 2008; Sasaki *et al*., 2009; Ghahremaninezhad *et al*., 2010; Sequeira and Santos, 2010; Velázques-Yévenes *et al*., 2010).

Elemental sulfur (S_8) has been identified as a common product of chalcopyrite dissolution in both the ferric sulfate and ferric chloride solutions by means of X-ray diffraction (XRD), X-ray photoelectron spectroscopy (XPS), X-ray absorption spectroscopy (XAS), Raman spectroscopy (RS), scanning electron microscopy (SEM) coupled with energy dispersive spectrometry (EDS) and electron probe microanalyses (EPMA). The formation of sulfur on chalcopyrite in ferric sulfate media has been pointed out as the main cause for the slow and parabolic leaching rate (Linge, 1976; Muñoz *et al*., 1979; Dutrizac, 1981, 1989; Majima *et al*. 1985; Hirato *et al*., 1987a; Klauber, 2008). In contrast, for ferric chloride media, linear kinetics and formation of a porous elemental sulfur layer, throughout which soluble products and reactants can diffuse, have been reported (Jones and Peters, 1976; Ammou-Chokroum *et al*., 1979; Palmer *et al*., 1981; Majima *et al*., 1985; Hirato *et al*., 1986; Dutrizac, 1978, 1989, 1990).

Regarding the metal-deficient sulfides ($Cu_{1-x}Fe_{1-y}S_{2-z}$), many authors have claimed that these phases are formed on chalcopyrite during its dissolution in acidic media (Jones and Peters, 1976; Linge, 1976; Ammou-Chokroum *et al*., 1979; Biegler and Swift, 1979; Parker *et al*., 1981; Warren *et al*., 1982; Biegler and Horne, 1985; Price and Warren, 1986; Yin *et al*., 1995; Lu *et al*., 2000; Arce and González, 2002; Elsherief, 2002; Lázaro and

Nicol, 2003; Abraitis *et al*., 2004; Mikhlin *et al*., 2004; Nava and González, 2006; Parker *et al*., 2008; Ghahremaninezhad *et al*., 2010). The formation of these intermediate phases, mainly demonstrated by the preferential leaching of Fe over Cu, formation of the anodic prewave during the electrochemical polarization of chalcopyrite electrodes, and also non-stoichiometric Cu/Fe ratio on oxidized surfaces, is often linked to the observed hindered dissolution effect: that is, the inhibition of the reaction progress. To the knowledge of the author no direct identification of these phases has been provided.

Covellite (CuS) has also been proposed as an intermediate product phase of chalcopyrite dissolution in acidic, oxidizing media, under atmospheric conditions (Ammou-Chokroum, 1979; Warren *et al*., 1982; Biegler and Horne, 1985; Nava and González, 2006; Córdoba *et al*., 2008b; Ghahremaninezhad *et al*., 2010; Nicol *et al*., 2010; Velásquez-Yévenes *et al*., 2010) on the basis of the preferential leaching of Fe over Cu, thermodynamic modeling and electrochemical studies, mainly by cyclic voltammetry. This mineral phase was positively detected on oxidized chalcopyrite particles by using XRD and Mineral Liberation Analysis (MLA) (Córdoba *et al*., 2008b; Velásquez-Yévenes *et al*., 2010). CuS was also detected as an intermediate layer on chalcopyrite particles after bioleaching in acidic solution using Raman spectroscopy (Sasaki *et al*., 2009).

Among the efforts to improve chalcopyrite dissolution at low temperatures, the use of many catalysts has been quite investigated. Metallic copper (Cu) (Hiskey and Wadsworth, 1975) and gold (Au) (Lorenzen and Denventer, 1992); manganese dioxide (MnO_2) (Madhuchhanda *et al*., 2000); metallic ions such as bismuth (Bi^{3+}) and mercury (Pb^{2+}) (Mateos *et al*., 1987; Gómez *et al*. 1997; Hiroyoshi *et al*., 2007) and mainly silver (Ag^{+}) (Miller and Portillo, 1979; Miller *et al*., 1981; Warren *et al*., 1984; Price and Warren, 1986; Mateos *et al*., 1987; Osseo-Asare, 1993; Scaini *et al*., 1995; Hiroyoshi *et al*., 2002, 2007; Parker *et al*., 2003; Nazari *et al*., 2011); chloride (Cl^{-}) ions (Dutrizac, 1978, 1981, 1992; Palmer *et al*., 1981; Majima *et al*., 1985; Hirato *et al*., 1986, 1987; Lu *et al*., 2000a; Carneiro and Leão, 2007; McDonald and Muir, 2007b); carbon particles (Wan *et al*., 1984; Nakazawa *et al*., 1998; Liang *et al*., 2010); silver sulfide (Ag_2S) (Mateos *et al*., 1987; Scaini *et al*., 1995); and pyrite (FeS_2) (Berry *et al*., 1978; Mehta and Murr, 1983; Nowak *et al*., 1984; Abraitis *et al*., 2004; You *et al*., 2007; Dixon *et al*., 2008; Miller *et al*., 2008; Littlejohn and Dixon, 2008; Sylwestrzak *et al*., 2009; Nazari *et al*., 2011), usually favor the

reaction kinetics promoting a different reaction mechanism. Nevertheless, the mechanisms by which the catalysts affect the chalcopyrite dissolution in both the sulfate and chloride media are not fully established.

In light of the above brief review, it becomes evident that considerable advances on the chalcopyrite dissolution mechanism have been made under atmospheric conditions by means of leaching and electrochemical methods and characterization techniques. However, the nature of the product layers, as well as the mechanisms by which they form and affect the leaching reaction are not fully understood, and neither are the details of the oxidative process in the presence of catalysts, such as pyrite. Since pyrite is a mineral phase often found in copper sulfide ores (Jensen and Bateman, 1981; Berry *et al*., 1983), the beneficial effects of this impurity phase on the dissolution rate of chalcopyrite has important practical implications for the leaching processes.

In this context, a better understanding of the chalcopyrite oxidation mechanisms under practical, low-temperature leaching conditions, represents a relevant contribution to copper hydrometallurgy, in view of the commercial and technological importance of this sulfide.

1.2. Objectives

A systematic investigation of the electrochemical oxidation of chalcopyrite coupled with a detailed study of chalcopyrite surface by using advanced characterization techniques will help to elucidate unclear issues on the nature of the product layers and their effects on the dissolution rate of this copper sulfide. A systematic investigation of the effects of pyrite on chalcopyrite electrochemistry under typical leaching conditions will help to elucidate the unclear issues on the mechanisms of copper extraction in the presence of this important natural catalyst.

Therefore, the overall objective of this investigation was to improve the knowledge on the chalcopyrite oxidation mechanisms in acidic sulfate solutions – by far the most adopted leaching media – under atmospheric conditions, aiming at enhancing copper extraction from low-grade, chalcopyrite ores. The specific objectives of the present thesis were:

(i) To evaluate the magnitude of the effect of pyrite on the electrochemical behavior of chalcopyrite under typical, low-temperature leaching conditions, that is, in the presence of ferric (Fe^{3+}) ion and oxygen, with a method that better represents the association in the ore;

(ii) To investigate the nature and the role of the intermediate- and end-product phases that forms on chalcopyrite under anodic prewave conditions, which includes the typical potentials for the ferric ion leaching of copper ores (*i.e.*, potential of about 0.7 V *vs.* SHE);

(iii) To establish the kinetics and mechanisms of chalcopyrite oxidation under anodic prewave conditions, by an *in situ* investigation of the mineral transition to crystalline and amorphous product phases.

For the first time, to the author's knowledge, an investigation of chalcopyrite oxidation was conducted by *ex situ* synchrotron small angle X-ray diffraction (S-SAXRD), and *in situ* synchrotron time-resolved X-ray diffraction (S-TRXRD); and the galvanic effect of pyrite on chalcopyrite oxidation was quantified by experimental approach that allowed a better assessment of the magnitude of the galvanic current. The findings of the present thesis are an original contribution to the current understanding on chalcopyrite oxidation in acidic media.

1.3. Thesis structure and organization

This thesis was organized in 6 chapters. Chapter 1 provides an introduction to the theme of this investigation and a critical summary of important works found in the literature.

Chapter 2 offers a detailed and critical literature review on extractive metallurgy of copper; copper hydrometallurgy; fundamental properties of chalcopyrite; chalcopyrite oxidation processes, and analytical techniques used in the present investigation.

In Chapter 3, the effects of pyrite inclusions, dissolved oxygen, and ferric ion on the electrochemistry of chalcopyrite was investigated by using potentiometry and linear sweep voltammetry.

In Chapter 4, chalcopyrite electrodes oxidized under anodic prewave conditions by means of chronoamperometry were analyzed by *ex situ* synchrotron small angle X-ray diffraction and Raman spectroscopy. The synchrotron measurements were conducted at the beamline XRD1, Brazilian Synchrotron Light Laboratory (LNLS) – Campinas, with the assistance of Prof. Rogério Magalhães Paniago, from the Department of Physics, UFMG.

In Chapter 5, an *in situ* investigation of chalcopyrite dissolution under anodic prewave conditions was conducted by means of synchrotron time-resolved X-ray diffraction. The measurements were conducted at the beamline 13-BM-C, Advanced Photon Source (APS) of the Argonne National Laboratory (ANL) – Chicago, U.S, with the assitance of Dr. Peter Eng, from the University of Chicago.

Finally, Chapter 6 brings the final considerations of the present thesis, including the main conclusions, original contributions, and suggestions to future works.

Chapter 2 – Literature review

2.1. Extractive metallurgy of copper

Different metallurgical routes are required to produce copper depending on the mineralogy of the deposit and metal content. Two main processing routes may be distinguished: the pyrometallurgical and the hydrometallurgical ones.

The copper ores typically treated by hydrometallurgy may be represented by the oxidized minerals such as oxides, carbonates, sulfates, hydroxy-silicates and hydroxy-chlorides, and chalcocite (Cu_2S) in the presence of oxidants. Treatment of oxidized ores involves heap leaching with sulfuric acid (H_2SO_4) as leaching solution, followed by solvent extraction, and electrowinning (Davenport *et al*., 2002; Habashi, 1993).

Regarding the sulfides, the treatment of low-grade ores involves heap bioleaching, an option very well revised by Dreisinger (2006), Watling (2006) and Pradhan *et al*. (2008). Chalcocite and covellite are amenable to dissolve under heap bioleaching conditions, but the leaching kinetics of chalcopyrite is very slow and tends to decline with time, when assisted by mesophilic microorganisms. Several papers on chalcopyrite bioleaching with termophilic microorganisms or mixed cultures are available in the literature, and in spite of the promising results the processes continue in developmental stage.

Regarding the high-grade ores, these are mostly treated by pyrometallurgical processes, but the treatment at high pressure conditions has being used as well. About 80% of the total production of copper comes from the pyrometallurgical treatment of sulfide concentrates (Bravo, 2006). It has dominated the copper industry since the 1800's, but it is expected a slow modification of this scenario in function of limitations of this processing route. Treatment of copper sulfide ores by hydrometallurgy offer many important advantages over the smelting-refining processes such as the ability to treat low-grade and complexes ores and more flexibility in product design (Prasad and Pandey, 1998; Davenport *et al*., 2002; Dreisinger, 2006).

2.1.1. Hydrometallurgical processing of copper sulfide ores

Tab. II.1 and II.2 summarizes the hydrometallurgical alternatives for processing copper sulfide ores, especially chalcopyrite concentrates. It may be noticed that all the chloride- (Tab. II.1) and sulfate-based (Tab. II.2) processes include fine grinding and result in high copper leaching (≥ 95%). Ferric chloride ($FeCl_3$) and cupric chloride ($CuCl_2$) leaching (Tab. II.1) has received a large attention, mainly as a result of the higher leaching rate and higher copper solubility (*i.e.*, the formation of stable chloro-complexes) in chloride media (Jones and Peters, 1976; Ammou-Chokroum *et al*., 1979; Dutrizac, 1981, 1990, 1992; Majima *et al*. 1985; Hirato *et al*., 1986, 1987a; Winand, 1991; Senanayake and Muir, 2003; Liddicoat and Dreisinger, 2007).

Negative aspects of the chloride-based hydrometallurgical processes are related to purity and morphology of the metal recovered and corrosion problems as well. In consequence, the progress of these processes toward commercial plants has been slow, in spite of the recognized effectiveness.

The sulfate-based processes (Tab. II.2) offer many advantages over the chloride-based processes, such as the lower costs; minimal corrosion problems; simpler copper recovery from the sulfate solutions by solvent extraction and electrowinning; and easier regeneration of the sulfuric acid during the electrowinning (Hackl *et al*., 1995; Davenport *et al*., 2002; Dreisinger, 2006; Klauber, 2008). However, such processes present a critical disadvantage that is the slow leaching kinetics, comparatively to that reported in chloride media (Jones and Peters, 1976; Dutrizac, 1978, 1981; Majima *et al*., 1985; Hirato *et al*., 1987b), as will be better discussed later.

It may also be noticed from Tab. II.2 that the sulfate-based processes include ferric (Fe^{3+}) ion leaching, high pressure leaching or bioleaching, but only industrial plants with leaching into autoclaves are operating in commercial scale. Although claimed as the technology of future (Habashi, 2009), economically attractive processing of copper sulfides under high pressure conditions requires high-grade ores.

Table II.1. Chloride-based processes for copper sulfide ores (Dutrizac, 1992; Wang, 2005; Liddicoat and Dreisinger, 2007).

Process	Scale	General characteristics
U.S. Bureau of Mines	Mini plant	▪ Single-stage leach ($FeCl_3$ solution; 105°C; 2 h); ▪ Copper electrowinning directly from CuCl solution.
Cyprus Metallurgical Processes Corporation (CYMET Process)	Pilot plant	▪ Two-stage leach ($FeCl_3/CuCl_2/NaCl$ solution; 98°C; 3 h); ▪ Copper crystallization as CuCl and reduction with hydrogen gas (H_2) at 500°C; ▪ Melting of the product to produce copper.
Duval Corporation (CLEAR Process)	Pilot plant	▪ 1st stage leach: oxidation ($FeCl_3/CuCl_2/NaCl/KCl$ solution; 105°C); ▪ Treatment of the pregnant solution with Cu powder and copper electrowinning; ▪ 2nd stage leach: leaching of the 1st stage leach residue (150°C; pO_2 3 atm).
CUPREX Process	Pilot plant	▪ Two-stage leach ($FeCl_3$ solution; atmospheric conditions); ▪ Selective $CuCl_2$ extraction by solvent extraction and copper electrowinning.
Intec Limited (INTEC Process)	Pilot plant	▪ Four-stage leach ($BrCl_2$ solution; atmospheric conditions); ▪ Precipitation of impurities and copper electrowinning from the $CuCl_2$ solution.
Outokumpu HydroCopper™ Process	Pilot Plant	▪ Single-stage leach ($CuCl_2/O_2$ solution; 80-100°C); ▪ Purification of the CuCl solution with NaOH to precipitate Cu_2O; ▪ Cu_2O is reduced with H_2 to produce metallic copper.
Goethite / Hematite Process	Bench	▪ Two-stage leach ($FeCl_3/CuCl_2/O_2$ solution; 95°C; 3 h); ▪ Copper extraction by solvent extraction and precipitation of FeOOH or Fe_2O_3; ▪ Copper electrowinning from the sulfate solution.

Table II.2. Sulfate-based processes for copper sulfide ores (Dreisinger, 2006; Wang, 2005; McDonald and Muir, 2007a, 2007b).

Process	Scale	General characteristics
BacTech/Mintek Process	Demonstration plant	▪ Bioleaching (stirred reactors; 25-55°C; pH 0.5-2.5; 30 days); ▪ Recovery of copper by solvent extraction and electrowinning.
BHP Billiton and Codelco (BioCOP^{TM} Process)	Commercial Facility*	▪ Bioleaching (two stirred reactors; O_2 bubbling; 60-90°C; pH 1.5-2.5; 10 days); ▪ Recovery of copper by solvent extraction and electrowinning.
Albion Process	Pilot plant	▪ Ultra-fine grinding/atmospheric cc leach (85°C; Fe^{3+} addition); ▪ Recovery of copper by solvent extraction and electrowinning.
Mt. Gordon Copper Process	Commercial facility	▪ Pressure leach (90°C; pO_2 8 atm; 1 h; Fe^{3+} addition) ; ▪ Recovery of copper by solvent extraction and electrowinning.
ACTIVOX® Process	Demonstration plant	▪ Ultra-fine grinding/pressure leach (90-110°C; pO_2 10-12atm; Cu^{2+}, Cl^- additions); ▪ Recovery of copper by solvent extraction and electrowinning.
Anglo/UBC Process	Pilot plant	▪ Pressure leach (150°C; pO_2 10-12 atm; 2 h; Fe^{3+}, Cu^{2+}, surfactants additions); ▪ Recovery of copper by solvent extraction and electrowinning.
Cominco Engineering Services Limited (CESL Process)	Demonstration plant	▪ Pressure leach (140-150°C; pO_2 10-12 atm; pH 3; 2 h; Cu^{2+}, Cl^- additions) ; ▪ Recovery of copper by solvent extraction and electrowinning.
Dynatec Process	Pilot plant	▪ Pressure leach (150°C; pO_2 10-12 atm; coal as anti-agglomerant); ▪ Recovery of copper by solvent extraction and electrowinning.
Phelps Dodge-Placer Dome and total POX Processes	Commercial facility	▪ Pressure leach (200-230°C; pO_2 30-40 atm); ▪ Recovery of copper by solvent extraction and electrowinning.

* In fact, a commercial plant was not implemented due to economic constrains.

2.2. Chalcopyrite: Fundamental properties

2.2.1. Structure and bonding

The theoretical composition of chalcopyrite is 34.6% wt. Cu, 30.4% wt. Fe, and 35.0% wt. S. Chalcopyrite is recognized by its brass-yellow color and its greenish-black stripes. Its atomic weight is 183.5 g/mol and it has a hardness of 3.5 to 4.0 Mohs and density of 4.1 to 4.3 g/cm^3 (Weast and Selby, 1968). Chalcopyrite has similar crystal structure to sphalerite (ZnS), however its unit cell is almost double the size of the ZnS cell (Rosso and Vaughan, 2006). Cu and Fe atoms replace Zn atoms according to the tetragonal space group $I\bar{4}2d$, and the parameters of the crystal lattice are a = 5.25 Å and c = 10.32 Å (Lavrentyev *et al.*, 2004). Fig. 2.1 illustrates the crystalline structure and atomic arrangement of chalcopyrite. It should be noticed that Cu and Fe atoms are in tetrahedral coordination with S and they are ordered into alternate cation sites. Each S atom is bonded to two Fe and two Cu atoms and there are not S-S bonds, such as in pyrite. Fe-S and Cu-S bond lengths are 2.26 Å and 2.33 Å, respectively (Gibbs *et al.*, 2007), and the inter-atomic distances between the atoms are $d_{Cu\text{-}Fe} = d_{Cu\text{-}Cu} = d_{Fe\text{-}Fe} = 3.71$ Å (Edelbro *et al.*, 2003).

Due to the complexity of its electronic structure and chemical bonding, there has been a debate in the literature regarding the valence states of Cu and Fe in chalcopyrite (Tossell *et al.*, 1982; van der Laan *et al.*, 1992; Li *et al.*, 1994; Yin *et al.*, 1995; Todd *et al.*, 2003; Mikhlin *et al.*, 2004, 2005; Goh *et al.*, 2006; Pearce *et al.*, 2006). Evidences obtained by Mössbauer spectroscopy, X-ray photoelectron spectroscopy (XPS) and X-ray absorption near edge structure spectroscopy (XANES) supports the formal electronic configuration $Cu^+Fe^{3+}S_2^{2-}$ (Pearce *et al.*, 2006). The authors concluded that Cu is nominally monovalent ($3d^{10}$), whereas Fe is nominally trivalent ($3d^5$). However, it has been recognized the difficulty in defining a fixed number of electrons for *d* metal orbitals in function of the difficulty of evaluate accurately if the electron density is localized on specific atoms or then delocalized in the chemical bonds among them. In consequence, the copper oxidation state has been considered mixed in character. Edelbro *et al.* (2003) argued that the mineral electronic structure reveals the nature of the bond among S and the transition metal atoms: Half covalent and half formed by delocalized electrons. Its structure has been modeled by clusters $(CuS_4)^{7-}$ and $(FeS_4)^{5-}$ (Vaughan and Tossell, 1983; Vaughan and Rosso, 2006).

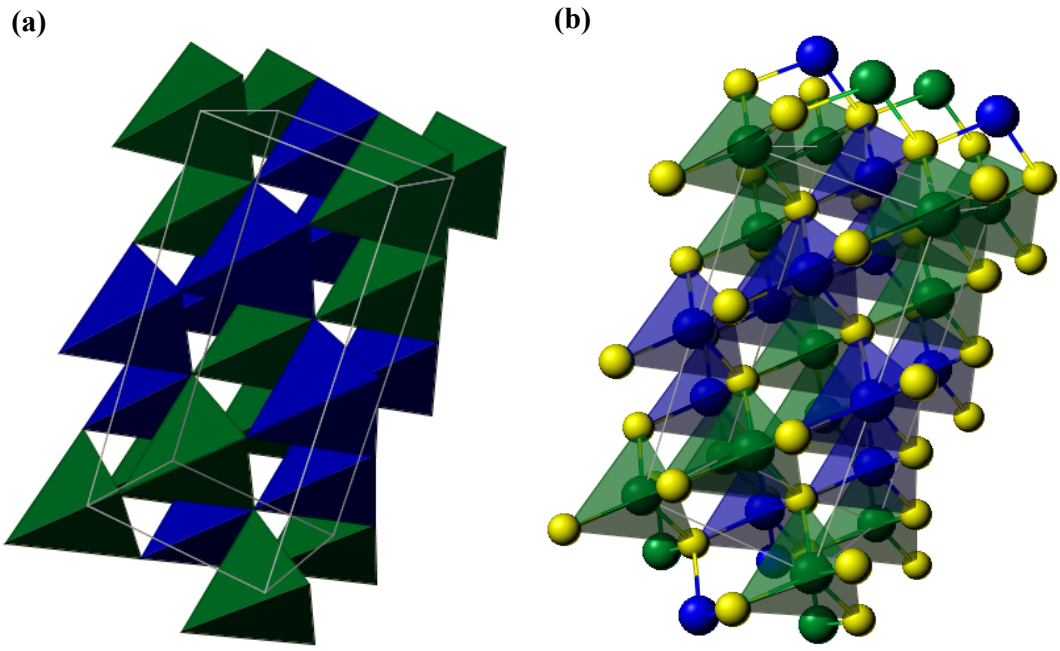

Figure 2.1. $CuFeS_2$: (a) Crystal structure and (b) Atomic arrangement. The yellow spheres represent S atoms, while the blue and green spheres Cu and Fe atoms (Webmineral, 2010).

Several authors claim that the electronic structure and chemical bonds in chalcopyrite characterize its stability and physical properties, such as its electrical conductivity, and that is essential to consider these to understand the electrochemical reactions involved in the dissolution of this mineral, a semiconductor. The influence of electrical properties on the electrochemical behavior of sulfide minerals, such as $CuFeS_2$, FeS_2, ZnS and PbS has been previously discussed (Biegler and Swift, 1979; McMillan *et al.*, 1982; Crundwell, 1988; Mishra and Osseo-Asare, 1988; Osseo-Asare, 1992; Hiskey, 1993; Wei and Osseo-Asare, 1997). However, it is not of the authors' knowledge that a full understanding on the effects of electronic structure and chemical bonds on copper extraction rate is currently available.

2.2.2. Semiconductor character

Chalcopyrite is a semiconductor material with a band gap of 0.5-0.6 eV and mean resistivity of 10^{-2}-10^{-3} Ωm (Biegler and Swift, 1979; McMillan *et al.*, 1982; Hiskey, 1993).

The conduction band edge of chalcopyrite is constituted by Fe 3*d* orbitals, while the valence band edge is Cu 3*d* and S 3*p* in character (Shuey, 1975). A simplified energy-band structure of chalcopyrite is shown in Fig. 2.2a. The highest occupied energy level is the filled Cu 3*d* $4t_{2g}$ antibonding orbital and the lowest unoccupied is the Fe 3*d* $2e_g$ antibonding orbital (Vaughan and Tossell, 1983).

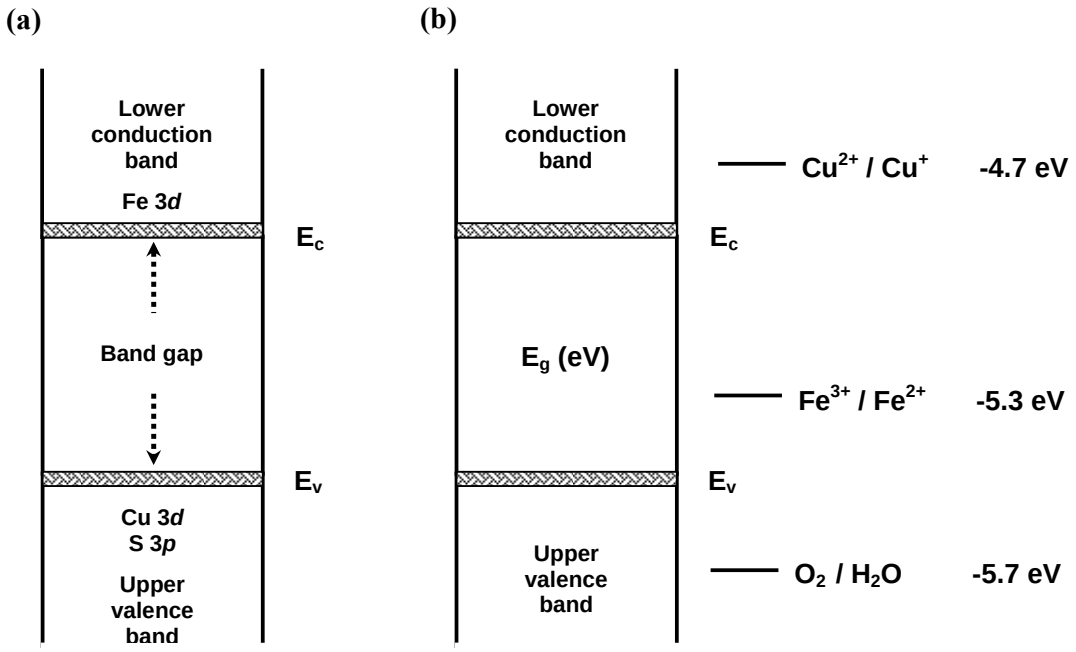

Figure 2.2. (a) Simplified energy-band diagram of chalcopyrite: E_g = band gap; E_v = upper valence band edge; E_c = lower conduction band edge; and (b) Relative position of the energy levels of common redox couples into solution (adapted of Crundwell, 1988).

The relative position of the energy levels of redox couples commonly found in leaching processes such as Cu^{2+}/Cu^{+}, Fe^{3+}/Fe^{2+} and O_2/H_2O, in relation to the energy-band structure of $CuFeS_2$, is indicated in Fig. 2.2b. The position of each redox couple was obtained after conversion of standard redox potentials (E) in units of electron volts (eV) (*i.e.*, E(eV) = - E(V) - 4.5). The couples are usually depicted in terms of a single energy level, which is positioned equidistant of the energy level of the oxidant (E_{oxi}) and that of the reductant (E_{red}). These energy levels are different, since they have different ionic charges and interact

differently with the water dipoles. According to Osseo-Asare (1992), for charge transfer, the energy level of the aqueous species must fluctuate to the same energy as the conduction or valence band of the solid phase. The resulting alignment of these energy levels allows charge transfer to occur. The charge transfer may then be established by comparing the energy levels of the redox couples with the energy bands of the solid. If E_{oxi} is relatively closer to E_c, the electron transfer from the conduction band is the favored pathway for charge transfer. If E_{red} is closer to E_v, hole (h^+) exchange with the valence band is the preferred pathway. In addition, if E_{oxi} is closer to E_v, hole injection into the valence band of the solid takes place. Using this approach, Parker *et al*. (1981) attributed faster chalcopyrite dissolution in the presence of Cu^{2+} ion, comparatively with Fe^{3+} ion, to a good overlap among the energy levels of the mineral conduction band and the corresponding couple (Cu^{2+}/Cu^+).

Biegler and Swift (1979) observed that the anodic oxidation of chalcopyrite in 1.0 mol/L H_2SO_4 solution at high potentials (about 1.3 to 2.5 V *vs.* the Standard Hydrogen Electrode - SHE) under atmospheric conditions is not affected by illumination, but the corresponding experimental evidences have not been provided in this paper. Under lighting, it is expected the creation of holes in the valence band of semiconducting minerals by photoexcitation. When a hole is created the electron originally residing in that bonding orbital is excited to an antibonding orbital in the conduction band, and this loss of bonding electron weakens the interaction among the adjacent atoms, thus favoring the oxidation reaction. Biegler and Swift (1979) then concluded that the semiconducting character of chalcopyrite did not affect its dissolution behavior. It may also be relevant to mention that the redox potential range investigated by them is very different from that found in practical leaching systems, as will be better discussed later.

Experiments conducted by Hiskey (1993) revealed that chalcopyrite typically displays *n*-type semiconduction due to the excess of metal cations (*i.e.*, electron donor elements) in its structure and, therefore, electrons are the main charge carriers in this mineral. This author did not consider a hole dissolution pathway for this sulfide as well. On the contrary, Crundwell (1988) proposed that the anodic oxidation of chalcopyrite takes place with a contribution of holes (from the valence band) and electrons (from the conduction band). It was assumed that the initial step is the reaction with holes, which represents the breaking

of the Fe–S bonds and implies that Cu remains in the crystal lattice (Eq. 2.1). The second step would involve electron (Eq. 2.2) or hole transfer (Eq. 2.3), which represents the breaking of the Cu–S bonds. This mechanism involves the decomposition of an undetected, unstable radical intermediate ($\bullet CuS_2$) to covellite (CuS) (Eq. 2.4).

$$CuFeS_2 + 3\,h^+ \rightarrow Fe^{3+} + \bullet CuS_2 \quad (2.1)$$

$$\bullet CuS_2 \rightarrow Cu^{2+} + 2\,S + 2\,e^- \quad (2.2)$$

$$\bullet CuS_2 + 2\,h^+ \rightarrow Cu^{2+} + 2\,S \quad (2.3)$$

$$\bullet CuS_2 \rightarrow CuS + S \quad (2.4)$$

It is evident from the few papers available in the literature that unresolved controversies exist concerning the mechanisms by which the semiconducting character of chalcopyrite affects its dissolution. The contribution of electrons and holes to the dissolution of this sulfide are still to be investigated.

2.2.3. Thermodynamic stability

It is well-known that the relative thermodynamic stability of metals and minerals into aqueous phase may be used to predict possible dissolution reactions. Garrels and Christ (1965) and Peters (1976) first investigated the thermodynamic stability of chalcopyrite by means of Pourbaix diagrams. Regularly named Eh-pH diagrams, the predominance areas of several species (neutral and ionic) are presented as a function of pH and redox potential scales. Information on the rate and mechanisms of the probable reactions are not provided by these diagrams.

Under atmospheric conditions (25ºC and 1 atm), Pourbaix diagrams by Garrels and Christ (1965) and Peters (1976) indicated that in acid, neutral and alkaline media (pH range 0-14) chalcopyrite is stable at low redox potential values (about -1 V ≤ Eh ≤ 0 V). In acidic media, the extraction of copper (Cu^{2+}) from this mineral depends strongly on the potential.

In pH values lesser than 4, this reaction is favorable only at potentials higher than about 0.40 V *vs.* SHE (*i.e.*, under oxidizing conditions). The equilibrium modeling calculated by Garrels and Christ (1965) and Peters (1976) revealed that chalcopyrite dissolves under oxidizing, non-oxidizing, and also reducing conditions, and that intermediate phases are expected to be formed.

According to calculations made by Garrels and Christ (1965) the oxidation of chalcopyrite may involve the formation of bornite (Cu_5FeS_4), covellite (CuS) and chalcocite (Cu_2S), sulfide phases with decreasing content in iron. Under non-oxidizing conditions (*i.e.*, the dissolution by protonic attack), Cu_5FeS_4 and Cu_2S may be formed, and under reducing conditions, these same products may be formed.

Peters (1976) reported that the oxidation of this mineral may involve the formation of the intermediates CuS and Cu_2S, and also elemental sulfur (S). On the other hand, under non-oxidizing conditions, CuS may be formed, while under reducing conditions, Cu_5FeS_4 and Cu_2S may be produced.

By means of the HSC Chemistry® (v.6) software (HSC Chemistry©, 2007), Pourbaix diagrams were calculated for the Cu-Fe-S-H_2O system under atmospheric conditions (Fig. 2.3). The exhibited simulation was carried out assuming the ideality condition (*i.e.*, the activity coefficient is equal to 1). Only very acidic conditions ($-1 \leq pH \leq 3$) are represented here. It can be observed that Cu^{2+} extraction from $CuFeS_2$ occurs at potentials higher than about 0.40 V *vs.* SHE, a finding similar to those obtained by others. On the basis of thermodynamic, chalcopyrite oxidizes to bornite, covellite and chalcocite. It can be seen that the formation of cuprous oxide (Cu_2O) was predicted at pH around 3 and, in addition, that chalcopyrite oxidizes to ions such as bisulfate (HSO_4^-) and sulfate (SO_4^{2-}) only at high potentials.

Once presented the fundamental properties of chalcopyrite (*i.e.*, structure and bonding, semiconductor character, and thermodynamic stability), the dissolution behavior of this commercial and technological important copper sulfide, during the aqueous processing, will be presented.

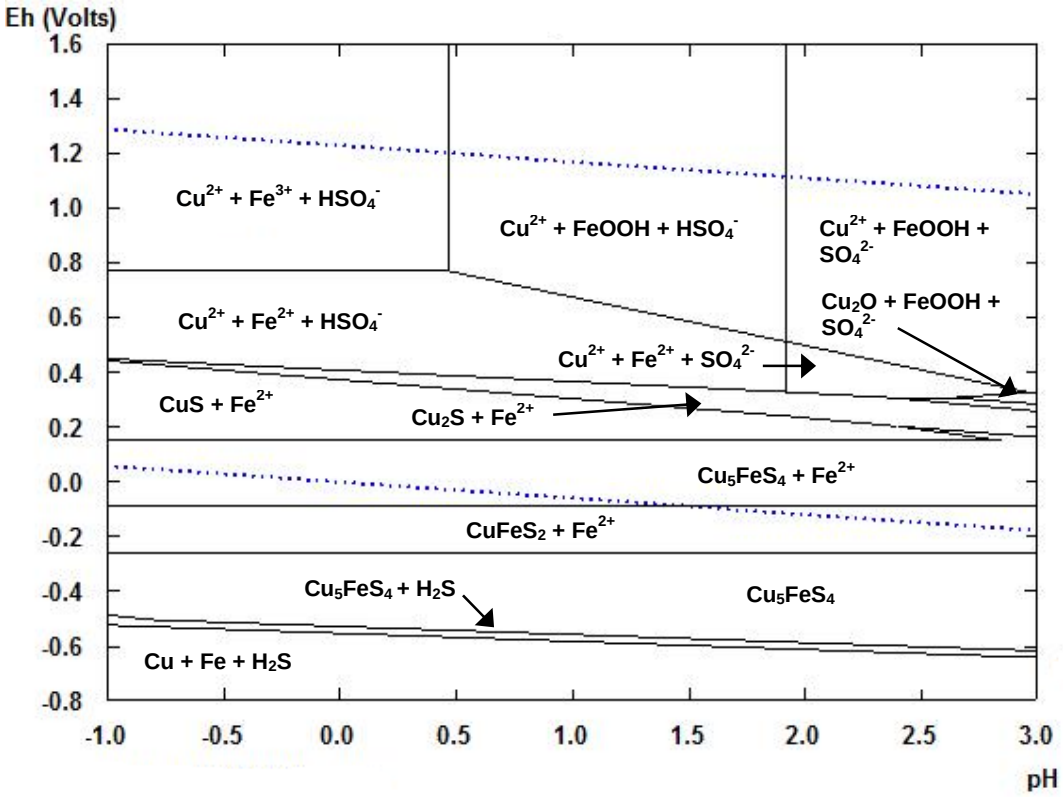

Figure 2.3. Eh-pH diagram for the Cu-Fe-S-H_2O system at 25°C: [S] = 0.1 mol/L; [Fe] = [Cu] = 0.01 mol/L (HSC Chemistry®, version 6).

2.3. Chalcopyrite dissolution

There have been numerous investigations on the dissolution mechanisms of chalcopyrite under atmospheric conditions. The overall processes have being described by the following reactions:

$$CuFeS_2 \rightarrow Cu^{2+} + Fe^{2+} + 2\,S + 4\,e^- \qquad (2.5)$$

$$CuFeS_2 + 8\,H_2O \rightarrow Cu^{2+} + Fe^{3+} + 2\,SO_4^{2-} + 16\,H^+ + 17\,e^- \qquad (2.6)$$

The mineral oxidation rate depends on the redox potential, and as discussed in the last section, at low pH, Cu^{2+} is expected to be leached from chalcopyrite at potentials larger than about 0.40 V *vs.* SHE. On the basis of standard redox potential values (Bockris and

Reddy, 1998; Brett and Brett, 1998), *e.g.*, chalcopyrite oxidation is expected to be more favored in the presence of chlorine (Cl_2) (+1.36 V *vs.* SHE) and oxygen (O_2) (+1.23 V *vs.* SHE) gases, and less favored in the presence of aqueous species as ferric (Fe^{3+}) (+0.77 V *vs.* SHE) and cupric (Cu^{2+}) (+0.16 V *vs.* SHE) ions. However, this hypothesis has not been verified in practice. Peters (1986) observed that ferric ion gives faster sulfide dissolution comparatively with oxygen. The reactivity of these oxidants was also evaluated by Osseo-Asare (1993), according to their electronic structure. The electron transfer between the electron source (*i.e.*, the highest occupied molecular orbital – HOMO) of the sulfide (S^{2-}) and the electron receptor (*i.e.*, the lowest unoccupied molecular orbital – LUMO) of the oxidant follows the order $Cl_{2(g)} > Cu^{2+}_{(aq)} > Fe^{3+}_{(aq)} > O_{2(g)}$, trend which is consistent with experimental evidences. This order of reactivity takes into account the availability of the unoccupied *d* orbitals, constraints on orbital overlap, and also the rearrangement of the electronic configurations.

In spite of this trend, ferric ion has being quite investigated to dissolve chalcopyrite, especially because it is a cheap oxidant and can be regenerated in the hydrometallurgical processes. The dissolution reactions are given by (Jones and Peters, 1976; Dutrizac, 1978; Muñoz *et al*., 1979):

$$CuFeS_2 + 4\,Fe^{3+} \rightarrow Cu^{2+} + 5\,Fe^{2+} + 2\,S \qquad (2.7)$$

$$CuFeS_2 + 16\,Fe^{3+} + 8\,H_2O \rightarrow Cu^{2+} + 17\,Fe^{2+} + 2\,SO_4^{2-} + 16\,H^+ \qquad (2.8)$$

At low temperatures, ferric ion, either in sulfate or chloride media, attacks chalcopyrite slowly and incompletely. The copper leaching rate typically exhibits one of the three behaviors: parabolic, linear and parabolic-linear (Tab. II.3). For the parabolic shape, Cu^{2+} leaching rate becomes very slow, but it not actually stops. In the case of linear, a complete conversion (100% Cu^{2+} leaching) is expected, but this is not attained, except at extended reaction times. When the leaching rate exhibits the parabolic-linear behavior, an initial high leaching rate followed by a decreasing rate, followed by a linear increasing rate is observed. This behavior has been attributed to changes in the morphology of the product layer that develops on the mineral (Jones and Peters, 1976; Ammou-Chokroum *et al*., 1979; Hirato *et al*., 1987a; Maurice and Hawk, 1998; Córdoba *et al*., 2008a; Kauber,

2008). It has been discussed that at the beginning, an elemental sulfur layer forms on chalcopyrite and after growth it peels off, leaving a roughened surface. It causes an increase of the exposed surface area of chalcopyrite and, as a result, the mineral leaching rate becomes linear. Most of authors agree that chalcopyrite dissolution rate in ferric chloride media follows a linear behavior (Jones and Peters, 1976; Dutrizac, 1978, 1981; Palmer *et al*., 1981; Majima *et al*. 1985; Hirato *et al*., 1986; Al-Harahsheh *et al*., 2008), while in sulfate media it is better described by a parabolic pattern (Dutrizac, 1978, 1981; Muñoz *et al*., 1979; Majima *et al*. 1985). This behavior has been often related with the formation of product layers on the mineral, hindering the dissolution reaction. Tab. II.3 also indicates an agreement on the apparent activation energy, which varies from 46 to 69 kJ/mol in chloride, and from 63 to 84 kJ/mol in sulfate media. Based on these values, dissolution kinetics is less dependent on temperature in chloride solutions, and apparent activation energies are within the normal range for leaching processes controlled by reaction (*i.e.*, Ea > 40 kJ/mol). It can be seen that in chloride media, chalcopyrite leaching rate has been considered to be under reaction control, and in sulfate media, it has been assumed to be limited by reaction or electron transfer through an elemental sulfur layer.

The main discrepancies observed in the literature for the leaching kinetics of chalcopyrite are possibly related to the nature of the chalcopyrite sample; the experimental conditions (*i.e.*, oxidant concentration, reaction time and temperature range); and also the method used for calculating the rates. In chloride media, Cu^{2+} leaching rate is directly proportional to the oxidant concentration and a linear kinetics is reported (Jones and Peters, 1976; Ammou-Chokroum *et al*., 1977; Dutrizac, 1978; Palmer *et al*., 1981; Majima *et al*., 1985; Hirato *et al*., 1986). A 0.3 (Ammou-Chokroum *et al*., 1977; Jones and Peters, 1976) and 0.5 reaction orders (Palmer *et al*., 1981; Majima *et al*., 1985; Hirato *et al*., 1986) with respect to the Fe^{3+} ion concentration have been obtained. Dutrizac (1978) found a 0.8 reaction order for synthetic samples and a 0.3 for natural samples. In sulfate solutions, Dutrizac (1981) reported that the leaching rate depends on the Fe^{3+} ion concentration below 0.01 mol Fe^{3+}/L, but it is independent above this value. In agreement, Dutrizac (1978) and Muñoz *et al.* (1979) found a zero reaction order with respect to the oxidant concentration larger than 0.01 mol Fe^{3+}/L. Regarding the calculation of rates, it is well-known that data fitting depends on the number of experimental points, and this factor is not similar in these investigations.

Table II.3. Leaching kinetics of chalcopyrite in ferric sulfate and ferric chloride solutions: Curve shape, apparent activation energy (Ea, in kJ/mol) and rate-determining step.

References	Leaching conditions	Curve	Ea	Rate-determining step
Jones and Peters, 1976	0.5 mol/L $Fe_2(SO_4)_3$ - 0.2 mol/L H_2SO_4; 90°C	L	-	Electrochemical reaction
	1.0 mol/L $FeCl_3$ - 0.2 mol/L HCl; 90°C	L	-	Electrochemical reaction
Dutrizac, 1978*	0.05 mol/L $Fe_2(SO_4)_3$ - 0.3 mol/L H_2SO_4; 50-100°C	P	63	Chemical reaction
	0.1 mol/L $FeCl_3$ - 0.3 mol/L HCl; 50-100°C	L	46	Chemical reaction
Ammou-Chokroum *et al*., 1979*	$FeCl_3$ - HCl (pH 0-3; 0.45-0.70 V SHE); 25-70°C	P-L	29-42	Mixed control
Muñoz *et al*., 1979	0.25 mol/L $Fe_2(SO_4)_3$ - 1.0 mol/L H_2SO_4; 60-90°C	P	84	Electron transfer
Dutrizac, 1981	0.1 mol/L $Fe_2(SO_4)_3$ - 0.3 mol/L H_2SO_4; 40-100°C	P	75	Chemical reaction
	0.2 mol/L $FeCl_3$ - 0.3 mol/L HCl; 40-100°C	L	63	Chemical reaction
Palmer *et al*., 1981	0.1 mol/L $FeCl_3$ - 1.0 mol/L HCl; 75-96°C	L	62	Electrochemical reaction
Majima *et al*., 1985	0.5 mol/L $Fe_2(SO_4)_3$ - 0.2 mol/L H_2SO_4; 70°C	P	-	-
	1.0 mol/L $FeCl_3$ - 0.2 mol/L HCl; 55-85°C	L	69	Chemical reaction
Hirato *et al*., 1986	0.1 mol/L $FeCl_3$ - 0.2 mol/L HCl; 52-85°C	L	69	Electrochemical reaction
Hirato *et al*., 1987b	0.05 mol/L $Fe_2(SO_4)_3$ - 0.2 mol/L H_2SO_4; 50-78°C	P-L	77-88	Chemical reaction
Hackl *et al*., 1995	5 g/L $Fe_2(SO_4)_3$ - 98 g/L H_2SO_4 - $CuSO_4$; 110°C	P-L	-	Mixed control
Maurice and Hawk, 1998	1.0 mol/L $FeCl_3$ - 0.25 mol/L HCl; 60-90°C	P-L	68	-
Al-Harahsheh *et al*., 2008	0.5 mol/L $FeCl_3$ - 0.5 mol/L HCl; 70-90°C	L	69	Chemical reaction
Córdoba *et al*., 2008b	$Fe_2(SO_4)_3$/$FeSO_4$ - H_2SO_4 (pH 1.8; 0.60 V SHE); 35-68°C	P-L	131	Chemical reaction

Legend: L = Linear shape; P = Parabolic shape; Ea = Apparent activation energy.

* Experiments conducted with synthetic samples.

In an effort to improve the knowledge on the nature of the product layers that forms on chalcopyrite during its dissolution in acidic media at low temperatures and affects the reaction rate, many characterization techniques such as X-ray photoelectron spectroscopy (XPS), X-ray diffraction (XRD), small angle X-ray diffraction (SAXRD), X-ray absorption spectroscopy (XAS), Raman spectroscopy (RS), mineral liberation analyses (MLA), and scanning electron microscopy (SEM) coupled with energy dispersive spectrometry (EDS) or electron probe micro-analyses (EPMA), have been applied (Tab. II.4). It may be noted that elemental sulfur has been commonly detected as a product phase of chalcopyrite dissolution in both ferric sulfate and ferric chloride media. Many authors have claimed that the formation of elemental sulfur in ferric sulfate solutions is responsible for the observed hindered dissolution effect (*i.e.*, the slow and parabolic leaching kinetics) (Muñoz *et al*., 1979; Dutrizac, 1981, 1989; Majima *et al*. 1985; Hirato *et al*., 1987). In contrast, in ferric chloride solutions linear kinetics with the formation of a porous elemental sulfur layer, throughout which soluble products and reactants can diffuse, have been reported (Jones and Peters, 1976; Ammou-Chokroum *et al*., 1979; Majima *et al*., 1985; Dutrizac, 1981, 1990). The formation of the elemental sulfur layer has been reported to take place at broad potential range, from 0.50 to 1.50 V *vs.* SHE (Ammou-Chokroum *et al*., 1979; Biegler and Swift, 1979; Warren *et al*., 1982; Yin *et al*., 1995; Klauber *et al*., 2001; Parker *et al*., 2003; Viramontes-Gamboa *et al*., 2007; Córdoba *et al*., 2008; Parker *et al*., 2008).

As the oxidation of chalcopyrite to elemental sulfur involves more than one electron transfer (Eq. 2.5). the overall reaction may involves steps with formation of sulfur species of intermediate oxidation states, since electron transfer reactions are typically limited to one, or at most two electrons. Many authors have claimed the formation of disulfide (S_2^{2-}) and polysulfides (S_n^{2-}) on oxidized chalcopyrite (Parker *et al*., 1981; Hackl *et al*., 1995; Yin *et al*., 1995; Mikhlin *et al*., 2004; Ghahremaninezhad *et al*., 2010). By synchrotron XPS, Acres *et al*. (2010) detected disulfide and polysulfides on chalcopyrite samples after leaching in chloride solutions (pH ≈ 1), under atmospheric conditions. The formation of disulfide on oxidized chalcopyrite was also confirmed by XPS analysis (Klauber *et al*., 2001; Parker *et al*., 2003) and density functional theory (DFT) calculations (Oliveira and Duarte, 2010).

Table II.4. *Ex situ* analysis of chalcopyrite after dissolution in acidic solutions under atmospheric conditions.

Reference	**Experimental conditions**	**Phase(s) detected and technique**
Jones and Peters, 1976	Particles (-400 mesh), 0.2 M H_2SO_4, 0.5 M $Fe_2(SO_4)_3$, 90°C, 71 h	Elemental sulfur (S) by SEM
Linge, 1976	Particles (0.22 m^2/g), 10^{-2} M HNO_3, 10^{-4} M $Fe(NO_3)_3$ 10^{-3} M $Fe(NO_3)_2$, 25-40°C, 2.5 h, N_2	S by carbon disulfide (CS_2)
Ammou-Chokroum *et al*., 1979	Particles (size not reported), HCl (pH 1-3), 0.4-0.7 V *vs.* SCE, 1.0-4.0 M NaCl, 50-75°C	S by powder XRD
Biegler and Swift, 1979	Electrodes, 1.0 M H_2SO_4, 1.0 V *vs.* SHE, 25°C, 18 h, N_2	S by SEM coupled with EPMA
Muñoz *et al*., 1979	Particles (4 to 47 mm), 1.0 M H_2SO_4, 0.25 M $Fe_2(SO_4)_3$, 95°C, 150 h	S by SEM coupled with EDS
Warren *et al*., 1982	Electrodes, 1.0 M H_2SO_4, 1.09 V *vs.* SHE, 25°C, 17-84 h	S by SEM coupled with EDS
Majima *et al*., 1985	Particles, 0.2 M H_2SO_4, 0.5 M $Fe_2(SO_4)_3$, or 0.2 M HCl, 1.0 M $FeCl_3$, 85°C, 120 h	S by SEM coupled with EPMA
Hirato *et al*., 1987	Particles, 0.2 M H_2SO_4, 0.5 M $Fe_2(SO_4)_3$, 85°C, 432 h	S by SEM coupled with EPMA
Dutrizac, 1989	Particles (-14+10 μm), 0.3 M H_2SO_4, 0.15 M $Fe_2(SO_4)_3$ 95°C, 1-72 h	S by SEM/EDS
Yin *et al*., 1995	Electrodes, 1.0 M $HClO_4$, 0.5-1.8 V *vs.* SCE, 25°C, N_2	S by XPS
Klauber *et al*., 2001	Particles (31 μm), H_2SO_4 (pH 1.3-1.9), 0.2 M $Fe_2(SO_4)_3$ 0.1 M $FeSO_4$, 50-80°C, 2 h	Elemental sulfur (S_8) and disulfide (S_2^{2-}) by XPS
Abraitis *et al*., 2004	Particles (-45+150 μm), HCl (pH 2.5), 0.3 V *vs.* SHE 25ºC, 3 h	Sulfate (SO_4^{2-}) by XPS

(Cont.) Table II.4. *Ex situ* analysis of chalcopyrite after dissolution in acidic solutions under atmospheric conditions.

Reference	Experimental conditions	Phase(s) detected and technique
Mikhlin *et al*., 2004	Particles (64 μm), 0.5 M H_2SO_4, 0.2 M $Fe_2(SO_4)_3$ or 1.0 M HCl, 0.4 M $FeCl_3$, 50°C, 1 h	S_8 by powder XRD, XPS and XAS
Carneiro and Leão, 2007	Particles (5.5 μm), H_2SO_4 (pH 0.15), 0.45 L O_2/min, 0-2 mol/L NaCl, 25 g/L $Fe_2(SO_4)_3$ 95°C, 10 h	S by powder XRD
Viramontes-Gamboa *et al*., 2007	Particles (size not reported), H_2SO_4 (15-30 g/L), 0.5-0.7 V *vs.* SCE, 80°C	S by SEM
Córdoba *et al*., 2008b	Particles (70 μm), H_2SO_4 (pH 1.8) + nutrient, 0.3-0.6 V *vs.* Ag/AgCl, 35-68°C	S, CuS, goethite (FeOOH) and jarosite by powder XRD
Parker *et al*., 2008	Electrodes, 0.1 M HCl, 0.57 V *vs.* Ag/AgCl, 24 h, 25°C	S_8 by RS
Sasaki *et al*., 2009	Particles (size not reported), H_2SO_4 (pH 2) + nutrient, 25°C, 3-81 days	S_8, CuS and jarosite by RS
Velásquez-Yévenes *et al*., 2010	Particles (-38+25 μm or -38 μm), 0.2 M HCl, 0.45 V vs. Ag/AgCl, 35°C, 936 h	CuS by MLA

Legend: SCE – Saturated Calomel Electrode (+0.241 *vs*. SHE at 25ºC); Ag/AgCl – Silver / Silver chloride Electrode (+0.207 *vs*. SHE at 25ºC, 3.0 mol/L KCl).

From Eq. 2.6, it can be noticed that the oxidation of chalcopyrite to sulfate ion (SO_4^{2-}) involves 17 electron transfers. Similarly, the overall reaction may involve steps with formation of sulfur species of intermediate oxidation states. Results by Lázaro and Nicol (2006) indicated that, under oxidative conditions, the formation of thiosulfate ion ($S_2O_3^{2-}$) would be expected to occur during chalcopyrite oxidation in acidic solution (Eq. 2.9). However, the number of electrons of this equation also implies in the formation of other intermediate sulfur species during the dissolution process.

$$CuFeS_2 + 3\,H_2O \rightarrow Cu^{2+} + Fe^{2+} + S_2O_3^{2-} + 6\,H^+ + 8\,e^- \qquad (2.9)$$

In order to better understanding the chalcopyrite oxidation mechanism at low temperatures, especially at redox potentials typically found in practical leaching systems, electrochemical techniques have been quite applied (Tab. II.5). The use of potentiometric and voltammetric methods allows establishing essential information on the behavior of this mineral, such as the potential range where the active and passive behaviors prevails; and also fundamental parameters, such as the critical potential and the steady-state current. The nature of the product phases has also been investigated by means of electrochemical methods. As will be discussed in the next sections, despite the large number of papers available in the literature, there are many inconsistencies on the dissolution mechanisms of chalcopyrite, and there are many uncertainties regarding the formation of intermediate layers on chalcopyrite, its nature and effect on the mineral dissolution rate.

2.3.1. Anodic oxidation

Anodic polarization measurements of chalcopyrite electrodes depict the anodic prewave, that is, a potential-independent region occurring at potentials lower than those of the main peak (Fig. 2.4). In such region, when the critical or transpassive potential is reached, the oxidation current becomes strongly dependent on potential. The anodic prewave has been detected in an interval of 0.35 and 0.90 V *vs.* SHE (Biegler and Swift, 1979; Warren *et al.*, 1982; Biegler and Horne, 1985; Yin *et al.*, 1995; Arce and González, 2002; Lázaro and Nicol, 2003; Mikhlin *et al.*, 2004; Nava and González, 2006; Parker *et al.*, 2008; Ghahremaninezhad *et al.*, 2010, but this range depends on the nature of the mineral sample

used for preparing the electrodes (*i.e.*, elemental stoichiometry and minor impurities on the reaction area, defects and crystal orientation given that polycrystalline samples are used); experimental conditions (*i.e.*, acidity, temperature, potential range and scan rate); and time of immersion of the electrode prior to the application of potential.

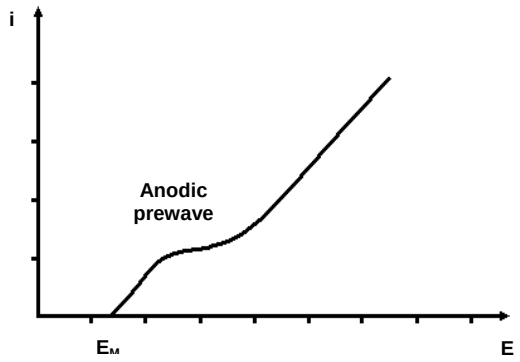

Figure 2.4. Typical linear sweep voltammogram for a chalcopyrite electrode.

The detection of the anodic prewave in polarization curves of chalcopyrite electrodes has been attributed to the formation of intermediate non-stoichiometric product phases on the mineral (Eq. 2.10), where y is larger than x (Ammou-Chokroum *et al.*, 1979; Biegler and Swift, 1979; Warren *et al.*, 1982).

$$CuFeS_2 \rightarrow Cu_{1-x}Fe_{1-y}S_{2-z} + x\,Cu^{2+} + y\,Fe^{2+} + z\,S + 2(x+y)\,e^- \qquad (2.10)$$

The identification of intermediate iron-deficient sulfides on chalcopyrite has important practical implications, since the potential range of the anodic prewave includes potential values expected for the ferric ion leaching of copper ores (*i.e.*, potential of about +0.77 V *vs.* SHE). Many authors have claimed that metal-deficient sulfides are formed at low temperatures (Linge, 1976; Biegler and Swift, 1979; Warren *et al.*, 1982; Biegler and Horne, 1985; Yin *et al.*, 1995; Arce and González, 2002; Lázaro and Nicol, 2003; Abraitis *et al.*, 2004; Mikhlin *et al.*, 2004; Nava and González, 2006; Parker *et al.*, 2008; Ghahremaninezhad *et al.*, 2010), and the formation of these products is often linked to the observed hindered dissolution effect: that is, the layer inhibits the reaction progress.

Table II.5. Experimental conditions and electrochemical techniques applied in investigations of chalcopyrite dissolution in acidic solutions.

References	Electrochemical system	Electrochemical method
Biegler and Swift, 1979	TC; RRDE (3000 rpm); 25°C; N_2 1.0 mol/L H_2SO_4 or 1.0 mol/L HCl	LSV (E ≈ 0.4-1.2 V SHE; υ = 20 mV/s) CA (E ≈ 0.99-1.19 V SHE)
Warren *et al*., 1982	TC; ME; MS; 0.01-1.0 mol/L H_2SO_4; 25°C 0.002-0.8 mol/L Fe^{2+} or Cu^{2+}	LSV (E ≈ 0.59-1.04 V SHE; υ = 30 mV/s) CA (E ≈ 0.59-1.04 V SHE)
Biegler and Horne, 1985	TC; RRDE (3000 rpm); 25°C; N_2 1.0 mol/L (H_2SO_4, HCl, HNO_3 or $HClO_4$)	LSV (E ≈ 0.24-0.94 V SHE; υ = 20 mV/s) CV (E ≈ -0.21-0.94 V SHE; υ = 20 mV/s)
Price and Warren, 1986	TC; ME; 1.0 mol/L H_2SO_4; 25°C 0-0.001 mol/L Ag^+	CV (E ≈ -0.2-1.0 V SHE; υ = 10 mV/s) CV (E ≈ 0.0-1.4 V SHE; υ = 10 mV/s)
Yin *et al*., 1995	TC; ME; 1.0 mol/L HCl or $HClO_4$; 25°C	LSV (E ≈ -0.25-0.56 V SHE; υ = 20 mV/s)
Lu *et al*., 2000b	TC; CPE; 1.0 mol/L H_2SO_4; 20°C; N_2 0-0.5 mol/L NaCl	CV (E ≈ -0.4-1.1 V SHE; υ = 20 mV/s) CA (E ≈ 0.615-0.815 V SHE)
Arce and González, 2002	TC; CPE; 2.0 mol/L H_2SO_4; 25°C; N_2	CV (E ≈ -0.40-0.55 V SHE; υ = 30 mV/s)
Elsherief, 2002	TC; CPE; 1.0 mol/L H_2SO_4; 20°C 0-0.27 mol/L Fe^{2+}; 0.002-0.14 mol/L Cu^{2+}	CV (E ≈ -1.25-1.00 V SHE; υ = 20 mV/s) CA (E ≈ 0.55 V SHE)
Lázaro and Nicol, 2003	TC; ME; 0.1 mol/L H_2SO_4; 60°C	CV (E ≈ 0.45-0.95 V SHE; υ = 5 mV/s) CA (E ≈ 0.50-0.75 V SHE)
Hiroyoshi *et al*., 2004	TC; ME; MS; 0.1 mol/L H_2SO_4; 25°C 0-0.1mol/L Fe^{2+} or Cu^{2+}; N_2	LSV (E ≈ 0.45-0.95 V SHE; υ = 10 mV/s) EIS (amplitude = 5 mV; frequency = 10^5-10^{-1} Hz)

(Cont.) Table II.5. Experimental conditions and electrochemical techniques applied in investigations of chalcopyrite dissolution in acidic solutions.

References	Electrochemical system	Electrochemical method
Mikhlin *et al*., 2004	TC; ME; 1.0 mol/L HCl - 0.4 mol/L $FeCl_3$ or 0.5 mol/L H_2SO_4 - 0.2 mol/L $Fe_2(SO_4)_3$; 20°C	LSV (E ≈ -0.2-1.0 V SHE; υ = 5 mV/s)
Lázaro and Nicol, 2006	TC; RRDE (200 rpm); 0.1 mol/L H_2SO_4; N_2 0.01-1.0 mol/L Fe^{3+}; 60°C	CV (E ≈ 0.4-0.9 V SHE; υ = 5 mV/s) AS (E ≈ 0.05-0.8 V SHE; E_{ring} = -0.06 V SHE)
Nava and González, 2006	TC; CPE; 1.7 mol/L H_2SO_4; 25°C; N_2	CV (E ≈ 0.62-1.58 V SHE; υ = 100 mV/s) CA (E ≈ 0.62-1.22 V SHE)
Viramontes-Gamboa *et al*., 2007	TC; ME; 0.02-1.0 mol/L H_2SO_4; 25-80°C N_2	LSV (E ≈ 0.44-1.24 V SHE; υ = 10 mV/s) CA (E ≈ 0.74-0.99 V SHE)
Hiroyoshi *et al*., 2008	TC; ME; MS; 0.01-1.0 mol/L H_2SO_4; 25°C 0.001-0.1 mol/L Fe^{3+}, Fe^{2+} or Cu^{2+}; N_2	LSV (E ≈ 0.45-0.95 V SHE; υ = 10 mV/s)
Nava *et al*., 2008	TC; CPE; 1.7 mol/L H_2SO_4; 25°C; N_2	CV (E ≈ -0.385-0.695 V SHE; υ = 100 mV/s)
Ghahremaninezhad *et al*., 2010	TC; ME; 0.5 mol/L H_2SO_4; 25°C	LSV (E ≈ 0.24-2.04 V SHE; υ = 0.05-50 mV/s) EIS (amplitude = 10 mV; frequency = 10^5-10^{-2} Hz)

Legend: TC = three electrode cell; ME = massive electrode; RRDE = rotating ring-disk electrode; CPE = carbon paste electrode; MS = magnetic stirred system; EIS = electrochemical impedance spectroscopy; AS = anodic stripping; CA = chronoamperometry; CV = cyclic voltammetry; LSV = linear sweep voltammetry; E = applied potential; υ = scan rate.

Nava and González (2006) (Tabs. II.4 and II.5) reported that the anodic oxidation of chalcopyrite in acidic sulfate solutions at low potentials occurs to form a passive metal-deficient sulfide phase ($Cu_{1-r}Fe_{1-s}S_{2-t}$), where s > r. At higher potentials, this product oxidizes forming a porous layer of another metal-deficient sulfide ($Cu_{1-x}Fe_{1-y}S_{2-z}$). Thus, at least two non-stoichiometric products would be involved in chalcopyrite dissolution. Warren *et al.* (1982) (Tabs. II.4 and II.5) investigated the anodic oxidation of chalcopyrite in acidic media as well. Two intermediate phases have also been considered: the first one, which inhibits the oxidation reaction, at about 0.50 V *vs.* SHE, via preferential release of Fe over Cu (Eq. 2.10); and the second one, at 0.70 V *vs.* SHE, via congruent release of Fe and Cu (Eq. 2.11). On the basis of thermodynamic analysis, these authors suggested the formation of bornite (Cu_5FeS_4), a typical iron-deficient sulfide, and covellite (CuS) as the intermediate phases. The authors proposed that at E < 0.70 V *vs.* SHE, the magnitude of the anodic current is associated with the oxidation of these intermediate phases: Cu_5FeS_4 oxidation to CuS and, successively, to S, through consecutive steps (Eqs. 2.11 and 2.12) or, then, directly (Eq. 2.13). At E > 0.70 V *vs.* SHE (*i.e.*, in the transpassive region), the oxidation of these intermediate products would still occur, but the corresponding anodic current would be negligible compared with the anodic current of chalcopyrite oxidation (Eqs. 2.5 and 2.6).

$$Cu_{1-x}Fe_{1-y}S_{2-z} \rightarrow (2-z)\,CuS + (-1-x+z)\,Cu^{2+} + (1-y)\,Fe^{2+} + 2(-x-y+z)\,e^- \quad (2.11)$$

$$CuS \rightarrow Cu^{2+} + S + 2e^- \quad (2.12)$$

$$Cu_{1-x}Fe_{1-y}S_{2-z} \rightarrow (1-x)\,Cu^{2+} + (1-y)\,Fe^{2+} + (2-z)\,S + 2(2-x-y)\,e^- \quad (2.13)$$

Without experimental evidence, the formation of bornite as an intermediate product of chalcopyrite oxidation was also suggested in the anodic prewave region by Kelsall and Page (1984):

$$5\,CuFeS_2 \rightarrow Cu_5FeS_4 + 4\,Fe^{3+} + 6\,S + 12\,e^- \quad (2.14)$$

Yin *et al.* (1995) (Tabs. II.4 and II.5) suggested bornite as a possible intermediate product phase of chalcopyrite oxidation at E < 0.77 V *vs.* SHE. However, the authors mentioned

that polarization curves of bornite electrodes (not discussed in their paper) have indicated that this phase oxidizes at lower potential than chalcopyrite, suggesting that the iron-deficient sulfide could not cause the hindered dissolution of chalcopyrite.

With respect to the formation of covellite as an intermediate product (vide Eq. 2.10), it has also been suggested by Jones and Peters (1976), Ammou-Chkroum *et al*. (1979), Biegler and Horne (1985), Nava and González (2006) and Ghahremaninezhad *et al*. (2010) on the basis of the preferential leaching of Fe over Cu and electrochemical results, mainly by cyclic voltammetry. By using MLA and conventional powder XRD, respectively, CuS was positively detected on mineral particles after leaching in chloride (Velásquez-Yévenes *et al*., 2010) and sulfate media (Córdoba *et al*., 2008) at potentials around 0.60 V *vs.* SHE (Tab. II.4). By using Raman spectroscopy, Sasaki *et al*. (2009) (Tab. II.4) detected CuS as a passive intermediate product phase on chalcopyrite particles after bioleaching in acidic media under atmospheric conditions.

Covellite has also been considered an intermediate product of bornite oxidation in acidic media at low temperatures (Warren *et al*., 1982; Arce and González, 2002). This phase was positively detected on oxidized bornite by means of powder XRD (Pesic and Olson, 1984; Bevilaqua*et al*., 2010).

The anodic oxidation of chalcopyrite was investigated by Hiroyoshi *et al*. (2004) (Tab. II.5) in acidic sulfate media in the presence of both Cu^{2+} and Fe^{2+} ions (Fig. 2.5), ions which are first released during the reaction. The anodic current increased with potential to reach a peak in the active region (I) (E ≈ 0.70-0.85 V *vs.* SHE), and decreased in the transient region (II) (E ≈ 0.85-0.91 V *vs.* SHE), which was ascribed to the growth of a passive layer. In the passive region (III) (E ≈ 0.91-1.01 V *vs.* SHE), potential-independent current was registered. In the transpassive region (IV) (E > 1.01 V *vs.* SHE), the current increased, which was assumed to be caused by the passive layer oxidation. These authors assumed that the rate-determining steps are the reaction in the active region and diffusion through the passivating layer in the passive region. By impedance spectroscopy, the formation of two product layers was proposed in region (I). The inhibition of the passive layer growth in this region is related to chalcocite (Cu_2S) oxidation (Eqs. 2.15 and 2.16). It was discussed that as the second reaction is slower, the elemental sulfur layer does not

form when Cu_2S is present on chalcopyrite. In the transient region, the oxidation rate of Cu_2S becomes higher than the formation rate and in the passive region, Cu_2S does not form, only the elemental sulfur layer grows up.

$$Cu_2S \rightarrow Cu_{2-x}S + x\,Cu^{2+} + 2x\,e^- \quad (1 \geq x > 0) \tag{2.15}$$

$$CuS \rightarrow S + Cu^{2+} + 2\,e^- \tag{2.16}$$

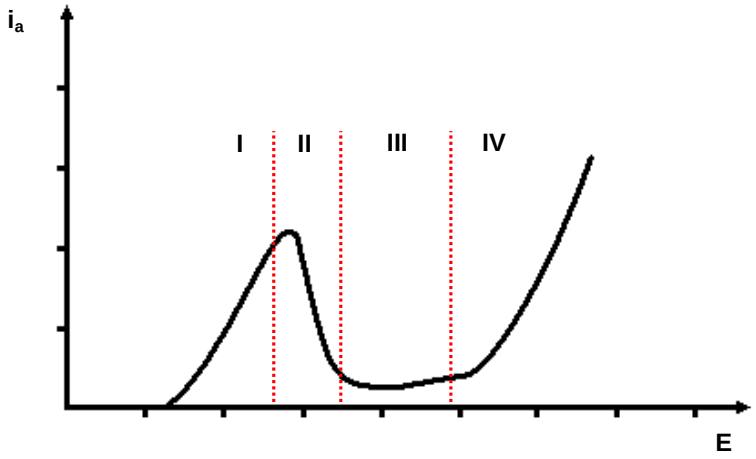

Figure 2.5. Electrochemical behavior of anodic polarized chalcopyrite electrode in acidic sulfate solution containing ferrous and cupric ions (adapted of Hiroyoshi *et al*., 2004).

On the basis of thermodynamic modeling, Hiroyoshi *et al*. (2001) proposed that in the presence of enough Fe^{2+} and Cu^{2+} ions, chalcopyrite is reduced by Fe^{2+} ions to form Cu_2S (Eq. 2.17). These authors also assume that the elemental sulfur layer hinders the progress of the oxidation reaction.

$$CuFeS_2 + 3\,Cu^{2+} + 3\,Fe^{2+} \rightarrow 2\,Cu_2S + 4\,Fe^{3+} \tag{2.17}$$

In light of the above review, it becomes evident that there are considerable advances on chalcopyrite oxidation mechanisms by combining leaching and electrochemical methods with *ex situ* characterization tools. And since the practical, typical dissolution processes of

copper ores are designed at oxidizing conditions, the oxidation of chalcopyrite has received considerable more attention than the reduction processes of this mineral.

From electrochemical measurements conducted with different cathodic limits (*i.e.*, the minimum potential value), particular reduction current peaks have been registered and it has been proposed the reduction of chalcopyrite to intermediate phases such as talnakhite ($Cu_9Fe_8S_{16}$), bornite and chalcocite (Lu *et al.*, 2000b; Elsherief, 2002; Arce and González, 2002; Nava *et al.*, 2008). The reactions have been described as:

$$9\ CuFeS_2 + 4\ H^+ + 2\ e^- \rightarrow Cu_9Fe_8S_{16} + Fe^{2+} + 2\ H_2S \quad (2.18)$$

$$9\ CuFeS_2 + 12\ H^+ + 4\ e^- \rightarrow Cu_5FeS_4 + 4\ Fe^{2+} + 6\ H_2S \quad (2.19)$$

$$2\ CuFeS_2 + 6\ H^+ + 2\ e^- \rightarrow Cu_2S + 2\ Fe^{2+} + 3\ H_2S \quad (2.20)$$

By cyclic voltammetry, Arce and González (2002) (Tab. II.5) claimed that the absence of cathodic current peaks related to covellite and bornite reductions, after the anodic sweep of chalcopyrite electrodes in acidic sulfate media, suggests that the oxidation mechanism of this sulfide does not involve the formation of these intermediates. However, CuS and Cu_5FeS_4 have been positively detected on oxidized chalcopyrite samples.

By cyclic voltammetry and XPS, Nava *et al.* (2008) (Tab. II.5) investigated the nature of products formed at different potential pulses on chalcopyrite electrodes in acidic sulfate solutions. In the potential region $0.115 \geq E \geq -0.085$ V *vs.* SHE, the formation of an intermediate copper sulfide, such as talnakhite, was observed. The reduction of this product phase to bornite occurs at $E < -0.085$ V *vs.* SHE. In the interval $-0.085 \geq E$ -0.185 V *vs.* SHE, bornite converts incompletely to chalcocite. At $-0.185 > E \geq -0.285$ V *vs.* SHE, fast bornite conversion to chalcocite was detected.

Fuentes-Aceituno *et al.* (2008) proposed an electrochemical model in which transient hydrogen (H•) reduces chalcopyrite (Eq. 2.21), H• being formed at inert cathodes (Eq. 2.22). The intermediate product Cu_2S would be easier oxidized, thereby allowing Cu^{2+} extraction. The authors suggested that the reduction kinetics is controlled by the generation

rate of H• and its transportation to the reacting interface, however enough experimental evidences of this mechanism were not provided.

$$2\ CuFeS_2 + 2\ H\bullet + 4\ H^+ \rightarrow Cu_2S + 3\ H_2S + 2\ Fe^{2+} \quad (2.21)$$

$$H^+ + e^- \rightarrow H\bullet \quad (2.22)$$

Complementing the oxidation mechanisms of chalcopyrite in acidic media at low temperatures, main focus of this paper, a critical review on the qualitative and quantitative galvanic effect on the oxidation rate of chalcopyrite is presented in the next section.

2.3.2. Galvanic interaction

Among the efforts for improving chalcopyrite oxidation rate at low temperatures, the effect of catalysts has being quite investigated. Metallic copper (Cu) (Hiskey and Wadsworth, 1975) and gold (Au) (Lorenzen and Denventer, 1992); manganese dioxide (MnO_2) (Madhuchhanda *et al*., 2000); metallic ions such as bismuth (Bi^{3+}) and mercury (Pb^{2+}) (Mateos *et al*., 1987; Gómez *et al*. 1997; Hiroyoshi *et al*., 2007) and mainly silver (Ag^+) (Miller and Portillo, 1979; Miller *et al*., 1981; Warren *et al*., 1984; Price and Warren, 1986; Hiroyoshi *et al*., 2002, 2007; Parker *et al*., 2003; Nazari *et al*., 2011); chloride (Cl^-) ions (Dutrizac, 1978, 1981, 1992; Palmer *et al*., 1981; Majima *et al*., 1985; Hirato *et al*., 1986, 1987; Lu *et al*., 2000b; Carneiro and Leão, 2007; McDonald and Muir, 2007b); carbon (C) particles (Wan *et al*., 1984; Nakazawa *et al*., 1998; Liang *et al*., 2010); silver sulfide (Ag_2S) (Mateos *et al*., 1987; Scaini *et al*., 1995); and pyrite (FeS_2) (Berry *et al*., 1978; Mehta and Murr, 1983; Nowak *et al*., 1984; Abraitis *et al*., 2004; You *et al*., 2007; Dixon *et al*., 2008; Miller *et al*., 2008; Littlejohn and Dixon, 2008; Nazari *et al*., 2011), generally enhance the reaction kinetics by promoting a different dissolution mechanism.

It is well-established that galvanic interactions increase the oxidation rate of one of the minerals that constitute a galvanic couple. The galvanic effect occurs when conducting or semiconducting minerals are in intimate contact in a medium that allows charge transfer. This electrochemical interaction may be understood by the anodic and cathodic half-cell

reactions that occur at the mineral surfaces. The mineral with the higher mixed potential (E_M) acts as the cathode in the galvanic couple and is protected, while the mineral with the lower mixed potential serves as the anode and, thus, dissolves preferentially (Nowak *et al.*, 1984; Rao and Finch, 1988; Holmes and Crundwell, 1995). The enhancement of copper extraction from chalcopyrite when in contact with Cu and Au, MnO_2, Ag_2S, C, and FeS_2, has been attributed to galvanic effects. Fig. 2.6 exemplifies the interaction involving chalcopyrite and pyrite. It may be noticed that electrons are released from $CuFeS_2$ during the oxidation and then transferred to FeS_2, giving rise to the galvanic current. A similar electrochemical cell is operative when chalcopyrite is in contact with the phases mentioned above.

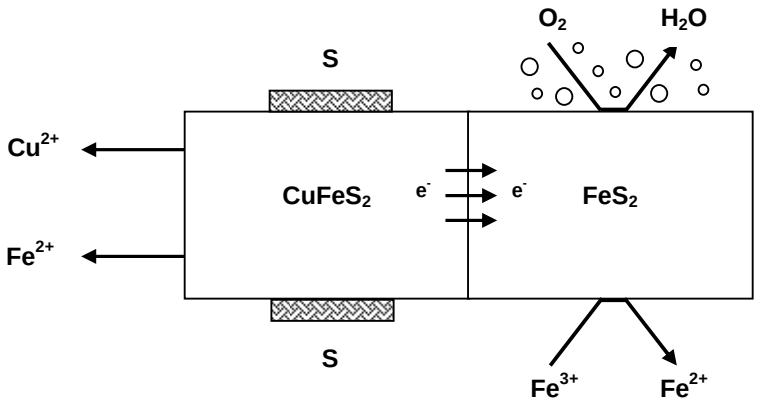

Figure 2.6. Galvanic interaction between $CuFeS_2$ and FeS_2 (adapted of You *et al.*, 2007).

Since pyrite is a mineral phase typically found in copper sulfide ores (Berry *et al.*, 1983), a better understanding of the magnitude of the galvanic interaction involving these two sulfides may help to improve chalcopyrite leaching rate from low-grade ores. With the aid of leaching experiments and scanning electron microscopy (SEM) coupled with energy dispersive spectrometry (EDS), Berry *et al.* (1978) demonstrated that the presence of pyrite in intimate contact with chalcopyrite in acidic sulfate media (pH ≈ 2), under atmospheric conditions, enhances the oxidation rate of chalcopyrite. The sulfide minerals establish a galvanic couple; $CuFeS_2$ reacts anodically (Eq. 2.5), whereas FeS_2 acts as a cathodic site for the oxygen reduction reaction (Eq. 2.23).

$$CuFeS_2 \rightarrow Cu^{2+} + Fe^{2+} + 2\,S + 4\,e^- \quad (2.5)$$

$$O_{2(g)} + 4\,H^+ + 4\,e^- \rightarrow 2\,H_2O \quad (2.23)$$

Mehta and Murr (1983) also investigated the galvanic effect of pyrite on $CuFeS_2$ oxidation rate. These authors evaluated the mixed potential of this mineral couple in 1.0 mol/L H_2SO_4 solutions at 30°C, by connecting a FeS_2 electrode and a $CuFeS_2$ electrode by a copper wire. The mixed potential was found to be 0.56 V *vs.* SHE, an intermediate value between those obtained for FeS_2 and $CuFeS_2$, separately (0.63 and 0.52 V *vs.* SHE, respectively), under similar conditions. By the same experimental design (*i.e.*, electrodes connected via Cu wire), You *et al*. (2007) investigated the effect of pH (5-7) and Fe^{3+} ion concentration (10^{-2}-10^{-4} mol Fe^{3+}/L) on the mixed potential and current density at the mixed potential of chalcopyrite and pyrite electrodes. It was observed that the lower the pH value and higher the Fe^{3+} ion concentration, the higher the current density of the galvanic couple and the more positive the mixed potential. It should be mentioned that when electrodes are connected by a wire, lower is the electrical contact between the mineral phases and, therefore, higher is the resistance across the sulfides. Thus, it is possible that this type of interaction may not represent accurately the association in the ore, affecting the effect under analysis.

In the Galvanox™ process, copper extraction from chalcopyrite is conducted in the presence of pyrite particles in ferric sulfate solutions, at approximately 0.44-0.48 V *vs.* Ag/AgCl and 80°C. High copper extractions (> 98%) have been reported, depending on the leaching time, acidity, and pyrite addition (Littlejohn and Dixon, 2008; Dixon *et al*., 2008). These authors have ascribed the enhanced dissolution rate of chalcopyrite to the faster reduction rate of ferric ions (Eq. 2.24) on galvanically-coupled pyrite particles, thereby assuming the cathodic half-cell reaction as the slower step of chalcopyrite dissolution. The elemental sulfur layer, which grows up on chalcopyrite under Galvanox™ conditions, affects the electrical contact between the sulfide particles, consequently, decreasing the galvanic effect.

$$Fe^{3+} + e^- \rightarrow Fe^{2+} \quad (2.24)$$

The effects of pyrite particles treated with silver on chalcopyrite leaching kinetics have been investigated (Nazari *et al.*, 2011). Under Galvanox^{TM} conditions, the chalcopyrite leaching rate increases significantly when minor amounts of silver ions (*e.g.*, 50 g Ag^{+}/t FeS_2) are added.

Results by Littlejohn and Dixon (2008) indicated that the presence of pyrite in ferrous sulfate media has an enhancing effect on the initial kinetics of ferrous (Fe^{2+}) ion oxidation (Eq. 2.25). The oxidation rate is affected by the initial Fe^{2+} ion concentration, acidity, leaching time, and pyrite addition.

$$4\,Fe^{2+} + O_{2(g)} + 4\,H^{+} \rightarrow 4\,Fe^{3+} + 2\,H_2O \qquad (2.25)$$

In contrast to the classical electrochemical mechanisms, it has been proposed that the chalcopyrite dissolution involves an electron-independent formation of hydrogen sulfide (H_2S) (Ammou-Chokroum *et al.*, 1981; Dutrizac, 1989, 1990; Nicol and Lázaro, 2006), and elemental sulfur is produced from the oxidation of this intermediate sulfide. Nicol *et al.* (2010) demonstrated that pyrite surface acts as a catalyst for sulfide oxidation. It was observed that in the absence of pyrite, the oxidation rate of sulfide (S^{2-}) ions (*i.e.*, the consumption rate of oxygen into the solution) is very low, while in the presence of fine pyrite particles the process is very fast. The authors also demonstrated that for chalcopyrite leaching in 0.2 mol/L chloride media at 580 mV *vs.* SHE in the presence of pyrite particles, most of the elemental sulfur was associated with pyrite and the amount of associated sulfur increased as the pyrite content increased and the particle size decreased.

It is noticeable from the above review that unresolved controversies exist concerning the mechanisms by which pyrite affects chalcopyrite dissolution. In addition, it is important to say that this galvanic interaction is generally described qualitatively. The role of pyrite on the oxidation rate of chalcopyrite may go beyond the recognized galvanic effect, and such effect is expected to be magnified by the occurrence of a permanent contact between the two sulfides. By investigating pyrite crystallites naturally associated with chalcopyrite (*i.e.*, pyrite inclusions), the electrical contact between these phases is undoubtedly optimized, which possibly minimizes the voltage losses across $CuFeS_2$ and FeS_2. This experimental approach allows a quantification of the galvanic current.

2.4. Electrochemical techniques

In the present thesis, potentiometry, linear sweep voltammetry and chronoamperometry were applied aimed at determining the oxidation behavior of chalcopyrite in acidic sulfate solutions under atmospheric conditions. A brief review on these techniques is presented in the next sections.

2.4.1. Potentiometry

The monitoring of the variation of the open circuit potential (OCP) of working electrodes with time is obtained by potentiometry. The OCP value is that exhibited by an electrode when immersed in an electrolyte solution without any externally applied potential (Bockris and Reddy, 1998; Brett and Brett, 1998). Potentiostat is the equipment that controls the potential applied to working electrodes and permits the measurement of the current flow.

In solution, the mineral surface establishes two electron-transfer sites at redox potentials E_1 and E_2. These distinct potentials characterize a non-steady state and, then, electrons begin to flow from the anodic to the cathodic sites in order to achieve constant surface potential. The steady-state condition is achieved when the net current is zero (*i.e.*, the anodic and the cathodic current densities are equal and of opposite sign). The potential in this condition is the so-called mixed potential (E_M), given by the kinetics of all the contributing half-cell reactions taking place on the mineral surface (Bockris and Reddy, 1998; Brett and Brett, 1998).

The mixed potential theory is schematically illustrated in Fig. 2.7. The surface of a metal sulfide electrode immersed in solution containing Fe^{3+} ion as oxidant is exemplified. As will be discussed in this thesis (Chapter 3), the mixed potential depends not only on the electrolyte conditions, but also on the nature of the solid sample. Parameters such as the temperature, acidity, nitrogen bubbling, presence of external ions, and the characteristics of the electrode reaction area, such as the presence of impurities, may affect this fundamental, electrochemical property.

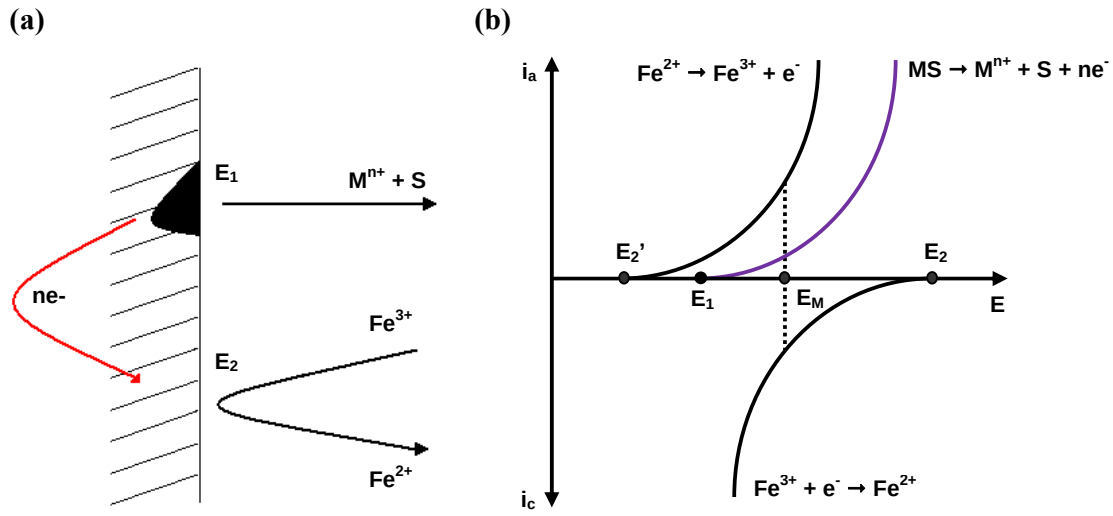

Figure 2.7. (a) Anodic and cathodic sites on the surface of metal sulfide electrode; and (b) The mixed potential diagram: i_a and i_c are the anodic and the cathodic current densities, respectively (adapted of Nicol and Lázaro, 2002).

2.4.2. Linear sweep voltammetry

Of all techniques available for investigating electrochemical reactions, the potential sweep methods such as linear sweep voltammetry and cyclic voltammetry are the most widely applied (Brett and Brett, 1998). These methods consist in the application of continuously time-varying potentials to the working electrode, which in turn results in the occurrence of oxidation and reduction reactions on the electrode surface.

In linear sweep voltammetry (LSV), the potential sweep is made in only one direction, stopping at selected potential value. The main operating parameters are the initial potential, (E_i); scan rate, (υ); and maximum potential, (E_{max}) (Brett and Brett, 1998). The rate of a particular electrode reaction is indicated by the direction and magnitude of the electric current. The anodic oxidation reaction, which has positive overpotential, is schematically illustrated in Fig. 2.8. As earlier mentioned, the overpotential corresponds to the difference between the applied and mixed potential. By convention, the anodic current is denoted as positive. In the present thesis, the application of the LSV technique was extremely helpful to improve the knowledge on the electrochemical behavior and properties of chalcopyrite

and mixed (chalcopyrite-pyrite) electrodes in acidic media, under atmospheric conditions. The potential range at which the oxidation reaction starts, the anodic peak potential with the corresponding anodic current, the potential at which a passive behavior prevails, and the dissolution current density of many mineral electrodes, were determined by LSV.

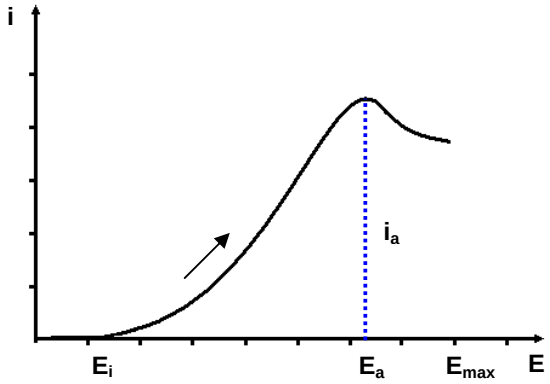

Figure 2.8. Typical linear sweep voltammogram: E_a = anodic peak potential; i_a = anodic peak current. The solid arrow indicates the sweep direction.

2.4.2.1. Tafel plots

The Tafel plots represent the straight lines for the variation of the logarithm of the current density with the overpotential. In this case, the potential sweep is also made in only one direction, but a minimum potential value, (E_{min}), which is inferior to the mixed potential, is selected (Brett and Brett, 1998). Thus, not only the anodic oxidation, which has a positive overpotential, but also the cathodic reduction, which has a negative overpotential, occurs on the electrode surface, as shown in Fig. 2.9. Tafel plots have been mainly elucidative in investigations of metallic corrosion, where elementary information, such as the corrosion potential, exchange current density and anodic and cathodic slopes have been determined (Gileadi and Kirowa-Eisner, 2005; Mansfeld, 2005). The Butler-Volmer equation relates the current density and the overpotential for the anodic and cathodic processes as:

$$i = i_0\left[\exp\left(\alpha\frac{nF}{RT}\eta\right) - \exp\left(-(1-\alpha)\frac{nF}{RT}\eta\right)\right] \qquad (2.25)$$

where R is the universal gas constant, F the Faraday constant, T the absolute temperature, n the number of electrons involved in the corresponding reaction and α the symmetry factor (Bockris and Reddy, 1998; Brett and Brett, 1998).

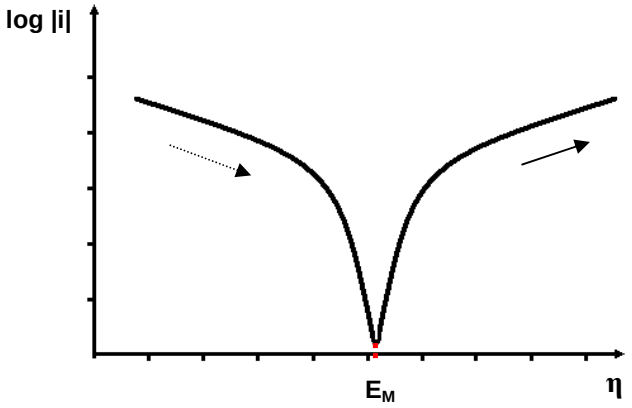

Figure 2.9. Tafel plots: E_M = mixed potential (zero overpotential). The solid and dotted arrows indicate the sweep direction in the anodic and cathodic regions, respectively.

The overpotential (η) (Eq. 2.26) is a measure of how far the reaction is from equilibrium. At equilibrium ($\eta = 0$), no measurable current flows; however, this equilibrium is dynamic. At this condition, the rate of the electrode dissolution, i_a, is equal to the rate of the oxidant reduction, $-i_c$. Hence, $i_a = -i_c = i_0$, which is the exchange current density (Bockris and Reddy, 1998; Brett and Brett, 1998).

$$\eta = E_{applied} - E_M \tag{2.26}$$

When the anodic and cathodic reactions represent a corrosion process, $i_a = -i_c = i_{corr}$, which is the corrosion current, and the mixed potential corresponds to the corrosion potential, (E_{corr}). If the applied potential is made more positive than this equilibrium potential, the mineral dissolution proceeds, $i_a > |i_c|$. Correspondingly, for cathodic potentials, the oxidant reduction reaction proceeds on the mineral surface, $i_a < |i_c|$. Then, over a specific potential range, these two reactions oppose each other and one reaction may occur at a negligible rate. In this case, the overpotential is in the Tafel region (Bockris and Reddy, 1998; Brett and Brett, 1998). When $\eta > 0$ (anodic region), the last term in (Eq. 2.25) can be neglected:

$$i_a = i_{corr}\left[\exp\left(\alpha\frac{nF}{RT}\eta\right)\right] \tag{2.27}$$

$$Log(i_a) = Log(i_{corr}) + \left(\frac{\alpha nF}{2.303RT}\right)\eta \tag{2.28}$$

Similarly, when $\eta < 0$ (cathodic region), the first term in (Eq. 2.25) can be neglected:

$$i_c = -i_{corr}\left[\exp\left(-(1-\alpha)\frac{nF}{RT}\eta\right)\right] \tag{2.29}$$

$$Log(i_c) = Log(i_{corr}) - \left(\frac{(1-\alpha)nF}{2.303RT}\right)\eta \tag{2.30}$$

Corrosion current density (or exchange current density) and Tafel slopes can be determined from experimental data (Bockris and Reddy, 1998; Brett and Brett, 1998; Gileadi and Kirowa-Eisner, 2005; Mansfeld, 2005). By definition, the anodic and cathodic Tafel slopes can be given by, respectively, (Eqs. 2.31 and 2.32). Fundamental properties, such as the number of electrons involved in the electrochemical process and the symmetry factor, may be estimated from Tafel slopes.

$$b_a = \frac{2.303RT}{\alpha nF} \tag{2.31}$$

$$b_c = \frac{-2.303RT}{(1-\alpha)nF} \tag{2.32}$$

2.4.3. Chronoamperometry

The chronoamperometry is the electrochemical technique used to observe the variation of the electric current with time under potentiostatic control, being possible to determine the steady-state current. This technique involves the application of a constant potential to the

working electrode (Brett and Brett, 1998). When coupled with characterization techniques, chronoamperometry is a crucial method to obtain oxidized surfaces, whose nature may be investigated.

The application of a positive potential pulse produces an anodic current in function of the oxidation of the electrode surface. In contrast, a negative pulse produces a cathodic current as a result of its reduction. A positive potential chronoamperogram is illustrated in Fig. 2.10. It should be noted that there is an initial capacitance charging current followed by a current decay with time to a steady-state value. Such current plateau generally indicates that the reaction rate is controlled by diffusion of reactants through the reaction products formed on the electrode surface or then by electron transfer (Bockris and Reddy, 1998; Brett and Brett, 1998). Other behaviors, such as the increase of current with time, which possibly indicates an active dissolution process, is also commonly observed. In this thesis, application of chronoamperometry showed to be helpful to elucidate the effect of product phases on the oxidation rate of chalcopyrite.

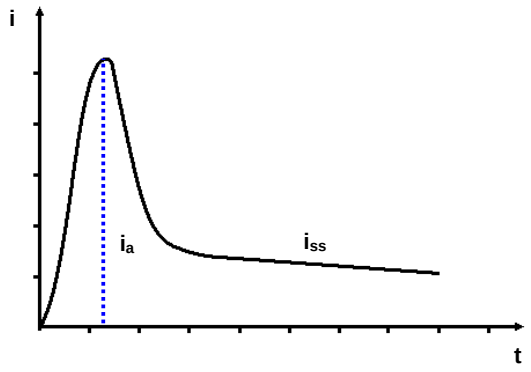

Figure 2.10. Typical chronoamperogram obtained under a positive potential pulse: i_a = anodic peak current; and i_{ss} = steady-state current.

2.5. Characterization techniques

A vibrational technique (Raman spectroscopy) and advanced X-ray diffraction techniques (*ex situ* small angle X-ray diffraction and *in situ* time-resolved X-ray diffraction), using

synchrotron radiation, were applied to identify the nature of the oxidation product phases formed on chalcopyrite in acidic sulfate media, under atmospheric conditions.

2.5.1. Raman spectroscopy

Raman spectroscopy (RS) is a vibrational technique used to identify functional groups on materials. While in infrared spectroscopy (IR) the material is irradiated by a laser beam in the IR region, in RS it is irradiated by beam in the ultraviolet-visible region. The scattered light consists of two types: Rayleigh scattering, which is strong and has the same frequency of the incident laser beam (ν_0); and Raman scattering, which is weak and has frequencies $\nu_0 \pm \nu_m$, where ν_m is the vibrational frequency of the molecule that constitute the material irradiated. $\nu_0 - \nu_m$ and $\nu_0 + \nu_m$ lines are called the Stokes and anti-Stokes lines, respectively (Smith, 1999; Ferraro *et al*., 2003). The electric part of light interacts with molecules and cause radiation absorbance. Chemical bonds vibrate at the same frequency of the electric vector (Fig. 2.11). Thus, when the positive pole of electric vector encounters the positive end of the molecule, it will repel the partial positive charge on the atom and then the bond will contract. If the negative pole encounters this positive end, it will attract the positive charge and the bond will stretch. Then, bonds can stretch, contract or bend, giving rise to a peak in the radiation spectrum at the wavenumber of light absorbed. Absorbance occurs when the energy of the light impinging on the molecule is equal to the vibrational energy difference among excited and ground state energies for the molecule (Smith, 1999). By IR spectroscopy, a normal vibration is active only if the electric dipole moment (P) of a molecule changes with respect to bond distance (d) (*i.e.*, $\partial P/\partial d \neq 0$). P is a measure of the charge asymmetry of a molecule. If a molecule with no net electric dipole moment is irradiated by a laser beam, P can be induced (Fig. 2.12). The polarizability (α) measures the relative tendency of charge distribution among atoms of a molecule to be distorted from its normal shape by the electric field of the incident electromagnetic radiation, which fluctuates with time by a constant vibrational amplitude and frequency (ν_0). If a molecule vibrates with frequency ν_m, a nuclear dislocation (x) occurs. In RS, only normal vibrations that change α with respect to nuclear dislocation are Raman active (*i.e.*, $\partial\alpha/\partial x \neq 0$) (Smith, 1999; Ferraro *et al*., 2003).

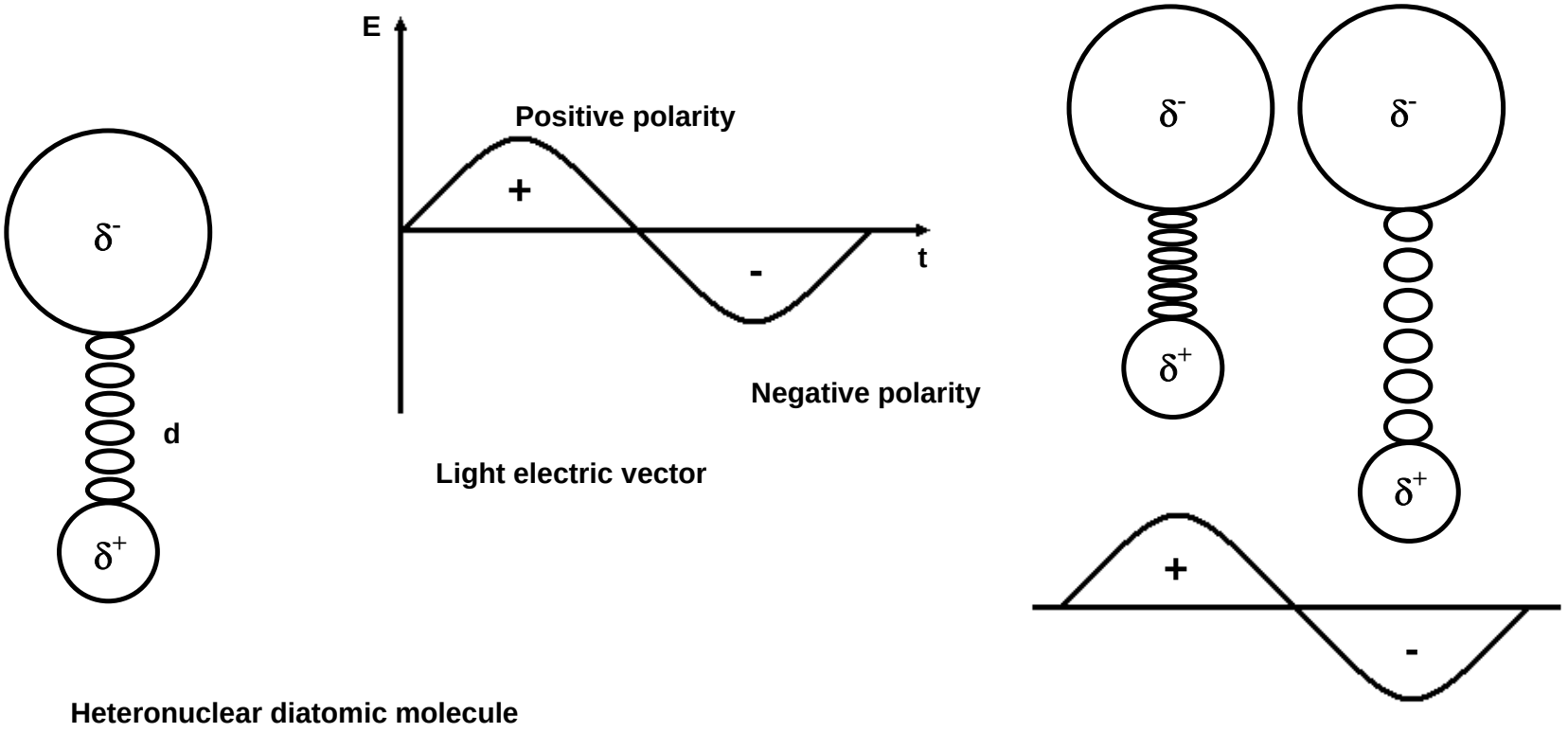

Figure 2.11. Schematic interaction between the light electric vector with a heteronuclear diatomic molecule. The δ^+ and δ^- symbols denote partial positive and negative charges on the atoms ends of the molecule. The molecule contains two charges separated by a distance (d) (adapted of Smith, 1999).

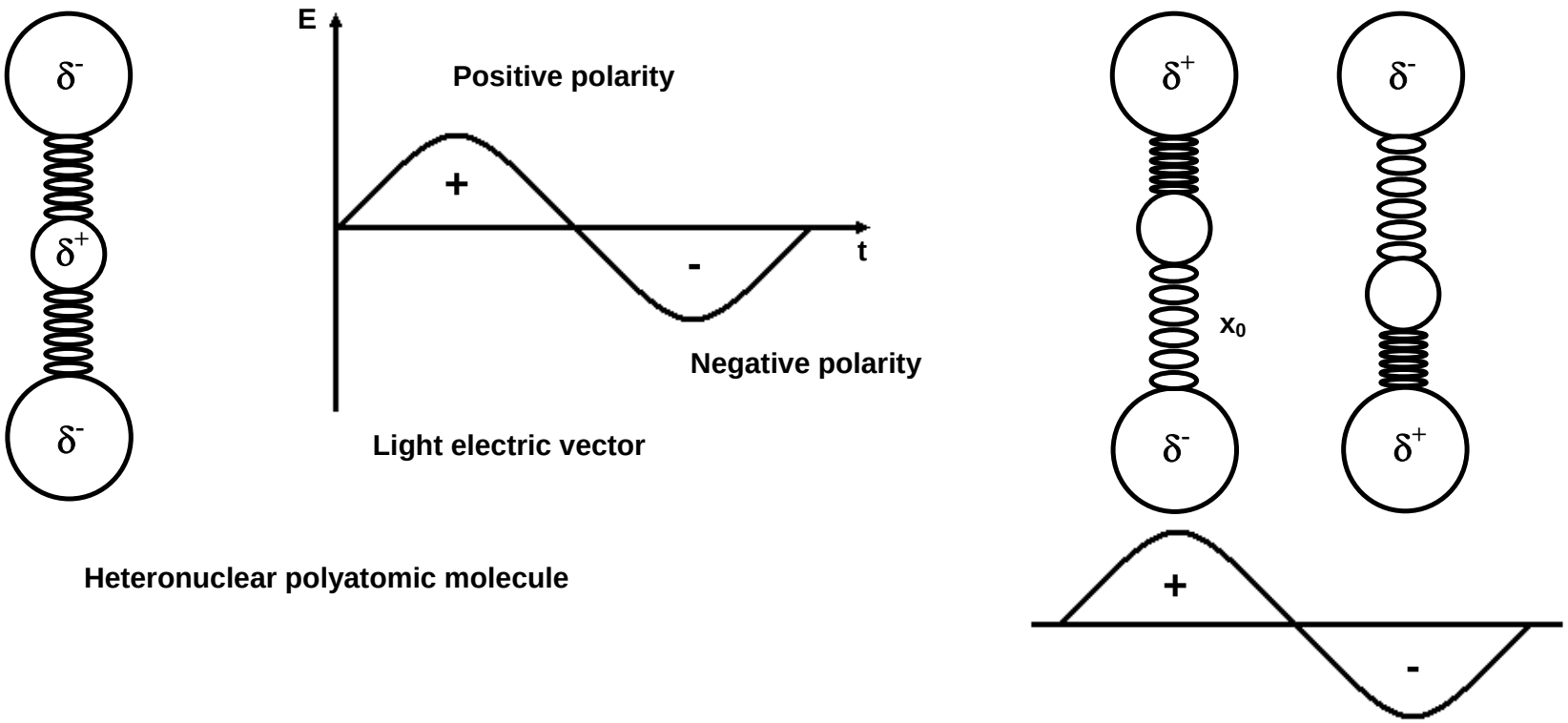

Figure 2.12. Schematic interaction between the light electric vector with a heteronuclear polyatomic molecule. When the positive pole of the electric vector encounters the negative end of the molecule, it will attract some of molecule's electrons, making the charge distribution asymmetric. The molecule will now have an induced dipole moment. For the negative pole, some of molecule's electrons are repelled by it, and they will move toward the opposite end of the molecule. This induced dipole moment is opposite in direction than that previous induced (adapted of Smith, 1999).

Fig. 2.13 shows the normal vibrations modes of heteronuclear polyatomic molecule. As a linear molecule, it has 4 normal vibrations, which are analyzed through normal modes of vibrations, independent of each other. Since each atom moves in 3 directions (*i.e.*, x, y and z), an N-atom molecule has 3N degrees of freedom; however, 3N includes 6 degrees of freedom derived from the translational and rotational motions of the whole molecule. Thus, the total number of normal vibrations is 3N – 6 and for linear molecules, it becomes 3N – 5, since the rotation about the molecular axis does not occur. Stretching vibrations are shown in Fig. 2.13 (ν_1 and ν_2), while ν_{3a} (plan of the paper) and ν_{3b} (perpendicular plan to the paper) are identical bending vibrations. It should be noted that in ν_1 the bonds stretch and contract in phase and this vibration is symmetric in relation to the center of symmetry. Therefore, the molecule has no net dipole moment and ν_1 is IR inactive. In contrast, ν_1 is Raman active, since the polarizability of the molecule changes during the vibration. In ν_2, IR active, one of the bonds stretches, while the other contracts. Thus, this molecule has alternate induced dipole moment during the vibration. In ν_3, IR active, an induced dipole moment also appears during the molecular bending. ν_2 and ν_3, asymmetric with respect to the center of symmetry, are then Raman inactive.

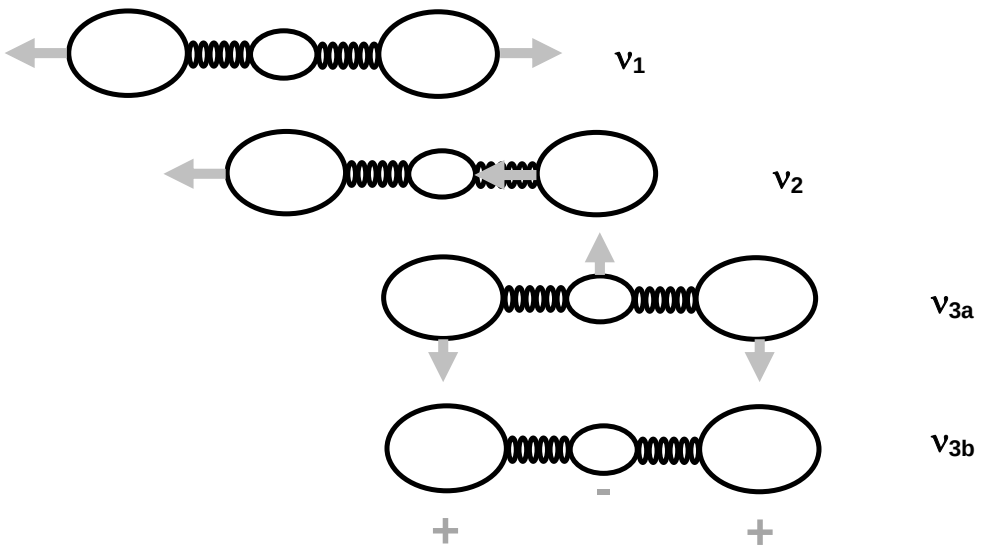

Figure 2.13. Normal vibrations of a heteronuclear polyatomic molecule. The arrows indicate the direction of atoms motion and the signs + and – the atoms motion upward and down relatively to the plan of paper, respectively (adapted of Ferraro *et al*., 2003).

2.5.2. X-ray diffraction

The X-Ray techniques are very important tools for electrode studies (Robinson and Walsh, 1993; Morón, 2000; De Marco *et al*., 2006a). When crystalline phases are involved in oxidative processes, the X-ray diffraction (XRD) is powerful in obtaining information on phase composition, structure, preferred orientation, crystal size, and texture (Norby, 1996).

The X-ray diffraction by crystals results from a scattering process in which the X-rays are scattered by electrons of the constituent atoms of the crystal (Klug and Alexander, 1974; Cullity and Stock, 2001). The X-rays are electromagnetic waves and as such these have a periodically changing electric field. An electron in the path of such a wave is excited, and itself becomes a source of electromagnetic waves of the same frequency and wavelength of the incident beam. Therefore, arises from this interaction a new wave front of X-rays, which derives its energy from the impinging beam (Klug and Alexander, 1974; Cullity and Stock, 2001). The electron is said then to scatter the original beam. These scattered waves combine, so that the scattering effect from an atom is essentially that of a point source of scattered X-rays. The constructive interference of these scattered X-rays represents the diffraction pattern.

The Bragg law, given by (Eq. 2.33), where λ is the wavelength of the X-ray beam, d the interplanar spacing and n an integer that represents the orders of reflection, which occur only at precise values of θ that satisfy the Bragg equation, states that the diffracted beam, which is produced only when certain geometrical conditions are satisfied, behaves as if it were specularly reflected from a regular plane of atoms in the crystal (Klug and Alexander, 1974; Cullity and Stock, 2001).

$$n\lambda = 2d\sin\theta \qquad (2.33)$$

As a result, when an X-ray beam is impinged on a surface of a crystalline material at an incident angle θ, a fraction is scattered by the atoms on the surface. The portion not scattered of the X-ray beam reaches deeper atoms in the crystal where then a fraction is scattered (Fig. 2.14). At other θ angles there is no reflected beam as a result of destructive interferences (Klug and Alexander, 1974; Cullity and Stock, 2001).

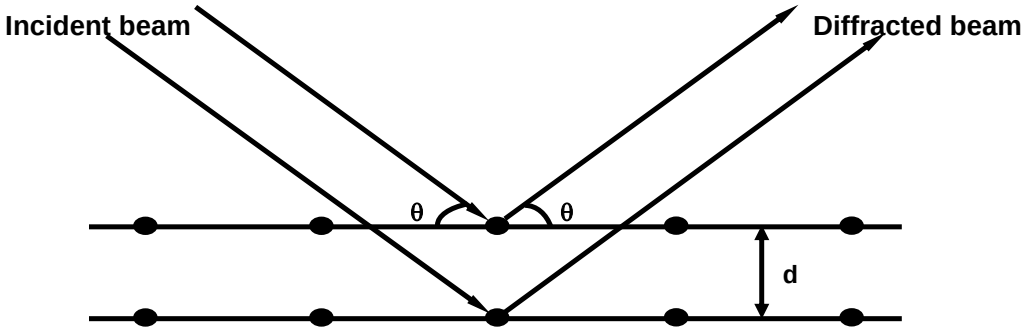

Figure 2.14. X-ray diffraction by crystal (adapted of Klug and Alexander, 1974).

In the case of small angle X-ray diffraction techniques, the scattering of X-rays by the crystal is detected at very low angles. For the grazing incidence technique, the scattered X-rays are detected at grazing θ' angle with respect to the sample surface, and at 2θ' angle with respect to the transmitted beam (Fig. 2.15) (Bachrach, 1992; Cullity and Stock, 2001). The 2θ' angle (*i.e.*, the angle of deviation of the diffracted beam), normally not exceeds 2° and the surface sensitivity of this technique relies on the fact that the penetration depth of the incident beam at grazing angles is reduced by three orders of magnitude, normally from 1-10 μm to 1-10 nm (10-100 Å) (Stepanov and Köhler, 1994). Consequently, the grazing incidence permits an accurate analysis of the layer that forms on the surface of oxidized materials, as the interferences resulting from the substrate (bulk) analysis are minimized.

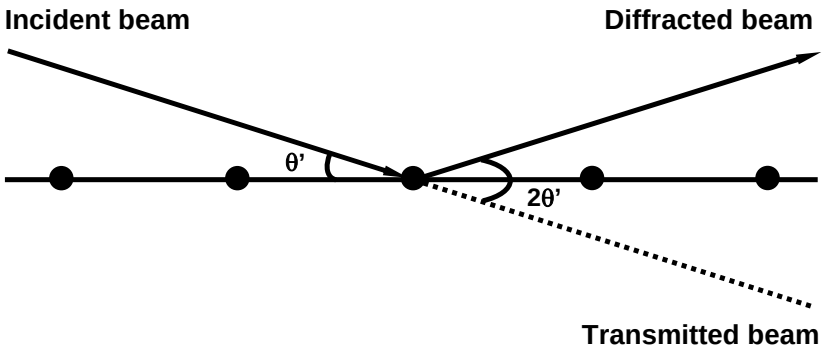

Figure 2.15. X-ray diffraction: relation between the incident and diffracted beams at grazing angles (adapted of Klug and Alexander, 1974).

Although conventional diffractometers can be used to conduct X-ray measurements, the quality of the signal is lower than that obtained by measurements with the synchrotron radiation. It is well-known that the high intensity of synchrotron X-ray beams greatly improves the signal-to-noise ratio, allowing the analysis of minor amounts of material. The ability to produce X-rays beams with extremely short wavelengths, smaller than the size of an atom, allows analysis of minute grains or layers. In addition, the signal may be detected with enough time resolution to obtain detailed information on the product phases (Kunz and Codling, 1979; Bachrach, 1992; Robinson and Walsh, 1993). Synchrotron radiation, the electromagnetic radiation emitted by charged particles, moving on circular orbits with highly relativistic velocities, is a powerful source of X-ray beams, which may be used to investigate the structure of matter and several physical, chemical, and biological processes. A brief description of this technology is presented, and a complete review can be found in Kunz and Codling (1979) and Bachrach (1992).

Synchrotron radiation

Synchrotron is a particular type of cyclic particle accelerator in which a magnetic field (to turn the particles) and an electric field (to accelerate the particles) are synchronized with the moving particle beam. The ability of this device to accelerate particles is limited by the fact that particles must be charged to be accelerated. Charged particles under acceleration emit photons, thereby losing energy. Lighter particles, such as the electrons, lose a larger fraction of their energy when turning (Kunz and Codling, 1979; Bachrach, 1992).

The design and operation of the electron accelerators usually involve main components as the linear accelerator, booster synchrotron, electron storage ring, and experiment hall. The generation of brilliant X-ray beams may begin with electrons emitted from a cathode material heated to high temperatures, typically superior to 1000°C. The electrons are then accelerated by high-voltage alternating electric fields in the linear accelerator, and selective phasing of these electric fields accelerates the electrons to hundreds of million electron volts (MeV). At these conditions, electrons are moving with highly relativistic velocities, larger than 99.999% of the speed of light (APS/ANL, 2010).

Next, the electrons are then injected into the booster synchrotron, a racetrack-shaped ring of electromagnets, and accelerated from MeV to billions electron volts (GeV). At these conditions, the electrons are moving at velocities larger than 99.999999% of the speed of light. Inside the booster synchrotron, bending and focusing electromagnets increase the electron field strength in synchronization with the electric fields applied to accelerate the electrons aimed at maintaining the orbital path of the electrons (APS/ANL, 2010).

The GeV electrons are then injected into the storage ring, a circle of tens or hundreds of electromagnets and associated equipment, located in a radiation-proof concrete enclosure inside the experiment hall. A powerful electromagnetic field focuses the electrons into a narrow beam that is bent on a circular path as it orbits within vacuum chambers running through the centers of the electromagnets. The sequencing of these magnets in the storage ring produces a beam of very small size and low angular divergence (APS/ANL, 2010). The design of the electron storage ring also involves straight sections or sectors, which are instrumented to provide brilliant X-ray radiation. Crystal and mirror optics are designed to adapt the beam for specific types of experiments.

2.5.2.1. *Ex situ* synchrotron small angle X-ray diffraction

In this thesis (Chapter 4), *ex situ* synchrotron small angle X-ray diffraction (S-SAXRD) was used to investigate the nature of the product phases that form on chalcopyrite in acidic sulfate media, under controlled potential and atmospheric conditions. The measurements were conducted at the Brazilian Synchrotron Light Laboratory (LNLS), Campinas, Brazil. For the first time, to the author's knowledge, the S-SAXRD technique was applied to improve the understanding on chalcopyrite oxidation mechanism.

It is known that the small angle X-ray diffraction technique is superior to the conventional powder X-ray diffraction in the investigation of the crystalline structure of thin films (Levine *et al*., 1989; Kondrashkina *et al*., 1997). The SAXRD technique has been applied successfully to investigate oxidized surfaces on many different substrates and under varied experimental conditions (Sathiyanarayanan *et al*., 1999; De Marco *et al*., 2006a, 2006b; Suzuki *et al*., 2007).

2.5.2.2. *In situ* synchrotron time-resolved X-ray diffraction

In order to establish the structural crystallographic changes that occur on a material during its oxidation it is necessary to apply an *in situ* technique. The development both in the reaction cells and in the radiation sources, instrumentation and detectors, have made the time-resolved powder X-ray diffraction a powerful and versatile tool for studying chemical reactions of particular interest, such as the oxidation reactions (Robinson and Walsh, 1993; Norby, 1996, 2006; Morón, 2000). Of particular interest when studying oxidation reactions by *in situ* time-resolved powder X-ray diffraction is information on the dissolution rate of the crystalline sample and formation rate of intermediate- and end-product phases.

In the present thesis (Chapter 5), *in situ* synchrotron time-resolved X-ray diffraction (S-TRXRD) was used to investigate the nature of the intermediate- and end-product phases that form on chalcopyrite in acidic sulfate media, under controlled potential and at different temperature conditions. Although conventional diffractometers can be used to conduct *in situ* measurements, the quality of the signal is lower than that obtained by the synchrotron radiation, as a result of the attenuation of the incident X-ray beam by the aqueous phase whitin the experimental cell (De Marco *et al*., 2006a). The measurements were conducted at the Advanced Photon Source (APS) of the Argonne National Laboratory (ANL), in Chicago, U.S. To the author's knowledge, this is the first investigation of chalcopyrite oxidation by *in situ* XRD.

Chapter 3 – Quantitative assessment of the effect of pyrite inclusions on chalcopyrite electrochemistry under oxidizing conditions

Abstract

The present paper quantifies the separate and combined effects of pyrite (FeS_2) inclusions, dissolved oxygen (0.001 mol/L) and ferric ion (0.01-0.05 mol/L) on the electrochemical behavior of chalcopyrite ($CuFeS_2$) electrodes by means of potentiometry and linear sweep voltammetry. The experiments were carried out in 0.1 mol/L H_2SO_4 solutions at room temperature (26±1 °C). Naturally associated pyrite-chalcopyrite electrodes were selected with the aims to better represent the sulfide association in the ore, thus minimizing the voltage losses across the mineral-mineral contact. The presence of ferric ion and oxygen was shown to increase in approximately 53% the mixed potential of $CuFeS_2$ electrodes; the dissolution current density increased up to 55 times. In the presence of these oxidants and pyrite (42% FeS_2 of the electrode surface), the mixed potential was further increased in 14%. For these mixed electrodes, the dissolution current density increased by a factor of approximately 2.6 and 2.2, respectively, in solutions containing 0.001 mol O_2/L and 0.05 mol Fe^{3+}/L, and by 1.6 times in presence of both oxidants (0.001 mol O_2/L with 0.05 mol Fe^{3+}/L). Therefore, more pronounced effect of pyrite inclusions on chalcopyrite oxidation rate was observed under the lower oxidizing conditions. The effects of the oxidants were described by electrochemical models. The galvanic effect of pyrite on the dissolution of this important sulfide was discussed by the kinetics of the half-cell reactions occurring in the pyrite-chalcopyrite coupling.

Key-words: chalcopyrite, pyrite, galvanic interaction, electrochemistry.

3.1. Introduction

The aqueous processing of copper sulfide ores has been extensively investigated aimed at treating chalcopyrite ($CuFeS_2$), the most abundant copper mineral. The interest in the development of low-temperature processes to treat the low-grade chalcopyrite ores is mainly related to the slow leaching rate of this sulfide under heap bioleaching conditions. For low temperatures, the dissolution rate of chalcopyrite in acidic media is known to be slow and often tends to decline with time (Jones and Peters, 1976; Dutrizac, 1981; Muñoz *et al*., 1979; Majima *et al*., 1985; Hirato *et al*., 1987a). Numerous investigations have been conducted aimed at understanding the kinetics and dissolution mechanisms of chalcopyrite in an effort to overcome this constraint. Most of the studies ascribe the slow leaching rate to the formation of an insoluble layer, which prevents further mineral dissolution.

The effect of catalysts on the mineral dissolution rate has also been investigated. It is well-established that the galvanic interactions increase the dissolution rate of one of the minerals that constitute a galvanic couple. The enhancement of copper extraction from chalcopyrite when in contact with metallic copper (Cu) (Hiskey and Wadsworth, 1975), and gold (Au) (Lorenzen and Denventer, 1992), manganese dioxide (MnO_2) (Madhuchhanda *et al*., 2000), acanthite (Ag_2S) (Mateos *et al*., 1987; Scaini *et al*., 1995), carbon (Wan *et al*., 1984; Nakazawa *et al*., 1998; Liang *et al*., 2010), and pyrite (FeS_2) (Berry *et al*., 1978; Mehta and Murr, 1983; Nowak *et al*., 1984; Abraitis *et al*., 2004; You *et al*., 2007; Littlejohn and Dixon, 2008; Dixon *et al*., 2008; Nazari *et al*., 2011), has been attributed to galvanic effects. This electrochemical interaction may be understood by the anodic and cathodic half-cell reactions that occur at the mineral surfaces. The mineral with the higher mixed potential (E_M) acts as the cathode in the galvanic couple and is protected, while the mineral with the lower mixed potential serves as the anode and, thus, dissolves preferentially.

Since pyrite is a mineral phase typically found in copper sulfide ores (Berry *et al*., 1983), a better understanding of the magnitude of the galvanic interaction involving these two sulfides may help to improve the chalcopyrite leaching rate from low-grade ores. Such interaction is generally described qualitatively. Thus, the purpose of this investigation is to evaluate the role of pyrite crystallites naturally associated with chalcopyrite ore on the

electrochemical behavior of the copper sulfide, under typical, low-temperature leaching conditions (*i.e.*, acidic sulfate solutions containing ferric (Fe^{3+}) ion and dissolved oxygen).

3.2. Effects of pyrite on chalcopyrite dissolution rate

With the aid of leaching experiments and scanning electron microscopy (SEM) coupled with energy dispersive spectrometry (EDS), Berry *et al.* (1978) demonstrated that the presence of pyrite in intimate contact with chalcopyrite in acidic sulfate media (pH ≈ 2), under atmospheric conditions, enhances the dissolution rate of chalcopyrite. The sulfide minerals establish a galvanic couple; chalcopyrite reacts anodically (Eq. 3.1), while pyrite acts as a cathodic site for the oxygen reduction reaction (Eq. 3.2).

$$CuFeS_2 \rightarrow Cu^{2+}_{(aq)} + Fe^{2+}_{(aq)} + 2\,S + 4\,e^- \quad (3.1)$$

$$O_{2(g)} + 4\,H^+_{(aq)} + 4\,e^- \rightarrow 2\,H_2O \quad (3.2)$$

Mehta and Murr (1983) also investigated the galvanic effect of pyrite on chalcopyrite oxidation rate. These authors evaluated the mixed potential of this mineral couple in 1.0 mol/L H_2SO_4 solutions at 30°C, by connecting a FeS_2 electrode and a $CuFeS_2$ electrode by a copper wire. The mixed potential was found to be 0.56 V *vs.* the Standard Hydrogen Electrode (SHE), an intermediate value between those obtained for pyrite and chalcopyrite separately (0.63 and 0.52 V *vs.* SHE, respectively), under similar conditions. By the same experimental design (electrodes connected via Cu wire), You *et al.* (2007) investigated the effect of pH (range 5-7) and ferric ion concentration (from 10^{-2} to 10^{-4} mol Fe^{3+}/L) on the mixed potential and current density at the mixed potential of chalcopyrite and pyrite electrodes, under atmospheric conditions. It was observed that the lower the pH value and higher the Fe^{3+} ion concentration, the higher the current density of the galvanic couple and the more positive the mixed potential. It should be mentioned that when electrodes are connected by a wire, lower is the electrical contact between the mineral phases and, therefore, higher is the resistance across the sulfides. Thus, it is possible that this type of interaction may not represent accurately the association in the ore, affecting the effect under analysis.

In the Galvanox™ process, copper extraction from chalcopyrite is conducted in the presence of pyrite particles in ferric sulfate solutions, at approximately 440-480 mV *vs.* Ag/AgCl and 80 °C. High copper extractions (> 98%) have been reported, depending on the leaching time, acidity, and pyrite addition (Littlejohn and Dixon, 2008; Dixon *et al*., 2008). These authors have ascribed the enhanced dissolution rate of chalcopyrite to the faster reduction rate of Fe^{3+} ions (Eq. 3.3) on galvanically-coupled pyrite particles, thereby assuming the cathodic half-cell reaction as the slower step of chalcopyrite dissolution. It has not been discussed in these papers how the elemental sulfur layer, which grows up on chalcopyrite surface under the Galvanox™ process conditions, affects the electrical contact between the sulfide phases, which, consequently, may decreases the galvanic effect.

$$Fe^{3+}_{(aq)} + e^{-} \rightarrow Fe^{2+}_{(aq)} \qquad (3.3)$$

Results by Littlejohn and Dixon (2008) also indicated that the presence of pyrite in ferrous sulfate media has an enhancing effect on the initial kinetics of ferrous (Fe^{2+}) ion oxidation (Eq. 3.4). The oxidation rate is affected by initial Fe^{2+} ion concentration, acidity, leaching time, and pyrite addition.

$$4\,Fe^{2+}_{(aq)} + O_{2(g)} + 4\,H^{+}_{(aq)} \rightarrow 4\,Fe^{3+}_{(aq)} + 2\,H_2O \qquad (3.4)$$

In contrast to the classical electrochemical mechanisms, it has been proposed that the chalcopyrite dissolution involves an electron-independent formation of hydrogen sulfide (H_2S), that is, chalcopyrite dissolution by protonic attack (Ammou-Chokroum *et al*., 1981; Dutrizac, 1989, 1990; Nicol and Lázaro, 2006), and elemental sulfur is produced from the oxidation of this intermediate sulfide. Nicol *et al.* (2010) demonstrated that pyrite surface acts as a catalyst for sulfide oxidation. It was observed that in the absence of pyrite, the oxidation rate of sulfide (S^{2-}) ions (*i.e.*, the consumption rate of oxygen in the solution) is very low, while in the presence of fine pyrite particles the process is very fast. The authors also demonstrated that for chalcopyrite leaching in 0.2 mol/L chloride media at 580 mV *vs.* SHE in the presence of pyrite particles, most of the elemental sulfur was associated with pyrite and the amount of associated sulfur increased as the pyrite content increased and the particle size decreased.

It is evident from the above review that unresolved controversies exist concerning the mechanisms by which pyrite affects chalcopyrite dissolution. The role of pyrite on the dissolution rate of this commercially and technologically important copper sulfide may go beyond the recognized galvanic interaction, and such effect is expected to be magnified by the occurrence of a permanent contact between the two mineral phases. In this context, the aim of this investigation is to evaluate the magnitude of the galvanic effect of pyrite on the electrochemical behavior of chalcopyrite, with a method that better represents the mineral association in the ore. By investigating FeS_2 crystallites naturally associated with $CuFeS_2$ ore, the electrical contact between these sulfides is optimized, which possibly minimizes the voltage losses across the FeS_2-$CuFeS_2$ contact. Consequently, it is expected that this experimental design allows a more accurate assessment of the magnitude of the galvanic current, a parameter better described by electrochemical techniques.

The present investigation focuses on the separate and combined effects of pyrite inclusions, dissolved oxygen, and ferric ion on key electrochemical parameters of the chalcopyrite dissolution, that is, the mixed potential (E_M) and the current density at the mixed potential, denoted in this paper as dissolution current density (i_{diss}). Electrochemical models and schematic diagrams were utilized to elucidate the observed trends.

3.3. Experimental

3.3.1. Mineral electrodes

The mineral samples used in the present investigation were obtained from Ward's Natural Science, N.Y. Chalcopyrite and pyrite samples consisted of massive pieces from Durango (Mexico) and Huanzala (Peru), respectively. The preparation of the pyrite-free chalcopyrite (CE) electrode, chalcopyrite-free pyrite (PE) electrode, and mixed (chalcopyrite-pyrite) (ME) electrodes involved the following procedures. Firstly, a massive sample was cut using a diamond wafering blade (Buehler®, n.11-4246), thus obtaining regular specimens (1.0 cm^2 of exposed area and 0.5 cm thick), which were rinsed with double-distilled water and dried with analytical grade acetone (100%) (Synth®). Next, a copper wire within a glass tube was connected to the specimens using a conducting silver paint (Dotite®, D-

550). The samples were then mounted in Epoxy resin (Epofix®, Struers). Fresh electrode surfaces were prepared by wet mechanical polishing using SiC papers (grit sizes 1200 and 2400) and alumina paste (1.0 μm). Next, the electrodes were rinsed with double-distilled water in an ultrasonic bath for 15 min, dried with analytical grade ethyl alcohol 95% (Synth®), and kept under vacuum at room temperature.

3.3.2. Characterization of the mineral electrodes

The quantitative chemical analysis of the mineral (chalcopyrite and pyrite) samples used to prepare the electrodes was obtained by the following procedure. Firstly, samples were digested in a hot plate at 150 °C (±5 °C sensitivity) for 5 h with aqua regia (3 HCl : 1 HNO_3) (analytical grades HCl 37% and HNO_3 65%) (FMaia®). Next, the solution was vacuum filtered and the concentration of iron, copper and other elements was determined by inductively coupled plasma optical emission spectrometry (ICP-OES), using a Perkin Elmer Spectrophotometer (Optima 7300 DV). The residual solid was roasted in a furnace at 1000 °C (±25 °C sensitivity) for 1 h in a platinum crucible. The residue was, then, digested in a hot plate at 150 °C for 1 h with analytical grade hydrofluoric acid (HF) 40% (FMaia®). The silicon content was obtained by weight difference using analytical balance. The concentration of iron, copper and other elements was analyzed in this solution again. The sulfur content was obtained using a LECO® (SC 632) induction furnace. It is important to mention that the pyrite-free chalcopyrite (CE) and chalcopyrite-pyrite (ME) electrodes were obtained from the same source.

Before the electrochemical experiments, diverse mineral electrodes were analyzed by scanning electron microscopy (SEM) with energy dispersive spectrometry (EDS), using a JEOL (JSM 6360 LV) Microscope and a Thermo Noran (Quest) Spectrometer; optical microscopy, using a Leica (Metallux DFC 290) Microscope, equipped with lenses of 10, 50, and 100x; and Raman spectroscopy, using a Horiba Jobin Yvon (Labram HR 800) Spectrograph, equipped with a 633 nm He-Ne laser (20 mW total power, 0.02 mW incident beam power). Raman signal was collected by an Olympus (BHX) Microscope equipped with lenses of 10, 50 and 100x. The spectral resolution was about 2 cm^{-1} and a minimum of

10 scans with 60 s integration time were recorded. The grating angle was calibrated using the 520 cm^{-1} silicon band.

Particularly for the mixed electrodes (MEs), the Standard Test Method ASTM E562 (2008) was used to estimate the content of pyrite on the mineral surface. This point counting method was carried out using optical microscopy coupled with a square test grid of 9 intersections. A total of 50 photomicrographs were taken from each analyzed electrode and the square grid was successively superimposed on each photomicrograph. Following this method, three MEs were selected.

3.3.3. Electrochemical measurements

The electrochemical measurements were conducted at room temperature (26±1°C) using the conventional three-electrode cell (*i.e.*, the mineral working electrode, platinum counter-electrode and Ag/AgCl/KCl (3.0 mol/L) reference electrode) and Autolab® (Eco Chemie) Potentiostat, coupled with data acquisition system (GPES, v.4.9). The potential difference between the CE, PE, and ME working electrodes and the reference electrode was obtained by a Luggin capillary, positioned as close as possible to the surface of the electrodes, in fixed cell geometry. Ultra-pure nitrogen gas (N_2, 99.999%) was bubbled in the electrolyte solution (0.1 mol/L H_2SO_4; pH≈1) for at least 20 min before the start of the measurements. Open circuit potentials (OCPs) of freshly polished electrodes were obtained by means of potentiometry (zero current). The mixed potentials (E_M) were measured after 60 min of immersion of each electrode into the solution. The current densities at the mixed potentials (i_{diss}) were obtained by linear sweep voltammetry (LSV) at low anodic and low cathodic overpotentials ($\eta \pm 150$ mV), and at 5 mV/s scan rate; the overpotential representing the difference between the applied and mixed potentials. The measurements were conducted after an equilibration time of 20 min. The dissolution current densities were all calculated after the extrapolation of the Tafel regions (*i.e.*, the anodic and cathodic linear correlations of log|i| with overpotential) to the mixed potential values. These linear correlations were obtained by determining the best data fitting, using the Microcal Origin™ (v.8) software. In order to evaluate the effect of dissolved oxygen, ultra-pure oxygen gas (O_2, 99.999%) was bubbled in the 0.1 mol/L H_2SO_4 solution for at least 20 min before the start of the

experiments and during the experiments. The dissolved oxygen concentration, measured by a dissolved oxygen sensor (Corning®, 312), was found to be approximately 0.001 mol/L. The effect of ferric ion was investigated by adding 0.01 or 0.05 mol Fe^{3+}/L from a solution prepared with ferric sulfate hydrate 97% ($Fe_2(SO_4)_3.xH_2O$) (Sigma-Aldrich®). All the solutions were prepared with double-distilled water and analytical grade sulfuric acid 96% (FMaia®). All the potentials were converted to the SHE scale. All the measurements were performed in duplicate and thus the standard deviations are provided.

3.4. Results

3.4.1. Characterization of the mineral electrodes

The quantitative chemical analysis indicated that the chalcopyrite sample used to prepare the CE and ME electrodes contained 92.1% $CuFeS_2$ and 3.4% FeS_2, with minor silicon and other elements (31.9% wt. Cu; 30.3% wt. Fe; 34.1% wt. S; 2.0% wt. Si; 0.8% wt. Ca; 0.4% wt. Mg; 0.1% wt Al; 0.1% wt. Mn). The pyrite sample used to prepare the PE electrode contained 98.3% FeS_2, with minor silicon and other elements.

Raman spectroscopy and EDS analyses were employed to assess the features of the surface of the mineral electrodes. Fig. 3.1 shows typical micrographs of pyrite-free chalcopyrite (CE), chalcopyrite-free pyrite (PE), and mixed (ME) electrodes. One may observe smooth surfaces, with fissures and micrometric dark points, which represent cavities or impurities. The electrode matrix and massive dark point were shown by Raman and EDS analyses to be constituted, respectively, by chalcopyrite (area 1) – Cu (32.9% wt.), Fe (28.9% wt.), and S (33.6% wt.) – and diopside (area 2) – Si (34.7% wt.), Ca (25.3% wt.), O (23.0% wt.), and Mg (10.3% wt.) (Fig. 3.1a). The Raman spectrum obtained for area 1 (Fig. 3.2) indicates only one intense band at 294 cm^{-1} and additional bands of lower intensity at 268, 322, 360, and 378 cm^{-1}, which represent the diagnostic bands of chalcopyrite (Mernagh and Trudu, 1993; Parker *et al.*, 2008). The bands depicted in the spectrum obtained for area 2 are typical of diopside ($CaMgSi_2O_6$) (Richet *et al.*, 1998). This spectrum was assigned to an iron-bearing diopside, due to the iron content obtained via EDS (4.6% wt.). Tiny inclusions of diopside were the main impurities detected in the electrode samples. The silicate is

expected to be inert under the investigated experimental conditions. Similarly to area 2, the presence of diopside was also suggested in area 4 – Si (31.5% wt.), O (22.8% wt.), Ca (24.8% wt.) and Mg (9.2% wt.). The Raman spectra obtained from areas 3 and 5 (Fig. 3.2) indicated intense bands at 353 and 387 cm^{-1}, and an additional band at 445 cm^{-1}, which can be assigned to pyrite, as discussed by Mernagh and Trudu (1993). The EDS analyses of S (49.3% wt.) and Fe (42.9% wt.) (area 3), and S (50.1% wt.) and Fe (42.6% wt.) (area 5) are consistent with the Raman findings.

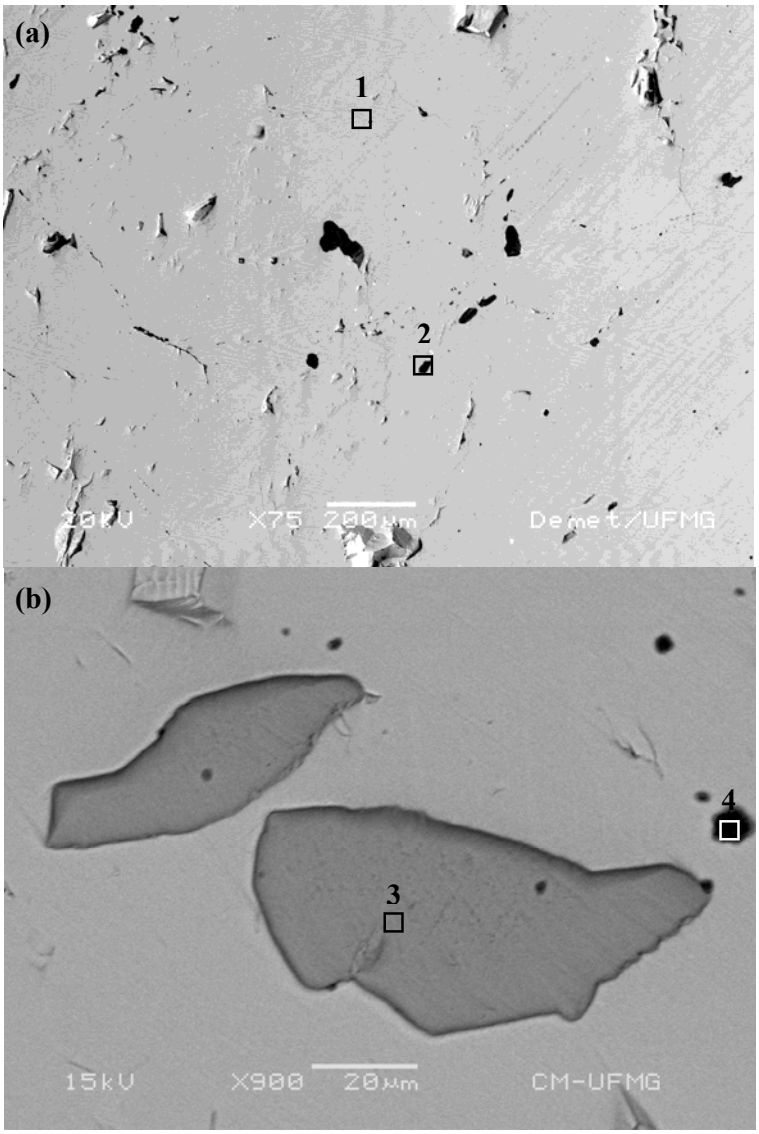

Fig. 3.1. Back-scattered electron micrographs of (a) CE, (b) ME and (c) PE electrodes, and selected areas analyzed by EDS.

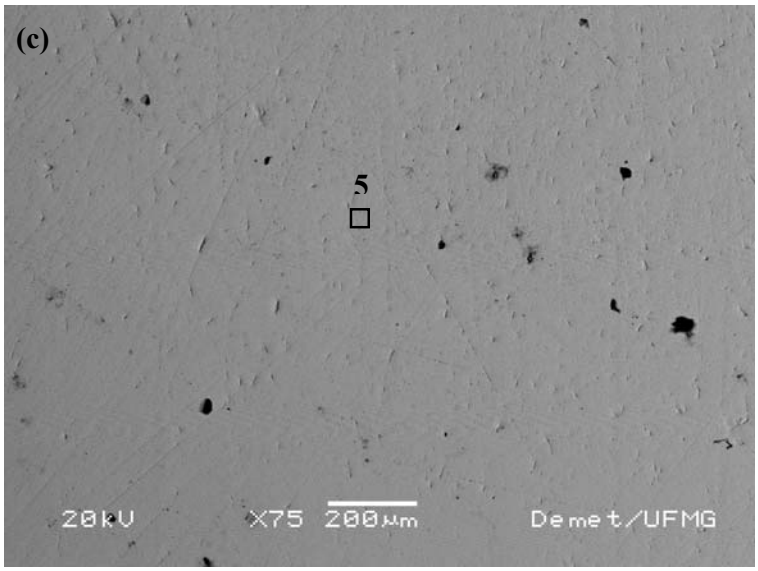

(Cont.) Fig. 3.1. Back-scattered electron micrographs of (a) CE, (b) ME and (c) PE electrodes, and selected areas analyzed by EDS.

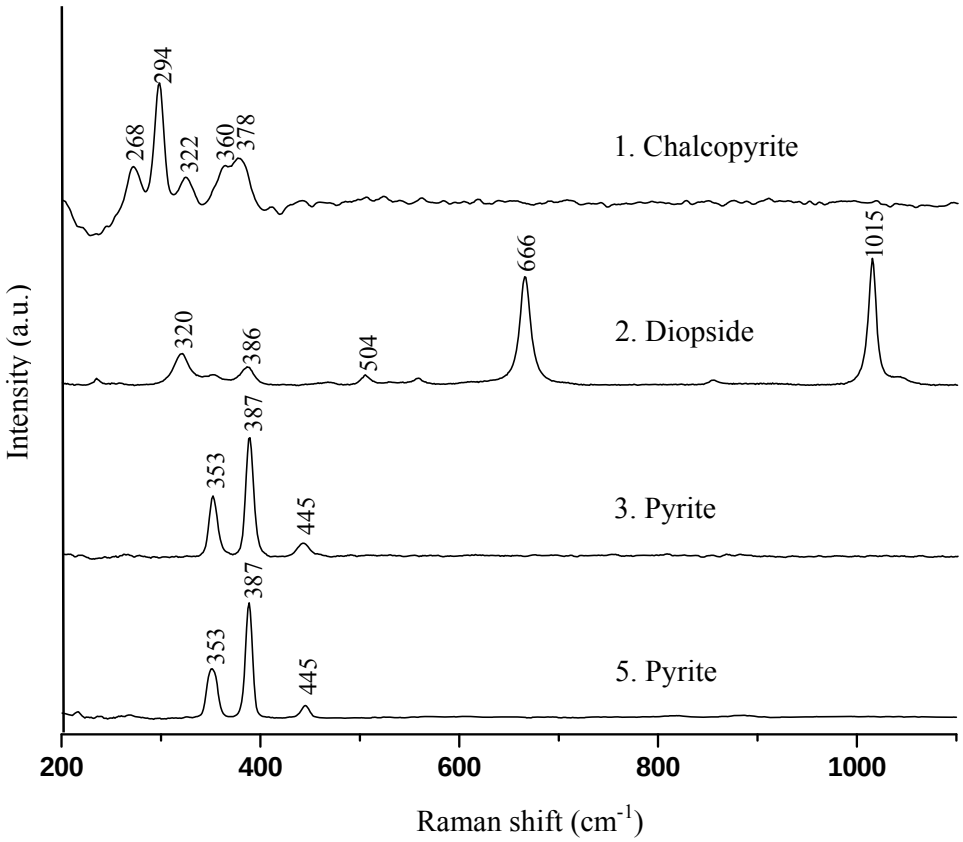

Fig. 3.2. Raman spectra obtained for areas 1, 2, 3 and 5 (vide Fig. 3.1).

Table III.1 presents the pyrite content on the reaction area of the mixed chalcopyrite-pyrite electrodes. A chalcopyrite electrode containing about 42% pyrite dispersed on its surface area (ME3) was selected. An electrode containing lower pyrite content (ME1) and another containing an intermediate value (ME2) were also selected.

Table III.1. Pyrite content on the surface of mixed (chalcopyrite-pyrite) electrodes.

Electrode	Content (%)[1]
ME1	14 ± 3
ME2	31 ± 3
ME3	42 ± 4

[1] Including the relative 95% confidence limits.

3.4.2. Electrochemical measurements: Mixed potential

3.4.2.1. Effect of pyrite inclusions

The potentials on freshly polished CE, PE, and ME electrodes immersed in 0.1 mol/L H_2SO_4 solutions, when no oxidant was added, were followed as a function of time. The results are shown in Fig. 3.3 and summarized in Table III.2. The mixed potential (E_M) increased as follows: $E_{M\ CE} < E_{M\ ME1} < E_{M\ ME2} < E_{M\ ME3} < E_{M\ PE}$. The average mixed potentials of the ME1, ME2 and ME3 electrodes were, respectively, approximately 80, 100 and 120 mV higher than the potential of the CE electrode (*i.e.*, 0.47 V). The effect of pyrite inclusions represents therefore increases of 17, 21, and 26%, respectively. The divergences among the potentials measured for the CE electrode and those reported in the literature (E_M ≈ 0.40-0.52 V *vs.* SHE) (Biegler and Swift, 1979; Hiskey and Wadsworth, 1981; Warren *et al*., 1982; Mehta and Murr, 1983; Lázaro and Nicol, 2003; Nava and González, 2006) may be associated with the elemental composition of each sample; the type and content of inclusions on the reaction surface, such as sulfides; the crystal orientation of the exposed surface; and the different experimental conditions. The results achieved with the ME electrodes (*i.e.*, about 0.55 V for the ME1 (14% FeS_2), 0.57 V for the ME2 (31% FeS_2), and 0.59 V for the ME3 (42% FeS_2)), intermediate values between the values found for the

CE and PE electrode, agreed with the findings of Mehta and Murr (1983). The intermediate mixed potential of attached chalcopyrite-pyrite electrodes was found to be 0.56 V *vs.* SHE.

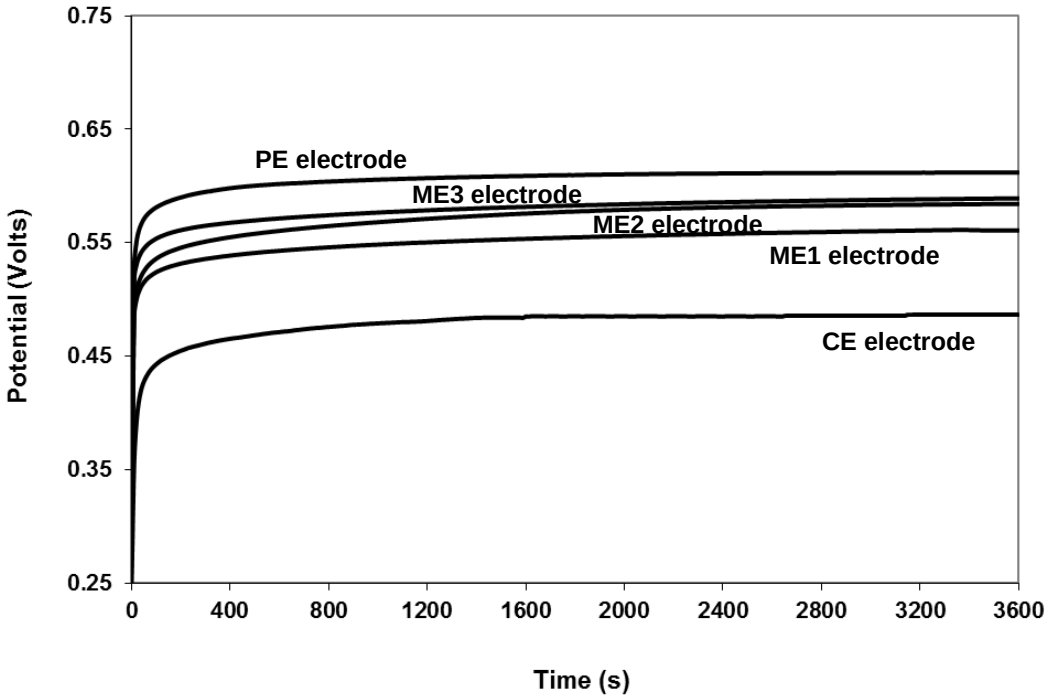

Fig. 3.3. Potentials on chalcopyrite, pyrite and pyrite-containing chalcopyrite electrodes in 0.1 mol/L H_2SO_4 solutions after nitrogen bubbling, under atmospheric conditions.

4.2.2. Effects of dissolved oxygen and ferric ion

The potentials of freshly polished CE, PE and ME electrodes immersed in the 0.1 mol/L H_2SO_4 solutions with O_2 bubbling (0.001 mol/L) and Fe^{3+} ion (0.01 or 0.05 mol/L) were also followed as a function of time. The results are shown in Fig. 3.4 and summarized in Table III.2. It should be noted that the average mixed potential of the CE and PE electrodes increased, respectively, about 80 and 90 mV in the presence of oxygen. The average mixed potentials of all the mineral electrodes increased significantly in the presence of ferric ion: about 160 and 170 mV, at 0.01 mol Fe^{3+}/L; and about 210 and 200 mV, at 0.05 mol Fe^{3+}/L, for the CE and PE electrodes, respectively. An analogous increase was also reported by others (Jones and Peters, 1976; Hirato *et al.*, 1987; You *et al.*, 2007).

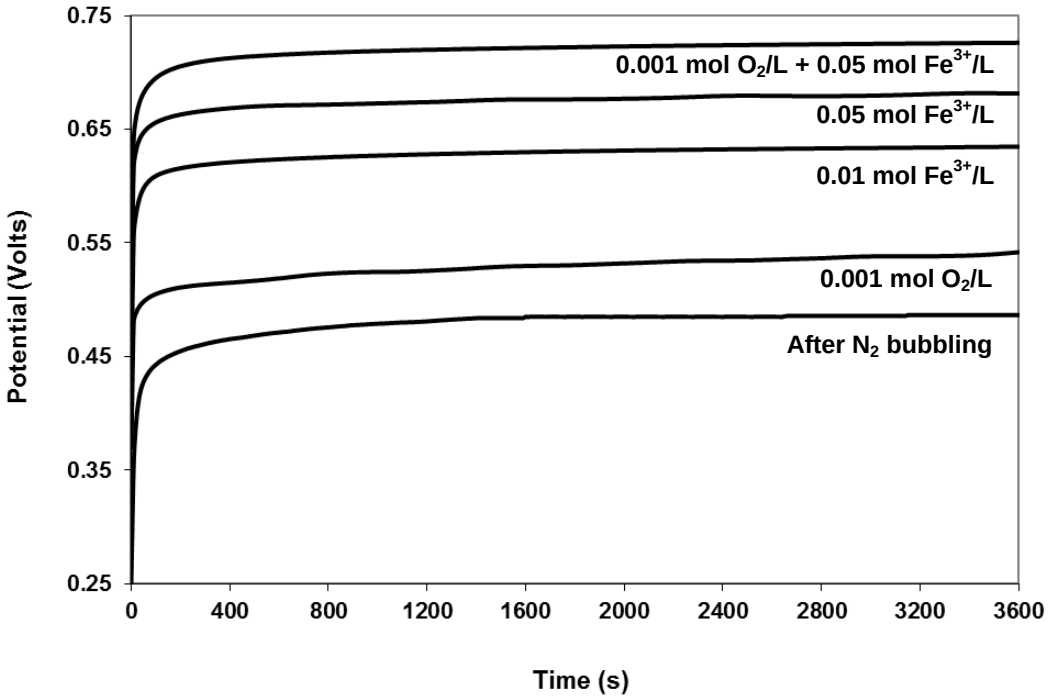

Fig. 3.4. Potentials on the CE electrode in 0.1 mol/L H_2SO_4 solutions after nitrogen bubbling and in the presence of different oxidants, under atmospheric conditions.

In order to better simulate practical leaching conditions, the magnitude of the combined effects of pyrite, oxygen, and ferric ion on the mixed potential of chalcopyrite was also investigated. The mixed potentials measured in the presence of both the oxidants (0.001 mol O_2/L + 0.05 mol Fe^{3+}/L) are summarized in Table III.2. It should be noticed that the average mixed potential increased significantly for all samples. For the CE electrode, the mixed potential value was 250 mV (53% increase) higher than the potential measured after nitrogen bubbling. Taking into account the individual effect of Fe^{3+} ion at 0.05 mol/L, this noteworthy effect may be explained by the oxidation of Fe^{2+} to Fe^{3+} ions by dissolved oxygen in the acidic solution (Eq. 3.4), with further discharge of Fe^{3+} ions mainly on FeS_2, cathodic site of the galvanic couple, as will be discussed later. Regarding the galvanic effect of pyrite, for the ME3 electrode, *e.g.*, the mixed potential measured in the presence of both the oxidants was about 100 mV (14% increase) larger than the potential measured on the CE electrode in the presence of both the oxidants.

Table III.2. Mixed potentials (V/SHE) for the mineral electrodes in 0.1 mol/L H_2SO_4 solutions after nitrogen bubbling and in the presence of ferric ion and dissolved oxygen, under atmospheric conditions.

Electrode	**E_M**	**E_M (0.001 M O_2)**	**E_M (0.01 M Fe^{3+})**	**E_M (0.05 M Fe^{3+})**	**E_M (0.001 M O_2 + 0.05 M Fe^{3+})**
CE	0.47 ± 0.02	0.55 ± 0.01	0.63 ± 0.01	0.68 ± 0.01	0.72 ± 0.02
ME1	0.55 ± 0.02	0.58 ± 0.01	0.71 ± 0.01	0.75 ± 0.01	0.78 ± 0.02
ME2	0.57 ± 0.01	0.61 ± 0.01	0.72 ± 0.01	0.77 ± 0.01	0.81 ± 0.01
ME3	0.59 ± 0.01	0.63 ± 0.01	0.74 ± 0.01	0.78 ± 0.01	0.82 ± 0.01
PE	0.61 ± 0.02	0.70 ± 0.01	0.78 ± 0.01	0.81 ± 0.01	0.85 ± 0.01

3.4.3. Electrochemical measurements: Dissolution current density

3.4.3.1. Effect of pyrite inclusions

The current density at the mixed potential was measured at low anodic and low cathodic overpotentials ($\eta \pm 150$ mV). Fig. 3.5 shows the Tafel plots obtained for the CE and ME electrodes in 0.1 mol/L H_2SO_4 solutions after nitrogen bubbling. It is important to observe that the polarization curves are not symmetrical. The shape of each curve is determined by the current density and corresponding anodic and cathodic Tafel slopes. It can be noted that the presence of pyrite inclusions caused a positive shift in the Tafel plots of chalcopyrite, that is: it increased the dissolution current density of chalcopyrite.

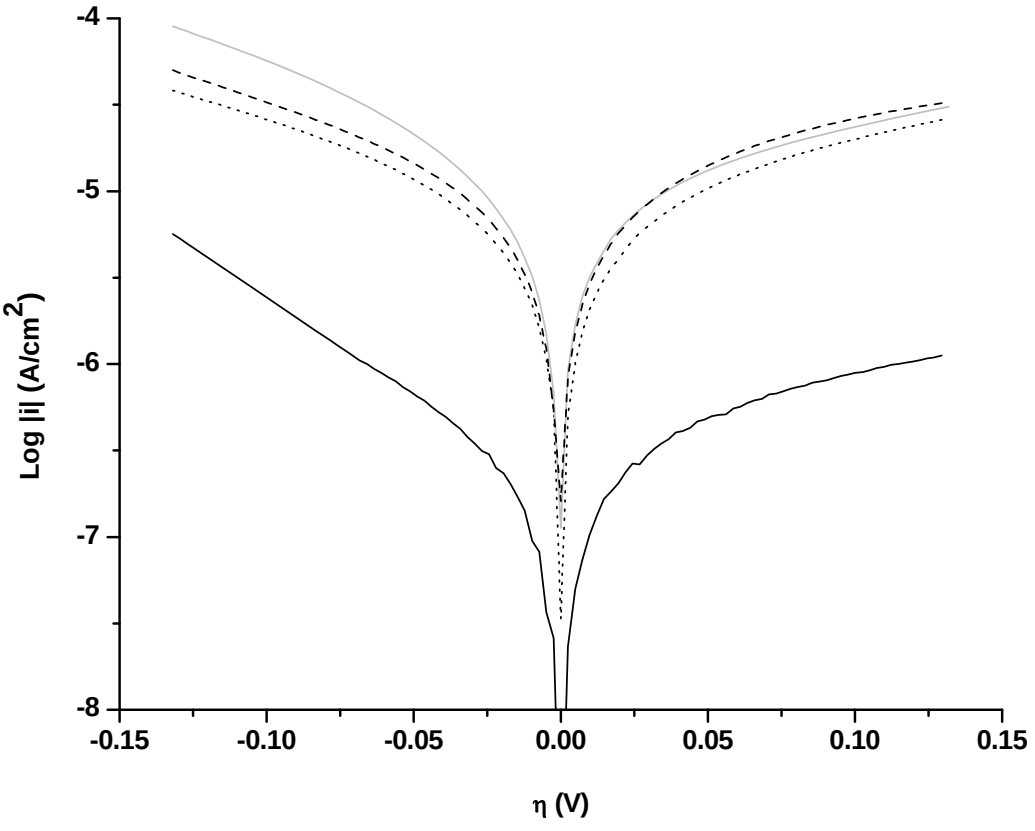

Fig. 3.5. Tafel plots for the CE and ME electrodes in 0.1 mol/L H_2SO_4 solutions after nitrogen bubbling, under atmospheric conditions. Legend: Solid (black) - CE electrode; Dot (black) - ME1 electrode; Dash (black) - ME2 electrode; Solid (gray) - ME3 electrode.

The average values calculated for these electrodes are summarized in Table III.3. It can be seen that the i_{diss} values for the ME electrodes are higher than the values obtained for the CE electrode, as follows: $i_{diss\ CE} < i_{diss\ ME1} < i_{diss\ ME2} < i_{diss\ ME3}$. Significant increases of the order of 15, 24, and 40 times were observed, respectively, for the ME1 (14% FeS_2), ME2 (31% FeS_2), and ME3 (42% FeS_2) electrodes.

3.4.3.2. Effects of dissolved oxygen and ferric ion

Fig. 3.6 shows the Tafel plots obtained in the presence of Fe^{3+} ion (0.01 or 0.05 mol/L) and O_2 bubbling (0.001 mol O_2/L). It can be seen that the presence of these oxidants increased the i_{diss} value calculated for the pyrite-free chalcopyrite electrode.

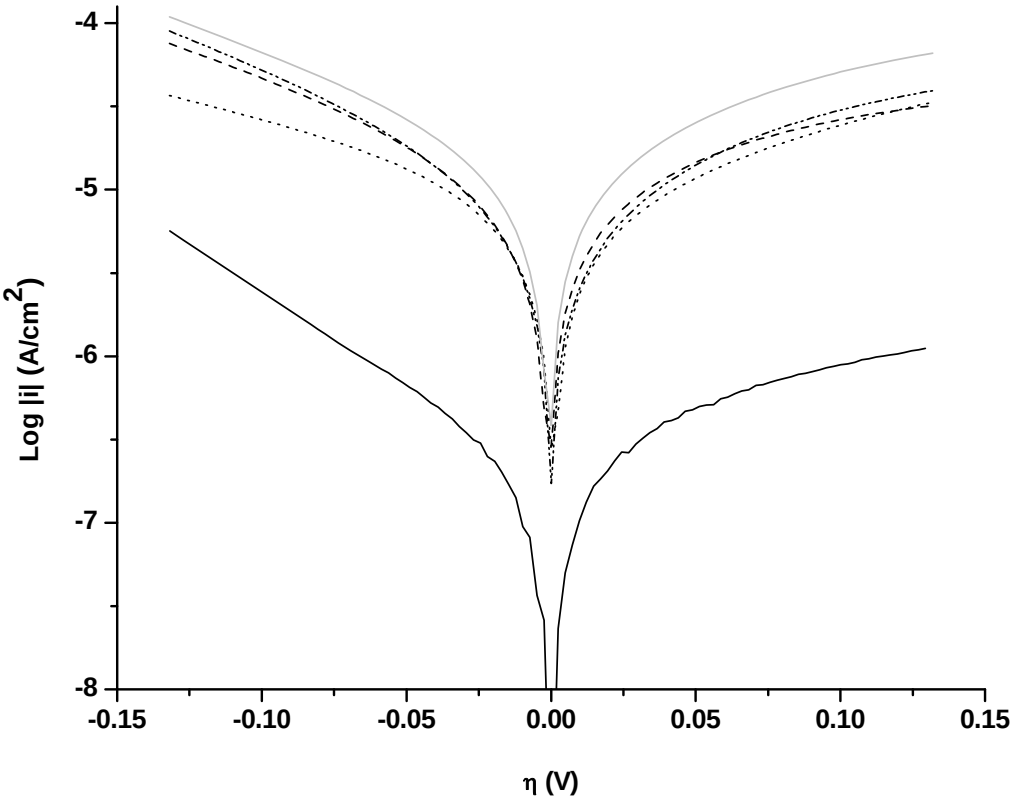

Fig. 3.6. Tafel plots for the CE electrode in 0.1 mol/L H_2SO_4 solutions under atmospheric conditions. Legend: Solid (black) - After N_2 bubbling; Dot (black) - 0.001 mol O_2/L; Dash (black) - 0.01 mol/L Fe^{3+}; Dash Dot Dot (black) - 0.05 mol/L Fe^{3+}; Solid (gray) - 0.001 mol O_2/L + 0.05 mol/L Fe^{3+}.

Table III.3. Dissolution current densities ($\mu A/cm^2$) for the mineral electrodes in 0.1 mol/L H_2SO_4 solutions after nitrogen bubbling and in the presence of ferric ion and dissolved oxygen, under atmospheric conditions.

Electrode	**i_{diss}**	**i_{diss} (0.001 M O_2)**	**i_{diss} (0.01 M Fe^{3+})**	**i_{diss} (0.05 M Fe^{3+})**	**i_{diss} (0.001 M O_2 + 0.05 M Fe^{3+})**
CE	0.26 ± 0.08	4.80 ± 0.49	8.00 ± 0.88	9.33 ± 0.97	14.55 ± 0.96
ME1	4.00 ± 0.38	5.87 ± 0.49	11.19 ± 1.25	14.94 ± 1.10	18.48 ± 1.31
ME2	6.32 ± 0.62	8.75 ± 0.71	12.74 ± 1.24	17.43 ± 1.46	20.72 ± 1.55
ME3	10.40 ± 0.94	12.23 ± 0.97	16.73 ± 1.46	20.09 ± 1.43	23.66 ± 1.94

Table III.3 summarizes the values obtained for all the electrodes in the presence of oxygen and ferric ion. It may be noted that for the CE electrode, increases of the order of 18, 31, 36, and 56 times were calculated, respectively, in the presence of 0.001 mol O_2/L, 0.01 mol Fe^{3+}/L, 0.05 mol Fe^{3+}/L and 0.001 mol O_2/L with 0.05 mol Fe^{3+}/L. In relation to the magnitude of the galvanic effect of pyrite on the dissolution current density of chalcopyrite in the presence of oxidants, an interesting result has been achieved. When approximately 42% FeS_2 was dispersed on chalcopyrite reaction area (ME3 electrode), the current density at the mixed potential increased by approximately 2.6, 2.1, 2.2, and 1.6 times, respectively, in solutions containing 0.001 mol O_2/L, 0.01 mol Fe^{3+}/L, 0.05 mol Fe^{3+}/L, and 0.001 mol O_2/L with 0.05 mol Fe^{3+}/L.

Therefore, taking into account the standard deviation of the electrochemical measurements, a slightly more pronounced effect of pyrite inclusions on chalcopyrite oxidation rate (increases of 2.6 times) was observed under the lower oxidizing conditions (*i.e.*, only in the presence of O_2). Under the higher oxidizing conditions (*i.e.*, in the presence of both O_2 and Fe^{3+} ions), a slightly less pronounced effect (increases of 1.6 times) was noted. A probable reason for such behavior will be discussed later.

3.5. Discussion

3.5.1. Effects of oxidants on the electrochemistry of chalcopyrite

Fig. 3.3 reveals that the potentiometric curves exhibited a similar pattern: a high initial rate followed by an approximately steady-state condition, where the open circuit potential (OCP) – potential exhibited by the electrode surfaces in the absence of externally applied potential – stabilizes at the mixed potential (E_M). At this condition, the net current is zero (*i.e.*, the anodic and cathodic current densities are equal and of opposite sign) (Bockris and Reddy, 1998) and, thus, the following condition holds:

$$\frac{I_{anodic}}{A_{anodic}} = -\frac{I_{cathodic}}{A_{cathodic}} \qquad (3.5a)$$

$$i_{anodic} = -i_{cathodic} = i_{diss} \quad (3.5b)$$

where I is the electrical current, A the surface area and i_{diss} the current density at the mixed potential, denoted here as dissolution current density. For the pyrite-free chalcopyrite (CE) electrode, the surface area available for both half-cell reactions is assumed equivalent (*i.e.*, $A_{anodic} \approx A_{cathodic}$), thus, the anodic and cathodic processes would occur over the entire surface of the mineral. At the steady-state condition (*i.e.*, low redox potential values), it is assumed that the dissolution of chalcopyrite occurs as a simultaneous combination of an anodic non-stoichiometric oxidation (Eq. 3.6) with the reduction of residual dissolved oxygen on the mineral surface (Eq. 3.7).

$$CuFeS_2 \underset{k1}{\overset{k1'}{=}} Cu_{1-x}Fe_{1-y}S_{2-z} + x\,Cu^{2+}_{(aq)} + y\,Fe^{2+}_{(aq)} + z\,S + 2(x+y)\,e^- \quad (3.6)$$

$$O_{2(g)} + 4\,H^+_{(aq)} + 4\,e^- \underset{k2}{\overset{k2'}{=}} 2\,H_2O \quad (3.7)$$

Many authors have claimed that metal-deficient sulfides, generally iron-deficient phases, are intermediate products formed on chalcopyrite during its dissolution in acidic media at low redox potentials (0.35-0.75 V *vs.* SHE) (Linge, 1976; Biegler and Swift, 1979; Warren *et al.*, 1982; Yin *et al.*, 1995; Lázaro and Nicol, 2003; Abraitis *et al.*, 2004; Mikhlin *et al.*, 2004; Nava and González, 2006; Parker *et al.*, 2008). The formation of these intermediate phases is commonly associated with "passivation"; that is, the inhibition of the reaction progress.

Writing the anodic current density (i_{anodic}) and cathodic current density ($i_{cathodic}$) in terms of the Butler-Volmer equation (Bockris and Reddy, 1998), and also assuming that the mineral oxidation is irreversible (*i.e.*, the cathodic reduction of the reaction products can be ignored at the potentials encountered during oxidation):

$$i_a = k_1 \exp\left[\frac{\alpha_a n_a F E}{RT}\right] \quad (3.8)$$

$$i_c = -k_2 [O_2]^{x'} [H^+]^{x''} \exp\left[\frac{-(1-\alpha_c) n_c F E}{RT}\right] \quad (3.9)$$

where k is the rate constant, n the number of electrons involved in the corresponding reactions, F the Faraday constant, α the transfer coefficient, R the universal gas constant, T the absolute temperature and x the reaction order. Therefore, at the steady-state condition (Eq. 3.10), the potential measured on the electrode surface depends on the rate constants of the half-cell reactions, hydrogen ion and oxygen concentration (Eq. 3.11).

$$i_a = -i_c = -(i_{O2}) = i_{diss} \tag{3.10}$$

$$E_M = \left(\frac{RT}{F}\right)\ln\left(\frac{k_2[O_2]^{x'}[H^+]^{x''}}{k_1}\right) \tag{3.11}$$

In the absence of measured data, the values of $\alpha_a = \alpha_c = 0.5$ were adopted; α represents the symmetry of the activation barrier for the anodic and the cathodic charge transfer reactions, and for symmetrical barriers $\alpha = 0.5$. The assumption of $n_a = n_c = 1$, that is, one electron transfer, was based on the fact that one electron transfer reactions are thermodynamically more favorable (Hiskey and Wadsworth, 1981; Bockris and Reddy, 1998). As predicted by Eq. 3.11 and experimentally verified by others (Rao and Finch, 1988; You *et al*., 2007), when the acidity of the electrolyte solution increases (*i.e.*, lower pH values), the mixed potential of chalcopyrite also increases.

Fig. 3.4 shows the potentials on the CE electrode after nitrogen bubbling and in the presence of oxidants. It should be noticed that the potentiometric curves exhibited a similar pattern. Assuming that the dissolution of chalcopyrite takes place via combination of the anodic non-stoichiometric reaction (Eq. 3.6) with parallel cathodic overall reactions (*i.e.*, reduction of oxygen (Eq. 3.7) and Fe^{3+} ion (Eq. 3.12) on the solid surface), the steady-state condition when oxygen is bubbled in the solution can be described by Eq. 3.10, while the steady-state conditions when ferric ion is added in the solution or when both the oxidants are added can be described by Eq. 3.13, where i_{O2} corresponds to the cathodic current associated with the oxygen reduction process and i_{Fe} the cathodic current involved in the ferric ion reduction.

$$Fe^{3+}_{(aq)} + e^- \underset{k3}{\overset{k3'}{=}} Fe^{2+}_{(aq)} \tag{3.12}$$

$$i_a = (i_a + i_{Fe}) = -i_c = -(i_{O2} + i_{Fe}) = i_{diss} \quad (3.13)$$

For i_a (Eq. 3.8) and i_c: that is, (Eq. 3.9) in the presence of oxygen; and (Eq. 3.14) when ferric ion is added,

$$i_c = -k_2[O_2]^{x'}[H^+]^{x''}\exp\left[\frac{-(1-\alpha_c)n_cFE}{RT}\right] - k_3[Fe^{3+}]^{x'''}\exp\left[\frac{-(1-\alpha_c)n_cFE}{RT}\right] + k_{3'}[Fe^{2+}]^{x''''}\exp\left[\frac{\alpha_a n_a FE}{RT}\right] \quad (3.14)$$

the mixed potentials in the presence of oxygen (Eq. 3.11), and ferric ion (Eq. 3.15) are given by the rate constants of the half-cell reactions, H^+ ion and oxidant concentrations. The assumptions $\alpha_a = \alpha_c = 0.5$ and $n_a = n_c = 1$ were made once more.

$$E_M = \left(\frac{RT}{F}\right)\ln\left(\frac{k_2[O_2]^{x'}[H^+]^{x''} + k_3[Fe^{3+}]^{x'''}}{k_1 + k_{3'}[Fe^{2+}]^{x''''}}\right) \quad (3.15)$$

By similar assumptions to those made for the effects of oxidants on the mixed potential of pure chalcopyrite (CE) electrodes, which are (i) the steady-state condition (Eqs. 3.10 and 3.13); (ii) anodic non-stoichiometric oxidation (Eq. 3.6); (iii) parallel oxygen (Eq. 3.7) and ferric ion (Eq. 3.12) reductions; and (iv) $A_{anodic} \approx A_{cathodic}$; the current densities at the steady-state conditions also depend on the rate constants of the half-cell reactions, H^+ ion and oxidant concentrations, according to (Eq. 3.16) in the presence of oxygen,

$$i_{diss} = \left[k_1\left(k_2[O_2]^{x'}[H^+]^{x''}\right)\right]^{\frac{1}{2}} \quad (3.16)$$

and (Eq. 3.17) in the presence of ferric ion,

$$i_{diss} = k_1\left(\frac{k_2[O_2]^{x'}[H^+]^{x''} + k_3[Fe^{3+}]^{x'''}}{k_1 + k_{3'}[Fe^{2+}]^{x''''}}\right)^{\frac{1}{2}} \quad (3.17)$$

Thus, when the acidity of the electrolyte solution increases, the current density at the mixed potential of chalcopyrite becomes larger, as verified experimentally by You *et al.* (2007). The observed increase of the mixed potential (Fig. 3.4) and corresponding current density (Fig. 3.6) of chalcopyrite when oxygen was bubbled in the solution may be related to the higher contribution of the term $k_2[O_2]^{x'}[H^+]^{x''}$ in the corresponding models (Eqs. 3.11 and 3.16, respectively). Likewise, the increase of the mixed potential and current density when ferric ion was added in the solution may be associated with the addition of the term $k_3[Fe^{3+}]^{x'''}$ in the corresponding models (Eqs. 3.15 and 3.17, respectively). Thus, if the Fe^{3+} ion concentration increases in the solution (from 0.01 to 0.05 mol/L), the values of the mixed potential and the corresponding current density increase as well, as verified experimentally. The considerable increase verified in the presence of both the oxidants may be related to the higher contribution of the terms $k_2[O_2]^{x'}[H^+]^{x''}$ and $k_3[Fe^{3+}]^{x'''}$, and the lower contribution of the term $k_{3'}[Fe^{2+}]^{x''''}$. The observed increases could be associated with the reduction rates of these two oxidants on the solid surface and, in addition, the ferrous oxidation rate. This process decreases the Fe^{2+} ion concentration in the solution and regenerates Fe^{3+} ions, which discharge again on the mineral surface.

According to the results obtained in the present investigation, the effects of ferric ion addition on the electrochemistry of chalcopyrite in acidic sulfate media appeared to be more pronounced than the effects of oxygen bubbling. These results may be related to the relatively higher Fe^{3+} ion concentration (0.01-0.05 mol/L) as compared to dissolved O_2 concentration (0.001 mol/L). The rate constants of the two reduction reactions cannot be compared at this point. Figure 3.7 displays the Tafel plots (only the cathodic branches) obtained for the CE electrode in 0.1 mol/L H_2SO_4 solutions with oxygen (0.001 mol O_2/L) and Fe^{3+} ion (0.01 mol/L) addition; the corresponding linear correlations of log|i| with overpotential are also provided. It is well-established that if the potential is made more negative than the mixed potential, where $\eta = 0$, then $i_a < |i_c|$ and the cathodic reduction reaction predominates. Under the investigated conditions and on the basis of the current densities at particular overpotential values, it may be observed that the reaction rate of the cathodic oxygen reduction on chalcopyrite is slower than that of the cathodic ferric ion reduction.

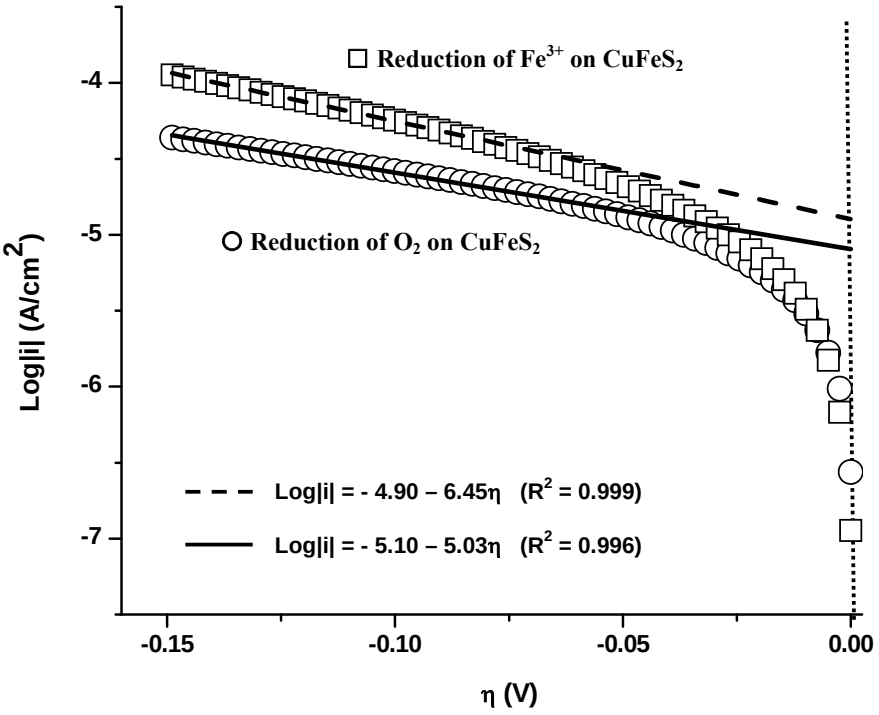

Fig. 3.7. Tafel plots (cathodic branch) for the CE electrode in 0.1 mol/L H_2SO_4 solutions in the presence of oxygen (0.001 mol O_2/L) and ferric ion (0.01 mol Fe^{3+}/L), under atmospheric conditions.

3.5.2. Effects of pyrite inclusions on the electrochemistry of the chalcopyrite

Regarding the galvanic effect of pyrite on chalcopyrite electrochemistry, it has been assumed that pyrite, when galvanically-coupled to chalcopyrite, provides a more favorable site for the reduction reactions (Berry *et al*., 1978; Mehta and Murr, 1983; Nowak *et al*., 1984; You *et al*., 2007; Dixon *et al*., 2008). On the basis of this approach, ferric ion and dissolved oxygen reduction reactions should occur with a lower overpotential on pyrite surface than on chalcopyrite.

Fig. 3.8 exhibits the Tafel plots (cathodic branches) obtained for the CE and PE electrodes in 0.1 mol/L H_2SO_4 solutions with oxygen bubbling (0.001 mol O_2/L) or ferric ion (0.01 mol Fe^{3+}/L). Again on the basis of current densities at specific overpotential values, the polarization curves suggest that the kinetics of oxygen reduction on chalcopyrite is faster than the reduction kinetics on pyrite (Fig. 3.8a).

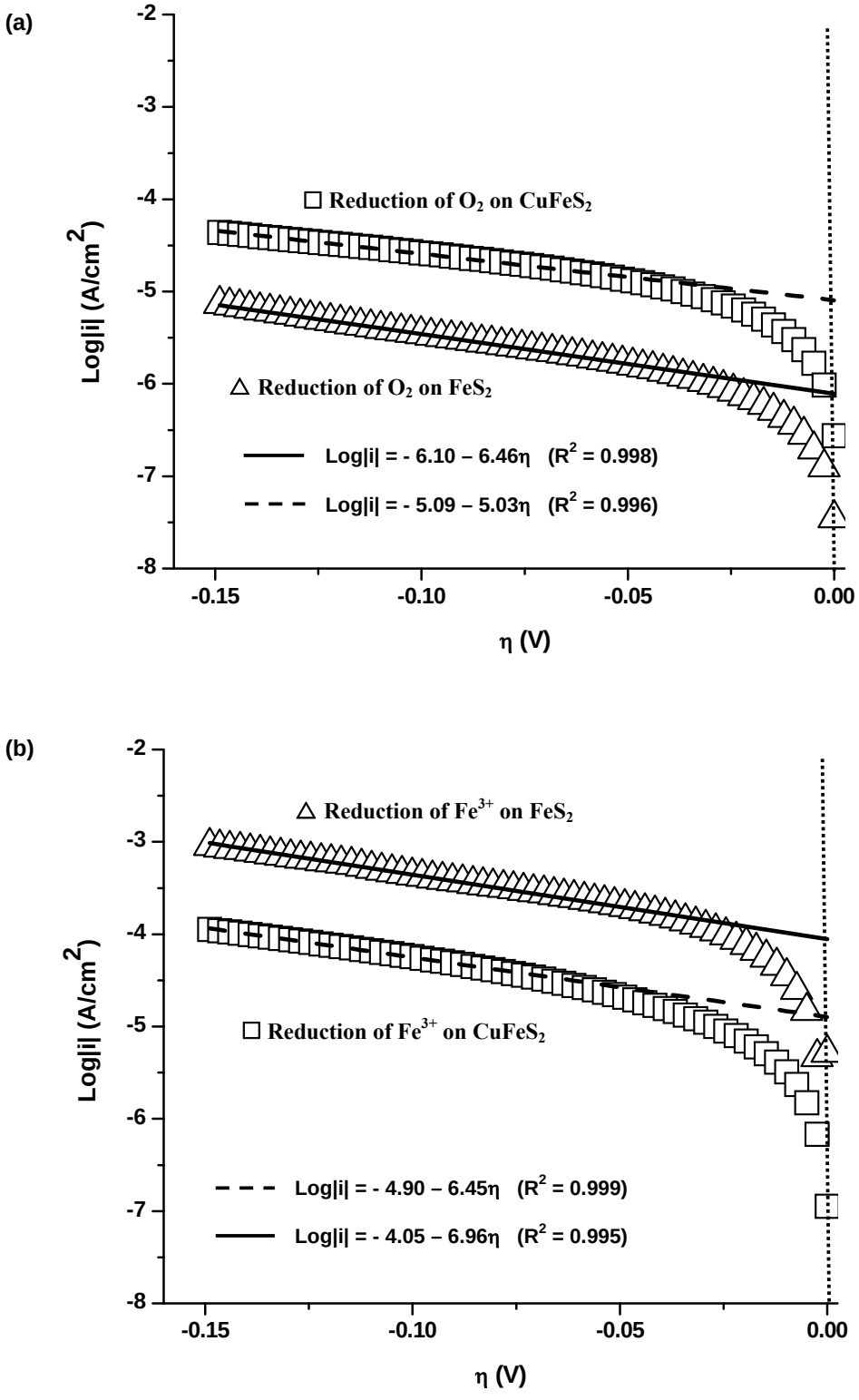

Fig. 3.8. Tafel plots (cathodic branch) for the CE and PE electrodes in 0.1 mol/L H_2SO_4 solutions in the presence of (a) oxygen (0.001 mol O_2/L) and (b) ferric ion (0.01 mol/L), under atmospheric conditions.

On the other hand, Fig. 3.8b indicates that the cathodic ferric ion reduction on chalcopyrite is kinetically slower than the cathodic reduction on pyrite. Thus, under the investigated conditions, pyrite is a more favorable cathodic site only for the reduction of ferric ions. It might be relevant to investigate the behavior of samples of equivalent purity from different sources.

Fig. 3.9 exhibits the Tafel plots (only the cathodic branches) obtained for the CE and ME3 electrodes in 0.1 mol/L H_2SO_4 solutions with oxygen bubbling (0.001 mol O_2/L) or ferric ion (0.01 mol Fe^{3+}/L) addition. It can be noticed that for both the oxidants the kinetics of the reduction reactions on the galvanic couple (mixed electrode) is faster than the reduction kinetics on chalcopyrite.

On the galvanic couple, the cathodic current density is associated with two processes (*i.e.*, the cathodic reductions of the oxidants on chalcopyrite and pyrite surfaces). In the presence of ferric ions, the current density associated with the reduction process on pyrite is possibly larger than the current density associated with the reduction process on chalcopyrite. In the presence of dissolved oxygen, an opposite trend is possibly verified.

Regarding both the increase of the mixed potential and dissolution current density of chalcopyrite when the pyrite content on the electrode surface increases, it was assumed that the pyrite inclusions acts only as a cathodic site in the galvanic coupling (*i.e.*, there are no anodic processes on pyrite surface). Thus, the surface areas for the anodic and the cathodic reactions are probably related as $A_{cathodic} > A_{anodic}$, since the cathodic reduction reactions are expected to occur on the cathodic sites on chalcopyrite as well (Fig 3.10).

As $I_{anodic}/A_{anodic} = -I_{cathodic}/A_{cathodic} = i_{galv}$ (*i.e.*, the current density at the galvanic potential, E_G), the cathodic current, that is, the flow of electrons from the electrode to the solution, is higher than the anodic current. The greater the cathodic discharge area, $A_{cathodic}$, available on mixed (ME) electrode surfaces, the higher the magnitude of the cathodic current and cathodic current density ($i_{cathodic}$) and in turn, the higher the anodic current density (i_{anodic}) or chalcopyrite oxidation rate.

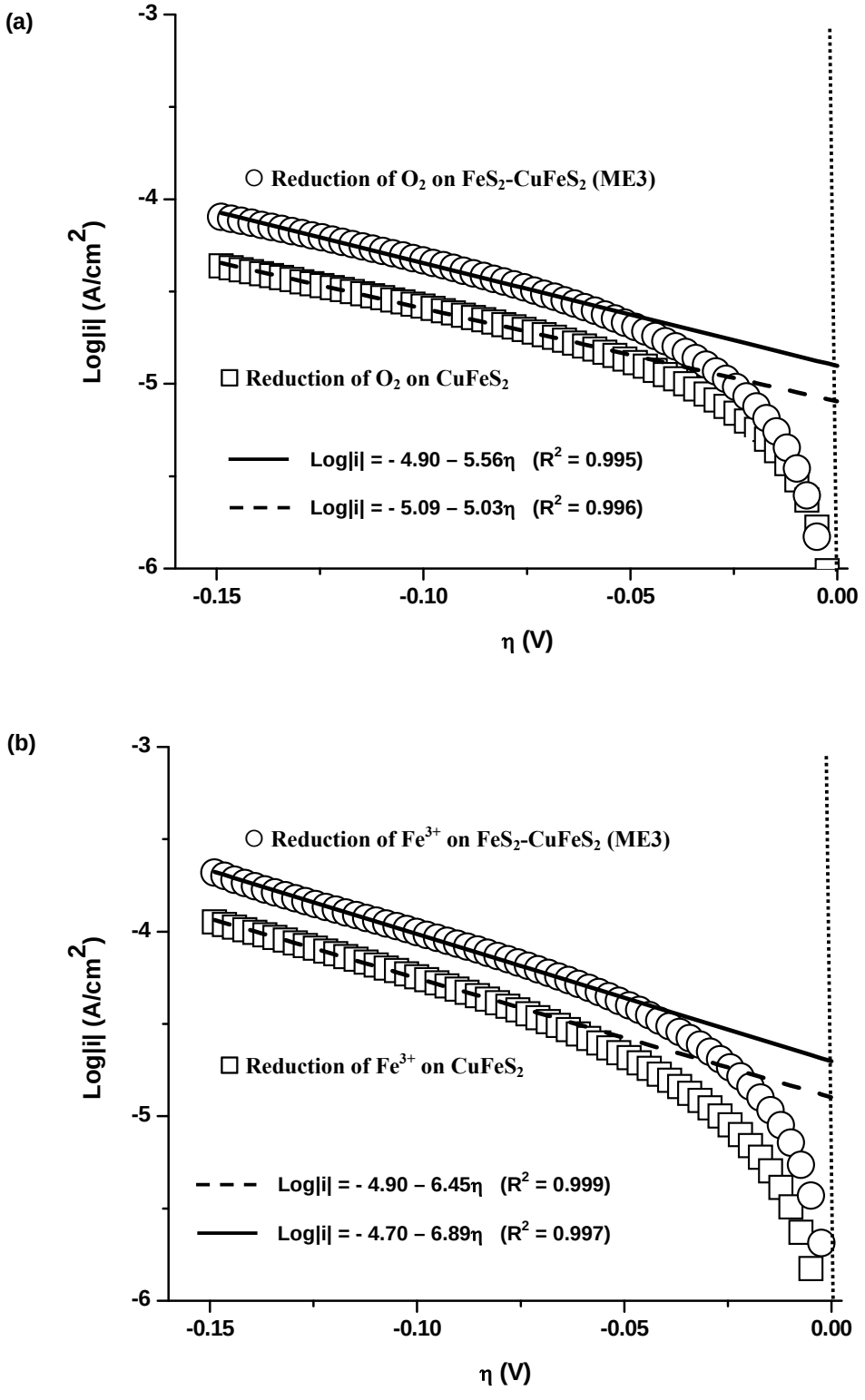

Fig. 3.9. Tafel plots (cathodic branch) for the CE and ME3 electrodes in 0.1 mol/L H_2SO_4 solutions in the presence of (a) oxygen (0.001 mol O_2/L) and (b) ferric ion (0.05 mol/L), under atmospheric conditions.

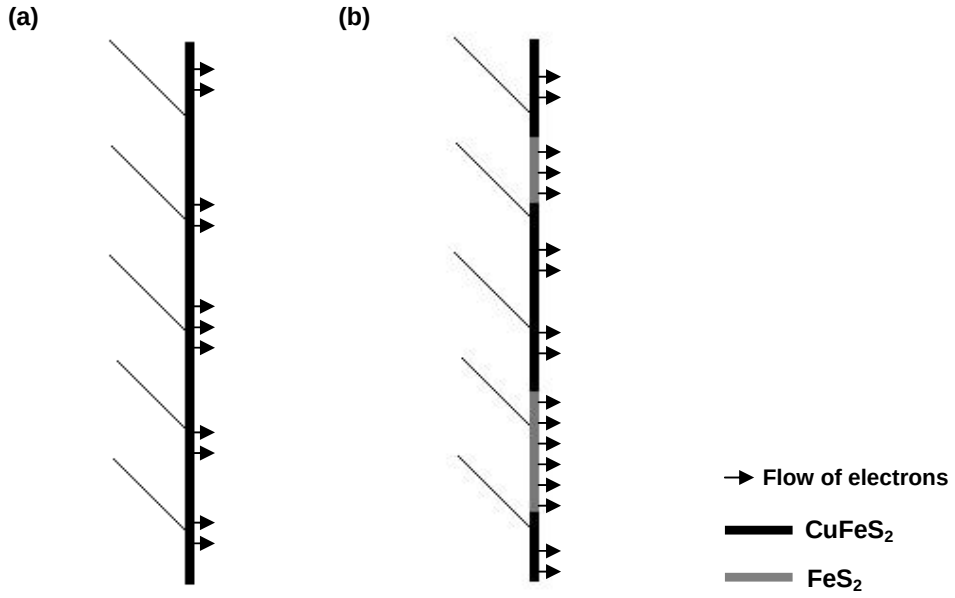

Fig. 3.10. Electrode-solution interface: (a) Area available for reduction reactions on the surface of CE electrodes ($A_{anodic} \approx A_{cathodic}$); and (b) area available for reduction reactions on the surface of ME electrodes ($A_{anodic} < A_{cathodic}$).

Finnaly, the larger effect of pyrite inclusions on the dissolution current density of chalcopyrite after nitrogen bubbling (increases of up to 40 times), comparatively to the effects observed under oxidizing conditions (increases of up to 2.6 times) may be related to the amount (or thickness) of a product layer that forms on chalcopyrite surface during the electrochemical measurements. As assumed, chalcopyrite acts as the anode, but also as cathodic site, when in contact with pyrite. After nitrogen bubbling, the product layer that grows up on chalcopyrite would not be thick enough to affect significantly the rate of the cathodic reduction of the residual dissolved oxygen. In contrast, the amount of product layer that forms on this mineral when oxygen is bubbled in the solution would be large enough to affect the kinetics of oxygen reduction. Therefore, the total discharge area available on chalcopyrite surface and, as a result, the proportion of oxygen that is reduced on this mineral, would be both reduced, which may explain the decrease in the magnitude of its dissolution current density from 40 to 2.6 times. In the presence of ferric ion or ferric ion and bubbled oxygen, a still thicker product layer possibly develops on chalcopyrite during the measurements, affecting to a larger extent the reduction rates of both the oxidants.

3.6. Conclusions

Quantitative assessments of the galvanic effect of pyrite on the electrochemistry of chalcopyrite in acidic sulfate media under atmospheric conditions are provided. Electrodes were prepared with chalcopyrite samples containing different proportions of pyrite inclusions. The positive effect of combining ferric (Fe^{3+}) ion and dissolved oxygen on chalcopyrite oxidation was quantified by measuring the increase in the mixed potential and dissolution current density. This effect was magnified by the galvanic chalcopyrite-pyrite interaction. The main conclusions were:

(i) The presence of pyrite inclusions on chalcopyrite increased the mixed potential value of this copper sulfide. The mixed potentials of the ME1 (14% FeS_2), ME2 (31% FeS_2), and ME3 (42% FeS_2) electrodes were 17, 21, and 26%, respectively, larger than the potential measured on the CE electrode (0% FeS_2). The mixed potential measured in the presence of pyrite, dissolved oxygen and ferric ion was up to 14% larger than the potential measured on the CE electrode after nitrogen bubbling;

(ii) The presence of pyrite inclusions on chalcopyrite caused a significant increase in the dissolution current density of chalcopyrite. The current densities of the ME1, ME2, and ME3 electrodes were 15, 24, and 40 times, respectively, higher than the current measured on the CE electrode. More pronounced effects of pyrite inclusions on the chalcopyrite oxidation rate was observed after nitrogen bubbling (increases of up to 40 times in the dissolution current density) and under the lower oxidizing conditions (increase of up to 2.6 times);

(iii) For the investigated conditions, it was demonstrated that only the ferric ion reduction reaction occurs with lower overpotential on pyrite than on chalcopyrite.

The results show that under conditions where there is a permanent contact between pyrite and chalcopyrite, the galvanic effect established between these sulfides is magnified under less oxidizing conditions. Hence, it is probable that this phenomenon will help to enhance copper extraction from chalcopyrite ores under practical, typical heap leaching conditions, especially in the heap sections where there is a reduction of the oxidants concentration.

Chapter 4 – Electrochemical dissolution of chalcopyrite: Detection of bornite by synchrotron small angle X-ray diffraction and its correlation with the hindered dissolution process

Abstract

The formation of bornite (Cu_5FeS_4), an iron-deficient sulfide, and its correlation with the slow oxidation rate of chalcopyrite ($CuFeS_2$) in acidic media under atmospheric conditions is demonstrated. Chalcopyrite electrodes oxidized in 0.1 mol/L H_2SO_4 solutions at room temperature (25±1°C) were analyzed by micro Raman spectroscopy and synchrotron small angle X-ray diffraction (S-SAXRD), techniques indicated for thin films analysis. Anodic polarization curves of chalcopyrite electrodes showed two well-defined behaviors: quasi-potential-independent regime and potential-dependent regime. When the critical potential (Ec) is attained, which ranged from 0.75 to 0.90 V *vs.* Standard Hydrogen Electrode (SHE), the mineral oxidation rate becomes strongly dependent on potential. Potentiostatic current-time profiles at 0.60 and 0.70 V *vs.* SHE indicated a current decay, which suggests the formation of a progressively thickening protective layer. The profiles at 0.80 V *vs.* SHE showed a similar current decay, but also an active oxidation process for some samples. After chronoamperometry at 0.70 and 0.80 V *vs.* SHE, respectively, for 6 and 2 h, analyses by using S-SAXRD revealed peaks of bornite on oxidized chalcopyrite electrodes. Elemental sulfur (S_8) was also detected by S-SAXRD at 0.80 and 1.00 V *vs.* SHE, respectively, for 2 and 0.5 h. An unidentified metal-deficient phase and covellite (CuS) were detected on chalcopyrite by micro Raman spectroscopy after chronoamperometry at 0.60 and 0.80 V *vs.* SHE, respectively. The formation or absence of these product phases under a constant applied potential correlated well with a hindered dissolution or active oxidation processes. The results of this work support the hypothesis that the formation of intermediate iron-deficient sulfides contributes to the slow oxidation rate of chalcopyrite under atmospheric conditions.

Key-words: chalcopyrite; bornite; chronoamperometry; synchrotron small angle X-ray diffraction; Raman spectroscopy.

4.1. Introduction

Chalcopyrite, the most abundant copper mineral, does not dissolve significantly under heap bioleaching conditions. For low temperatures, the mineral leaching rate is known to be very slow and typically tends to decline with time (Jones and Peters, 1976; Muñoz *et al*., 1979; Dutrizac, 1981; Majima *et al*., 1985; Hirato *et al*., 1987). In an attempt to overcome this constraint, a number of investigations have been conducted aimed at understanding the kinetics and mechanisms involved in the dissolution of this sulfide. Most of the studies ascribe the slow leaching kinetics of chalcopyrite to the formation of an insoluble layer, which prevents further mineral dissolution. Nevertheless, the nature of the product layer, as well as the mechanisms by which it is formed and affects the dissolution reaction are not completely understood.

Many authors have claimed that metal-deficient sulfides are intermediate product phases formed on chalcopyrite during its dissolutionat low-temperature conditions (Linge, 1976; Biegler and Swift, 1979; Warren *et al*., 1982; Biegler and Horne, 1985; Yin *et al*., 1995; Arce and González, 2002; Lázaro and Nicol, 2003; Abraitis *et al*., 2004; Mikhlin *et al*., 2004; Nava and González, 2006; Parker *et al*., 2008; Ghahremaninezhad *et al*., 2010). The formation of these phases, mainly indicated by the preferential leaching of Fe over Cu, detection of an anodic prewave in polarization curves of chalcopyrite electrodes, and non-stoichiometric Cu/Fe ratio on oxidized samples is often linked to the observed hindered dissolution effect: that is, the product layer inhibits the reaction progress.

Therefore, the objective of the present investigation is to examine the nature of the intermediate products that are formed on chalcopyrite under anodic prewave conditions, in addition to evaluate the corresponding effects of these products on the mineral oxidation rate. This investigation will combine electrochemical methods with analysis by means of Raman spectroscopy and synchrotron small angle X-ray diffraction (S-SAXRD), which are techniques commonly applied to thin-films analysis. This experimental approach provides useful information on effective transformations of chalcopyrite in an electrochemically controlled system. The advantages of using high brilliant synchrotron X-ray beam included a large improvement of the signal-to-noise ratio, which allowed the analysis of minor amounts of material.

4.2. Reaction products of chalcopyrite dissolution

Many characterization techniques such as X-ray photoelectron spectroscopy (XPS), X-ray diffraction (XRD), X-ray absorption spectroscopy (XAS), Raman spectroscopy (RS), and scanning electron microscopy (SEM) coupled with energy dispersive spectrometry (EDS) or electron probe micro-analyses (EPMA), have been applied in an effort to improve the knowledge on the nature of the product layers that are formed on chalcopyrite during its dissolution in acidic media under atmospheric conditions. Table IV.1 summarizes results of the analyses of chalcopyrite after dissolution. It should be noted that elemental sulfur has been commonly detected as a product of chalcopyrite dissolution in both ferric sulfate and ferric chloride media. Many authors have claimed that the formation of elemental sulfur on chalcopyrite in ferric sulfate solutions is responsible for the observed hindered dissolution effect (*i.e.*, the slow and parabolic leaching kinetics) (Muñoz *et al*., 1979; Dutrizac, 1981, 1989; Majima *et al*. 1985; Hirato *et al*., 1987). In contrast, in ferric chloride media linear kinetics with the formation of a porous elemental sulfur layer, throughout which soluble products and reactants can diffuse, have been reported (Jones and Peters, 1976; Ammou-Chokroum *et al*., 1979; Majima *et al*., 1985; Dutrizac, 1981, 1990). The formation of elemental sulfur has been reported to take place at a broad redox potential range, from about 0.50 to 1.50 V *vs.* SHE (Ammou-Chokroum *et al*., 1979; Biegler and Swift, 1979; Warren *et al*., 1982; Yin *et al*., 1995; Klauber *et al*., 2001; Parker *et al*., 2003; Viramontes-Gamboa *et al*., 2007; Córdoba *et al*., 2008; Parker *et al*., 2008).

Table IV.1 also indicates that the formation of metal-deficient sulfides on chalcopyrite in acidic media has been suggested on the basis of electrochemical polarization of mineral electrodes. The electrochemical curves depict the so-called anodic prewave (*i.e.*, a potential region occurring at potentials lower than those of the main anodic peak), which has been attributed to the formation of intermediate non-stoichiometric phases (Eq. 4.1), where y is larger than x (Ammou-Chokroum *et al*., 1979; Biegler and Swift, 1979; Warren *et al*., 1982). The anodic prewave has been detected in an interval of 0.35 and 0.75 V *vs.* SHE, but this potential range depends on the nature of the mineral sample, the experimental conditions, and the immersion time of the electrode prior to the application of potential.

$$CuFeS_2 \rightarrow Cu_{1-x}Fe_{1-y}S_{2-z} + x\,Cu^{2+} + y\,Fe^{2+} + z\,S + 2(x+y)\,e^- \qquad (4.1)$$

Table IV.1. *Ex situ* analysis of chalcopyrite after dissolution in acidic solutions under atmospheric conditions.

Reference	Experimental conditions	Phase(s) detected and technique	Intermediate phase(s) (hypothesis)
Jones and Peters, 1976	Particles (-400 mesh), 0.2 M H_2SO_4, 0.5 M $Fe_2(SO_4)_3$, 90°C, 71 h	Elemental sulfur (S) by SEM	-
Linge, 1976	Particles (0.22 m^2/g), 10^{-2} M HNO_3, 10^{-4} M $Fe(NO_3)_3$ 10^{-3} M $Fe(NO_3)_2$, 25-40°C, 2.5 h, N_2	S by carbon disulfide (CS_2)	Iron-deficient phase: on the basis of the preferential leaching of Fe over Cu
Ammou-Chokroum *et al*., 1979	Particles (size not reported), HCl (pH 1-3), 0.4-0.7 V *vs.* SCE, 1.0-4.0 M NaCl, 50-75°C	S by powder XRD	Covellite (CuS): formation during the initial stages only
Biegler and Swift, 1979	Electrodes, 1.0 M H_2SO_4, 1.0 V *vs.* SHE, 25°C, 18 h, N_2	S by SEM coupled with EPMA	-
Muñoz *et al*., 1979	Particles (4 to 47 mm), 1.0 M H_2SO_4, 0.25 M $Fe_2(SO_4)_3$, 95°C, 150 h	S by SEM coupled with EDS	-
Warren *et al*., 1982	Electrodes, 1.0 M H_2SO_4, 1.09 V *vs.* SHE, 25°C, 17-84 h	S by SEM coupled with EDS	Bornite (Cu_5FeS_4) and covellite (CuS): thermodynamic modelling
Majima *et al*., 1985	Particles, 0.2 M H_2SO_4, 0.5 M $Fe_2(SO_4)_3$, or 0.2 M HCl, 1.0 M $FeCl_3$, 85°C, 120 h	S by SEM coupled with EPMA	-
Hirato *et al*., 1987	Particles, 0.2 M H_2SO_4, 0.5 M $Fe_2(SO_4)_3$, 85°C, 432 h	S by SEM coupled with EPMA	-
Dutrizac, 1989	Particles (-14+10 µm), 0.3 M H_2SO_4, 0.15 M $Fe_2(SO_4)_3$ 95°C, 1-72 h	S by SEM/EDS	-

(Cont.) Table IV.1. *Ex situ* analysis of chalcopyrite after dissolution in acidic solutions under atmospheric conditions.

Reference	Experimental conditions	Phase(s) detected and technique	Intermediate phase(s) (hypothesis)
Yin *et al*., 1995	Electrodes, 1.0 M $HClO_4$, 0.5-1.8 V *vs*. SCE, 25°C, N_2	S by XPS	Iron-deficient phase and CuS_2: detection of the anodic prewave
Klauber *et al*., 2001	Particles (31 µm), H_2SO_4 (pH 1.3-1.9), 0.2 M $Fe_2(SO_4)_3$ 0.1 M $FeSO_4$, 50-80°C, 2 h	Elemental sulfur (S_8) and disulfide (S_2^{2-}) by XPS	-
Abraitis *et al*., 2004	Particles (-45+150 µm), HCl (pH 2.5), 0.3 V *vs*. SHE 25ºC, 3 h	Sulfate (SO_4^{2-}) by XPS	Iron-deficient phase
Mikhlin *et al*., 2004	Particles (64 µm), 0.5 M H_2SO_4, 0.2 M $Fe_2(SO_4)_3$ or 1.0 M HCl, 0.4 M $FeCl_3$50°C, 1 h	S_8 by powder XRD, XPS and XAS	Amorphous metal-deficient phase
Carneiro and Leão, 2007	Particles (5.5 µm), H_2SO_4 (pH 0.15), 0.45 L O_2/min, 0-2 mol/L NaCl, 25 g/L $Fe_2(SO_4)_3$ 95°C, 10 h	S by powder XRD	-
Viramontes-Gamboa *et al*., 2007	Particles (size not reported), H_2SO_4 (15-30 g/L), 0.5-0.7 V *vs*. SCE, 80°C	S by SEM	-
Córdoba *et al*., 2008	Particles (70 µm), H_2SO_4 (pH 1.8) + nutrient, 0.3-0.6 V *vs*. Ag/AgCl, 35-68°C	S, CuS, goethite (FeOOH) and potassium jarosites by powder XRD	CuS: formation only at lower redox potential
Parker *et al*., 2008	Electrodes, 0.1 M HCl, 0.57 V *vs*. Ag/AgCl, 24 h, 25°C	S_8 by RS	Metal-deficient phase

Legend: SCE – Saturated Calomel Electrode (+0.241 *vs*. SHE at 25ºC); Ag/AgCl – Silver / Silver chloride Electrode (+0.207 *vs*. SHE at 25ºC, 3.0 mol/L KCl).

Analysis by means of Raman spectroscopy of chalcopyrite after leaching in either ferric sulfate or ferric chloride media indicated the formation of an elemental sulfur layer and a Raman-inactive product, without detectable S-S bonding (Parker *et al.*, 2008). The authors suggested that this inactive phase is possibly a metal-deficient sulfide on the basis of similarities with the chalcopyrite Raman spectrum. Based on thermodynamic, Warren *et al.* (1982) suggested the formation of bornite (Cu_5FeS_4), a typical iron-deficient sulfide, as a passive intermediate product phase in sulfate solutions at 0.50 V *vs.* SHE. At higher potentials, this product phase would be oxidized to covellite (CuS) and, subsequently, to elemental sulfur (S), through consecutive stages (Eqs. 4.2 and 4.3) or, then, directly (Eq. 4.4). Without experimental evidence, the formation of bornite as an intermediate product of chalcopyrite oxidation was also suggested in the anodic prewave region by Kelsall and Page (1984).

$$Cu_{1-x}Fe_{1-y}S_{2-z} \rightarrow (2-z)\,CuS + (-1-x+z)\,Cu^{2+} + (1-y)\,Fe^{2+} + 2(-x-y+z)\,e^- \quad (4.2)$$

$$CuS \rightarrow Cu^{2+} + S + 2e^- \quad (4.3)$$

$$Cu_{1-x}Fe_{1-y}S_{2-z} \rightarrow (1-x)\,Cu^{2+} + (1-y)\,Fe^{2+} + (2-z)\,S + 2(2-x-y)\,e^- \quad (4.4)$$

The formation of covellite as an intermediate product of chalcopyrite dissolution in acidic solutions under atmospheric conditions was also suggested by Jones and Peters (1976), Ammou-Chkroum (1979), Biegler and Horne (1985), Nava and González (2006) and Ghahremaninezhad *et al.* (2010) on the basis of preferential leaching of Fe over Cu and electrochemical results, mainly by cyclic voltammetry. By means of mineral liberation analyses (MLA) and XRD, respectively, CuS was positively detected on mineral particles after leaching in chloride (Velásquez-Yévenes *et al.*, 2010) and sulfate solutions (Córdoba *et al.*, 2008) at potentials around 0.60 V *vs.* SHE. Using Raman spectroscopy, Sasaki *et al.* (2008) detected CuS as a passive intermediate product on chalcopyrite particles after bioleaching in acidic media under atmospheric conditions.

In light of this brief review, it becomes evident that advances on chalcopyrite dissolution mechanism have been made by leaching and electrochemical experiments coupled with spectroscopic techniques, but there are uncertainties regarding the nature of intermediate

product phases formed at anodic prewave conditions. In addition, the actual role of such products in the hindered dissolution behavior exhibited by chalcopyrite during atmospheric dissolution is not fully established.

Then, the objectives of this study are to investigate the nature of the product phases formed in the anodic prewave region and the corresponding effects on the chalcopyrite oxidation rate. The investigation of oxidized chalcopyrite electrodes by synchrotron small angle X-ray diffraction (S-SAXRD) may be helpful since it minimizes the interferences resulting from the analysis of the bulk. But in function of the features of the incident X-ray beam, there is X-ray penetration over a wide area of the sample under analysis. The combination of electrochemical methods with S-SAXRD are intended to better understand chalcopyrite dissolution, especially with respect to the nature of intermediate product phases formed at anodic prewave potentials and which had been proposed without experimental evidences.

4.3. Experimental

4.3.1. Chalcopyrite electrodes

The chalcopyrite samples were purchased from Ward's Natural Science, Rochester, N.Y. The preparation of electrodes involved the following procedures. Firstly, massive samples were cut using a diamond wafering blade (Buehler®, n.11-4246), thus obtaining specimens (1.0 cm^2 of exposed area; 0.5 cm thick) that were rinsed with double-distilled water and dried with analytical grade acetone 100% (Synth®). Next, a Cu wire within a glass tube was attached to each specimen using a conducting silver paint (Dotite®, D-550).

The samples were, then, mounted in Epoxy resin (Epofix®, Struers) and after that, fresh electrode surfaces were prepared by wet mechanical polishing using SiC papers (grit sizes 1000, 1200 and 2400) and alumina paste (1.0 μm). Next, the electrodes were rinsed with double-distilled water in an ultrasonic bath for 15 min, dried with analytical grade ethyl alcohol 95% (Synth®) and, then, kept under vacuum at room temperature.

4.3.2. Characterization of chalcopyrite electrodes

Chalcopyrite electrodes were analyzed by means of scanning electron microscopy (SEM) with energy dispersive spectrometry (EDS), using a JEOL (JSM 6360LV) Microscope and a Thermo Noran (Quest) Spectrometer; optical microscopy with a Leica (Metallux DFC 290) Microscope, equipped with lenses of 50 and 100X; Raman spectroscopy, using a Horiba Jobin Yvon (Labram HR800) Spectrograph, equipped with 633 nm He-Ne laser (20 mW power); and synchrotron small angle X-ray diffraction (S-SAXRD), at the beamline XRD1 of the Brazilian Synchrotron Light Laboratory (LNLS).

The Raman signal was collected by Olympus (BHX) Microscope, equipped with lenses of 10, 50 and 100X, and laser beam with fixed incident power (0.06 mW). Spectral resolution was about 2 cm^{-1}. A minimum of 10 scans with 60 s integration time were recorded. The grating angle was calibrated using the 520 cm^{-1} silicon (Si) band.

The XRD patterns were recorded using synchrotron light with energy and wavelength of 8 keV and 1.5426 Å, respectively. Fig. 4.1 shows the Huber diffractometer. A linear detector and a double crystal of Si (111) as monochromator were used. The XRD patterns were measured using constant incidence angle (θ) at 2° and the step size of 2θ scan was 0.1°. The dimensions of the focused beam were approximately 1.5 (horizontal) x 0.5 (vertical) mm. In the present investigation, the radiation beam was focused on the center of the electrode sample under analysis. The XRD patterns were identified by comparing the d-spacings with the standard reference patterns, supplied by the International Centre for Diffraction Data (ICDD). All the oxidized samples were analyzed by Raman spectroscopy (RS) immediately after oxidation and by S-SAXRD at a maximum of 24 h. Before the measurements, the electrode samples were kept under vacuum at room temperature.

4.3.3. Electrochemical measurements

The electrochemical measurements were conducted at room temperature (25±1°C) using the conventional three electrode cell (*i.e.*, the mineral working electrode, platinum counter-electrode and Ag/AgCl/KCl (3.0mol/L) reference electrode). An Autolab® (Eco Chemie,

PGSTAT 20) Potentiostat was used. The potential difference between the working electrode and the reference electrode was obtained by a Luggin capillary. Ultra-pure nitrogen gas (99.999%) was bubbled in the electrolyte solution (0.1 mol/L H_2SO_4; pH ≈ 1) for at least 20 min before the start of all the measurements. The electrochemical methods used here include linear sweep voltammetry (LSV) and chronoamperometry. By LSV, the anodic current measurements of freshly polished chalcopyrite electrodes were performed from the open circuit potential (OCP) to 1.1 V *vs.* SHE, at 0.5 mV/s scan rate. These measurements were conducted after an equilibration time of 20 min. By means of chronoamperometry, fixed anodic potentials were applied in chalcopyrite electrodes for different reaction times. Aimed at obtaining reproducible response, the polished electrodes were immersed in the solution for at least 20 min before sweeping. The solutions were prepared with double-distilled water and analytical grade sulfuric acid 96% (FMaia®). The potentials were converted to the SHE scale.

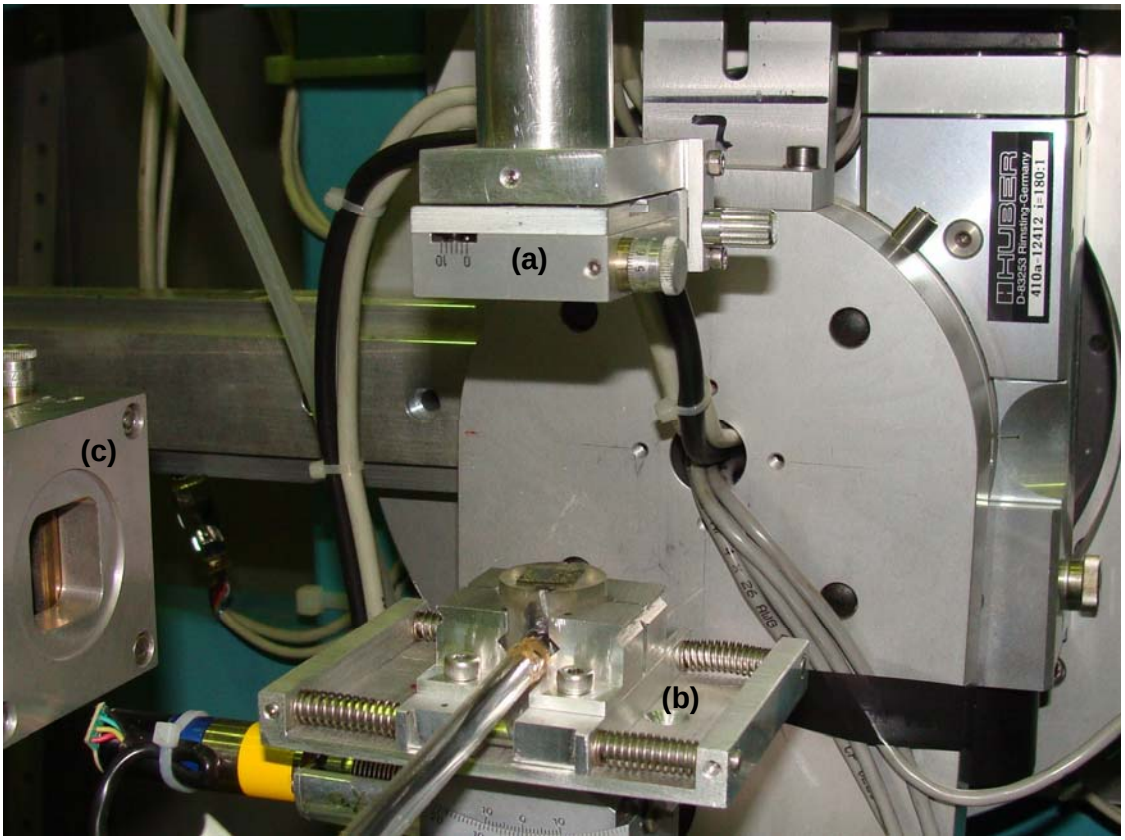

Figure 4.1. Huber diffractometer: (a) the detector; (b) the sample holder with electrode sample; and (c) the X-ray beam optics.

4.4. Results

4.4.1. Characterization of the chalcopyrite electrodes

In this investigation, a detailed analysis of the reaction area of freshly polished electrodes was conducted prior to the electrochemical measurements. Figure 4.2a shows a typical electron micrograph of an electrode. Visible is a smooth surface, accompanied by minor defects and dark points, which represent cavities or impurities. Semi-quantitative EDS analysis indicated that area 1 is constituted mainly by S (34% wt.), Cu (32% wt.), and Fe (28% wt.), while area 2 contains mostly Si (33% wt.), Ca (23% wt.), O (28% wt.) and Mg (11% wt.). The Raman spectrum of area 1 (Fig. 4.2b) indicates only one intense band at 294 cm^{-1} and additional bands of lower intensity at 268, 322, 360 and 374 cm^{-1}, which are the diagnostic bands of chalcopyrite (Mernagh and Trudu, 1993; Parker *et al*., 2008; RRUFF, 2010). The spectrum obtained for area 2 indicates intense bands at 666 and 1015 cm^{-1}; additional bands at 234, 320, 386, 504, 559, and 854 cm^{-1} were detected as well. Such spectrum is typical of diopside ($CaMgSi_2O_6$), calcium and magnesium silicate, as reported by Richet *et al*. (1998) and RRUFF (2010). Only small inclusions of diopside were detected on the electrode samples analyzed. The silicate is expected to be inert under the experimental conditions of the present work.

Freshly polished electrode samples were analyzed by S-SAXRD with the aim to identify minor impurity phases within the reaction area. Diopside was again the only phase detected on a few samples. Fig. 4.3 shows the S-SAXRD patterns obtained for electrode sample prior to the electrochemical treatment. It may be observed that crystallographic planes of tetragonal chalcopyrite (ICDD 83-0983) were identified, the predominant one the (2 0 4) at 2θ angle of 49.1°. The occurrence of diopside was evidenced by the S-SAXRD technique, but through peaks of low relative intensity. Some planes of monoclinic diopside ferroan (ICDD 83-0102), an iron-bearing diopside, such as (0 2 1), ($\bar{3}$ 1 3) and ($\bar{5}$ 3 3) at 2θ angles of 26.6, 55.3 and 71.6°, respectively, were identified. As a result of the feature of the technique (*i.e.*, the radiation beam was focused only on the center of the electrode), the XRD peaks detected in this investigation represent the crystal orientation of the specific area under analysis and not of the whole electrode surface area. As polycrystalline samples were used to prepare the electrodes, other crystal orientations were identified as well.

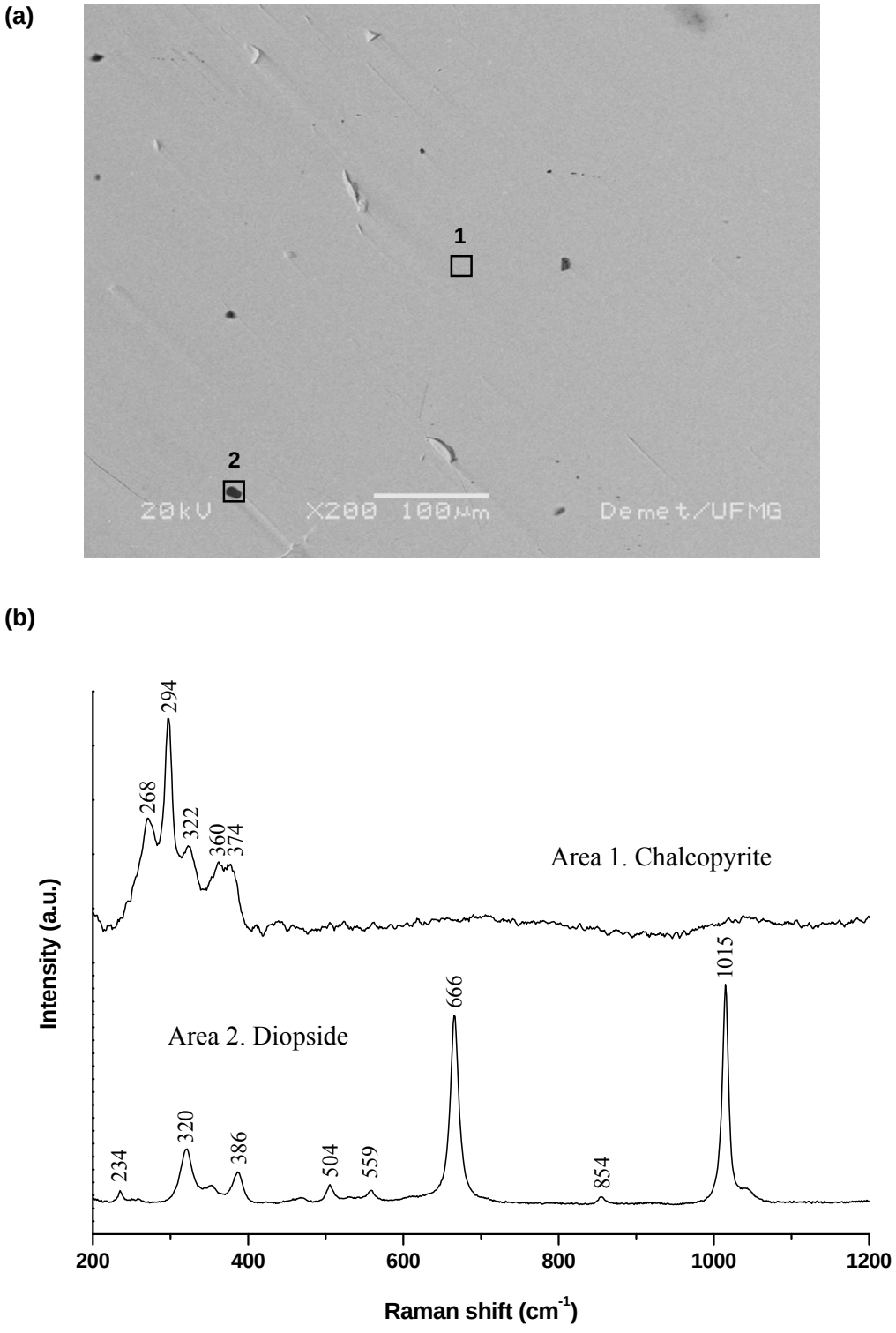

Figure 4.2. (a) Back-scattered electron micrograph of chalcopyrite electrode and selected areas analyzed by EDS and micro Raman spectroscopy; and (b) Raman spectra obtained for areas 1 and 2.

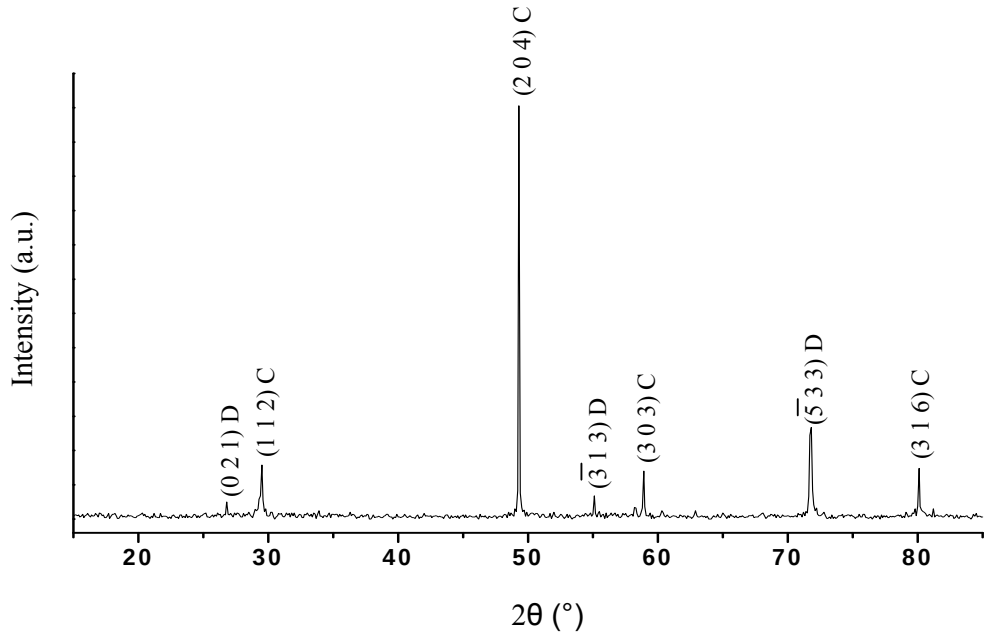

Figure 4.3. S-SAXRD patterns for chalcopyrite electrode and the corresponding Miller indices. Legend: $CuFeS_2$ (C); and Fe-$CaMgSi_2O_6$ (D).

4.4.2. Electrochemical measurements

4.4.2.1. Linear sweep voltammetry

$CuFeS_2$ electrodes were investigated by comparing their anodic electrochemical behavior in 0.1 mol/L H_2SO_4 solution at 25±1°C. Typical linear sweep voltammograms for freshly polished electrodes are shown in Fig. 4.4. It should be noted that the samples produced polarization curves that differed slightly from each other, regarding the oxidation rate (*i.e.*, the anodic current magnitude) and the potential from which there is a sudden change in magnitude of current, denoted in the present work as critical potential (Ec). Many samples were examined in this investigation and reproducibility regarding this electrochemical behavior was confirmed. Generally, the anodic oxidation current increased significantly (10 to 100 times) from the OCP value to potentials of about 0.60-0.65 V. This was followed by a slight increase to about 0.75-0.90 V. At higher potentials, there was a rapid increase in the oxidation rate; anodic current increased by the order of 100 to 1000 times,

approximately. Then, two well-defined behaviors may be distinguished: quasi-potential-independent regime (from 0.60-0.65 to 0.75-0.90 V) and potential-dependent regime (from 0.75-0.90 to 1.10 V). When the critical potential was reached, which ranged from about 0.75 to 0.90 V, the magnitude of anodic current became strongly dependent on potential.

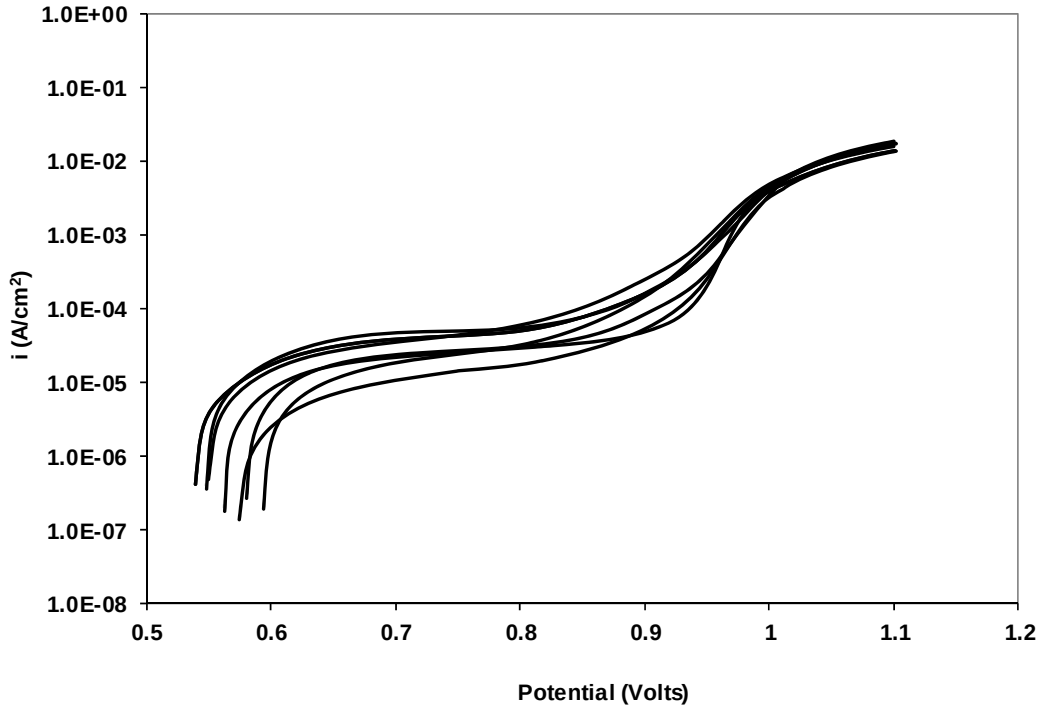

Figure 4.4. Linear sweep voltammograms (0.5 mV/s) of chalcopyrite electrodes in 0.1 mol/L H_2SO_4 solutions under atmospheric conditions.

Then, it was determined that the mineral oxidation is active but incomplete below 0.60-0.65 V, and not significantly affected by the applied potential between 0.60-0.65 and 0.75-0.90 V. Chalcopyrite oxidation rate increased largely above 0.75-0.90 V, a condition that is not accessible with common oxidants. Since the electrolyte remained unchanged, the slight variations in the anodic current magnitude and critical potential was ascribed to minor deviations in the elemental stoichiometry of the electrode reaction area, lattice defects and crystal orientation, given that polycrystalline samples were used to prepare the mineral electrodes.

4.4.2.2. Chronoamperometry

By chronoamperometry, the effect of applied potential on the potentiostatic current-time profiles of $CuFeS_2$ electrodes was investigated. The results were used to establish the conditions at which active and passive oxidation take place. The mineral electrodes were investigated by comparing their current-time profiles at 0.60, 0.70, 0.80, and 1.00 V. The profiles obtained in 0.1 mol/L H_2SO_4 solution at 25±1°C are shown in Fig. 4.5. Only the response obtained within the thirtieth minute is shown here. It can be noticed that at 0.60 and 0.70 V, the chalcopyrite electrodes exhibited an electric current decay, which suggests that a gradually thickening protective layer is formed on the surface. It can be seen further that, initially, the current decreased abruptly and, then, declined by a constant rate until the steady-state current was achieved. The observed anodic current decay was reported earlier by Warren *et al*. (1982), Biegler and Horne (1985) and Lázaro and Nicol (2003).

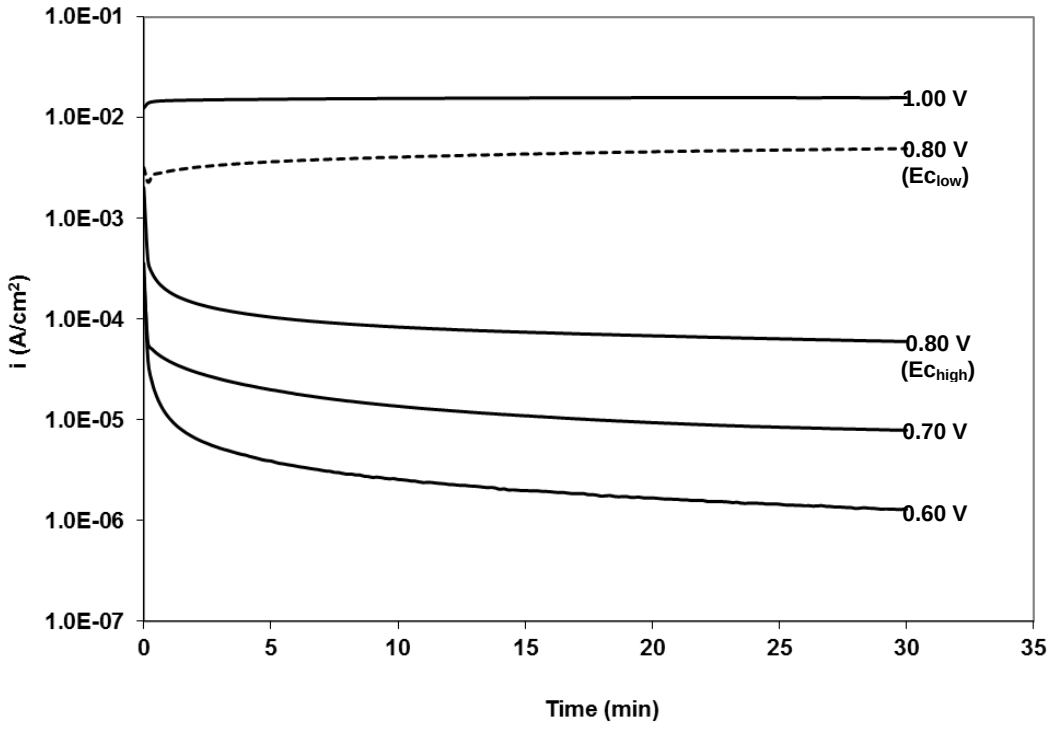

Figure 4.5. Effect of potential on the potentiostatic current-time profiles for chalcopyrite electrodes in 0.1 mol/L H_2SO_4 solutions under atmospheric conditions. Two electrode samples (Ec_{low} and Ec_{high}) were oxidized at 0.80 V.

By means of optical microscopy, a light brownish product layer was visualized on the electrode after chronoamperometry at 0.60 V, for 24 h, as will be discussed later. Optical microscopic observation of electrodes oxidized at 0.70 V for 2 h revealed the formation of a brownish or purplish layer (Fig. 4.6a), and for a 4 h reaction time, an extensive pitting was observed for some samples (Fig. 4.6b). These preferential sites of dissolution may be related to crystal orientation and lattice defects.

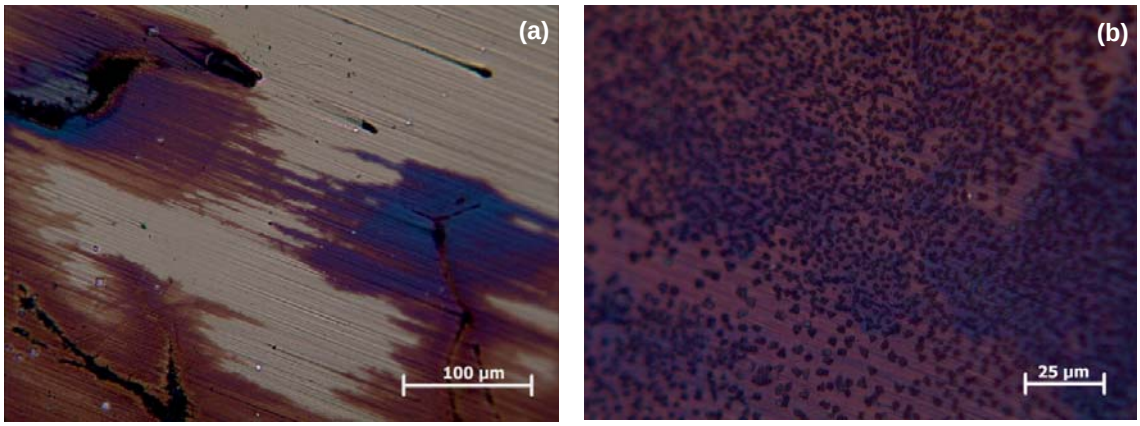

Figure 4.6. Optical micrographs of $CuFeS_2$ electrodes oxidized in 0.1 mol/L H_2SO_4 solutions under atmospheric conditions at: (a) 0.70 V, for 2 h; (b) 0.70 V, for 4 h.

With regard to the current-time profiles obtained at 0.80 V, two behaviors were observed (Fig. 4.5), depending on the critical potential value of each sample, which is within the range 0.75-0.90 V. The anodic current of electrode sample Ec_{low}, which exhibited a lower critical potential (Fig. 4.7), first decreased and, then, slowly increased, indicating an active oxidation process (Fig. 4.8). In contrast, for electrode sample Ec_{high}, which exhibited a higher critical potential (Fig. 4.7), the current decreased abruptly and, then, fell by a constant rate until the steady-state current was achieved, as observed at 0.60 and 0.70 V. However, the formation of a much thicker product layers was observed at 0.80 V (Fig. 4.9). It is probable that at such condition, not only chalcopyrite, but also its oxidation products undergo oxidation. Similarly to the LSV measurements, several samples were examined in the present investigation and reproducibility regarding the two current-time profiles observed at 0.80 V was confirmed (Fig. 4.10).

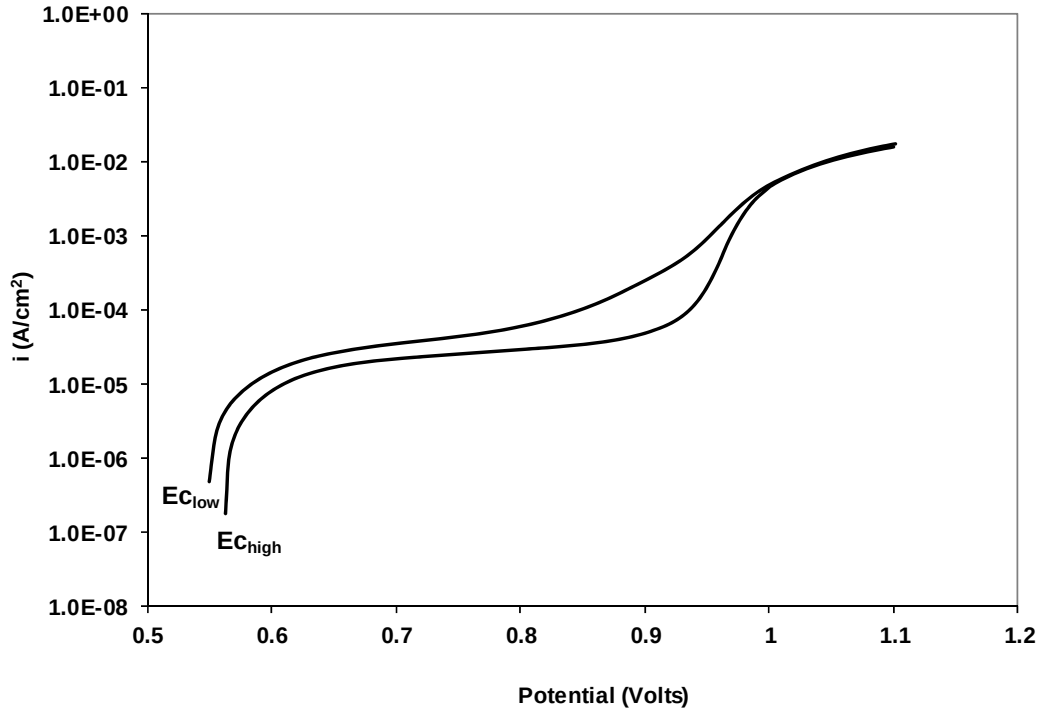

Figure 4.7. Linear sweep voltammograms (0.5 mV/s) of $CuFeS_2$ electrodes Ec_{low} (lower critical potential) and Ec_{high} (higher critical potential) in 0.1 mol/L H_2SO_4 solutions under atmospheric conditions.

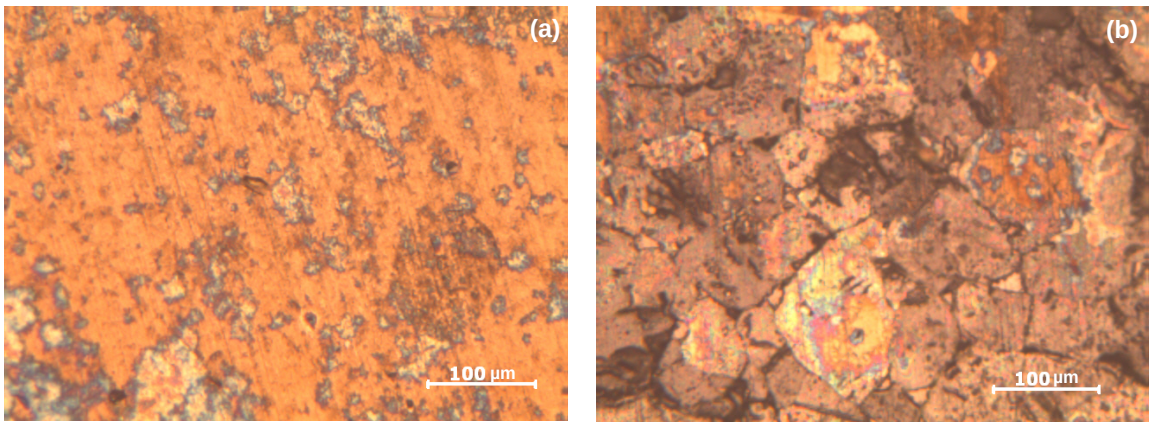

Figure 4.8. Optical micrographs of $CuFeS_2$ electrodes oxidized in 0.1 mol/L H_2SO_4 solutions under atmospheric conditions at: (a) 0.80 V (Ec_{low}), for 1 h; (b) 0.80 V (Ec_{low}), for 2 h.

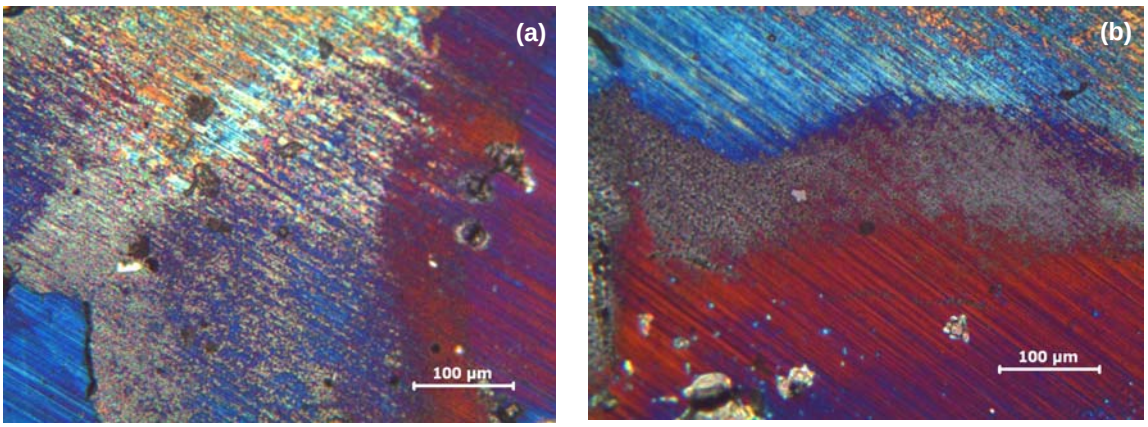

Figure 4.9. Optical micrographs of $CuFeS_2$ electrodes oxidized in 0.1 mol/L H_2SO_4 solutions under atmospheric conditions at: (a) 0.80 V (Ec_{high}), for 1 h; (b) 0.80 V (Ec_{high}), for 2 h.

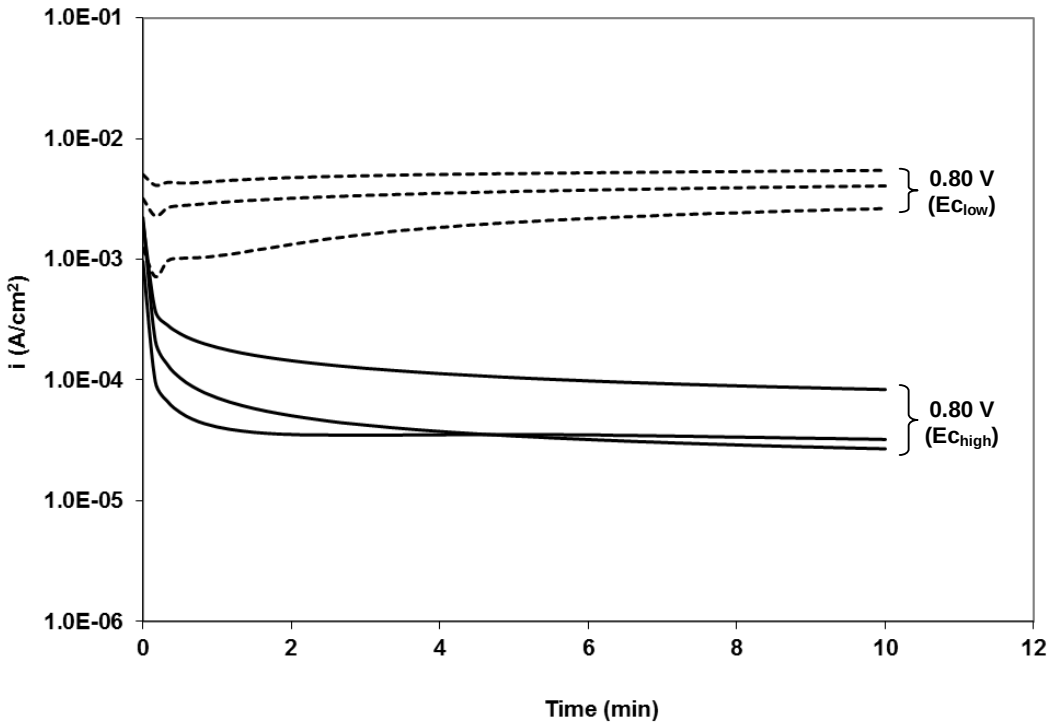

Figure 4.10. Potentiostatic current-time profiles at 0.80 V for six $CuFeS_2$ electrodes in 0.1 mol/L H_2SO_4 solutions under atmospheric conditions.

The current-time profiles obtained at 1.00 V indicated initial current increases (Fig. 4.5), which point to a mineral surface undergoing oxidation. However, after a few minutes, the current becomes relatively constant. At this potential condition it was observed that, for longer reaction times, the product layer peeled off after reaching a critical thickness, which causes an increase in the exposed surface area of chalcopyrite. As a result, the mineral oxidation rate may increase. Hirato *et al.* (1987) reported the peeling off of an elemental sulfur layer that forms on chalcopyrite in acidic solutions under atmospheric conditions. Optical microscopic observation of oxidized electrodes at 1.00 V revealed the rapid formation of dark layers on the mineral surfaces (Fig. 4.11a) and the occurrence of exposed surface areas for longer reaction times (Fig. 4.11b).

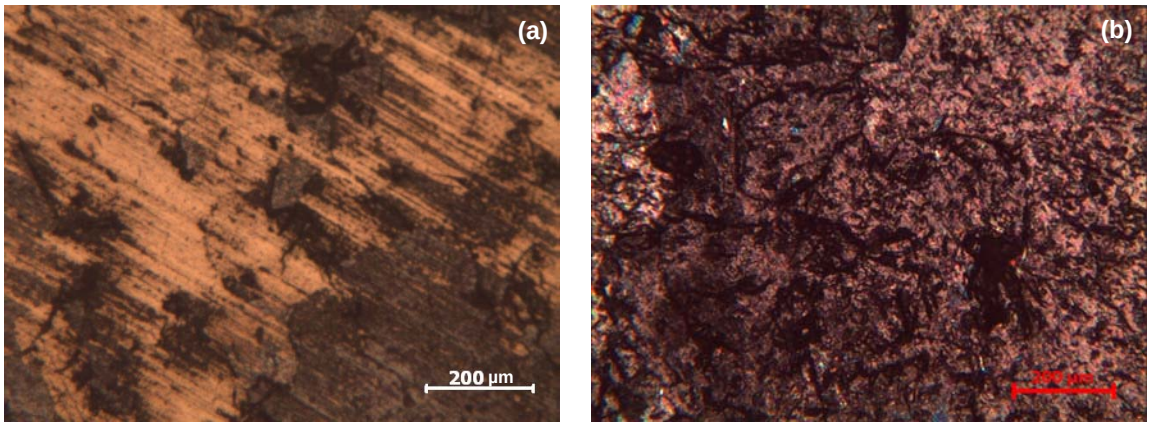

Figure 4.11. Optical micrographs of $CuFeS_2$ electrodes oxidized in 0.1 mol/L H_2SO_4 solutions under atmospheric conditions at: (a) 1.00 V, for 0.5 h; (b) 1.00 V, for 3 h.

4.4.3. Characterization of the oxidized chalcopyrite electrodes

4.4.3.1. At 0.60 V

Analysis of $CuFeS_2$ electrode by S-SAXRD, after chronoamperometry at 0.60 V for 24 h, showed similar patterns to those obtained before the electrochemical treatment. Only chalcopyrite peaks, main reflection (2 0 4) at 2θ angle of 49.1° (ICDD 83-0983), as seen in Fig. 4.3, were detected on the electrode sample.

Results from Raman spectroscopy suggest a possible structural change of the original electrode. Fig. 4.12 presents the spectra obtained for particular areas of $CuFeS_2$ electrode oxidized at 0.60 V for 24 h. The spectrum obtained for area 1 indicates the diagnostic bands of chalcopyrite, as earlier discussed. The spectrum obtained for area 2 shows a clear reduction in the intensity of the Raman bands at 268, 294, and 322 cm^{-1}. Such modification of the spectrum may be associated with the well-established selective removal of metals (*e.g.*, iron) from chalcopyrite, even though the Raman bands assigned to the molecular vibrations Cu-S and Fe-S in chalcopyrite can not be discerned with the current information available in the literature. Based also upon similarities in Raman spectra of chalcopyrite and product layer, Parker *et al*. (2008) suggested the formation of metal-deficient sulfide on oxidized chalcopyrite.

Therefore, on the basis of the electrochemical measurements and Raman findings it is suggested that the decreasing oxidation rate at 0.60 V is correlated to the formation of an unidentified metal-deficient sulfide layer on chalcopyrite and, therefore, an indication of the protective character of this product phase.

4.4.3.2. At 0.70 V

Fig. 4.13 shows the XRD patterns obtained for chalcopyrite electrode after treatment at 0.70 V for 6 h. At these conditions, low intensity peaks of orthorhombic bornite (Cu_5FeS_4), an iron-deficient sulfide, were detected. Three diffraction peaks may be distinguished, the predominant one corresponding to the (4 8 0) or (0 8 4) crystallographic planes, at 2θ angle of 46.9° (ICCD 42-1405). The detection of bornite as a product of chalcopyrite oxidation is an important finding of this investigation. The formation of this product phase in acidic media under atmospheric conditions had been previously suggested, with no experimental evidence, by Warren *et al*. (1982) and Kelsall and Page (1984). The possible mechanism of bornite formation on chalcopyrite will be discussed later.

Electrodes oxidized at 0.70 V were examined by micro Raman spectroscopy as well. Only product phases with a remnant chalcopyrite structure, as that described in the last section, were detectable on chalcopyrite at 0.70 V. Although it has been reported that bornite is a

poor Raman scatterer (Mernagh and Trudu, 1993), the characterization of bornite samples from different deposits by Raman spectroscopy and detection on oxidized chalcopyrite electrodes is being investigated. Thus, by electrochemical results and S-SAXRD findings, the formation of bornite on chalcopyrite electrode oxidized at 0.70 V is possibly correlated to the decreasing oxidation rate, also indicating the protective character of this phase.

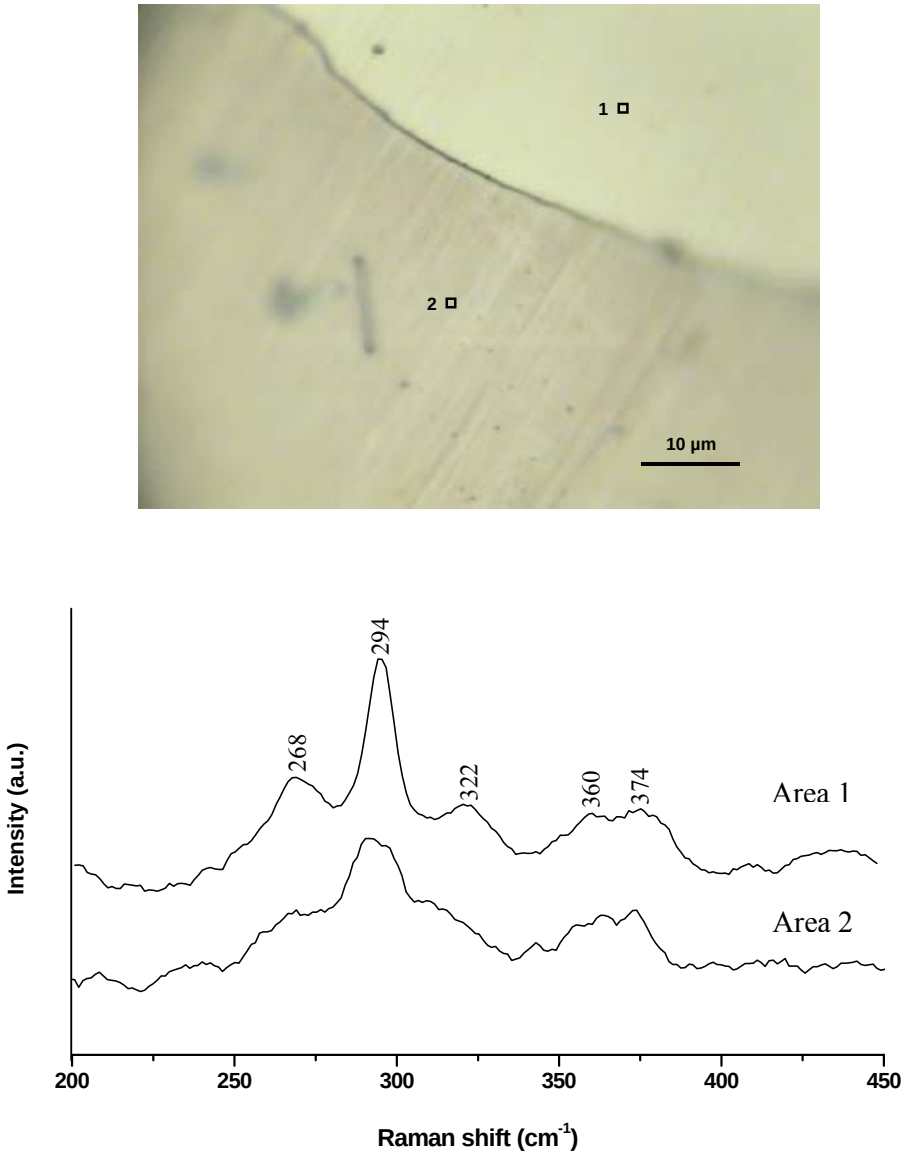

Figure 4.12. Optical micrograph of chalcopyrite electrode oxidized at 0.60 V in 0.1 mol/L H_2SO_4 solution under atmospheric conditions for 24 h, and Raman spectra obtained for areas 1 and 2.

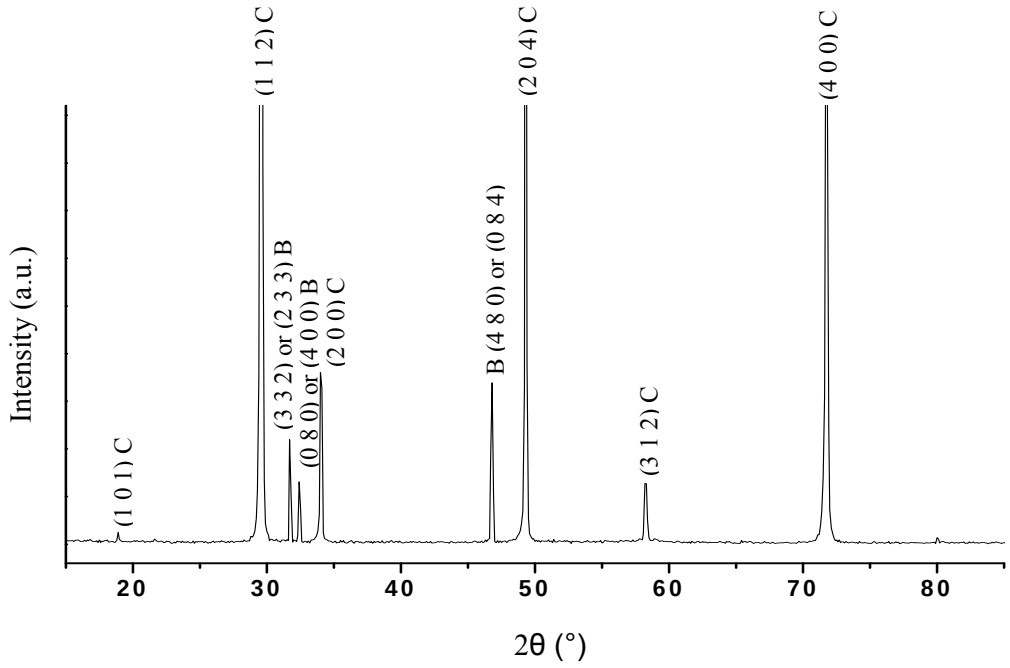

Figure 4.13. S-SAXRD patterns of chalcopyrite electrode oxidized at 0.70 V in 0.1 mol/L H_2SO_4 solution under atmospheric conditions for 6 h. Legend: $CuFeS_2$ (C); and Cu_5FeS_4 (B).

4.4.3.3. At 0.80 V

Fig. 4.14a presents the diffraction patterns obtained for chalcopyrite electrode after treatment at 0.80 V for 2 h. An electrode sample which exhibited a higher critical potential (Ec_{high}) was examined. In this case, noticeable are peaks of orthorhombic bornite with a higher relative intensity, compared with those detected after treatment at 0.70 V. XRD peaks of orthorhombic elemental sulfur (S_8) with a lower relative intensity can be observed as well. Here too, the main peak of bornite corresponds to the (4 8 0) or (0 8 4) planes, at 2θ angle of 46.9° (ICCD 42-1405). The predominant peaks of elemental sulfur corresponds to the (2 2 2) or (3 1 1) planes, at 2θ angles of 23.1° and 26.8°, respectively (ICCD 77-0145). By comparing Fig. 4.14a and 4.13, it may be observed that other planes were detected for chalcopyrite, most likely as a function of the polycrystalline character of the electrode sample.

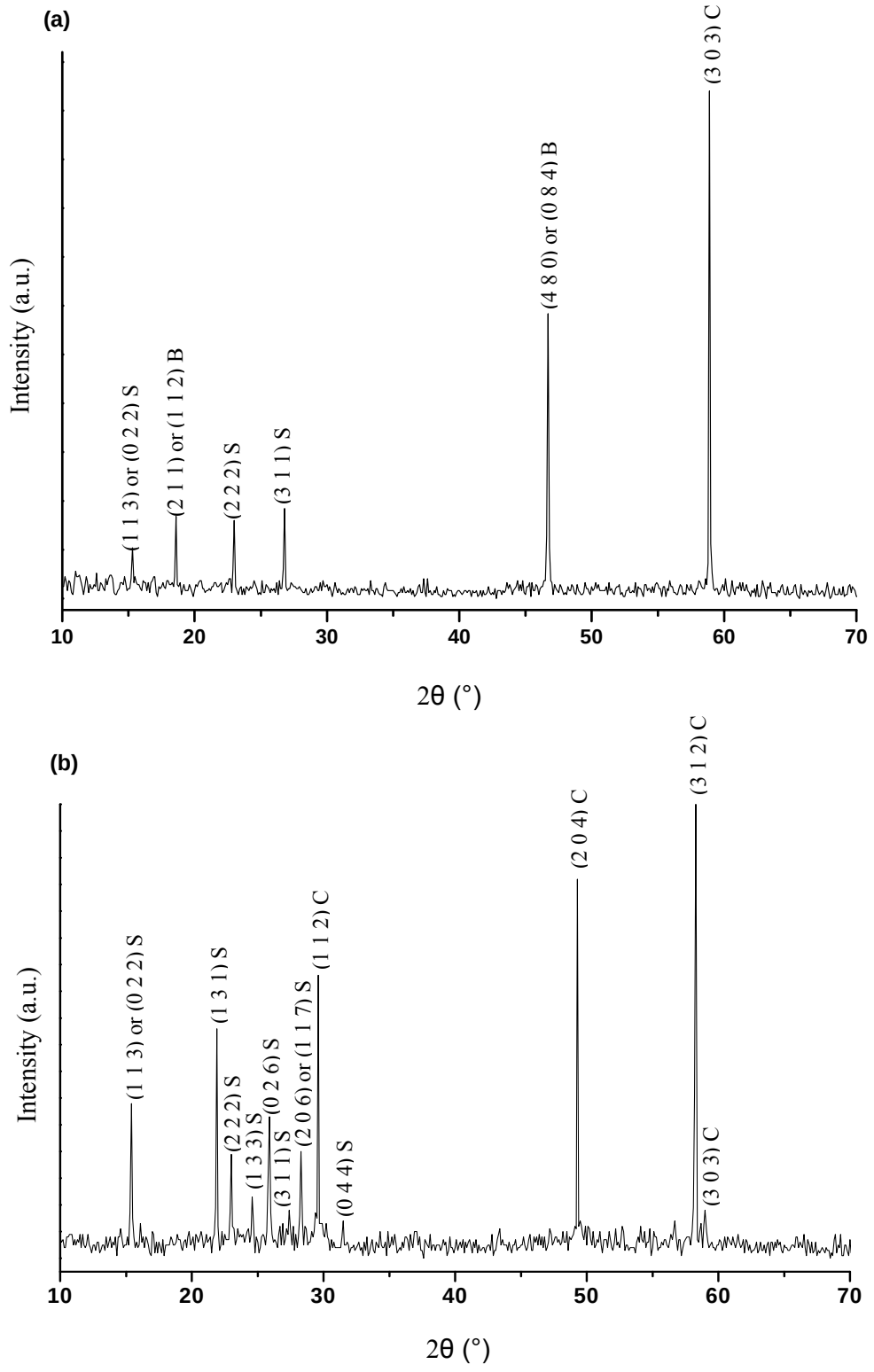

Figure 4.14. S-SAXRD patterns of chalcopyrite electrodes oxidized at 0.80 V in 0.1 mol/L H_2SO_4 solutions under atmospheric conditions for 2 h: (a) Ec_{high}; and (b) Ec_{low}. Legend: $CuFeS_2$ (C); Cu_5FeS_4 (B); and S_8 (S).

Fig. 4.14b shows the XRD patterns obtained for an electrode sample that exhibited a lower critical potential (Ec_{low}), after treatment at 0.80 V for 2 h. For samples like this one, which indicated an active oxidation behavior, as noticed by means of chronoamperometry, no XRD peak of bornite was detected. In addition to the chalcopyrite peaks, many peaks of orthorhombic elemental sulfur can be observed, and the main one corresponds to the (1 3 1) plane, at 2θ angle of 22.7° (ICCD 77-0145).

Fig. 4.15 presents the Raman spectra obtained for particular areas of chalcopyrite electrode (Ec_{high}), oxidized at 0.80 V for 1 h. The spectrum obtained for area 1 indicates diagnostic bands of chalcopyrite (*i.e.*, 268, 294, and 322 cm^{-1}), as earlier discussed, and Raman bands of low intensity at 221 cm^{-1} and at 474 cm^{-1}, which has a shoulder band. Orthorhombic elemental sulfur (S_8) yields Raman band at about 221 cm^{-1} and more intense band at about 470 cm^{-1} (Parker *et al*., 2008; Sasaki *et al*., 2009; RRUFF, 2010). Raman spectrum of hexagonal covellite (CuS) consists of band at about 474 cm^{-1} and band of low intensity at approximately 265 cm^{-1} (Mernagh and Trudu, 1993; Parker *et al*., 2008; Sasaki *et al*., 2009; RRUFF, 2010).

The spectrum obtained for area 2 (Fig. 4.15) shows (i) a clear reduction in intensity of chalcopyrite Raman bands; (ii) more intense vibration at 221 cm^{-1}; (iii) more intense and broader band at 474 cm^{-1}; and (iv) broader band at 268 cm^{-1} (*i.e.*, chalcopyrite Raman band and shoulder band). The broad band and shoulder detected at 474 cm^{-1} may be assigned to molecular vibrations of covellite and elemental sulfur, respectively. The broad band and shoulder band detected at 268 cm^{-1} may also be assigned to chalcopyrite and covellite, respectively. Sasaki *et al*. (2009) assigned Raman band at 476 cm^{-1} and shoulder band at 472 cm^{-1} to the formation of covellite and elemental sulfur on oxidized chalcopyrite.

Therefore, Raman analyses, which play an auxiliary role in this investigation, indicate the formation of CuS as an intermediate product phase of chalcopyrite oxidation at 0.80 V. As Raman can be used to analyze selected areas, it is possible to identify phases that are not detected with S-SAXRD. The absence of covellite detection in the S-SAXRD analyses indicated the need of a broader scanning of the electrodes; in the present work the beam (1.5 x 0.5 mm) was fixed only on the center of the electrode.

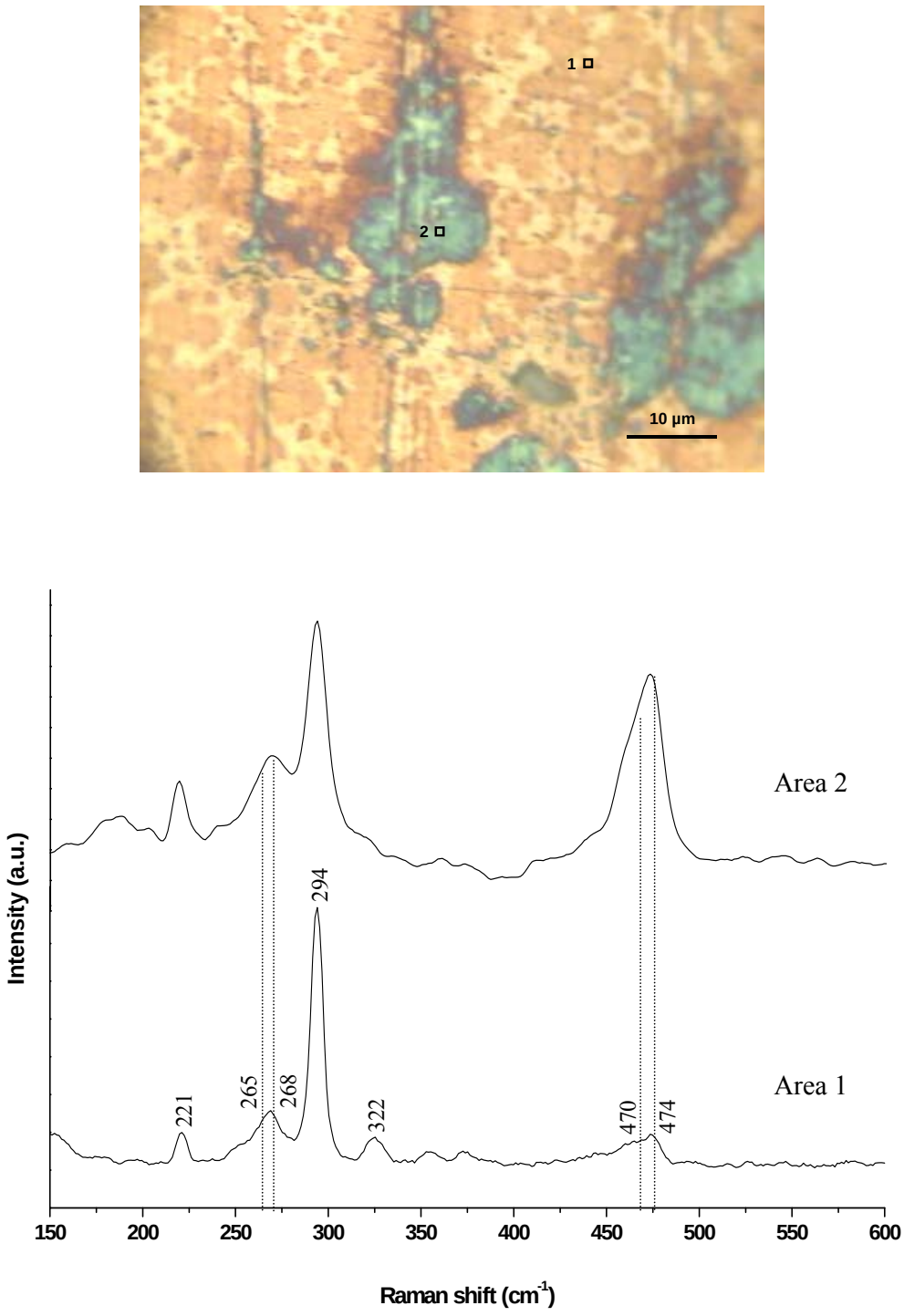

Figure 4.15. Optical micrograph of chalcopyrite electrode oxidized at 0.80 V in 0.1 mol/L H_2SO_4 solution under atmospheric conditions for 1 h, and Raman spectra obtained for areas 1 and 2.

Although without evidence at this point, the progressive growth of covellite's band at 474 cm^{-1} and shoulder band at 265 cm^{-1}, and comparable growth of elemental sulfur's band at 221 cm^{-1} and shoulder band at around 470 cm^{-1}, suggests that chalcopyrite may convert to both these product phases simultaneously. Possible mechanism of chalcopyrite oxidation to covellite and elemental sulfur will be discussed later. From Fig. 4.15, it may also be observed the growth of a broad band at 150-200 cm^{-1}, which will result in an elemental sulfur band, possibly at 158 cm^{-1}.

Fig. 4.16 presents the spectra obtained for products detected on similar electrode (Ec_{high}) oxidized at 0.80 V for 2 h. It indicates intense bands at 221 and 470 cm^{-1}, and additional bands of lower intensity at 158, 189, 250, and 440 cm^{-1}, which are typical of orthorhombic elemental sulfur (Parker *et al*., 2008; RRUFF, 2010). After chronoamperometry at 0.80 V of chalcopyrite samples whit a lower critical potential (Ec_{low}), only elemental sulfur was detected on the electrode and in notably shorter times (*e.g.*, 10-30 min).

On the basis of the electrochemical results, Raman and S-SAXRD findings, the formation of layers constituted by bornite, covellite and elemental sulfur on chalcopyrite electrodes (Ec_{high}) at 0.80 V produced a current decay, which indicate the protective character of these layers. This hindered dissolution effect was not observed at 0.80 V for electrodes with Ec_{low}, a condition in which only elemental sulfur was detected.

4.4.3.4. At 1.00 V

After treatment at 1.00 V for 0.5 h, analysis of oxidized chalcopyrite electrodes by S-SAXRD detected only chalcopyrite and elemental sulfur (ICCD 77-0145), as shown in Fig. 4.17. With Raman spectroscopy, only elemental sulfur was detected on chalcopyrite, by a similar spectrum to that discussed in Fig. 4.16. The fact that at this potential condition an active oxidation process is taking place – in contrast to the current decay observed under anodic prewave potentials (Fig. 4.5) – could be evidence that the hindered dissolution of chalcopyrite is not related to the formation of elemental sulfur.

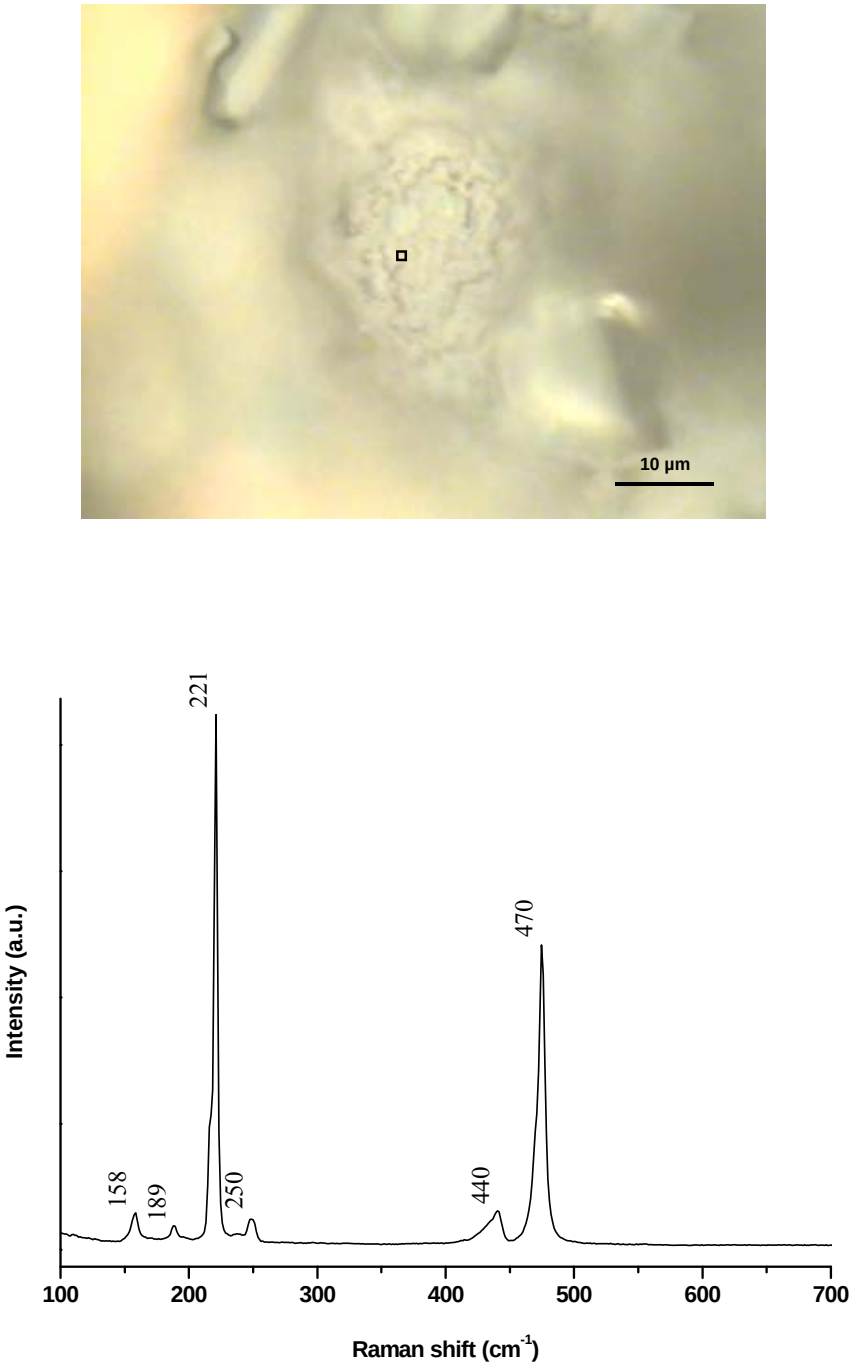

Figure 4.16. Optical micrograph of chalcopyrite electrode oxidized at 0.80 V in 0.1 mol/L H_2SO_4 solution under atmospheric conditions for 2 h, and corresponding Raman spectra.

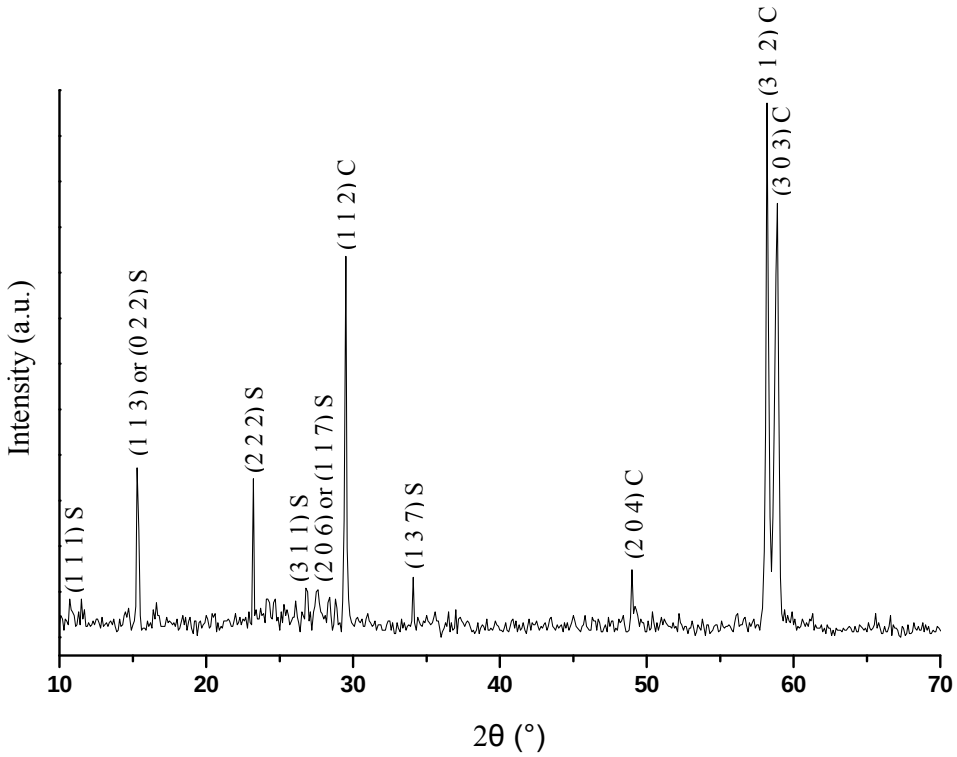

Figure 4.17. S-SAXRD patterns of chalcopyrite electrode oxidized at 1.00 V in 0.1 mol/L H_2SO_4 solution under atmospheric conditions for 0.5 h. Legend: $CuFeS_2$ (C); and S_8 (S).

4.4.4. Discussion

4.4.4.1. Formation of bornite as an intermediate product of chalcopyrite oxidation

Chronoamperometry revealed that the protective character of the product layer that forms on chalcopyrite in acidic sulfate media, under atmospheric conditions, diminishes as the overpotential increases. It was observed that at potentials below the critical potential value, which ranges from 0.75 to 0.90 V, the anodic current decreases continuously with time to values that are independent of potential. In such conditions, the anodic current is possibly maintained constant by the inter-diffusion of atoms in the mineral lattice. This hypothesis was discussed for binary metallic alloys, which exhibited selective dissolution and similar electrochemical behavior (Pickering and Wagner, 1967; Pickering and Byrne, 1971). Above the critical potential, the anodic current increases, indicating an active oxidation process, but become relatively constant with time. In such conditions, a thick elemental

sulfur layer forms on chalcopyrite and possibly through equivalent rate, it peels off or then oxidizes.

As previously mentioned, the detection of bornite (Cu_5FeS_4), an iron-deficient sulfide, as an intermediate product of chalcopyrite oxidation at potentials below the critical potential, represents an important finding of this investigation. Although the formation of bornite on oxidized chalcopyrite had been earlier suggested by others (Warren *et al*., 1982; Kelsall and Page, 1984), to the author's knowledge, this is the first experimental evidence of bornite formation. In addition to the detection of bornite, the formation of a possible non-stoichiometric metal-deficient phase, with remnant chalcopyrite structure, was suggested on electrodes oxidized at potentials below the critical potential. More importantly, the formation or absence of these phases under a constant applied potential correlated well with hindered or active oxidation processes, respectively.

In order to better understand the electrochemical reactions involved in the dissolution of chalcopyrite, it is important to consider the mineral's electronic structure and chemical bonds. The chalcopyrite electronic structure has been modeled in terms of two sets of clusters: $(CuS_4)^{7-}$ and $(FeS_4)^{5-}$ (Vaughan and Tossell, 1983; Vaughan and Rosso, 2006). Chalcopyrite is a semiconductor with a narrow band gap of 0.5-0.6 eV (Vaughan and Craig, 1978; Biegler and Swift, 1979; McMillan *et al*., 1982; Hiskey, 1993). The conduction band edge is constituted by Fe 3*d* molecular orbitals, while the valence band edge is Cu 3*d* and S 3*p* in character (Shuey, 1975). The highest occupied energy level is the filled Cu 3*d* $4t_{2g}$ antibonding orbital, whereas the lowest unoccupied orbital is the Fe 3*d* $2e_g$ antibonding orbital (Vaughan and Tossell, 1983). Cu is nominally monovalent ($3d^{10}$) in chalcopyrite, whereas Fe is nominally trivalent ($3d^5$) – formal electronic configuration $Cu^+Fe^{3+}(S^{2-})_2$ (Goh *et al*., 2006; Pearce *et al*., 2006). By using an electronic structure approach, the selective removal of iron from chalcopyrite was discussed by Osseo-Asare (1993). During the initial stages of the oxidative reaction, the formation of Cu^{2+} ions occurs when an electron transfers from a Cu 3*d* $4t_{2g}$ orbital into an empty Fe 3*d* $2e_g$ orbital. As the Cu 3*d* $4t_{2g}$ molecular orbital is antibonding, the loss of one electron corresponds to a strengthening of the Cu-S bond. On the other hand, the gain of one electron into the Fe 3*d* $2e_g$ orbital results in the formation of Fe^{2+} ions. As this orbital is antibonding as well, the gain of one electron corresponds to a weakening of the Fe-S bond. Thus, the coincident

strengthening of the Cu-S bonds and weakening of the Fe-S bonds are the possible reason for the experimentally observed preferential leaching of iron from chalcopyrite during its dissolution.

The formation of bornite, an iron-deficient sulfide, is a result of the electron transfer in chalcopyrite under oxidizing conditions. Chalcopyrite possibly transforms to bornite, with the sulfur atoms being oxidized to elemental sulfur and only the iron atoms being released (Eq. 4.5), as suggested by Kelsall and Page (1984).

$$5\ CuFeS_2 \rightarrow Cu_5FeS_4 + 4\ Fe^{3+} + 6\ S + 12\ e^- \quad (4.5)$$

Although without direct evidence, it was assumed that the oxidation of Fe^{2+} to Fe^{3+} occurs in the solution upon release, according to the related potentials values (*i.e.*, 0.70 and 0.80 V *vs.* SHE) and the standard redox potential of the (Fe^{3+}/Fe^{2+}) couple (*i.e.*, 0.68 V *vs.* SHE in 0.1 mol/L H_2SO_4 solution at 25 °C, 1 atm). The simultaneous formation of elemental sulfur in this particular reaction as an oxidation product (Eq. 4.5) was assumed mainly based on detection of a product layer containing bornite and elemental sulfur (S_8). The large number of electrons involved in this reaction (Eq. 4.5) suggests the formation of non-stoichiometric intermediate phases prior to bornite formation.

4.4.4.2. The role of bornite in the chalcopyrite oxidation mechanism

At the oxidizing conditions in which bornite was detected by means of S-SAXRD, that is, below the critical potential value, it was noticed that the chalcopyrite oxidation rate decreased by a constant rate at 0.70 and 0.80 V, thereby indicating the protective character of this product phase.

There is evidence in the literature that bornite may adversely affect the dissolution rate of chalcopyrite. Acres *et al.* (2010) investigated the effect of locked bornite on the oxidation rate of chalcopyrite in chloride media (pH = 1) under atmospheric conditions by synchrotron X-ray photoelectron spectroscopy (S-XPS). By probing leached chalcopyrite, it was observed a higher proportion of disulfides (S_2^{2-}) than polysulfides (S_n^{2-}), both

oxidation products. Formation of disulfide on oxidized chalcopyrite was also confirmed by XPS analysis (Klauber *et al*., 2001; Parker *et al*., 2003) and density functional theory (DFT) calculations (Oliveira and Duarte, 2010). By assuming that the disulfides act as precursor to polysulfides formation, Acres *et al*. (2010) concluded that bornite is possibly decreasing the formation rate of polysulfides, which indicate a slower oxidation rate of chalcopyrite. These authors suggested that the galvanic interaction involving chalcopyrite and bornite enhances the oxidation rate of bornite (*i.e.*, the anode of the galvanic couple) and slow down the chalcopyrite oxidation rate.

Investigations on bornite oxidation in acidic media are scarce in the literature and there are uncertainties on its oxidation mechanism under atmospheric conditions. On the basis of an initial removal of iron from this mineral, it has been suggested that covellite (CuS) forms as an oxidation product (Eq. 4.6), a phase which was positively detected on oxidized bornite by means of X-ray diffraction (Pesic and Olson, 1984; Bevilaqua *et al*., 2010).

$$Cu_5FeS_4 + 2\,H^+ \rightarrow 3\,CuS + 2\,Cu^{2+} + Fe^{2+} + H_2S + 4\,e^- \quad (4.6)$$

Other authors assume that bornite oxidation proceeds by a different mechanism under atmospheric conditions. On the basis of a non-stoichiometric Cu/Fe ratio on oxidized samples, it has been proposed that a copper-deficient phase would be formed (Eq. 4.7) (Price and Chilton, 1980, 1981), which oxidizes to CuS (Eq. 4.8) (Arce and González, 2002), or elemental sulfur (Eq. 4.9) (Price and Chilton, 1980, 1981).

$$Cu_5FeS_4 \rightarrow Cu_{5-x}FeS_4 + x\,Cu^{2+} + 2x\,e^- \quad (4.7)$$

$$Cu_{5-x}FeS_4 + 6\,H^+ \rightarrow CuS + (4-x)\,Cu^{2+} + 3\,H_2S + Fe^{3+} + (5-2x)\,e^- \quad (4.8)$$

$$Cu_{5-x}FeS_4 \rightarrow (5-x)\,Cu^{2+} + Fe^{3+} + 4\,S + (13-2x)\,e^- \quad (4.9)$$

Therefore, by both oxidative mechanisms (*i.e.*, selective removal of Fe from bornite or preferential leaching of Cu), covellite is considered an intermediate product of bornite dissolution in acidic media at low-temperature conditions. The elemental sulfur, a phase

which was positively detected by XRD on oxidized bornite (Bevilaqua *et al.*, 2010), would be formed from the oxidation of the intermediate copper-deficient sulfide (Eq. 4.9), a product phase of bornite oxidation (Eq. 4.7). Elemental sulfur could also be formed from hydrogen sulfide (H_2S) oxidation (Eq. 4.10) and from covellite oxidation (Eq. 4.11).

$$H_2S \rightarrow 2\,H^+ + S + 2\,e^- \quad (4.10)$$

$$CuS \rightarrow Cu^{2+} + S + 2\,e^- \quad (4.11)$$

On the basis of evidences obtained in the present investigation, the elemental sulfur – a product phase detected by S-SAXRD and Raman spectroscopy on electrodes oxidized at 0.80 and 1.00 V, and covellite – a product phase detected by micro Raman spectroscopy on electrodes oxidized at 0.80 V, could be formed directly from chalcopyrite oxidation (Eq. 4.12) as earlier suggested or, then, from the bornite oxidative process, as discussed in this section.

$$2\,CuFeS_2 \rightarrow CuS + Cu^{2+} + 2\,Fe^{3+} + 3\,S + 8\,e^- \quad (4.12)$$

Regarding the possible protective character of covellite, results by Mehta and Murr (1983) indicated that the mixed potential of chalcopyrite is more positive than that of covellite. Thus, in a micro cell chalcopyrite (electrode)-covellite (film), covellite acts as the anode and chalcopyrite acts as the cathode. This association chalcopyrite-covellite may enhance the oxidation rate of covellite and slow down the dissolution rate of chalcopyrite. The galvanic effect of covellite on chalcopyrite dissolution rate remains to be better investigated.

4.5. Conclusions

A systematic investigation of the electrochemical behavior of chalcopyrite in combination with analysis by synchrotron small angle X-ray diffraction and micro Raman spectroscopy added some useful information to the understanding of the chalcopyrite dissolution process in abiotic, acidic media, under atmospheric conditions. It was shown that chalcopyrite

oxidation at potentials lower than the critical potential value, which ranges from 0.75 to 0.90 V (*i.e.*, in the anodic prewave region), involves the formation of a layer of bornite (Cu_5FeS_4), covellite (CuS) and elemental sulfur (S_8). The results also suggest the formation of an unidentified metal-deficient phase. The formation of intermediate product phases on chalcopyrite was demonstrated in the present investigation by characterizing the products formed on the electrodes, which were oxidized under a constant applied potential. The formation of these intermediate phases correlated well with hindered dissolution behavior (*i.e.*, a decrease of oxidation current with time), as observed at 0.60, 0.70, and 0.80 V, the latter for electrodes with a higher critical potential. At such potential conditions, bornite and covellite were detected on chalcopyrite. The absence of these intermediate product phases also correlated well with active oxidation process (*i.e.*, an increase of the anodic current with time), as observed at 1.00 and also 0.80 V, the latter for electrodes with a lower critical potential. At such conditions, only elemental sulfur was identified on chalcopyrite.

Therefore, the results of this investigation support the hypothesis that the formation of iron-deficient sulfides contributes to the slow dissolution rate of chalcopyrite under atmospheric conditions. In addition, there is no evidence to ascribe the hindered dissolution of chalcopyrite to the formation of elemental sulfur.

Chapter 5 – Applications of *in situ* synchrotron XRD in hydrometallurgy: Literature review and new results for chalcopyrite dissolution

Abstract

In situ synchrotron X-ray diffraction (S-XRD) techniques are potentially powerful and versatile research tools for advancing our understanding in dissolution reactions of commercially important minerals. This chapter presents a review on the applications of S-XRD to investigate solid transformations in aqueous media, with emphasis in reactions relevant to hydrometallurgy. It includes the dissolution reactions of nickel laterite ores and important metal sulfides, such as pyrite (FeS_2), bornite (Cu_5FeS_4) and chalcocite (Cu_2S). This chapter also reports results of an *in situ* synchrotron time-resolved X-ray diffraction (S-TRXRD) study of the dissolution of chalcopyrite ($CuFeS_2$). S-TRXRD measurements were carried out in capillary-based cells containing fine $CuFeS_2$ particles by using two experimental approaches – flow method (FM) and non-flow method (NFM). The S-TRXRD patterns obtained in 0.1 mol.L^{-1} H_2SO_4 solutions at 0.75 V *vs.* the Standard Hydrogen Electrode – SHE (*i.e.*, 0.0062 mol.L^{-1} Fe^{2+} + 0.0938 mol.L^{-1} Fe^{3+}), 25 °C (FM), revealed no modification of the mineral crystal structure up to 10 h. This finding is in agreement with the slow dissolution rate of the mineral. In the temperature range 100-200 °C (NFM), the formation of covellite (CuS), elemental sulfur (S_8), and metal sulfates (ferrous or cupric sulfates) were detected on $CuFeS_2$ particles. By comparing the detection time, our results suggest that the formation of molten elemental sulfur is possibly related to an initial oxidation of $CuFeS_2$ by Fe^{3+} ions, followed by CuS oxidation by the same oxidant. Although only a few publications are currently available on applications of *in situ* S-XRD to sulfides and oxides dissolution, the presented results indicate that this technique may be used to significantly improve the current knowledge on key hydrometallurgical systems.

Keywords: *In situ* synchrotron time-resolved X-ray diffraction; metal sulfides; chalcopyrite.

5.1. Introduction

Various characterization techniques, such as X-ray photoelectron spectroscopy (XPS), X-ray diffraction (XRD), X-ray absorption spectroscopy (XAS), and Raman spectroscopy have been applied to investigate the kinetics and transformation mechanisms of a variety of solid phases in hydrometallurgically relevant aqueous media. To date, the significant advances that have been made into the nature of the end-product phases and into the mechanisms by which they affect the reaction rates have resulted mostly from *ex situ* techniques. This means that the steps involved in the solid phase transformations have not been tracked in place; additionally, as the samples under analysis would have been removed from the reaction environment, the solid surfaces may have been altered prior to the characterization experiments.

The present work is motivated by the recognition that application of *in situ* techniques, occasionally combined with theoretical calculations and molecular simulations, may lead to a considerable jump in our understanding of solid decomposition reactions in hydrometallurgical systems. Already, there are an increasing number of publications that demonstrates that *in situ* analytical techniques, particularly those that rely on *in situ* XRD and allow the study of dynamic changes under local and, therefore, more realistic environmental conditions, can lead to significant advances in many research areas of hydrometallurgical interest. Selected examples of these hydrometallurgy-related advances will be reviewed in the following section of the present paper.

As crystalline phases are frequently encountered in aqueous systems, the use of XRD, a technique based on scattering of X-rays by electrons of the constituent atoms of the crystal (Cullity and Stock, 2001), has provided valuable information on reaction paths and rates, existence of crystalline and amorphous intermediate product phases, and on crystal size as a function of time (Norby, 1996). Although a conventional diffractometer can be used to conduct *in situ* measurements, a consequence of the attenuation of the incident X-ray beam by the aqueous phase within the reaction cells is that the quality of the measured signal is adversely affected (De Marco *et al*., 2006a). Use of high brilliant synchrotron radiation permits XRD measurements with increased energy (Bachrach, 1992). So far, only a limited number of *in situ* synchrotron XRD investigations have appeared, which were inspired by

strictly hydrometallurgical questions. Nonetheless, investigations that are motivated by other considerations can still be of interest, especially when they examine minerals encountered in hydrometallurgical systems.

Aiming at establishing the rates in which intermediate phases grow and decompose to end products under practical conditions and, in addition, to correlate the dynamic structural changes of the solid phases with the amount of metals released into solution, *in situ* synchrotron XRD techniques have been applied to elucidate the dissolution mechanisms of important sulfides, such as pyrite (FeS_2) (De Marco *et al*., 2006b), chalcocite (Cu_2S) (Wall *et al*., 2011a), and bornite (Cu_5FeS_4) (Wall *et al*., 2011b), and also of nickel laterite ores (Scarlett *et al*., 2008). In order to highlight the unique scientific contributions that such *in situ* synchrotron technique can provide, the main findings reported in these previous investigations are also discussed below.

Finally, recent results obtained through an *in situ* synchrotron time-resolved X-ray diffraction (S-TRXRD) investigation of the dissolution of chalcopyrite ($CuFeS_2$), the most commercially important copper mineral, are presented. Direct measurements, as provided by this *in situ* technique, on the conversion rate of chalcopyrite to intermediate- and end-product phases, as well as on the effect of temperature on this process are not available in the literature, to the authors' knowledge.

5.2. *In situ* investigations in aqueous media by synchrotron X-ray diffraction

5.2.1. Synchrotron X-ray diffraction (S-XRD)

As already noted above, in principle, conventional diffractometers can be used to conduct *in situ* measurements. However, the quality of the measured signal is affected as a function of the attenuation of the incident X-ray beam by the aqueous phase within the reaction cells (De Marco *et al*., 2006a). The special niche provided by synchrotron radiation (*i.e.*, the electromagnetic radiation emitted by charged particles moving on circular orbits with relativistic velocities) is that it permits XRD measurements with increased energy and time resolution (Bachrach, 1992). Compared to the conventional X-ray tubes, the synchrotron

radiation is 10^4 to 10^{12} times brighter and counting statistics is 10^6 times faster, on similarly sized samples (Parise, 2000). The high intensity of synchrotron X-ray beams greatly improves the signal-to-noise ratio obtained, which allows the examination of minor amounts of material. It has made it possible to track very fast reactions with useful time resolution (Norby, 2006). Other advantages of using synchrotron X-ray beams include the acquisition of data of sufficient quality for Rietveld refinements, ability to adjust the wavelength of the incoming radiation and choice of energy dispersive geometries (Norby, 1996; Morón, 2000).

Synchrotron radiation has been increasingly attractive for studying chemical and electrochemical reactions under well-controlled conditions, as synchrotron storage rings have become available worldwide to experimentalists. Advances in the development of synchrotron radiation sources, as well as reaction cell designs, instrumentation and detectors have helped to stimulate new research in aqueous media, especially hydrothermal reactions (*i.e.*, materials synthesis and crystallization) (Munn *et al*., 1992; Norby, 1997; Christensen *et al*., 1998; Cahill *et al*., 2000; Fogg *et al*., 2000; Loh *et al*., 2000; Walton and O'Hare, 2001; Walton *et al*., 2001; Beale and Sankar, 2003; Shen *et al*., 2006; Hummer *et al*., 2009; Murray *et al*., 2009; Chen *et al*., 2011; Webster *et al*., 2011; Ferer *et al*., 2012; Webster *et al*., 2012). Table V.1 lists some scientific papers on the application of *in situ* S-XRD to elucidate materials and minerals reaction systems, which are relevant to hydrometallurgy. The emphasis is on the different methodologies available and the corresponding reaction systems subjected to investigation. Firstly, it may be noticed that powder diffraction is typically conducted in capillary-based or pressure reaction cells, while grazing incidence XRD analysis is typically applied in investigations of thin film layers or multilayers. The selection of each one of the cell designs (*i.e.*, capillary-based, electrochemical, and pressure reaction cells) takes into account the configuration of the synchrotron beam line accessed, and principally the required conditions for the reaction to takes place. Important advances in the construction materials of the reaction cells have allowed *in situ* XRD measurements in acidic and alkaline solutions, at low and high temperatures, as can be seen in Table V.1. More detailed information on the specifications of the different cell designs can be found in the original publications (Barlow *et al*., 1989; Evans *et al*., 1994; Norby, 1996; Leyssens *et al*., 2005; Loan *et al*., 2005; De Marco *et al*., 2006a; Ingham *et al*., 2008; Webster *et al*., 2009; Wall *et al*., 2011a; Ferer *et al*., 2012).

Table V.1 – Applications of *in situ* S-XRD techniques in reactions relevant to hydrometallurgy and corrosion reactions in aqueous media.

HYDROMETALLURGY			
References	**Technology**	**Starting material / solution**	**Experimental conditions**
Fogg *et al.*, 2000	- Stirred reaction cell; - Information on the beam wavelength and size, and type of detector not available.	Supersaturated solutions of sodium aluminate ($NaAlO_2$).	Measurements were conducted at 65, 80 and 90 ºC from 3.77 and 6 $mol.L^{-1}$ NaOH solutions during about 600 min.
De Marco *et al.*, 2006b	- Electrochemical flow-cell; - Beam wavelength: ~1.000 Å; - Beam size: ~100 μμ x 2 mm; - Incident angle: 0.6°; - Fuji image plate system.	Pyrite (FeS_2) electrodes.	Alkaline solutions (0.1 $mol.L^{-1}$ NaCl in 0.01 $mol.L^{-1}$ $NaHCO_3$/0.01 $mol.L^{-1}$ Na_2CO_3 solution; pH 10.5) at room temperature was continuously pumped through the cell at a flow rate of 4 $mL.min^{-1}$ during 42-100 min. The electrode was polarized at 0.5 and 0.8 V *vs.* SSRE.
Scarlet *et al.*, 2008	- 1 mm quartz capillary; - Beam wavelength: ~1.000 Å; - Curved one-dimensional wide-angle X-ray scattering (WAXS) RAPID2 detector.	Nickel laterite ores.	Acid solutions (19.4 or 32.7% wt. H_2SO_4 solutions) at 210 or 250 ºC continuously flowed through the cell.
Murray *et al.*, 2009	- Pressure reaction vessel with agitation; - Single germanium detector.	Goethite and hematite (synthetic samples).	Material immersed in 3.77 $mol.L^{-1}$ NaOH + 2.65 $mol.L^{-1}$ $Al(OH)_3$ + 0.24 $mol.L^{-1}$ Na_2CO_3 solutions, at 230-250 °C (42 bar), during 1400-4000 seconds. The effects of goethite/hematite molar ratios (0.9-9), hematite surface area (5.5-18.6 $m^2.g^{-1}$) and addition of anatase (TiO_2) were investigated.
Wall *et al.*, 2011a	- 0.7–1.0 mm glass capillaries; - MAR345 image plate detector; - MAR165 CCD camera.	Chalcocite (Cu_2S) particles.	Solutions (not mentioned) flowed through the material at room temperature during about 120 min.

(Cont.) Table V.1 – Applications of *in situ* S-XRD techniques in reactions relevant to hydrometallurgy and corrosion reactions in aqueous media.

HYDROMETALLURGY			
References	**Technology**	**Starting material / solution**	**Experimental conditions**
Wall *et al*., 2011b	- 0.7–1.0 mm glass capillaries; - MAR345 image plate detector; - MAR165 CCD camera.	Bornite (Cu_5FeS_4) particles (< 10 μm).	Solutions of ferric sulfate (2.8-65 mmol.L^{-1} Fe^{3+}, pH 2.0-2.5) flowed through the material (0.01-0.34 mL.min^{-1}) at room temperature during about 100 min.
Webster *et al*., 2011	- Sealed 1.0 mm quartz-glass capillaries; - MAR345 image plate detector; - MAR165 CCD camera.	Sodium aluminate liquor containing seeds (seed loading 14.3 wt. %).	Measurements conducted at 70 °C using synthetic goethite (d_{50} = 0.8 μm), hematite (d_{50} = 1.2 μm), magnetite (d_{50} = 7.7 μm), and gibbsite (d_{50} = 19.7 μm) seeds, during about 248 min.
Webster *et al*., 2012	- Sealed 1.0 mm quartz-glass capillaries; - Beam wavelength: ~0.825 Å; - MAR345 image plate detector; - MAR165 CCD camera.	Sodium aluminate liquor containing seeds (seed loading 14.3 wt. %).	*In situ* measurements undertaken at 70 °C using synthetic lepidocrocite (γ-FeOOH) (d_{50} = 7.8 μm), and ferrihydrite ($Fe_2O_3.0.5H_2O$) (d_{50} = 61.7 μm) seeds, during about 415 min.
CORROSION SCIENCE			
References	**Technology**	**Starting material / solution**	**Experimental conditions**
Robinson and Walsh, 1993	- Electrochemical cell; - Beam wavelength: ~1.307 Å; - Incident angle: 4°; - 120° CPS detector.	α-PbO_2 (lead dioxide) layer, deposited on platinum electrode.	Material immersed in 1 mol.L^{-1} H_2SO_4 solution at room temperature and polarized at 1.25-1.50 V *vs.* SCE.
De Marco *et al*., 2005	- Electrochemical flow-cell; - Beam wavelength: ~1.000 Å; - Beam size: ~100 μm x 2 mm; - Fuji image plate system.	Carbon steel electrodes.	Brine solutions (3% w/v NaCl containing 100 mg.L^{-1} $NaHCO_3$, CO_2-saturated) at room temperature was continuously pumped through the cell at a flow rate of 4 mL.min^{-1} during about 27 h.

(Cont.) Table V.1 – Applications of *in situ* S-XRD techniques in reactions relevant to hydrometallurgy and corrosion reactions in aqueous media.

CORROSION SCIENCE			
References	**Technology**	**Starting material / solution**	**Experimental conditions**
Leyssens *et al*., 2005	- Electrochemical cell; - Beam wavelength: ~1.598 Å; - Incident angle: 10°; - 2-circle high-resolution diffractometer.	Metal copper covered with nantokite (CuCl), or a mixture of cuprite (Cu_2O), atacamite and paratacamite (isomers of $Cu_2(OH)_3Cl$).	Material immersed in 0.05 $mol.L^{-1}$ sodium sesquicarbonate solution ($NaHCO_3$. Na_2CO_3) at room temperature during about 56-308 min.
Ingham *et al*., 2010	- Electrochemical cell; - Beam wavelength: ~0.826 Å; - Beam size: ~0.2 x 0.7 mm; - Incident angle: <1.0°; - VHR CCD detector.	Carbon steel electrodes.	Material immersed in 0.5 $mol.L^{-1}$ NaCl solutions (pH 6.3) containing CO_2 (1 bar) and 0-100 ppm ATMPA (amino trimethylene phosphonic acid), at 50-90 °C. An anodic current of +12.5 $mA.cm^{-2}$ was applied on the electrodes. Measurements conducted up to about 120 min.
Ingham *et al*., 2012	- Electrochemical cell; - Beam wavelength: ~0.826 Å; - Beam size: ~0.2 x 0.7 mm; - Incident angle: <1.0°; - VHR CCD detector.	Carbon steel electrodes.	Material immersed in 0.5 $mol.L^{-1}$ NaCl and 0.5 $mol.L^{-1}$ NaCl + 0.02-0.1 $mol.L^{-1}$ $MgCl_2$ CO_2-saturated solutions (pH 6.3) at 80 ºC. The electrodes were polarized at -0.5 V *vs.* Ag/AgCl. *In situ* measurements undertaken during about 140 min.

Legend: SCE = Saturated Calomel Electrode (+0.241 *vs*. SHE at 25ºC); Ag/AgCl – Silver/Silver Chloride Electrode (+0.207 *vs*. SHE at 25ºC, 3.0 mol/L KCl); SSRE = Stainless Steel Pseudo Reference Electrode (redox potential against SHE not found).

Table V.2 – Main findings obtained by *in situ* S-XRD techniques applied to investigate reactions relevant to hydrometallurgy and corrosion reactions in aqueous media.

HYDROMETALLURGY	
References	**Main findings**
Fogg *et al*., 2000	The *in situ* S-XRD measurements revealed the exclusive formation of gibbsite (γ-$Al(OH)_3$) throughout the experiment.
De Marco *et al*., 2006b	The *in situ* grazing incidence S-XRD measurements indicated a growth of amorphous humps at 2θ angles between 15 and 30º, mainly at the higher applied potential. The following products have been detected on pyrite (FeS_2) during polarization at 0.40 and 0.50 V: $FeSO_4$, $Fe(OH)SO_4$ and $Fe(OH)_2$. No crystalline phases were detected during polarization at 0.70 and 0.80 V.
Scarlet *et al*., 2008	- For the nickel saprolite ore, the *in situ* XRD patterns indicated the formation of hematite (Fe_2O_3) and a slight decrease in the content of maghemite (γ-Fe_2O_3). It was also revealed that jarosite precipitation was suppressed at the higher temperature; - For the nickel limonite ore, at both acid concentrations, goethite (FeOOH) and magnetite (Fe_3O_4) phases dissolved at different rates, and jarosite was precipitated. At the lower acid level, a slow formation of Fe_2O_3 was observed, while at the higher level, basic ferric sulfate ($Fe(OH)SO_4$) was quickly detected after jarosite precipitation; - For the nickel nontronite ore, at the lower acid concentration, $Fe(OH)SO_4$ was formed along with a poorly crystalline jarosite. At the higher acid level, the same product phase was formed, but no jarosite was detected.
Murray *et al*., 2009	The *in situ* S-XRD patterns showed the dissolution of goethite (α-FeOOH) and simultaneous growth and increase of hematite (α-Fe_2O_3) peaks after 30 min. In the presence of α-Fe_2O_3 seeds (goethite/hematite = 1.44), the complete transition was observed in about 35 min. The measurements also indicated that the rate of transformation of α-FeOOH to α-Fe_2O_3 increases with increasing hematite surface area, and that temperature has a significant effect on the reaction kinetics. In addition, the S-XRD patterns showed that higher caustic concentration results in faster kinetics, and that the presence of anatase did not affect the conversion rate.
Wall *et al*., 2011a	The time-resolved S-XRD measurements showed the conversion of chalcocite (Cu_2S) to covellite (CuS). According to the diffraction patterns, it was suggested the formation of transient copper sulfides during the reaction.
Wall *et al*., 2011b	The time-resolved S-XRD patterns revealed a contraction in the unit cell volume of bornite (Cu_5FeS_4), ascribed to a transition from stoichiometric to non-stoichiometric Cu_5FeS_4.

(Cont.) Table V.2 – Main findings obtained by *in situ* S-XRD techniques applied to investigate reactions relevant to hydrometallurgy and corrosion reactions in aqueous media.

HYDROMETALLURGY	
References	**Main findings**
Webster *et al*., 2011	For the magnetite-seeded experiment, the *in situ* S-XRD measurements indicated that after the induction period (about 90 min), the relative intensity of gibbsite peaks increased slowly until about 105 min, but after that it increased quickly. This change coincided with the appearance of bayerite and nordstrandite peaks. For the other *in situ* S-XRD measurements (seeded and unseeded experiments), only gibbsite peaks were detected. The induction periods for the goethite- and hematite-seeded experiments were about 11 and 29 min, respectively.
Webster *et al*., 2012	For the ferrihydrite-seeded *in situ* S-XRD measurements, gibbsite peaks, as well as bayerite and nordstrandite peaks were detected; there was no evidence for the formation of either goethite or hematite phases. For the lepidocrocite-seeded reaction, the same product phases were detected. The S-XRD patterns also showed that the induction period of gibbsite crystallization was 11and 38 min for the lepidocrocite and ferrihydrite-seeded reactions, respectively. After this period, the early stages of crystallization in both reactions were characterized by a slow increase in gibbsite formation, followed by a period of fast kinetics.
CORROSION SCIENCE	
References	**Main findings**
Robinson and Walsh, 1993	At the open circuit potential, 1.34 V, the *in situ* S-XRD patterns indicated that the phase α-PbO_2 predominates on the Pt electrode, but $PbSO_4$ peaks were detected. During polarization at 1.25 V, the $PbSO_4$ content increased, while at 1.55 V the measurements indicated the formation of β-PbO_2. The relative intensity corresponding to the α-PbO2 and $PbSO_4$ phases decreased under this condition.
De Marco *et al*., 2005	The *in situ* grazing incidence S-XRD measurements indicated the formation of $Fe_2O_2CO_3$ at around 8 h, followed by a gradual growth of both the $Fe_2O_2CO_3$ and $Fe_2(OH)_2CO_3$ phases. The formation of $Fe_6(OH)_{12}CO_3$ and $Fe_6(OH)_{12}CO_3 \cdot 2H_2O$ phases was also detected.
Leyssens *et al*., 2005	The *in situ* S-XRD patterns showed that CuCl transforms into Cu_2O in a few hours - after 120 min of immersion. The measurements of sample covered with CuCl, Cu_2O and $Cu_2(OH)_3Cl$ revealed in the first 140 min a significant decrease in the intensity of the CuCl peak; the amount of Cu_2O and $Cu_2(OH)_3Cl$ remained constant. After 140 min, a slight decrease in the intensity of $Cu_2(OH)_3Cl$ peaks was observed. After 200 min the Cu_2O peak started to decrease.

(Cont.) Table V.2 – Main findings obtained by *in situ* S-XRD techniques applied to investigate reactions relevant to hydrometallurgy and corrosion reactions in aqueous media.

CORROSION SCIENCE	
References	**Main findings**
Ingham *et al*., 2010	The *in situ* S-XRD patterns revealed the formation of siderite ($FeCO_3$) at temperatures between 40 and 90 ºC; two unidentified minor phases were observed: phase A, at 40 ºC, detected before $FeCO_3$ formation, and phase B, at 90 ºC, after $FeCO_3$ formation. Both these products grew slowly. The measurements also revealed that with increasing temperature, the scale formation rate increased, while the thickness and crystallite size decreased. It was also observed that these properties decreased with increasing ATMPA concentration. High concentrations of ATMPA appeared to inhibit the nucleation and growth of $FeCO_3$.
Ingham *et al*., 2012	The *in situ* S-XRD measurements revealed an induction period of about 30 min and the exclusive formation of $FeCO_3$ in NaCl media after about 120 min. The formation of both $FeCO_3$ (firstly) and $Fe_2(OH)_2CO_3$ was detected in the presence of $MgCl_2$. At low concentrations of $MgCl_2$, the change of $FeCO_3$ lattice d-spacings was more marked than that observed in the absence of $MgCl_2$ or at high concentrations of this reagent.

From Table V.1 it can also be seen that beams of different characteristics (*i.e.*, energy, wavelength, spot size, and angular position) have been focused on the materials and minerals under analysis, and that many types of detectors have been selected, depending on the data quality and time resolution desired for the *in situ* measurements.

Table V.2 summarizes the main findings provided by the *in situ* S-XRD experiments listed in Table V.1. It can be seen that important contributions have been made on the rates and mechanisms of many reactions of relevance to hydrometallurgy, such as studies on (i) gibbsite (γ-$Al(OH)_3$) crystallization (Fogg *et al.*, 2000; Webster *et al.*, 2011; Webster *et al.*, 2012) and transformation of goethite (α-FeOOH) to hematite (α-Fe_2O_3) under Bayer process conditions (Murray *et al.*, 2009); (ii) dissolution of pyrite in alkaline media containing chloride and carbonate ions at room temperature (De Marco *et al.*, 2006b); (iii) dissolution of nickel laterite ores in acidic sulfate solutions under high-temperature conditions (Scarlet *et al.*, 2008); and (iv) dissolution of copper minerals – bornite (Cu_5FeS_4) and chalcocite (Cu_2S) – in acidic, oxidizing solutions at room temperature (Wall *et al.*, 2011a, 2011b). Additional details are provided in the next section.

5.2.2. *In situ* investigations of mineral formation and dissolution reactions by S-XRD

Investigations on gibbsite crystallization are very important for hydrometallurgy since this hydroxide is produced in the Bayer process. After dissolution of bauxite ores in concentrated sodium hydroxide (NaOH) solution at about 150-250 ºC, the residue (red mud) is separated from the sodium aluminate liquor. This liquor is then cooled and seeded to precipitate gibbsite, which is further calcined to produce alumina (Al_2O_3) (Hind *et al.*, 2009). Both iron oxide phases goethite (α-FeOOH) and hematite (α-Fe_2O_3) are present in the bauxite ore and red mud. The conversion of α-FeOOH to α-Fe_2O_3 is extremely important in the context of Bayer process, because goethite can act as a seed for gibbsite precipitation, which causes aluminum losses (Webster *et al.*, 2011) and product contamination with iron. Iron oxide and oxyhydroxide effects on gibbsite crystallization are also implicated in the formation of scales (*i.e.*, build-up of insoluble species on the walls of the Bayer process equipment), which affects heat transfer and material flow (Murray *et al.*, 2009; Webster *et al.*, 2011). The application of *in situ* S-XRD techniques

allowed a better understanding of gibbsite crystallization and conversion of goethite to hematite under Bayer process conditions. Some conclusions to be highlighted are: magnetite (Fe_3O_4) seed was found less active for promoting gibbsite crystallization than goethite and hematite seeds, on the basis of a comparison of the induction time before the beginning of measurable crystallization (Webster *et al*., 2011); and (ii) in order for the transformation of α-FeOOH to α-Fe_2O_3 to take place under Bayer process conditions, hematite seeding is required (Murray *et al*., 2009).

Regarding investigations on dissolution reactions – the main focus of this literature review – the work of Robinson and Walsh (1993) on corrosion science holds a special place; it may be the pioneering paper on the application of *in situ* S-XRD to investigate dissolution reactions in aqueous media. In this work, the versatility of this *in situ* X-ray technique was demonstrated by the phase transformation of lead dioxide (α-PbO_2) in 1 mol.L^{-1} H_2SO_4 solution to $PbSO_4$ and β-PbO_2 during cathodic and anodic polarization, respectively. The approach was followed by others aiming at a better understanding of the corrosion rates and mechanisms of commercial materials, such as carbon steel and metallic copper (Tables V.1 and V.2).

In the case of the dissolution reactions of materials encountered in hydrometallurgical systems, such as nickel laterite ores, FeS_2, Cu_5FeS_4 and Cu_2S, application of *in situ* synchrotron XRD techniques has resulted in crucial information on the nature of intermediate phases, as well as kinetics and dissolution mechanisms (Tables V.1 and V.2). These minerals and related reactions are extremely important: Nickel laterite ores represent about 70% of the world's known deposits of this metal (Dalvi *et al*., 2004); bornite and chalcocite are typical phases in copper sulfide ores; and pyrite is a common mineral phase in gold and base metal ores and a main source for acid mine drainage.

Scarlett *et al*. (2008) evaluated the kinetics and dissolution mechanisms of nickel laterite ores using a capillary-based reaction cell (Tables V.1 and V.2). The authors investigated the dissolution behavior of the three laterite components (*i.e.*, saprolite ore – 1.8% wt. Ni; limonite ore – 1.3% wt.; and nontronite ore – 1.7% wt. Ni) at two acid (19.4 and 32.7% wt. H_2SO_4 solutions) and temperature (210 and 250ºC) levels, conditions typically found in processing plants. For the saprolite ore, the *in situ* synchrotron XRD patterns indicated the

hematite (α-Fe_2O_3) formation along with a slight decrease in the maghemite (γ-Fe_2O_3) content of the sample. The *in situ* measurements also revealed that jarosite precipitation was suppressed at 250ºC. For the limonite ore, two slightly different mechanisms were observed. At both acid concentrations, goethite (α-FeOOH) and magnetite (Fe_3O_4) dissolved at different rates and jarosite precipitated. In 19.4% wt. H_2SO_4 solutions, a slow formation of hematite was observed, while in 32.7% wt. H_2SO_4 solutions, basic ferric sulfate ($Fe(OH)SO_4$) was quickly detected after jarosite precipitation. For the nontronite ore and at the lower acid concentration, the sample dissolved and basic ferric sulfate was formed along with a poorly crystalline jarosite. At the higher acid level, the *in situ* XRD patterns revealed a fast dissolution of nontronite. Basic ferric sulfate appeared, but no jarosite was detected. Scarlett *et al*. (2008) did not correlate the *in situ* XRD patterns with the amount of nickel released into the solutions from leaching of the three laterite components, or with the nickel losses during the precipitation reactions.

In recent applications of the *in situ* synchrotron XRD technique, Wall and co-workers (2011a, 2011b) (Tables V.1 and V.2) evaluated the ratio of Cu isotopes ($^{65}Cu/^{63}Cu$) during dissolution of bornite (Cu_5FeS_4) and chalcocite (Cu_2S), at room temperature. An experimental set-up that combined S-TRXRD with time-resolved stable isotope analysis by inductively coupled plasma mass spectrometry (ICP-MS) was developed to investigate structural changes of the solid phases and possible correlations among those changes with variations in the isotopic composition in the aqueous phase. They used a flow-through capillary cell containing bornite (Cu_5FeS_4) particles (< 10 μm) through which ferric sulfate solutions (2.8-65 $mmol.L^{-1}$ Fe^{3+}, pH 2.0-2.5) flowed at a constant rate (0.01-0.34 $mL.min^{-1}$). For a 100 min experiment, Wall *et al*. (2011a) demonstrated that in the initial stages, the dissolved copper was enriched in ^{65}Cu relatively to the solid phase, and when more than 20 mol% Cu was dissolved, the difference between the isotope content in the solid and aqueous phases approached zero. The synchrotron *in situ* measurements indicated that the maximum ($^{65}Cu/^{63}Cu$) ratio was associated with a contraction in the volume of the mineral unit cell, which can be ascribed to a transition from stoichiometric to non-stoichiometric bornite. The measurements also revealed that Cu dissolution increased with time, but the reaction rate decreased drastically as 27 to 30 mol% of the total Cu was dissolved.

Using the same experimental set-up for chalcocite (Cu_2S) dissolution, Wall *et al*. (2011b) demonstrated for a 120 min experiment that the Cu content in the aqueous phase was initially enriched in ^{65}Cu relative to the solid, but this content decreased with time. The results further indicated that the ratio ($^{65}Cu/^{63}Cu$) depended on the sulfide phase in coexistence with the solution. The ratio was positive (preferential release of ^{65}Cu in the solution) when the solid phases were characterized by Cu/S ratios close to 2/1, but it became negative (preferential release of ^{63}Cu in the solution) when the Cu/S ratios approached 1/1. The *in situ* measurements revealed the conversion of chalcocite (Cu_2S) to covellite (CuS) and the diffraction patterns suggested the formation of transient copper sulfides during the reaction.

Although the works of Wall and co-workers (2011a, 2011b) were designed to describe copper mobilization into geochemical processes, the findings that the bornite dissolution under low-temperature conditions, involves transition from stoichiometric to non-stoichiometric phases and decreasing copper extraction rate, and that the conversion of chalcocite to covellite involves formation of transient sulfides are of hydrometallurgical interest, since information on the rate and mechanisms by which these minerals dissolves may be used to develop alternative processes for treating copper sulfide ores.

With a different experimental system as compared to the abovementioned, De Marco *et al*. (2006b) investigated the dissolution of pyrite by *in situ* synchrotron XRD (Table V.1 and V.2). A particular electrochemical flow-cell was designed, which allowed the oxidation of massive electrodes by chronoamperometry and *in situ* thin film analysis by synchrotron grazing incidence X-ray diffraction (S-GIXRD). The set-up was used to evaluate the reaction rate and mechanisms of pyrite oxidation in a solution containing chloride and carbonate ions (0.1 $mol.L^{-1}$ NaCl; 0.01 $mol.L^{-1}$ $NaHCO_3$/0.01 $mol.L^{-1}$ Na_2CO_3; pH 10.5), at room temperature. Different potentials were fixed during about 40-100 min: 0.40-0.80 V *vs.* a stainless steel pseudo reference electrode. De Marco *et al*. (2006b) demonstrated that the oxidation of pyrite electrode at 0.40 V resulted in fast formation of crystalline phases such as ferrous sulfate ($FeSO_4$), ferrous hydroxide ($Fe(OH)_2$), and a hydrated basic ferric sulfate ($Fe(OH)SO_4.2H_2O$). Similar diffraction patterns were detected at 0.50 and 0.60 V. At 0.70 and 0.80 V, no crystalline phase was detected. The *in situ* S-GIXRD measurements also indicated a large build-up in the relative intensity of amorphous humps, particularly at

the higher potential values. The authors suggested that the product phases that form on pyrite passivate the mineral surface, but unfortunately, they did not present evidences (as those provided by chronoamperometry) of the passive behaviors of this sulfide at the lower and higher potentials investigated. This combined approach may lead to improvements in the extraction of gold or other base metal from pyrite.

In light of the above review, it is clear that *in situ* synchrotron XRD techniques are versatile research tools. Conventional leaching methods and electrochemical techniques may be adjusted and utilized in the beam lines available worldwide. In particular, design of appropriate experiments involving important sulfides may be helpful towards the development of treatment processes for low-grade, complexes ores. Initial results are presented here of *in situ* synchrotron time-resolved XRD measurements undertaken to investigate the dissolution of chalcopyrite at low and high temperatures, using capillary-based cells. The dissolution of chalcopyrite is an especially important process for copper hydrometallurgy, since this sulfide accounts for about 70% of the world's known copper reserves (Davenport *et al*., 2002). It is the main constituent in many low-grade copper ores. The purpose of the new experiments described below was to evaluate structural changes and the rates of formation of crystalline and amorphous product phases on chalcopyrite by means of synchrotron time-resolved X-ray diffraction (S-TRXRD). Time-resolved measurements were conducted in acidic, oxidizing media under atmospheric conditions and at temperatures typically found in practical, leaching processes. Industrial leaching of chalcopyrite ores is undertaken on a commercial scale at the temperature range 90-230 °C (Dreisinger, 2006; McDonald and Muir, 2007b). In the present investigation, the *in situ* measurements were carried out by two experimental approaches – flow method and non-flow method – according to the temperature condition.

5.3. Experimental

5.3.1. Chalcopyrite sample

The initial sample – high-purity research mineral (Wards®, 49E5864) – consisted of small chalcopyrite grains (about 1.6-4.8 mm in size). This material was ground in a cup and puck

mill (NAEF®, 1694LA104), for 2 min. In order to obtain representative samples, the ground product was thoroughly homogenized, successively quartered and, then, kept under vacuum at room temperature. The sample used for the S-TRXRD measurements was characterized by the particle size distribution, quantitative chemical analysis and mineral composition. The particle size distribution analysis was conducted by dynamic light scattering using a Malvern® (Mastersizer) granulometer. Before analysis, the sample was kept in an ultrasonic bath (VWR®, 50T) for 5 min. The results obtained were quantified by the cumulative percent diameters (d_{10}, d_{50} and d_{90}), in μm. The mineral composition of the sample was obtained by X-ray diffraction using a Philips (PW 1710) X-ray diffractometer. The chemical composition was obtained by using the following procedure. Initially, three samples were digested in a hot plate at 150 °C (±5 °C sensitivity) for 5 h with aqua regia – 3HCl:HNO_3 – (analytical grade hydrochloric acid (HCl) 37% and nitric acid (HNO_3) 65%, FMaia®). Next, the solution was vacuum filtered and the concentration of Cu and Fe was determined by inductively coupled plasma optical emission spectrometry (ICP-OES) using a Perkin Elmer spectrophotometer (Optima 7300 DV). The residual solid was roasted in a furnace at 1000 °C (±25 °C sensitivity) for 1 h in a platinum crucible. The residue was then digested in a hot plate at 150 °C for 1 h with analytical grade hydrofluoric acid (HF) 40% (FMaia®). The silicon content was obtained by means of weight difference using an analytical balance. The concentration of Cu and Fe was analyzed in this solution. The elemental sulfur content was obtained using a LECO® (SC 632) induction furnace.

5.3.2. Reaction solution

The solution used in this investigation was 0.1 mol.L^{-1} H_2SO_4 (pH ≈ 1.0) and its redox potential (0.75 V *vs.* SHE) was established by the (Fe^{3+}/Fe^{2+}) couple. This potential value was selected initially since it is within the expected range for the ferric ion leaching of copper ores.

The potential (E) of a platinum electrode immersed in a solution containing Fe^{3+} and Fe^{2+} ions can be expressed by the Nernst equation as:

$$E = E° + \frac{RT}{F} \ln \frac{a_{Fe^{3+}}}{a_{Fe^{2+}}} = E°' + \frac{RT}{F} \ln \left[\frac{Fe^{3+}}{Fe^{2+}}\right] \quad (5.1)$$

where "a" represents the activity of the Fe^{3+} and Fe^{2+} ions, [ ] the molar concentration of the Fe^{3+} and Fe^{2+} ions, R the universal gas constant, T the absolute temperature and F the Faraday constant. E° and E°' indicate, respectively, the standard redox potential and the formal potential of the (Fe^{3+}/Fe^{2+}) couple. While the value of E° at 25 °C, 1 atm, is about 0.77 V *vs.* SHE, E°' in 0.1 mol.L^{-1} H_2SO_4 solution at 25 °C, 1 atm, is approximately 0.68 V *vs.* SHE, as determined by Stumm and Morgan (1981). The redox potential was measured by an Ag/AgCl/KCl (3.0 mol/L) reference electrode with a potential of +0.207 *vs.* SHE (at 25 °C). The oxidizing solution was obtained by adding iron (III) sulfate hydrate 97% ($Fe_2(SO_4)_3.xH_2O$) (Sigma-Aldrich®) and iron (II) sulfate heptahydrate 99% ($FeSO_4.7H_2O$) (Sigma-Aldrich®) into the acidic solution. A total Fe initial concentration equal to 0.1 mol.L^{-1} (or 5.585 g.L^{-1}) remained constant. All the solutions were prepared with double-distilled water using analytical grade sulfuric acid 96% (Sigma-Aldrich®).

5.5.3. S-TRXRD measurements

The synchrotron time-resolved X-ray diffraction (S-TRXRD) experiments were carried out by a flow method (FM), using the reaction cell design as reported by Wall *et al.* (2011b), and by a non-flow method (NFM), as first reported by Norby (1996), since the FM did not work well for measurements at high temperatures, as will be discussed later. By FM, *in situ* measurements were conducted at 25 °C (Fig. 5.1a), while by NFM the S-TRXRD patterns were obtained at 100, 150, and 200 °C (Fig. 5.1b).

The preparation of the capillary sample involved the following procedures. Firstly, the closed tip of a 0.5 mm (internal diameter) quartz capillary (Charles Supper®, 05-QZ) was cut in order to allow flow of solution, in the case of measurements by FM. A plug of cotton wool was then placed at the outlet of an about 3 cm capillary, in order to prevent the solid particles from passing into the solution collector. The mineral sample was weighed (0.001 g) using an analytical balance and, subsequently, packed into the capillary. Through the flow method, the diffraction patterns were recorded at 2 min intervals, during 10 h.

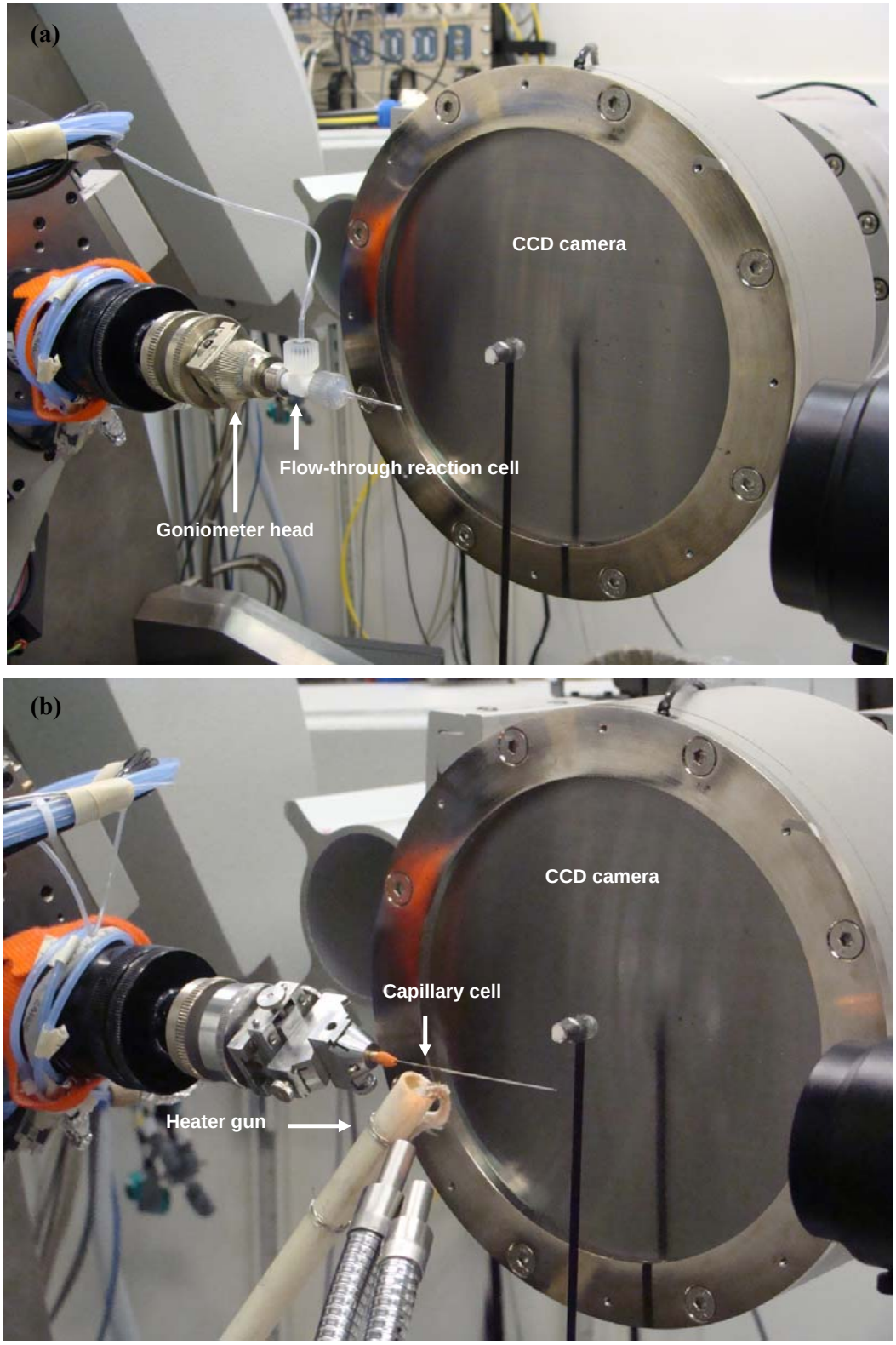

Figure 5.1. (a) Flow-through reaction cell attached to the goniometer head (flow method); and (b) Capillary sample attached to the goniometer head (no-flow method): APS/ANL.

In the case of measurements by NFM, the 0.5 mm quartz capillary was attached directly to the goniometer head using a copper pin, after sealing the open tip of the capillary with a high-temperature epoxy resin. The closed tip of the capillary was not cut, thus, there was no flow of solution through the mineral sample. By this method, the sample was initially conditioned in acidic, oxidizing solution for 1 h at room temperature (23±1 °C). After that, the solution was vacuum filtered and the slurry was filled into the quartz capillary. For obtaining the S-TRXRD patterns at the temperature range 100-200 °C, the sealed capillary sample was heated by a flow of hot air using a heater gun, 1 cm distant from the capillary. The temperature set point was monitored with a thermocouple in contact with the outside of the heater gun. Assuming no losses, the solution temperature was ramped to 100, 150, and 200 °C, at a heating rate of about 25 °C/min. The diffraction patterns were taken continuously throughout the heating of the capillary cell, at 2 min intervals, during 40 min in each temperature level.

High-quality patterns were obtained by a MAR 165 CCD camera at the beam line 13-BM-C at the Advanced Photon Source (APS), Argonne National Laboratory (ANL), Chicago, U.S. The patterns were recorded using synchrotron radiation with energy and wavelength of 12 keV and 1.0387 Å, respectively. The dimensions of the focused radiation beam are about 26 (horizontal) x 28 (vertical) μm. The device allows the rotation of the capillary sample about the phi axis by ±30°, therefore, minimizing preferred orientation. An exposure time of 60 sec was adopted for each measurement. The calibration procedure was performed with cerium dioxide (CeO_2). Diffraction images were integrated into relative intensity *vs.* 2θ plots using the Fit2D software (v. V12.077). The *in situ* diffraction patterns were identified by comparing d-spacings with the standard reference patterns, supplied by the International Centre for Diffraction Data (ICDD).

5.4. Results and discussion

5.4.1. Characterization of the chalcopyrite sample

The grinding of the chalcopyrite sample resulted in a product with 90% of the mineral particles smaller than about 6.5 μm and 10% smaller than about 0.2 μm. The median size,

for which 50% of the sample is smaller and 50% is larger than this size, was about 1.6 μm. The XRD patterns for the mineral sample are shown in Fig. 5.2. It should be noted that only chalcopyrite ($CuFeS_2$) (ICDD 83-0983) and quartz (SiO_2) (ICDD 82-0511) were detected. The quantitative chemical composition of the sample indicated 34.1±1.0% wt. Cu; 30.3±1.9% wt. Fe; 32.7±0.01% wt. S and 2.3±0.1% wt. Si. Accordingly, from the chemical and mineral analyses and theoretical compositions of chalcopyrite (*i.e.*, 34.6% wt. Cu; 30.4% wt. Fe; and 35.0% wt. S) and quartz (*i.e.*, 46.7% wt. Si; and 53.3% wt. O) (Weast and Selby, 1968), the composition of the sample used was estimated as 94% wt. $CuFeS_2$, 5% wt. SiO_2 and minor phases.

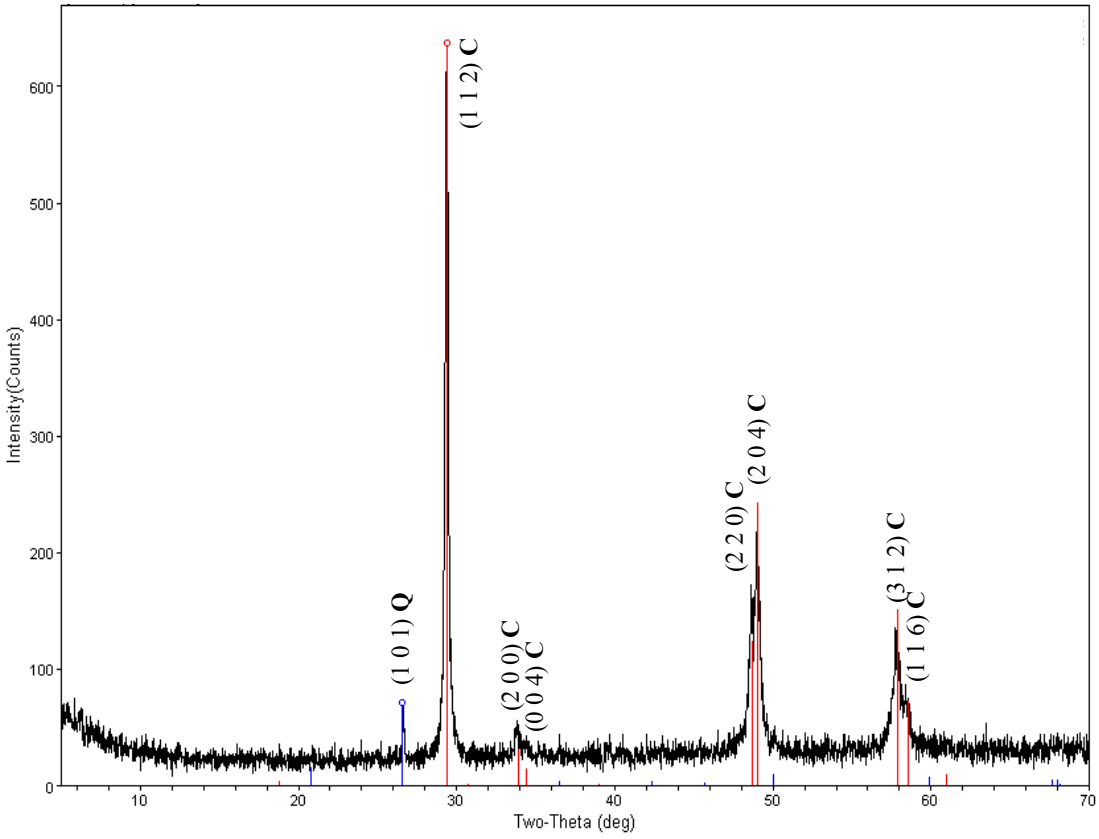

Figure 5.2. XRD patterns for the chalcopyrite sample and corresponding Miller indices. Legend: $CuFeS_2$ (C); and SiO_2 (Q).

5.4.2. S-TRXRD measurements: Flow method (FM)

Time-resolved XRD patterns for a 10 h experiment of high-purity chalcopyrite particles (d_{50} = 1.6 μm) under 0.1 H_2SO_4 mol.L^{-1} solution flow (about 0.05 mL.min^{-1}) at 25 °C is depicted in Fig. 5.3. A condition where soluble iron (*i.e.*, 0.1 mol.L^{-1}) was predominantly in the form of Fe^{3+} (*i.e.*, 0.0062 mol.L^{-1} Fe^{2+} + 0.0938 mol.L^{-1} Fe^{3+}), corresponding to 0.75 V *vs.* SHE, was selected. The z axis corresponds to the relative intensity (I) of the diffracted beam (in counts/s). It may be noticed that the time-resolved measurements, with time resolution of 2 min, revealed no product phase formation. It is well-established that the rate of chalcopyrite dissolution under atmospheric conditions is extremely slow. Therefore, the lack of reaction products, even after a period of 10 h, was ascribed to the slow leaching rate of the mineral sample used (*i.e.*, $CuFeS_2$ sample 94% wt. pure).

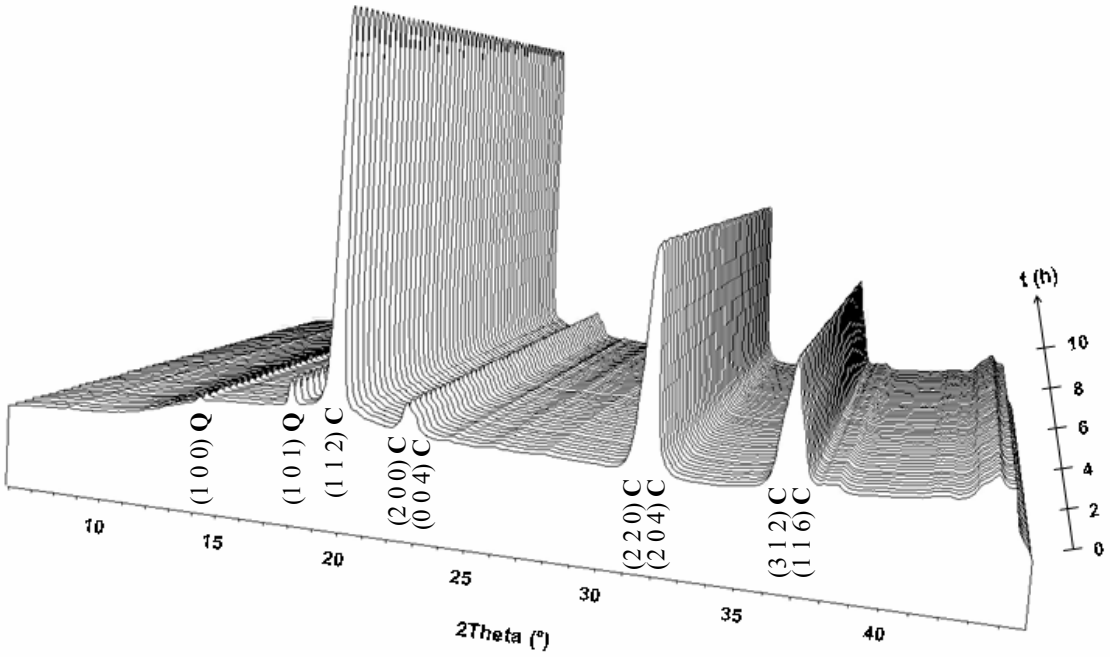

Figure 5.3. *In situ* S-TRXRD measurements of chalcopyrite under 0.1 mol.L^{-1} H_2SO_4 solution (0.75 V *vs.* SHE) flow. From 0 to 10 h the temperature was kept constant at 25 °C. Legend: Corresponding Miller indices of $CuFeS_2$ (C); and SiO_2 (Q).

From Fig. 5.3 it can be seen that the *in situ* XRD patterns indicated the same peaks detected in the original sample (vide Fig. 5.2): that is, peaks of tetragonal chalcopyrite (ICDD 83-0983) and hexagonal quartz (ICDD 82-0511). However, in Fig. 2 a diffracted beam at a 2θ angle of 14.2°, plane (1 0 0) of hexagonal SiO_2, can be detected, a peak which was not well resolved by the conventional measurement (Fig. 5.2). The more intense reflection in this plane was attributed to an improved signal-to-noise ratio achieved when high brilliant synchrotron radiation is applied. The background hump observed for these measurements was ascribed to X-ray scattering by the aqueous phase within the capillary cell combined with the scattering by the thin walls (0.01 mm) of the amorphous quartz capillary.

In order to investigate crystallographic changes in the solid phase, the relative intensities of the radiation beam diffracted by all atoms in a unit cell in a direction predicted by the Bragg's law and the corresponding values of the interplanar spacings (d_{hkl}) (*i.e.*, the distance between parallel planes of atoms, for a tetragonal crystal system) were evaluated with time. Fig. 5.4 shows the variation of the relative intensity of the quartz peak (plane (1 0 1) at 2θ angle of 17.9°) and strongest chalcopyrite peak (plane (1 1 2) at 2θ angle of 19.7°) as a function of time. For the SiO_2 phase (Fig. 5.4a), it may be noted a slight, continuous increase in the magnitude of the relative intensity of reflected beams in this particular plane. Conversely, for $CuFeS_2$ (Fig. 5.4b), it may be observed an increase until approximately 4 h measurement and from that time on, a slight decay was detected, a trend different from that registered for quartz after 4 h. On the other hand, an analysis of the XRD data did not reveal any shifting of the interplanar spacings of chalcopyrite and quartz with time, which would be related to a decrease in the volume of the corresponding unit cells. Quartz is inert under the investigated conditions and, thus, no structural change is expected for SiO_2. Conversely, if the drop of the magnitude of the chalcopyrite peak intensities at constant temperature (25 °C) was associated with the preferential removal of atoms from the crystal lattice (*e.g.*, iron) and, consequently, with formation of non-stoichiometric phases during dissolution, not only the relative intensities of the diffracted beams, but also the d_{hkl} spacings would have changed with time. Therefore, there is no evidence to support an alteration in the crystalline structure of chalcopyrite during dissolution under acidic, oxidizing solution flow for 10 h. The variation observed was

considered an artifact of the experimental cell, that is: a subtle dislocation of the mineral particles within the capillary as a result of the solution flow.

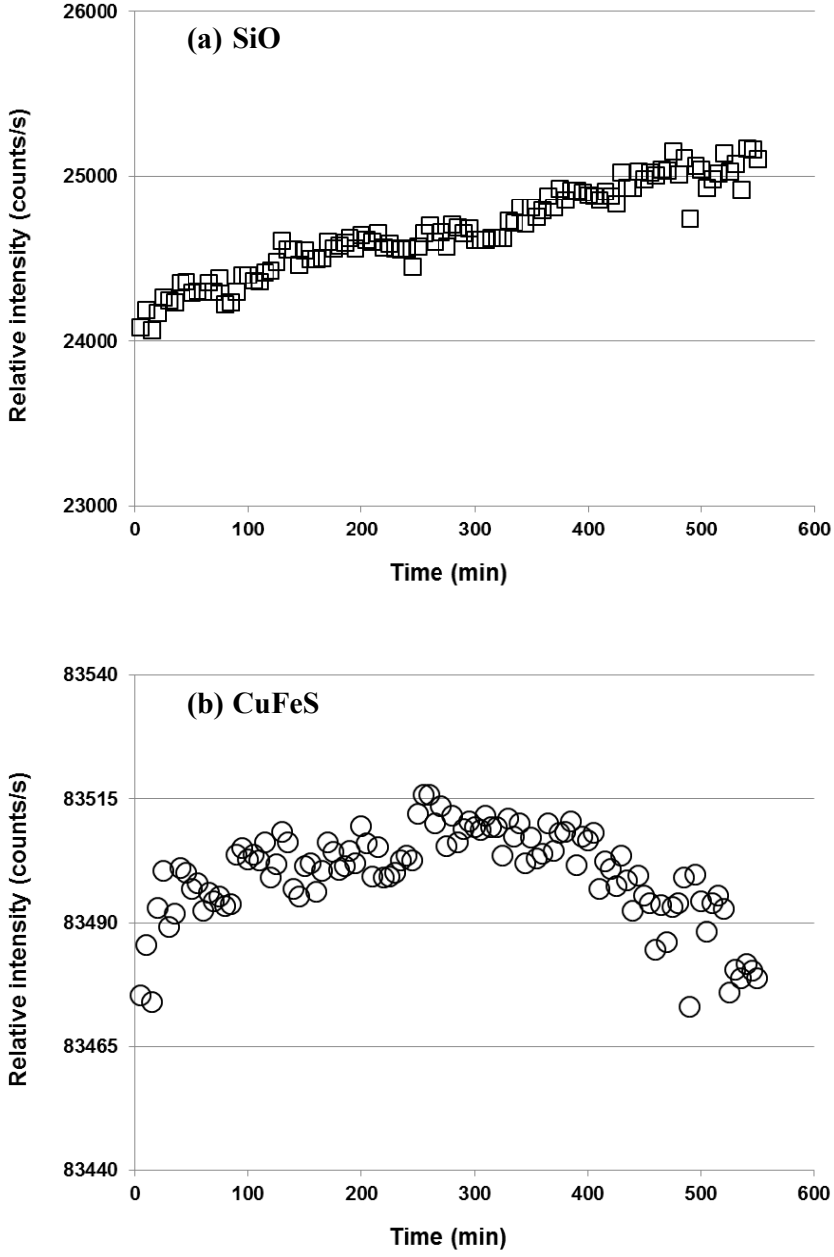

Figure 5.4. Variation of the relative intensity of the strongest (a) quartz XRD peak (plane (1 0 1) at 2θ angle of 17.9°) and (b) chalcopyrite XRD peak (plane (1 1 2) at 2θ angle of 19.7°), as a function of time.

It is relevant to comment that with the flow method (FM), the effects of packing (*i.e.*, density of particles within the capillary cell and amount of cotton wool used as plug) on the flow rate of solution was found to be significant. These effects have prevented the increase of flow rate. At pressures larger than about 10 psi and at temperatures above 100 °C, the flow-through reaction cell did not work. A combination of the thermal expansion of the quartz capillary, in spite of a low volumetric coefficient (*i.e.*, 1.7×10^{-6} °C^{-1}, 20-150 °C (Shackelford and Alexander, 2001)), with the higher pressures required by the packed sample led to the ejection of the sample from the capillary. Another parameter that should be taking into consideration when designing *in situ* measurements based on flow-through capillary cells is the particle size distribution of the mineral sample. The use of materials with a broad particle size distribution is expected to result in higher bed permeability, thereby allowing a better solution flow.

Aiming for a better understanding of chalcopyrite dissolution behavior (*i.e.*, the hindered dissolution process) under low-temperature conditions, which are appropriate for treating low-grade ores, future research will be extended to time-resolved XRD investigations at intermediate temperatures (below 80 ºC), using mineral samples with the typical compositions found in copper ores. It is known that the presence of other sulfide mineral phases in these ores, such as pyrite (FeS_2), enhances the dissolution rate of chalcopyrite by a galvanic effect (Majuste *et al*., 2012b).

5.4.3. S-TRXRD measurements: Non-flow method (NFM)

Given the above considerations, in order to evaluate the effect of higher temperature levels on chalcopyrite dissolution, thereby simulating conditions typically found in commercial leaching processes, a sealed capillary (non-flow method – NFM) was utilized. Time-resolved patterns of the chalcopyrite sample (d_{50} = 1.6 μm), after conditioning in 0.1 mol.L^{-1} H_2SO_4 solution at 0.75 V *vs.* SHE (*i.e.*, 0.0062 mol.L^{-1} Fe^{2+} + 0.0938 mol.L^{-1} Fe^{3+}) for 1 h, are exhibited in Fig. 5.5. The first patterns (*i.e.*, first XRD line) represent the measurement from the mineral sample at 25 °C. The diffraction patterns, with a time resolution of 2 min, for a 120 min reaction time (40 min in each temperature level: 100, 150, and 200 °C), reveal that a new product phase began to appear at 100 °C, as seen by

the reflections at 2θ angles of 21.3 and 21.9°. These reflections correspond to, respectively, the first and fourth most intense XRD peaks of hexagonal covellite (CuS) (ICDD 79-2321), crystallographic planes (1 0 3) and (0 0 6), respectively. The formation of CuS became apparent approximately 10 min after the start of the measurements and it can be further observed that during the temperature ramps there was an increase in the magnitude of the relative intensity of the CuS peaks, which could be related to a progressive growth of the product layer thickness.

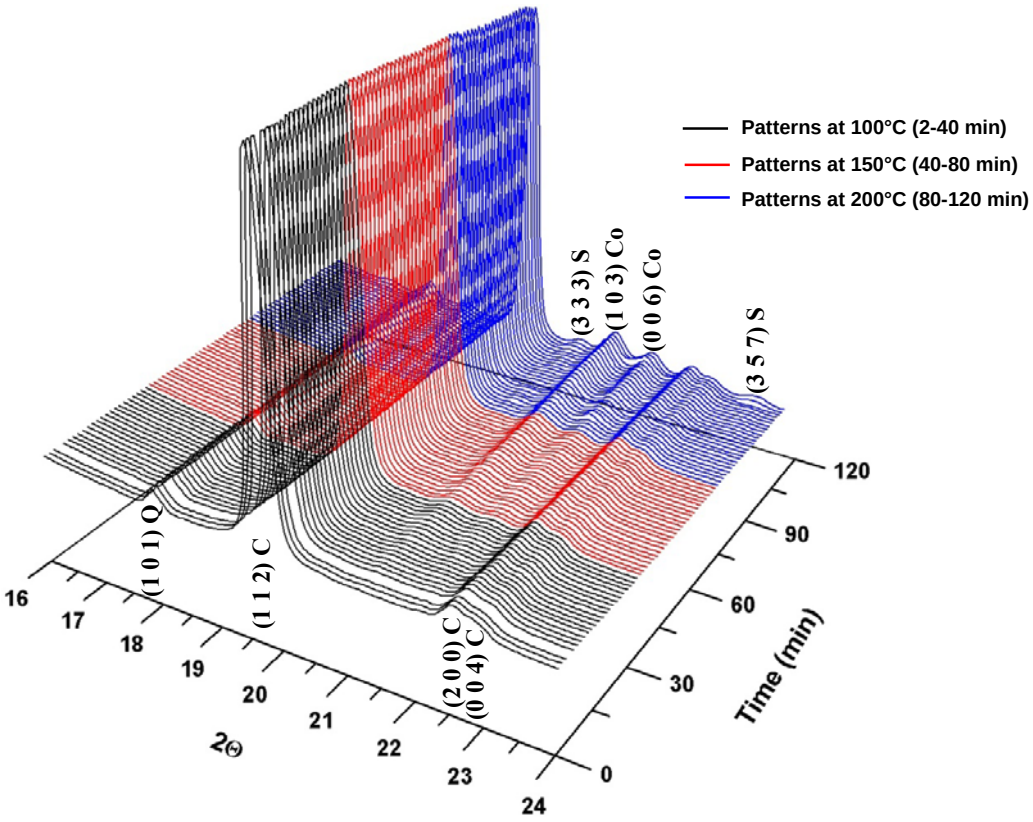

Figure 5.5. *In situ* S-TRXRD measurements of chalcopyrite sample conditioned in 0.1 mol.L^{-1} H_2SO_4 solution at 0.75 V *vs.* SHE. 2θ from 16 to 24°. Legend: Corresponding Miller indices of $CuFeS_2$ (C); SiO_2 (Q); CuS (Co); and S_8 (S).

The formation of bornite (Cu_5FeS_4), an intermediate iron-deficient sulfide detected on chalcopyrite after oxidation at 0.70 and 0.80 V *vs.* SHE, 25 °C (Majuste *et al.*, 2012a), and

of copper polysulfides, as suggested by Hackl *et al*. (1995), was not detected by the *in situ* time-resolved measurements at the temperature range 100-200 °C. This suggests that these intermediate phases are readily oxidized to covellite, but this assumption requires further investigation.

The S-TRXRD measurements also revealed a growth of amorphous humps at 2θ angle of 33.8° from 100 °C (Fig. 5.6a), and at 20.9 and 23.4° from 200 °C (Fig. 5.5). Such humps correspond to broad reflections for orthorhombic elemental sulfur (S_8) (ICDD 85-0799), crystallographic planes (0 4 4), (3 3 3), and (3 5 7), respectively. During the temperature ramps, the formation of amorphous elemental sulfur on chalcopyrite particles was observed after about 10 and 90 min of the start of the measurements. The amorphous character of the elemental sulfur detected in this investigation may be associated with the melting process of this mineral phase, which occurs at about 113 °C, for orthorhombic sulfur (Weast and Selby, 1968). As earlier discussed, it has been assumed that the chalcopyrite dissolution rate is affected by the formation of molten sulfur, which wets and agglomerates the mineral particles in leaching tanks (King *et al*., 1993; Hackl *et al*., 1995; McDonald and Muir, 2007a, 2007b).

The formation of elemental sulfur at the temperature range of 100-200 °C is likely the result of chalcopyrite oxidation by ferric ions (Eq. 5.2) – S_8 detected after about 10 min of the start of the measurements; and covellite oxidation by ferric ions (Eq. 5.3) – S_8 detected after about 90 min of the start of the measurements, as follows:

$$8\ CuFeS_2 + 16\ Fe^{3+} \rightarrow 8\ CuS + 24\ Fe^{2+} + S_8 \qquad (5.2)$$

$$8\ CuS + 16\ Fe^{3+} \rightarrow 8\ Cu^{2+} + 16\ Fe^{2+} + S_8 \qquad (5.3)$$

The S-TRXRD patterns at the temperature range of 100-200 °C also indicated a reflection at 2θ angle of 17.4°, from 100 °C, after about 10 min of the start of the measurement, whose relative intensity remained unchanged (Fig. 5.6b). According to the ICDD files, this reflection corresponds to the strongest XRD peak of (i) copper (II) sulfate hydrate ($CuSO_4.H_2O$), plane (2 0 0) (ICDD 12-0782), or (ii) iron (II) sulfate hydrate ($FeSO_4.H_2O$), plane (1 0 1) (ICDD 83-0078).

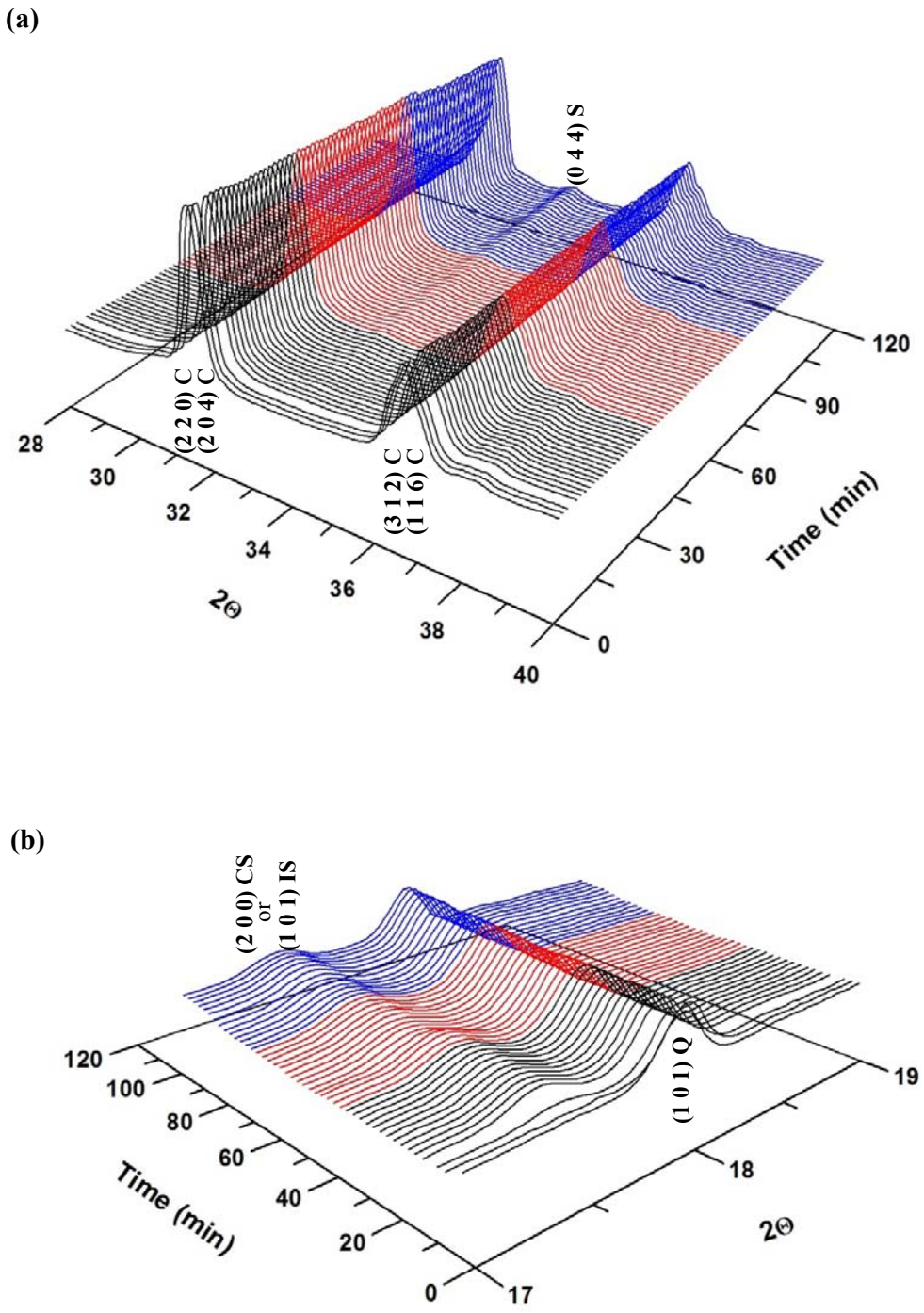

Figure 5.6. *In situ* S-TRXRD measurements of chalcopyrite sample conditioned in 0.1 mol.L^{-1} H_2SO_4 solution at 0.75 V *vs.* SHE: (a) 2θ from 28 to 40°; and (b) 2θ from 17 to 19°. Legend: Corresponding Miller indices of $CuFeS_2$ (C); SiO_2 (Q); S_8 (S); $CuSO_4.H_2O$ (CS); and $FeSO_4.H_2O$ (IS).

The precipitation of these metal sulfates on chalcopyrite (Eq. 5.4) at high temperatures, typical conditions of industrial leaching processes, had been earlier suggested (McDonald and Muir, 2007a, 2007b; Defreyne *et al*., 2008). High pressure leaching of chalcopyrite at 108 and 125-150 °C and analyses of residues by *ex situ* XRD indicated the precipitation of antlerite, $Cu_3(SO_4)(OH)_4$ at low acidity (about 0.05 mol.L^{-1} H_2SO_4 solutions) (McDonald and Muir, 2007a, 2007b). Taking into account the detection of S_8 in the present investigation, it is suggested that the favored formation of iron (II) sulfate proceeds according to the reaction stoichiometry represented by Eq. (5.5).

$$CuFeS_2 + 4\,Fe^{3+} + 6\,SO_4^{2-} \rightarrow CuSO_4 + 5\,FeSO_4 + 2\,S \qquad (5.4)$$

$$8\,CuFeS_2 + 32\,Fe^{3+} + 48\,SO_4^{2-} \rightarrow 8\,CuSO_4 + 40\,FeSO_4 + 2\,S_8 \qquad (5.5)$$

Therefore, the S-TRXRD measurements by the non-flow method illustrated the important effect of temperature on the dissolution rate of chalcopyrite. The mineral conversion was initiated readily from 100 °C with the formation of covellite, amorphous elemental sulfur and metal sulfates – approximately 10 min after the start of the measurements. The application of the *in situ* S-TRXRD technique permitted a further observation: The progressive growth of the product layer thickness, as indicated by an increase in the magnitude of the relative intensity of the CuS and S_8 peaks during the reaction.

A possible drawback of the non-flow method, which certainly affected the formation and growth rate of product layers on $CuFeS_2$, is the gradual reduction of the concentration of oxidant (Fe^{3+}) available within the capillary cell during the measurement. This factor may hinder a full analysis of the transformation rates of the mineral to the intermediate- and end-product phases, thereby limiting the applicability of the *in situ* S-TRXRD technique to investigate chalcopyrite dissolution under high-temperature conditions using sealed capillaries (*i.e.*, non-flow method). The use of pressure reaction cells, as those described in the works of Cahill *et al*. (2000), Loan *et al*. (2005), Murray *et al*. (2009) and Webster *et al*. (2009), may represent the correct method.

5.5. Conclusions

This chapter presented a review of previous applications of the *in situ* synchrotron XRD technique to solid transformations in aqueous media, with emphasis on mineral systems relevant to hydrometallurgy. Publications on gibbsite crystallization and goethite-hematite transformation under Bayer process conditions were presented and discussed. In the case of dissolution reactions – the focus of this review – considered were the following: (a) nickel laterite ores in acidic sulfate media under high-temperature conditions; (b) bornite and chalcocite in acidic, oxidizing solutions; and (c) pyrite in alkaline media containing chloride and carbonate ions. Taken together, these works demonstrate that by varying experimental parameters and configuration (*e.g.*, beam features, reaction cell design, and type of detector) important information hitherto inaccessible could be extracted, including crystallographic changes, plus rates and dissolution mechanisms under controlled conditions. The work on bornite dissolution in acidic, oxidizing solutions under low-temperature conditions, demonstrated bornite transition from stoichiometric to non-stoichiometric phases and a decreasing copper extraction rate. For chalcocite, conversion to covellite and possible formation of transient copper sulfides during reaction were demonstrated. In the case of pyrite electrooxidation in alkaline solutions containing chloride and carbonate ions, the formation of crystalline and amorphous product phases was detected. Although only a few publications are currently available on application of *in situ* synchrotron XRD to sulfides and oxides dissolution, it is evident that these techniques may be used to significantly improve our current knowledge on key dissolution processes, under conditions typically found in practical hydrometallurgical systems.

In this connection, the first (to our knowledge) *in situ* synchrotron XRD measurements were undertaken for chalcopyrite dissolution at low and high temperatures. *In situ* S-TRXRD measurements by the flow method (FM) illustrated the slow dissolution kinetics of chalcopyrite in acidic and oxidizing solutions under atmospheric conditions. For such conditions, there was no experimental evidence to support a modification in the mineral crystal structure during the 10 h timescale used. On the other hand, the time-resolved measurements by the non-flow method (NFM) made a contribution on the rates by which product phases such as covellite, elemental sulfur, and metal sulfates evolve from chalcopyrite at temperatures above 100 °C. Our results demonstrated that the mineral

conversion to such product phases initiated about 10 min after the start of measurements. Our results also suggested that the formation of molten elemental sulfur is possibly related to two processes: the initial oxidation of chalcopyrite by ferric ions followed by the oxidation of covellite by the same oxidant.

Chapter 6 – Final considerations

6.1. Main contributions

The findings of this thesis support the hypotheses that the formation of metal-deficient sulfides is correlated to the slow dissolution rate of chalcopyrite. Metal-deficient sulfides were identified on chalcopyrite electrodes oxidized under potentials of the anodic prewave region (*i.e.*, potentials lower than the critical potential value of chalcopyrite, which ranges from 0.75 to 0.90 V *vs.* SHE) by Raman spectroscopy and *ex situ* synchrotron small angle X-ray diffraction (S-SAXRD). The results showed that chalcopyrite dissolution involves the formation of an intermediate bornite (Cu_5FeS_4) layer – phase detected for the first time on oxidized chalcopyrite, and an unidentified metal-deficient sulfide. These products caused a diminution of chalcopyrite oxidation rate, respectively, at 0.70-0.80 and 0.60 V *vs.* SHE.

Covellite (CuS) and elemental sulfur (S_8) layers were detected on oxidized chalcopyrite electrodes at 0.80 and 0.80-1.00 V *vs.* SHE. While the formation of CuS was observed in a hindered dissolution condition as well, there is no evidence to correlate the formation of elemental sulfur, exclusively, to the diminution of the chalcopyrite dissolution rate. An elemental sulfur layer was detected in a potential condition (1.00 V vs. SHE) where the oxidation rate increases with time.

The dissolution of chalcopyrite was also examined by means of synchrotron time-resolved X-ray diffraction (S-TRXRD). Its purpose was to evaluate structural changes and the rates of formation of crystalline and amorphous product phases on chalcopyrite in acidic and oxidizing solutions under atmospheric conditions and at temperatures typically found in commercial leaching processes. Time-resolved measurements were carried out in capillary-based cells containing fine chalcopyrite particles by using two experimental approaches – flow (FM) and non-flow (NFM) methods – according to the temperature condition. The initial measurements by the NFM confirmed the well-established effect of temperature on the dissolution rate of chalcopyrite. The mineral conversion initiated readily from 100 °C. The measurements also made an initial contribution on the rates by which products such as covellite (CuS), elemental sulfur (S_8), and metal sulfates (cupric or ferrous sulfates) grows

up on chalcopyrite particles at the temperature range 100-200 °C. Our results indicated that the formation of molten elemental sulfur is possibly related to the oxidation of chalcopyrite and oxidation of covellite by ferric ions. The measurements by the FM, a method still in developmental stage, illustrated the slow dissolution kinetics of chalcopyrite under acidic, oxidizing solution flow, atmospheric conditions (25 °C). There was no evidence to support a modification in the mineral structure during the timescale selected here: that is, 10 h.

As mentioned, pyrite is a mineral phase often found in copper sulfide ores. The galvanic effect of this iron sulfide on key properties of chalcopyrite, such as the mixed potential and dissolution current density, was evaluated under low-temperature leaching conditions, in the presence of ferric ion and dissolved oxygen, with a method that better represents the association in the ore. By investigating pyrite micro-crystallites naturally associated with chalcopyrite ore, the electrical contact between these sulfides was optimized, allowing a more accurate assessment of the magnitude of the galvanic current. The results of such investigation indicated the positive effect of combining ferric ion and dissolved oxygen on the oxidation rate of chalcopyrite, and such effect is magnified by the interaction with pyrite, especially under less oxidizing conditions. The galvanic effect of pyrite on the rate of oxidation of this important sulfide was discussed by the new insights on the kinetics of the half-cell reactions that occurrs in the pyrite-chalcopyrite coupling.

In summary, the main contributions of the present thesis are methods and experimental evidences to advance in the understanding of chalcopyrite dissolution in aqueous solutions. The findings allowed a sound discussion of the current hypotheses found in the literature such as: (i) formation of intermediate metal-deficient product phases on chalcopyrite and its correlation with the hindered dissolution process; (ii) evidences of no contribution of elemental sulfur to the hindered dissolution phenomena; and (iii) quantification of the galvanic effect of pyrite on the dissolution of chalcopyrite.

6.2. Suggestions to future investigations

A number of relevant possibilities for investigations have arisen from the results found in the present thesis and are listed as follows:

(i) Expand the investigation of the nature of the product phases that are formed on oxidized chalcopyrite electrodes by combining techniques such as chronoamperometry and *ex situ* synchrotron small angle X-ray diffraction (S-SAXRD), respectively. The main purpose of this study would be to analyze multiple points on the oxidized electrodes. In this thesis, the radiation beam was focused only on the center of the electrode surface.

(ii) Investigation of the predominant crystallographic orientations and electric potentials on chalcopyrite electrodes with the help of techniques such as electron backscatter diffraction (EBSD) and atomic force microscopy (AFM). The aim of this investigation would be to identify preferential sites of oxidation, since a slight difference regarding the oxidation rate of different electrode samples was observed in the present thesis. In addition, by means of a crystal orientation mapping of chalcopyrite electrodes and electrochemical measurements by using chronoamperometry, at varied potentials and reaction times, a correlation between crystal orientation and oxidation rate would be established.

(iii) Investigation of structural changes of chalcopyrite during dissolution and identification of the intermediate and end products formed under acidic, oxidizing solution flow, at intermediate temperature values, by *in situ* synchrotron time-resolved X-ray diffraction (S-TRXRD). The aim of this study would be to establish the rate of conversion of chalcopyrite under atmospheric conditions and at temperatures suitable for treating low-grade ores.

(iv) Investigation of the rate and dissolution mechanisms of bornite and covellite in the absence and presence of catalysts such as pyrite. The main objective of this investigation would be a better understanding on the oxidative processes of these phases, taking into account their formation and adverse effect on the rate of chalcopyrite dissolution.

Appendice A – Characterization of chalcopyrite electrodes by means of Raman spectroscopy prior to electrochemical measurements

Abstract

This appendice discusses the importance of a preliminary, detailed analysis of chalcopyrite electrodes as a procedure for selecting the best samples to be used in the electrochemical measurements. The chalcopyrite electrodes were analyzed by means of scanning electron microscopy (SEM) with energy dispersive spectrometry (EDS) and Raman spectroscopy (RS). This last technique was employed in order to identify and discriminate the impurity phases (inclusions) present on the electrodes. Results obtained by SEM/EDS showed the presence of cavities, defects and fissures, as well as high content of impurities. RS, coupled with EDS microanalysis, allowed to identify the mineral phases on the analyzed samples. The occurrence of wurtzite (ZnS), pyrite (FeS_2), quartz (SiO_2), diopside ($CaMgSi_2O_6$), and a non-stoichiometric lead-bismuth sulfide was confirmed. It was discussed that naturally associated sulfide inclusions, such as ZnS and FeS_2, can establish galvanic couples with chalcopyrite, altering the electrochemical behavior of the copper sulfide. These possible interactions may affect both the rate and mineral oxidation mechanism, altering directly the results and conclusions obtained in the electrochemical investigations. Therefore, it was proposed that inconsistencies observed in the literature regarding the magnitude of the anodic current density, critical potential, steady-state current and fundamental properties such as the mixed potential, could be minimized by performing a preliminary, detailed analysis of the electrode prior to the electrochemical measurements.

Key-words: Raman spectroscopy; chalcopyrite electrodes; characterization.

A.1. Introduction

The electrochemical techniques, such as linear sweep voltammetry, cyclic voltammetry and chronoamperometry, have been extensively applied to investigate the dissolution behavior of chalcopyrite electrodes in acidic media, under atmospheric conditions (Jones and Peters, 1976; Biegler and Swift, 1979; Parker *et al*., 1981; Warren *et al*., 1982; Biegler and Horne, 1985; Price and Warren, 1986; Yin *et al*., 1995; Lu *et al*., 2000b; Arce and González, 2002; Elsherief, 2002; Lázaro and Nicol, 2003, 2006; Mikhlin *et al*., 2004; Nava and González, 2006; Viramontes-Gamboa *et al*., 2007; Hiroyoshi *et al*., 2004, 2008; Nava *et al*., 2008; Parker *et al*., 2008; Ghahremaninezhad *et al*., 2010; Sequeira and Santos, 2010). In spite of this noteworthy number of studies, many inconsistencies might be noticed in the literature regarding the potential region where the active and passive dissolution behaviors prevail, magnitude of the anodic current density measured for the working (chalcopyrite) electrodes, and electrochemical properties such as the mixed potential.

These inconsistencies are possibly associated with the experimental conditions of each one of the investigation as the acidity, temperature, potential range and scan rate selected; and also the nature of the mineral sample used for constructing the electrodes. The reactivity of chalcopyrite under potentiostatic control is affected not only by the type and content of impurities on the electrode reaction area, which is essentially related to the source of the mineral sample, but also by their polycrystalline character, which results in distinct crystal orientation (*i.e.*, different crystallographic planes exposed to the oxidizing media).

Warren *et al*. (1982), *e.g.*, investigated the anodic behavior of chalcopyrite samples from different sources in acidic sulfate media, under atmospheric conditions. Within the same origin, each mineral sample produced an anodic curve slightly different from the other ones. In contrast, samples from different sources showed large differences regarding the magnitude of the anodic current, mainly in the passive region. By using SEM and time-of-flight secondary ion mass spectrometry (TOF-SIMS), Al-Harahsheh *et al*. (2006) observed preferential oxidation of chalcopyrite planes. Data obtained in ferric sulfate solutions at 90°C suggests the preferential attack at particular fracture planes of the same chalcopyrite sample. The fracture planes were not characterized in that investigation.

Table A.1 indicates mixed potential values for chalcopyrite. As already discussed in this thesis, the mixed potential (E_M), that is, the potential exhibited by the electrode surface in the absence of externally applied potential, is given by the kinetics of all contributing half-cell reactions taking place on the electrode area (Bockris and Reddy, 1998; Brett and Brett, 1998). It can be seen that mixed potentials from 0.40 to 0.60 V *vs.* the Standard Hydrogen Electrode (SHE) are generally measured for chalcopyrite in acidic sulfate solutions. On the basis of the results obtained by Warren *et al*. (1979), it is possible to observe the effect of acidity on the potential measured on the chalcopyrite reaction area. By assessing the results obtained by Price and Warren (1986) and Hiroyoshi *et al*. (2004), it should be observed the effect of aqueous ions on the potential. The recognized effect of nitrogen (N_2) bubbling and the possible effect of the nature of the mineral sample (*i.e.*, elemental stoichiometry and exposed crystallographic planes) may be observed by comparing the results obtained by Biegler and Swift (1979) and Mehta and Murr (1983). The effect of the temperature conditions, in turn, possibly associated with the nature of the chalcopyrite sample, may be evaluated according to the values measured by Warren *et al*. (1982) and Lázaro and Nicol (2003).

Table A.1. Mixed potential of chalcopyrite in sulfate media under atmospheric conditions.

Reference	**Experimental conditions**	**E_M (V *vs.* SHE)**
Biegler and Swift, 1979	ME; 1.0 mol/L H_2SO_4; 25°C; N_2	0.40
Warren *et al*., 1982	ME; 0.01-1.0 mol/L H_2SO_4; 25°C	0.45-0.55
Mehta and Murr, 1983	ME; 1.0 mol/L H_2SO_4; 25°C	0.52
Price and Warren, 1986	ME; 1.0 mol/L H_2SO_4; 25°C 0.001 mol/L Ag^+	0.60
Arce and González, 2002	CPE; 2.0 mol/L H_2SO_4; 25°C; N_2	0.44
Elsherief, 2002	CPE; 1.0 mol/L H_2SO_4; 20°C	0.44
Lázaro and Nicol, 2003	ME; 0.1 mol/L H_2SO_4; 60°C	0.41
Hiroyoshi *et al*., 2004	ME; 0.1 mol/L H_2SO_4; 25°C; N_2 0-0.1 mol/L Fe^{2+} or Cu^{2+}	0.47-0.53
Lázaro and Nicol, 2006	RRDE; 0.1 mol/L H_2SO_4; 60°C; N_2	0.41
Nava and González, 2006	CPE; 1.7 mol/L H_2SO_4; 25°C; N_2	0.42

Legend: massive electrode = ME; rotating ring-disk electrode = RRDE; carbon paste electrode = CPE.

At the mixed potential, the anodic and cathodic current densities are equal and of opposite sign (Bockris and Reddy, 1998; Brett and Brett, 1998). In electrochemical experiments, the reaction area of the working electrode (*i.e.*, the chalcopyrite electrode) is a very important parameter, since the electric current density depends strongly on this value, as expressed by (Eq. A.1), where i represents the electric current density, I the electric current intensity (*i.e.*, the amount of charge flowing per unit time), and A the surface area through which current flows.

$$i = I / A \qquad (A.1)$$

The presence of impurities on the reaction area of chalcopyrite electrodes may modify its reactivity as a result of the increase or reduction of the number of sites available for the anodic and cathodic reactions. The formation of galvanic couple among sulfides, such as chalcopyrite ($CuFeS_2$), pyrite (FeS_2), sphalerite (ZnS), galena (PbS) and acanthite (Ag_2S), affects significantly the electrochemical behavior of the mineral under investigation (Mehta and Murr, 1983; Nowak *et al*., 1984; Holmes and Crundwell, 1995; Cruz *et al*., 2005; Urbano *et al*., 2007; You *et al*., 2007). As already discussed in Chapter 3, the galvanic interaction may be understood by the anodic and cathodic half-cell reactions that occur at the surface of each mineral. This interaction enhances the dissolution rate of one or both of the mineral phases that are in intimate contact, depending on the mixed potential values. The mineral with the higher mixed potential acts as the cathode of the galvanic cell and will be protected, whereas the mineral with the lower mixed potential acts as the anode and, therefore, its dissolution will be favored.

In this context, this investigation proposes that some of the inconsistencies observed in the literature for the electrochemical behavior of chalcopyrite electrodes could be minimized by performing a detailed analysis of the electrode reaction area. A preliminary observation of the chalcopyrite electrodes would be essential for selecting the samples to be used in the electrochemical measurements, that is, application of only those with the lowest impurity content on the reaction area. Assuming that the application of impurity-free natural mineral electrodes is improbable, the identification of impurities on the electrodes would be vital to minimize misinterpretations on the electrochemical behavior and properties. In the present investigation, Raman spectroscopy (RS) and scanning electron microscopy (SEM) coupled

with energy dispersive spectrometry (EDS) were used to characterize the impurity phases existing on chalcopyrite electrodes. RS is a suitable technique for identifying impurities, because it allows a precise detection of the usual constituents of mineral samples, such as sulfides, silicates, oxides, etc., and also it permits punctual analysis on the sample, even in micrometric grains (Ferraro *et al*., 2003).

A.2. Experimental

A.2.1. Chalcopyrite samples

The chalcopyrite samples used in this investigation were purchased from Ward's Natural Science, N.Y. The preparation of the mineral samples involved the following procedures. Firstly, the massive samples were cut using a diamond wafering blade (Buehler®, n.11-4246), thus obtaining regular mineral specimens (1.0 cm^2 of exposed area and about 0.5 cm thick), which were rinsed with double-distilled water and then dried with analytical grade acetone 100% (Synth®). These specimens were, then, mounted in Epoxy resin (Epofix®, Struers). Prior to each analysis, a fresh electrode surface was prepared by wet mechanical polishing with fine SiC papers (grit sizes 1200 and 2400). The surface was further polished with alumina paste (1.0 μm), rinsed with double-distilled water in an ultrasonic bath for 15 min, dried with analytical grade ethyl alcohol 95% (Synth®) and, then, kept under vacuum at room temperature. It should be noted that the electrical contact between the specimens and a conductor wire (*e.g.*, copper) was not carried out in this investigation, since the samples prepared here were only submitted to analysis; no electrochemical measurement was carried out. The whole experimental procedure of electrode preparation was discussed in Chapter 3.

A.2.2. Characterization of the chalcopyrite samples

Initially, the quantitative chemical composition of the chalcopyrite sample was obtained by the following procedure. Firstly, three mineral samples were digested in a hot plate at 150°C (±5°C sensitivity), for 5 h, with aqua regia (3 HCl : 1 HNO_3) (analytical grades HCl

37% and HNO_3 65%) (FMaia®). Next, the digestion solution was vacuum filtered, properly diluted and the concentration of seven metallic elements (Cu, Fe, Zn, Al, Ca, Mg, and Mn) was analyzed by means of atomic absorption spectrophotometry (AAS), using a Perkin Elmer Spectrophotometer (AAnalyst 300). The residual solid was then roasted in a furnace at 1000°C (±25°C sensitivity), for 1 h, in a platinum crucible. The residue was digested in a hot plate at 150°C, for 1 h, with analytical grade hydrofluoric acid (HF) 40% (FMaia®). The Si (silicon) content was determined by weight difference, using an analytical balance. The concentration of the metallic elements was analyzed in this second solution as well. Finally, the elemental sulfur (S) content was obtained using a LECO® (SC 632) induction furnace.

The chalcopyrite electrodes were analyzed by means of scanning electron microscopy (SEM) coupled with energy dispersive spectrometry (EDS), using a JEOL (JSM 6360LV) Microscope and a Thermo Noran (Quest) Spectrometer. The analysis was conducted aimed at detecting the presence of impurities grains on the mineral, on the basis of their aspect and semi-quantitative elemental composition. The electrodes were also analyzed by means of Raman spectroscopy (RS), using a Horiba Jobin Yvon (Labram HR800) Spectrograph equipped with a 633 nm He-Ne laser (20 mW power). The Raman signal was collected by an Olympus (BHX) Microscope, equipped with lenses of 10, 50 and 100X. The spectral resolution was approximately 2 cm^{-1} and a minimum of 10 scans (integration time 60 s) were recorded. The grating angle was calibrated using the 520 cm^{-1} Si Raman band. The Raman spectra were obtained immediately after sample preparation.

A.3. Results and discussion

A.3.1. Quantitative chemical composition of the mineral sample

Before discussing results obtained by SEM/EDS and RS, the quantitative chemical analysis of a possible chalcopyrite sample to be used for constructing the electrodes is shown in Table A.2. It should be noticed that Zn and Si represent the main impurities of the mineral sample. From the Cu (28.6% wt.), Fe (26.9% wt.), and S (33.3% wt.) content, and the theoretical composition of chalcopyrite (*i.e.*, 34.6% wt. Cu, 30.4% wt. Fe and 35.0% wt. S)

(Weast and Selby, 1968), the purity of the analyzed sample was estimated as about 84% wt. $CuFeS_2$. Therefore, the sample characterized in the present investigation, labeled as hand specimen (Wards®, 46V0069), was considered unsuitable for the main investigations proposed in this thesis. Thus, another chalcopyrite sample, labeled as bulk pack (Wards®, 46V0068), with higher purity, was used for constructing the electrodes. Its characterization was presented in Chapter 3.

Table A.2. Quantitative chemical composition (% wt.) of the chalcopyrite sample.

Fe	Cu	S	Zn	Ca	Mg	Al	Mn	Si
26.9±1.3	28.6±1.7	33.3±2.1	2.0±0.2	0.7±0.1	0.3±0.03	0.1±0.02	0.1±0.02	1.8±0.1

A.3.2. Analysis of mineral samples by SEM/EDS

Fig. A.1 shows typical micrographs of chalcopyrite samples (hand specimen) containing a high content of impurities on the reaction area. It should be noticed the homogeneity of the surface areas, although the presence of fissures and cavities are visualized. These fissures are possibly related to the geological formation of the sample, which were exposed during the cutting and polishing stages. The cavities may have been formed during the mechanical preparation of the sample. Impurity phases of different sizes, shapes, and colors can be visualized. The dark points represent naturally associated impurities or, then, cavities, as may be evidenced in Fig. A.1c. The massive dark points, which represent impurity phases, were analyzed semi-quantitatively by EDS, as will be discussed later.

In the micrograph represented in Fig. A.2, three areas were selected in the sample and the corresponding elemental semi-quantitative composition was determined by means of EDS (Table A.3). Analyses indicated that area 1 is constituted mainly by Zn (60.5% wt), and S (32.7% wt.), while area 2 is formed mostly by S (50.2% wt.), and Fe (42.4% wt.). Area 3, which represents the sample matrix, is constituted mainly by S (34.3% wt.), Cu (32.3% wt.), and Fe (28.1% wt.).

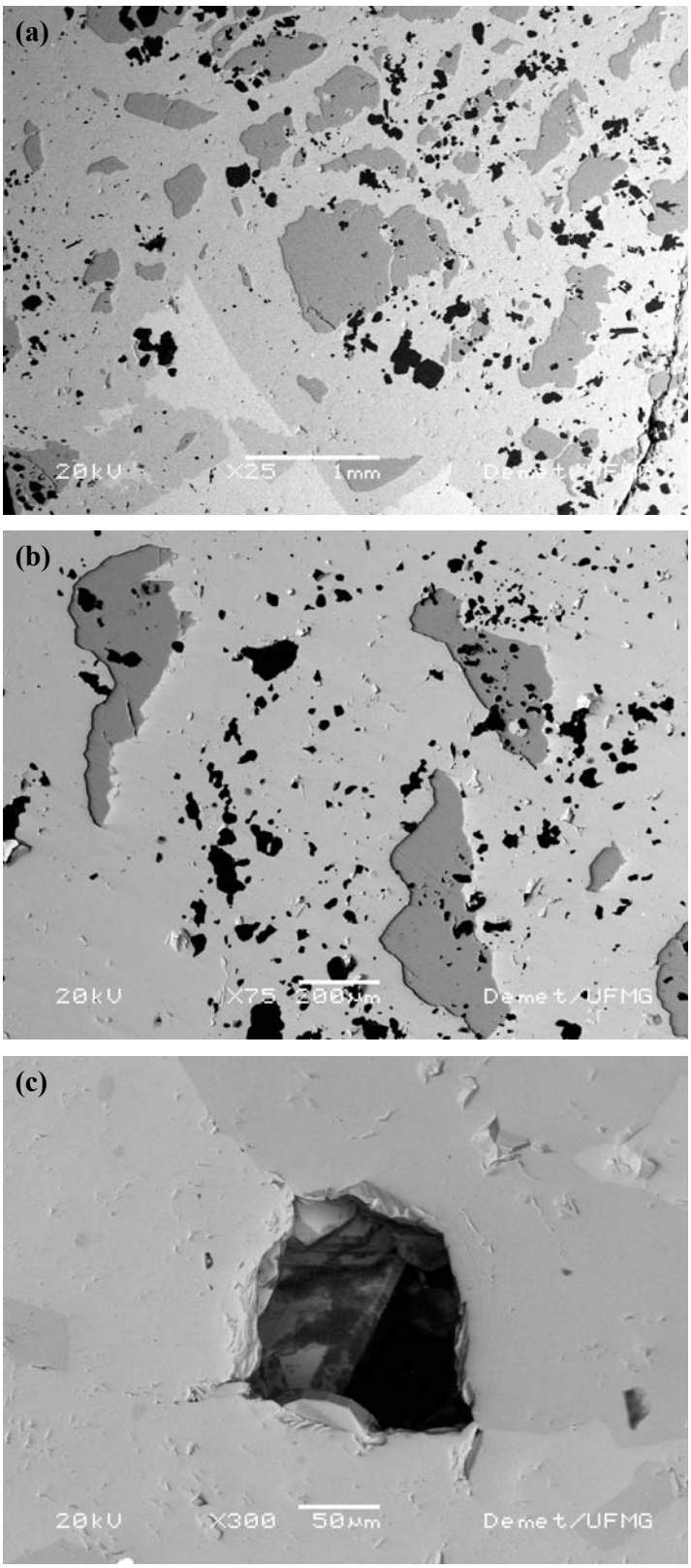

Figure A.1. Back-scattered electron micrographs of typical chalcopyrite samples. Magnification: (a) 25x; (b) 75x; and (c) 300x.

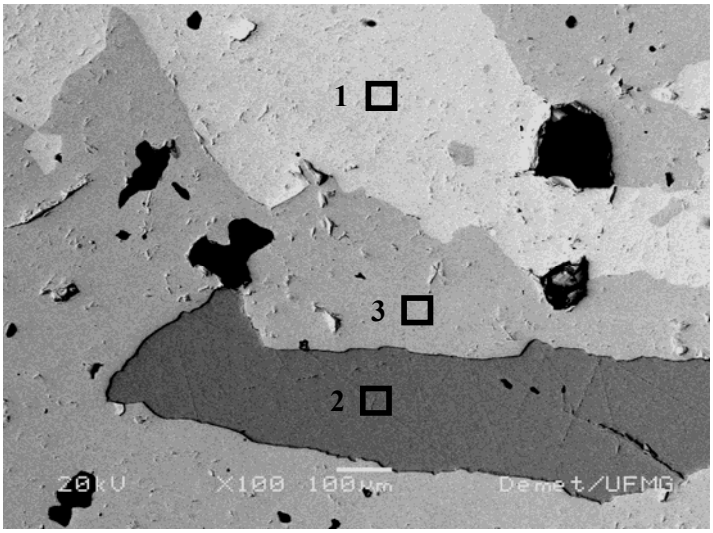

Figure A.2. Back-scattered electron micrograph of chalcopyrite sample. Magnification: 100x.

Table A.3. Selected areas analyzed by EDS (vide Fig. A.2 and A.3): Elemental semi-quantitative composition (% wt.).

Area	Fe	Cu	S	O	Zn	Ca	Mg	Si	Pb	Bi
1	1.2	0.3	32.7	4.4	60.5	0.4	0.1	0.2	-	-
2	42.4	0.3	50.2	5.4	0.3	0.3	0.3	0.5	-	-
3	28.1	32.3	34.3	3.7	0.3	0.3	0.3	0.4	-	-
4	1.6	1.3	1.2	51.9	0.8	0.3	0.2	42.5	-	-
5	1.6	0.6	0.6	28.4	0.5	22.7	10.8	33.1	-	-
6	0.7	0.9	13.8	2.2	0.2	0.2	0.3	0.3	43.1	39.1

The detection of oxygen (O) in areas 1, 2 and 3, as can be seen in Table A.3, is possibly associated with a slight atmospheric oxidation of the electrode surface. The atmospheric oxidation of chalcopyrite was earlier discussed by others (Yin *et al.*, 1995; Todd *et al.*, 2003; Goh *et al.*, 2006).

Fig. A.3 shows another micrograph of the chalcopyrite sample. Three areas were selected as well and then analyzed by EDS (Table A.3). Analyses pointed out that area 4 is formed

mostly by O (51.9% wt.), and Si (42.5% wt.), while area 5 is constituted mainly by Si (33.1% wt.), O (28.4% wt.), Ca (22.7% wt.), and Mg (10.8% wt.). The impurity phase represented by area 5 showed to be abundant in the analyzed sample, mostly as minute grains. Similar impurities to that, but containing a higher Fe content or a higher Ca content and a lower Mg content were detected. Finally, analyses indicated that area 6, scarce in the analyzed sample, is formed mostly by Pb (43.1% wt.), Bi (39.1% wt.), and S (13.8% wt.).

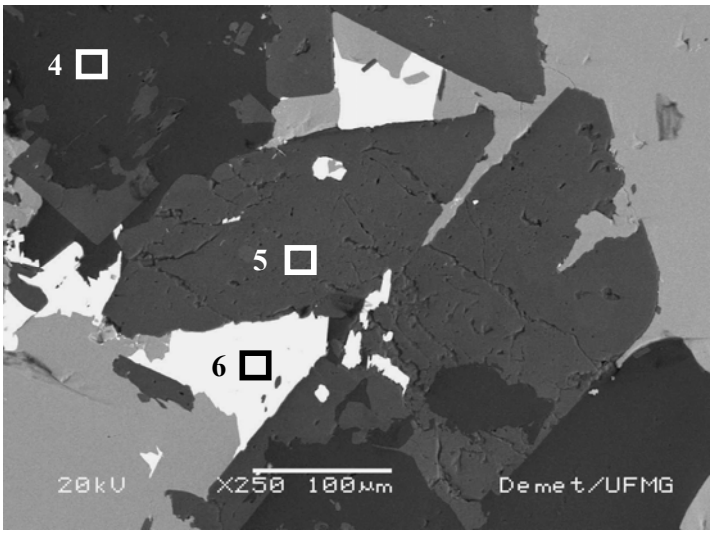

Figure A.3. Back-scattered electron micrograph of chalcopyrite sample. Magnification: 250x.

The preliminary analysis of the chalcopyrite surface by using SEM/EDS, which confirmed the presence of many impurities on the reaction area, showed to be an important criterion for selecting the samples to be used in the electrochemical measurements.

A.3.3. Analysis of mineral samples by Raman spectroscopy

With the aim of identify the impurity phases, the same areas analyzed by SEM/EDS were analyzed by Raman spectroscopy. Fig. A.4 shows the spectra obtained for areas 1, 2 and 3. The spectrum obtained for area 1 indicates more intense bands at 300, 312, 332 and 350 cm^{-1}, band of intermediate intensity at 217 cm^{-1}, and additional bands of lower intensity.

The more intense Raman band at 350 cm^{-1} is characteristic for wurtzite and sphalerite, zinc sulfides with hexagonal and cubic crystalline structure, respectively (Mernagh and Trudu, 1993). However, the spectrum obtained in this investigation is similar to that exhibited by wurtzite with a low Fe content (RRUFF, 2010). Thus, according to the Raman spectrum and also EDS results, area 1 possibly represents wurtzite. Regarding the spectrum obtained for area 2, it shows intense bands at 353 and 387 cm^{-1}, and additional band of lower intensity at 445 cm^{-1}. This spectrum is similar to that reported for pyrite, iron sulfide with cubic crystalline structure (Mernagh and Trudu, 1993; RRUFF, 2010). Mernagh and Trudu (1993) also exhibited a spectrum with intense bands at 342 and 377 cm^{-1}, and band of lower intensity at 428 cm^{-1}, therefore, different from the expected for cubic pyrite. Such spectrum was ascribed to iron sulfide with pseudo-cubic crystalline structure. Comparable spectrum to that was not observed in this investigation. In relation to the Raman bands depicted for area 3, it indicates a more intense band at 294 cm^{-1}, and additional bands of lower intensity at 268, 322, 356 and 378 cm^{-1}. These are diagnostic bands of chalcopyrite, copper iron sulfide with tetragonal crystalline structure (Mernagh and Trudu, 1993; Parker *et al*., 2008; RRUFF, 2010).

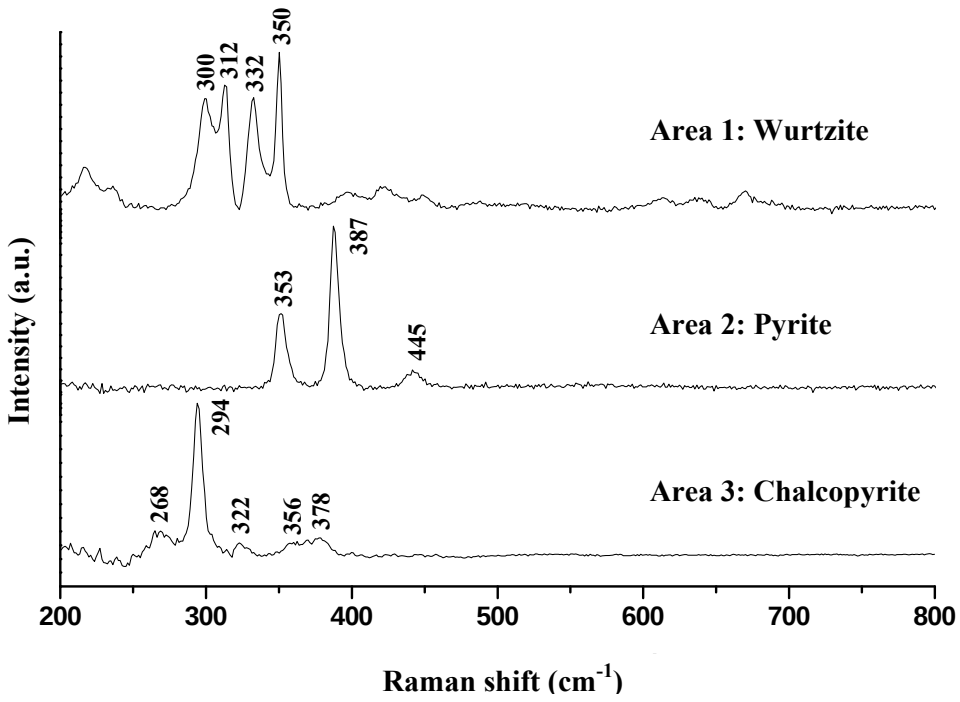

Figure A.4. Raman spectra obtained for areas 1, 2 and 3 (vide Fig. A.2).

Slight differences in intensity, broadness and position of the Raman bands reported in this thesis in relation to spectra discussed in the literature may be related to possible deviation in the elemental stoichiometric ratio and conditions of measurement (Ferraro *et al*., 2003). However, an additional aspect observed in this study concerns the effect of the mechanical preparation of the electrode samples (*i.e.*, cutting and polishing) on the broadness/position of some bands. Raman analyses of chalcopyrite samples from the same source indicated significant differences among spectra obtained for polished electrodes and for unpolished samples (*i.e.*, particles). From Fig. A.5 it is possible to observe that for the chalcopyrite particle more defined bands were obtained, but the positions of these bands are similar to those obtained for the polished samples, within an experimental error. Thus, differences among spectra obtained for polished electrodes and unpolished samples revealed subtle structural changes, which may be the result of the mechanical preparation. As a result of the pressure on the electrode surface, polishing can generate excessive heat by abrasion, which probably accounts for the reported effect. It is known that sample heating produces similar effects (Mernagh and Trudu, 1993; Ferraro *et al*., 2003). Then, the broadness of the bands discussed in the Raman spectrum of area 3 (vide Fig. A.4) and additional band at 331 cm^{-1} may be explained by a slight modification in the chalcopyrite crystal structure.

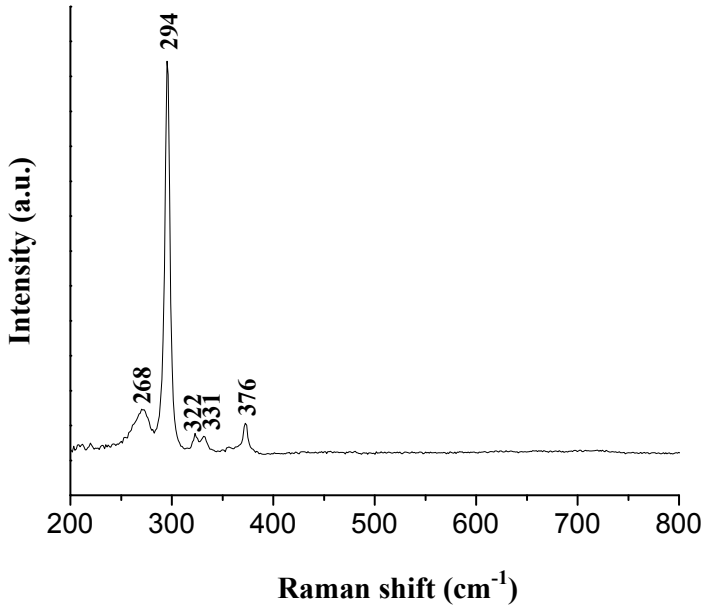

Figure A.5. Raman spectrum obtained for an unpolished chalcopyrite sample.

Fig. A.6 shows the Raman spectra obtained for areas 4, 5 and 6. The spectra obtained for area 4 and 5 presents the characteristic vibrational modes of crystalline materials: thin and well defined bands. The spectrum obtained for area 4 indicates more intense band at 466 cm^{-1}, band of intermediate intensity at 207 cm^{-1}, and additional bands of lower intensity. Such spectrum is typical of quartz, silicon dioxide (SiO_2), as discussed in the literature (Rodgers and Hampton, 2003; RRUFF, 2010). The spectrum obtained for area 5 shows more intense bands at 666 and 1015 cm^{-1}, bands of intermediate intensity at 320 and 386 cm^{-1}, and bands of lower intensity. Such spectrum is characteristic of diopside, calcium and magnesium silicate ($CaMgSi_2O_6$), as discussed by Richet *et al*. (1998) and also available in RRUFF (2010). Finally, it should be noticed that Raman bands for area 6 are not well defined. The spectrum indicates a broad band between 130 and 350 cm^{-1} and absence of additional bands. The spectrum obtained here is comparable to those obtained for lead and bismuth sulfides such as galenobismutite ($PbBi_2S_4$) and aschalmamite ($Pb_6Bi_2S_9$) (RRUFF, 2010). Therefore, the impurity represented by area 6 was not precisely identified in this investigation, and it is probably a non-stoichiometric phase.

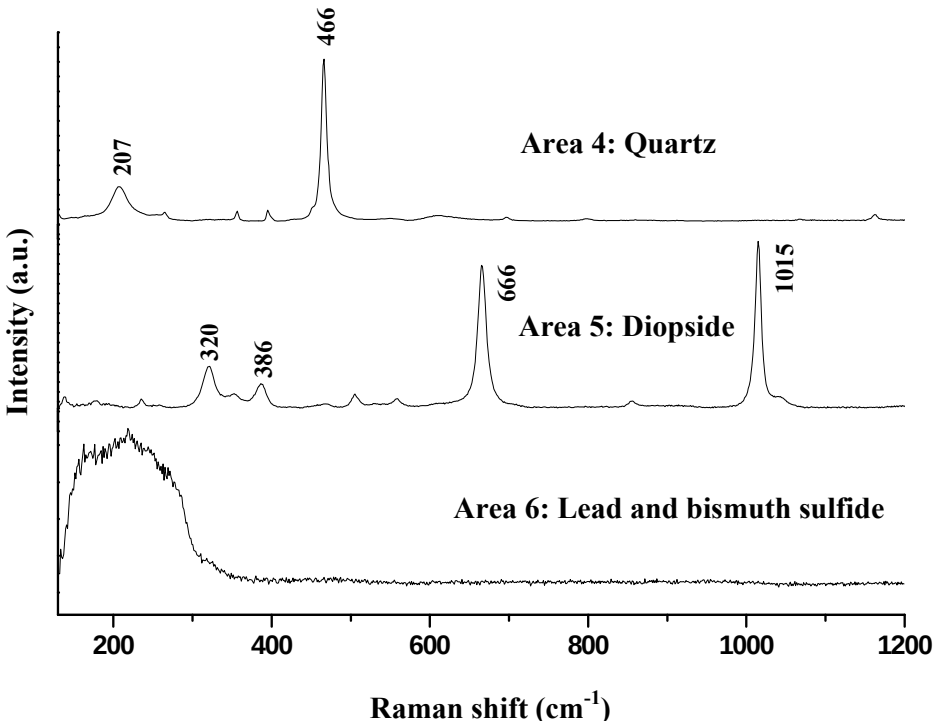

Figure A.6. Raman spectra obtained for areas 4, 5 and 6 (vide Figure A.3).

In summary, the Raman spectra allowed identifying and also distinguishing the impurity phases (inclusions) present on the mineral sample. Each Raman spectrum corresponds to a group of bands in well-defined positions and relative intensities, which characterize the main vibrational modes of the crystalline structures.

The presence of impurities on the mineral reaction area affects chalcopyrite reactivity due to the possible galvanic effects. For the particular case of wurtzite (area 1) and pyrite (area 2), their presence on the electrode samples affects the dissolution behavior of chalcopyrite. Some authors have evaluated the interaction between pyrite and chalcopyrite and also between wurtzite and chalcopyrite in acidic sulfate media. It has been demonstrated that chalcopyrite is less electroactive than wurtzite and, thus, chalcopyrite acts as the cathode in a galvanic cell, site where the reduction reactions occur. More electroactive, wurtzite acts as anode and then its oxidation is favored (Mehta and Murr, 1983). In contrast, for the pyrite-chalcopyrite coupling, pyrite is less electroactive than chalcopyrite, acting as the cathode in a galvanic cell. More electroactive, chalcopyrite acts as anode and the oxidation of this mineral is favored (Mehta and Murr, 1983; Nowak *et al*., 1984; You *et al*., 2007).

The galvanic interaction established between chalcopyrite and pyrite, mineral commonly associated with chalcopyrite in the porphyry copper ores, as earlier discussed in Chapter 2, was the theme of Chapter 3. The role of naturally associated pyrite crystallites (inclusions) on electrochemical properties of chalcopyrite electrodes immersed in acidic sulfate media under practical, low-temperature leaching conditions (*i.e.*, in the presence of ferric ion and dissolved oxygen), was investigated by potentiometric and voltammetric techniques. As already discussed, the presence and content of pyrite on chalcopyrite reaction area affects significantly the mixed potential and dissolution current density values, which may cause misinterpretations on the electrochemistry of this copper mineral when pyrite is present in the examined sample.

The occurrence of inert impurity phases, such as the silicates, on the reaction area of the chalcopyrite electrodes possibly alters the electron flow into the electrode, in function of differences in electrical conductivity, establishing new sites of oxidation. For that reason, in electrochemical investigations, the use of electrodes with high content of quartz and diopside should be avoided.

A.4. Conclusions

SEM/EDS and RS were used to identify impurity phases on chalcopyrite electrodes. The presence of sulfides on the electrode reaction area, such as pyrite and wurtzite, confirmed on the analyzed samples, affects the mineral reactivity in acidic sulfate solutions due to the formation of galvanic couples. Thus, the inconsistencies observed in the literature for the electrochemical behavior of chalcopyrite (*i.e.*, the magnitude of the anodic current density, critical potential, steady-state current, and properties, such as the mixed potential) could be minimized by performing a preliminary, detailed analysis of the electrode area prior to the electrochemical measurements and by selecting the working electrodes with a relatively lower impurity content. These preliminary steps allow a more consistent understanding of the electrochemical behavior and dissolution rate of this important copper sulfide.

References

ABRAITIS, P.K., PATTRICK, R.A.D., KELSALL, G.H., and VAUGHAN, D.J. (2004) Acid leaching and dissolution of major sulphide ore minerals: processes and galvanic effects in complex systems, Mineralogical Magazine 68 (2): pp. 343–351.

ACRES, R.G., HARMER, S.L., and BEATTIE, D.A. (2010) Synchrotron XPS studies of solution exposed chalcopyrite, bornite, and heterogeneous chalcopyrite with bornite, International Journal of Mineral Processing 94 (1-2): pp. 43-51.

AL-HARAHSHEH, M., RUTTEN, F., BRIGGS, D., and KINGMAN, S. (2006) Preferential oxidation of chalcopyrite surface facets characterized by TOF-SIMS and SEM, Applied Surface Science 252: pp. 7155-7158.

AMMOU-CHOKROUM, M., SEN, P.K., and FOUQUES, F. (1979) Electrooxidation of chalcopyrite in acid chloride medium: kinetics, stoichiometry and reaction mechanism, Thirteenth International Mineral Processing Congress, A, Laskowski, J. (ed.), Elsevier Scientific Publishing Company, Warsaw, Poland: pp. 759-809.

ANDERSEN, E.K., ANDERSEN, I.G.K., NORBY, P., and HANSON, J.C. (1998) Kinetics of oxidation of fuel cell cathode materials lanthanum strontium manganates (III) (IV) at actual working conditions: in situ powder diffraction studies, Journal of Solid State Chemistry 141: pp. 235-240.

APS (Advamced Photon Source), ANL (Argonne National Laboratory) (2010) Overview. Available at http://www.aps.anl.gov/. Accessed on July, 2010.

ARCE, E.M., and GONZÁLEZ, I. (2002) A comparative study of electrochemical behavior of chalcopyrite, chalcocite and bornite in sulfuric acid solution, International Journal of Mineral Processing 67: pp. 17-28.

ASTM E562 (2008) Standard Test Method for Determining Volume Fraction by Systematic Manual Point Count, American Society for Testing and Materials (ASTM) International, PA, U.S.A.: 11 pp.

BACHRACH, R.Z. (1992) Synchrotron radiation research: advances in surface and interface science, v.1, Plenum Press, New York, U.S.A.: 526 pp.

BARLOW, N., BRENNAN, C., DOYLE, S.E., GREAVES, G.N., MILLER, M., NAHLE, A.H., ROBERTS, K.J., ROBINSON, J., SHERWOOD, J.N. and WALSH, F.C. (1989) Instrumentation and data acquisition for in situ electrochemistry at the Daresbury SRS, Review of Scientific Instruments 60: 2386.

BEALE, A.M., and SANKAR, G. (2003) In situ study of the formation of crystalline bismuth molybdate materials under hydrothermal conditions, Chemistry of Materials 15: pp. 146-153.

BERRY, L.G., MASON, B., and DIETRICH, R.V. (1983) Mineralogy, 2nd ed., Freeman, San Francisco, U.S.A.: 621 pp.

BERRY, V.K., MURR, L.E., and HISKEY, J.B. (1978) Galvanic interaction between chalcopyrite and pyrite during bacterial leaching of low-grade waste, Hydrometallurgy 3: pp. 309-326.

BEVILAQUA, D., DIÉZ-PEREZ, I., FUGIVARA, C.S., SANZ, F., BENEDETTI, A.V., and GARCIA JR., O. (2004) Oxidative dissolution of chalcopyrite by *Acidithiobacillus ferrooxidans* analyzed by electrochemical impedance spectroscopy and atomic force microscopy, Bioelectrochemistry 64: pp. 79-84.

BEVILAQUA, D., GARCIA JR., O., and TUOVINEN, O.H. (2010) Oxidative dissolution of bornite by *Acidithiobacillus ferrooxidans*, Process Biochemistry 45: pp. 101-106.

BIEGLER, T., and HORNE, M.D. (1985) The electrochemistry of surface oxidation of chalcopyrite, Journal of the Electrochemical Society 132 (6): pp. 1363-1369.

BIEGLER, T., and SWIFT, D.A. (1979) Anodic electrochemistry of chalcopyrite, Journal of Applied Electrochemistry 9: pp. 545-554.

BOCKRIS, J.O.M., and REDDY, A.K.N. (1998) Modern electrochemistry, 2nd ed., v.2A, Kluwer Academic/Plenum Publishers, New York, U.S.A.: 1524 pp.

BRAVO, P. (2006) El panorama de la hidrometalurgia, Revista Mineria Chilena 303. Available at http://www.mch.cl; aceesed in 05/2008.

BRETT, C.M.A., and BRETT, A.M.O. (1998) Electrochemistry: principles, methods, and applications, Oxford University Press, Inc., Oxford, Great Britain: 427 pp.

BUCKLEY, A.N., and WOODS, R. (1983) X-ray photoelectron spectroscopic investigation of the tarnishing of bornite, Australian Journal of Chemistry 36: pp. 1793-1804.

BUCKLEY, A.N., HAMILTON, I.C., and WOODS, R. (1984) Investigation of the surface oxidation of bornite by linear potential sweep voltammetry and X-ray photoelectron spectroscopy, Journal of Applied Electrochemistry 14: pp. 63-74.

CAHILL, C.L., BENNING, L.G., BARNES, H.L., and PARISE, J.B. (2000) In situ time-resolved X-ray diffraction of iron sulfides during hydrothermal pyrite growth, Chemical Geology 167: pp. 53-63.

CARNEIRO, M.F.C, and LEÃO, V.A. (2007) The role of sodium chloride on surface properties of chalcopyrite leached with ferric sulphate, Hydrometallurgy 87: pp. 73-82.

CHEN, J., BAI, J., CHEN, H., and GRAETZ, J. (2011) In situ hydrothermal synthesis of LiFePO4 studied by synchrotron X-ray diffraction, The Journal of Physical Chemistry Letters 2: pp. 1874–1878.

CHMIELEWSKI, T., and LEKKI, J. (1985) The effect of contact of copper sulphide grain on the initial rate of leaching in oxygenated sulphuric acid solution, Hydrometallurgy 15: pp. 203-208.

CONTRERAS, L., TURRILAS, X., VAUGHAN, G.B.M., KVICK, A., and RODRÍGUEZ, M.A. (2004) Time-resolved XRD study of TiC-TiB2 composites obtained by SHS, Acta Materialia 52: pp. 4783-4790.

CÓRDOBA, E.M., MUÑOZ, J.A., BLÁZQUEZ, M.L., GONZÁLEZ, F., and BALLESTER, A. (2008a) Leaching of chalcopyrite with ferric ion. Part I: General aspects, Hydrometallurgy 93: pp. 81-87.

CÓRDOBA, E.M., MUÑOZ, J.A., BLÁZQUEZ, M.L., GONZÁLEZ, F., and BALLESTER, A. (2008b) Leaching of chalcopyrite with ferric ion. Part II: effect of redox potential, Hydrometallurgy 93: pp. 88-96.

CÓRDOBA, E.M., MUÑOZ, J.A., BLÁZQUEZ, M.L., GONZÁLEZ, F., and BALLESTER, A. (2008c) Leaching of chalcopyrite with ferric ion. Part IV: the role of redox potential in the presence of mesophilic and thermophilic bacteria, Hydrometallurgy 93: pp. 106-115.

CHRISTENSEN, A.N., JENSEN, T.R., NORBY, P., and HANSON, J.C. (1998) In situ synchrotron X ray powder diffraction studies of crystallization of microporous aluminophosphates and Me2q-substituted aluminophosphates, Chemistry of Materials 10: pp. 1688–1693.

CRUNDWELL, F.K. (1988) The influence of the electronic structure of solids on the anodic dissolution and leaching of semiconducting sulfide minerals, Hydrometallurgy 21: pp. 155-190.

CRUZ, R., LUNA-SÁNCHEZ, R.M., LAPIDUS, G.T., GONZÁLEZ, I., and MONROY, M. (2005) An experimental strategy to determine galvanic interactions affecting the reactivity of sulfide mineral concentrates, Hydrometallurgy 78: pp. 198-208.

CULLITY, B.D., and STOCK, S.R. (2001) Elements of X-ray diffraction, 3rd ed., Prentice Hall, Inc., New Jersey, U.S.A.: 664 pp.

CURFS, C., TURRILAS, X., VAUGHAN, G.B.M., TERRY, A.E., KVICK, A., and RODRÍGUEZ, M.A. (2007) Al-Ni intermetallics obtained by SHS: a time-resolved X-ray diffraction study, Intermetallics 15: pp. 1163-1171.

DAVENPORT, W.G., KING, M., SCHLESINGER, M., and BISWAS, A.K. (2002) Extractive metallurgy of copper, 4th ed., Pergamon, Oxford, U.K.: 460 pp.

DALVI, A.D., BACON, W.G., AND OSBORNE, R.C. (2004) The past and the future of nickel laterites, PDAC 2004 International Convention, pp. 1-27.

DE MARCO, R., BAILEY, S., JIANG, Z-T., MORTON, J., and CHESTER, R. (2006b) An in situ chronoamperometry/synchrotron radiation grazing incidence X-ray diffraction study of the electrochemical oxidation of pyrite in chloride media, Electrochemistry Communications 8: pp. 1661-1664.

DE MARCO, R., JIANG, Z-T., PEJCIC, B., and VAN RIESSEN, A. (2006a) In situ synchrotron radiation grazing incidence X-ray diffraction - A powerful technique for

the characterization of solid-state ion-selective electrode surfaces, Electrochimica Acta 51: pp. 4886-4891.

DE MARCO, R., JIANG, Z-T., JOHN, D., SERCOMBE, M., and KINSELLA, B. (2007) An in situ electrochemical impedance spectroscopy/synchrotron radiation grazing incidence X-ray diffraction study of the influence of acetate on the carbon dioxide corrosion of mild steel, Electrochimica Acta 52: pp. 3746-3750.

DEFREYNE, J., BRACE, T., MILLER, C., OMENA, A., MATOS, M., and COBRAL, T. (2008) Commissioning UHC: a VALE copper refinery based on CESL technology, In: Hydrometallurgy 2008 - Proceedings of the 6th International Symposium, Young, C.A., Taylor, P.R., Anderson, C.G., and Choi, Y. (Eds.), SME, CO, U.S.A.: pp. 357-366.

DIXON, D.G., MAYNE, D.D., and BAXTER, K.G. (2008) Galvanox - a novel galvanically assisted atmospheric leaching technology for copper concentrates, Canadian Metallurgical Quarterly 47: pp. 327–336.

DNPM - Departamento Nacional de Produção Mineral (2001) Balanço Mineral Brasileiro, Ministério de Minas e Energia. Brasília: DNPM, Brazil.

DNPM - Departamento Nacional de Produção Mineral (2009) Cobre, In: Sumário Mineral Brasileiro, Ministério de Minas e Energia. Brasília: DNPM, Brazil.

DREISINGER, D. (2006) Copper leaching from primary sulfides: options for biological and chemical extraction of copper, Hydrometallurgy 83: pp. 10-20.

DUTRIZAC, J.E. (1978) The kinetics of dissolution of chalcopyrite in ferric ion media, Metallurgical Transactions B 9: pp. 431-439.

DUTRIZAC, J.E. (1981) The dissolution of chalcopyrite in ferric sulfate and ferric chloride media, Metallurgical Transactions B 12: pp. 371-378.

DUTRIZAC, J.E. (1982) Ferric ion leaching of chalcopyrite from different localities, Metallurgical Transactions B 13: pp. 303-309.

DUTRIZAC, J.E. (1989) Elemental sulphur formation during the ferric sulphate leaching of chalcopyrite. Canadian Metallurgical Quarterly 28 (4): pp. 337-344.

DUTRIZAC, J.E. (1990) Elemental sulphur formation during the ferric chloride leaching of chalcopyrite, Hydrometallurgy 23: pp. 153-176.

DUTRIZAC, J.E. (1992) The leaching of sulphide minerals in chloride media, Hydrometallurgy 29: pp. 1-45.

DUTRIZAC, J.E., and MACDONALD, R.J.C. (1974) Ferric ion as a leaching medium, Minerals Science and Engineering 6: pp. 59-97.

EDELBRO, R., SANDSTRÖM, A., and PAUL, J. (2003) Full potential calculations on the electron band structures of sphalerite, pyrite and chalcopyrite, Applied Surface Science 206: pp. 300-313.

ELSHERIEF, A.E. (2002) The influence of cathodic reduction, Fe^{2+} and Cu^{2+} ions on the electrochemical dissolution of chalcopyrite in acidic solution, Minerals Engineering 15: pp. 215-223.

ENGLAND, K.E.R., CHARNOCK, J.M., PATTRICK, R.A.D., and VAUGHAN, D.J. (2003) Surface oxidation studies of chalcopyrite and pyrite by glancing-angle X-ray absorption spectroscopy (REFLEXAFS), Mineralogical Magazine 63 (4): pp. 559-566.

EVANS, J.S.O., FRANCIS, R.J., O'HARE, D., PRICE, S.J., CLARK, S.M., GORDON, J., NIELD, A., and TANG, C.C. (1994) An apparatus for the study of the kinetics and mechanism of hydrothermal reactions by in situ energy dispersive X-ray diffraction. Review of Scientific Instruments 66 (3): pp. 2442–2445.

FARQUHAR, M.L., WINCOTT, P.L., WOGELIUS, R.A., and VAUGHAN, D.J. (2003) Electrochemical oxidation of the chalcopyrite surface: an XPS and AFM study in solution at pH 4, Applied Surface Science 218: pp. 34-43.

FERRARO, J.R., NAKAMOTO, K., and BROWN, C.W. (2003) Introductory Raman Spectrosocpy, 2nd ed., Elsevier Science, U.S.A.: 396 pp.

FERRER, P., DA SILVA, I., RUBIO-ZUAZO, J., ALFONSO, B.F., TROBAJO, C., KHAINAKOV, S., GARCIA, J.R., GARCIA-GRANDA, S., and CASTRO, G.R. (2012) A flow-through reaction cell for in situ X-ray diffraction and absorption

studies of heterogeneous powder–liquid reactions and phase transformations, Journal of Synchrotron Radiation 19: pp. 93–100.

FOGG, A.M., PRICE, S.J., FRANCIS, R.J., O'BRIEN, S., and O'HARE, D. (200) Determination of the kinetics of crystallisation of gibbsite using time-resolved in situ energy dispersive powder X-ray diffraction, Journal of Materials Chemistry 10: pp. 2355-2357.

FUENTES-ACEITUNO, J.C., LAPIDUS, G.T., and DOYLE, F.M. (2008) A kinetic study of the electro-assisted reduction of chalcopyrite, Hydrometallurgy 92: pp. 26-33.

GESELBRACHT, M.J., WALTON, R.I., COWELL, E.S., MILLANGE, F., and O'HARE, D. (2000) A furnace for the in situ study of the formation of inorganic solids at high temperature using time-resolved energy-dispersive X-ray diffraction, Review of Scientific Instruments 71: pp. 4177.

GHAHREMANINEZHAD, A., ASSELIN, E., and DIXON, D.G. (2010) Electrochemical evaluation of the surface of chalcopyrite during dissolution in sulfuric acid solution, Electrochimica Acta 55 (18): pp. 5041-5056.

GIBBS, G.V., COX, D.F., ROSSO, K.M., ROSS, N.L., DOWNS, R.T., and SPACKMAN, M.A. (2007) Theoretical electron density distributions for Fe- and Cu-sulfide earth materials: a connection between bond length, bond critical point properties, local energy densities, and bonded interactions, Journal of Physics and Chemistry B 111: pp. 1923-1931.

GILEADI, E., and KIROWA-EISNER, E. (2005) Some observations concerning the Tafel equation and its relevance to charge transfer in corrosion, Corrosion Science 47: pp. 3068-3085.

GOH, S.W., BUCKLEY, A.N., LAMB, R.N., ROSENBERG, R.A., and MORAN, D. (2006) The oxidation states of copper and iron in mineral sulfides, and the oxides formed on initial exposure of chalcopyrite and bornite to air, Geochimica *et* Cosmochimica Acta 70: pp. 2210-2228.

GÓMEZ, C., ROMÁN, E., BLÁZQUEZ, M.L., and BALLESTER, A. (1997) SEM and AES studies of chalcopyrite bioleaching in the presence of catalytic ions, Minerals Engineering 10 (8): pp. 825-835.

HABASHI, F. (1978) Chalcopyrite: its chemistry and metallurgy, McGraw-Hill, Inc., New York, U.S.A.: 165 pp.

HABASHI, F. (1993) A textbook of hydrometallurgy, Librairie des Presses de l'Université Laval, Canada: 689 pp.

HACKL, R.P., DREISINGER, D.B., PETERS, E., and KING, J.A. (1995) Passivation of chalcopyrite during oxidative leaching in sulfate media, Hydrometallurgy 39: pp. 25-48.

HARMER, S.L., THOMAS, J.E., FORNASIERO, D., and GERSON, A.R. (2006) The evolution of surface layers formed during chalcopyrite leaching, Geochimica *et* Cosmochimica Acta 70: pp. 4392-4402.

HARVEY, P., AND BUTLER, I. (1986) Raman spectra of orthorhombic sulfur at 40K, Journal of Raman Spectroscopy 17: pp. 329-334.

HAVLÍK, T., and KAMMEL, R. (1995) Leaching of chalcopyrite with acidified ferric chloride and carbon tetrachloride addition, Minerals Engineering 8 (10): pp. 1125-1134.

HIND, A.R., BHARGAVA, S.K., and GROCOTT, S.C., (1999) The surface chemistry of Bayer process solids: a review, Colloids and Surfaces A 146: pp. 359–374.

HIRATO, T., KINOSHITA, M., AWAKURA, Y., and MAJIMA, H. (1986) The leaching of chalcopyrite with ferric chloride, Metallurgical Transactions B 17: pp. 19-28.

HIRATO, T., MAJIMA, H., and AWAKURA, Y. (1987a) The leaching of chalcopyrite with cupric chloride, Metallurgical Transactions B 18: pp. 31-39.

HIRATO, T., MAJIMA, H., and AWAKURA, Y. (1987b) The leaching of chalcopyrite with ferric sulfate, Metallurgical Transactions B 18: pp. 489-496.

HIROYOSHI, N., ARAI, M., MIKI, H., TSUNEKAWA, M., and HIRAJIMA, T. (2002) A new reaction model for the catalytic effect of silver ions on chalcopyrite leaching in sulfuric acid solutions, Hydrometallurgy 63: pp. 257-267.

HIROYOSHI, N., KUROIWA, S., MIKI, H., TSUNEKAWA, M., and HIRAJIMA, T. (2007) Effects of coexisting metal ions on the redox potential dependence of chalcopyrite leaching in sulfuric acid solutions, Hydrometallurgy 87: pp. 1-10.

HIROYOSHI, N., KITAGAWA, H., and TSUNEKAWA, M. (2008) Effect of solution composition on the optimum redox potential for chalcopyrite leaching in sulfuric acid solutions, Hydrometallurgy 91: pp. 144-149.

HIROYOSHI, N., KUROIWA, S., MIKI, H., TSUNEKAWA, M., and HIRAJIMA, T. (2004) Synergistic effect of cupric and ferrous ions on active-passive behavior in anodic dissolution of chalcopyrite in sulfuric acid solutions, Hydrometallurgy 74: pp. 103-116.

HIROYOSHI, N., MIKI, H., HIRAJIMA, T., and TSUNEKAWA, M. (2000) A model for ferrous-promoted chalcopyrite leaching, Hydrometallurgy 57: pp. 31-38.

HIROYOSHI, N., MIKI, H., HIRAJIMA, T., and TSUNEKAWA, M. (2001) Enhancement of chalcopyrite leaching by ferrous ions in acidic ferric sulfate solutions, Hydrometallurgy 60: pp. 185-197.

HISKEY, J. B. (1993) Chalcopyrite semiconductor electrochemistry and dissolution, In: Paul E. Queneau International Symposium of Extractive Metallurgy of Copper, Nickel Cobalt, Reddy, R. G., and Weizenbach, R. N. (Eds.), TMS, Vancouver, Canada: pp. 949-969.

HISKEY, J.B., and WADSWORTH, M.E. (1975) Galvanic conversion of chalcopyrite, Metallurgical Transactions B (6B): pp. 183-190.

HISKEY, J.B., and WADSWORTH, M.E. (1981) Electrochemical processes in the leaching of metal sulfides and oxides, Process and Fundamental Considerations of Selected Hydrometallurgical Systems, Society of Mining Engineers of AIME, New York, U.S.A.: pp. 303-325.

HOLMES, P.R., and CRUNDWELL, F.K. (1995) Kinetic aspects of galvanic interactions between minerals during dissolution, Hydrometallurgy 39: pp. 353-375.

HUMMER, D.R., KUBICKI, J.D., KENT, P.R.C., POST, J.E., and HEANEY, P.J. (2009) Origin of nanoscale phase stability reversals in titanium oxide polymorphs, The Journal of Physical Chemistry C 113: pp. 4240-4245.

ICSG - International Copper Study Group (2007) The world copper factbook. Available at http://www.icsg.org. Accessed in 01, 2008.

INGHAM, B., ILLY, B.N., TONEY, M.F., HOWDYSHELL, M.L., and RYAN, M.P. (2008) In situ synchrotron X-ray diffraction experiments on electrochemically deposited ZnO nanostructures, The Journal of Physical Chemistry C: pp 14863–14866

INGHAM, B., KOB, M., LAYCOCK, N., BURNELL, J., KAPPEN, P., KIMPTON, J.A., and WILLIAMS, D.E. (2012) In situ synchrotron X-ray diffraction study of scale formation during CO2 corrosion of carbon steel in sodium and magnesium chloride solutions, Corrosion Science 56: 96-104.

INGHAM, B., KOB, M., KEAR, G., KAPPEN, P., LAYCOCK, N., KIMPTON, J.A., and WILLIAMS, D.E. (2010) In situ synchrotron X-ray diffraction study of surface scale formation during CO2 corrosion of carbon steel at temperatures up to 90 ºC, Corrosion Science 52: pp. 3052-3061.

ISHII, M., SHIBATA, K., AND NOZAKI, H. (1993) Anion distribution and phase transitions in the CuS1−*x*Se*x* (*x* = 0–1) studied by Raman spectroscopy, Journal of Solid State Chemistry 105: pp. 504-511.

JENSEN, M.L., and BATEMAN, A.M. (1981) Economic mineral deposits, 3rd ed., John Wiley & Sons, Inc., Canada: 593 pp.

JONES, D. L. and PETERS, E. (1976) The leaching of chalcopyrite with ferric sulfate and ferric chloride, International Symposium on Copper Extraction and Refining, vol II, Yannopoulos, J.C., and Agarwal, J.C. (eds.), The Metallurgical Society of AIME, New York, United States of America: pp. 633-653.

JORDAN, H., SANHUEZA, A., GAUTIER, V., ESCOBAR, B., and VARGAS, T. (2006) Electrochemical study of the catalytic influence of *Sulfolobus metallicus* in the bioleaching of chalcopyrite at 70°C, Hydrometallurgy 83: pp. 55-62.

KAMETANI, K., and AOKI, A. (1985) Effect of suspension potential on the oxidation rate of copper concentrate in a sulfuric acid, Metallurgical Transactions B 18: pp. 489-496.

KELSALL, G.H., and PAGE, P.W. (1984) Aspects of chalcopyrite ($CuFeS_2$) electrochemistry, In: Proceedings of the International Symposium on Electrochemistry in Mineral and Metal Processing, Richardson, P.E., and Srinivasan, S. (eds.), The Electrochemical Society, New Jersey, U.S.A.: pp. 303-320.

KING, J.A., DREISINGER, D.B., and KNIGHT, D.A. (1993) The total pressure oxidation of copper concentrates, In: Extractive Metallurgy of Copper, Nickel and Cobalt, Volume l: Fundamental Aspects. Reddy, R.G., and Weizenbach, R.N. (Eds.), The Minerals, Metals and Materials Society of AIME, Warrendale, U.S.A.: pp. 735-756.

KLAUBER, C. (2008) A critical review of the surface chemistry of acidic ferric sulphate dissolution of chalcopyrite with regards to hindered dissolution, International Journal of Mineral Processing 86: pp. 1-17.

KLAUBER, C., PARKER, A., VAN BRONSWIJK, W., and WATLING, H.R. (2001) Sulphur speciation of leached chalcopyrite surfaces as determined by X-ray photoelectron spectroscopy, International Journal of Mineral Processing 62: pp. 65-94.

KLUG, H.P., and ALEXANDER, L.E. (1974) X-ray diffraction procedures: for polycrystalline and amorphous materials, 2nd ed., John Wiley & Sons, Inc., New York, U.S.A.: 966 pp.

KONDRASHKINA, E.A., STEPANOV, S.A., SCHMIDBAUER, M., OPITZ, R., KOHLER, R., and RHAN, H. (1997) High-resolution grazing-incidence X-ray diffraction for characterization of defects in crystal surface layers, Journal of Applied Physics 81 (1): pp. 175-183.

KONDRATENKO, E.V. (2010) Using time-resolved methods to monitor and understand catalytic oxidation reactions, Catalysis Today 157 (1-4): pp. 16-23.

KUNZ, C., and CODLING, K. (1979) Synchrotron radiation: techniques and applications, Springer-Verlag, Berlin, Germany: 442 pp.

LAVRENTYEV, A.A., GABRELIAN, B.V., NIKIFOROV, I.Y., REHR, J.J., and ANKUDINOV, A.L. (2004) The electron energy structure of some sulfides of iron and copper, Journal of Electron Spectroscopy and Related Phenomena 137-140: pp. 495-498.

LÁZARO, I. (2003) Electrochemistry of the leaching of chalcopyrite, Ph.D. Thesis, Murdoch University, Australia: 313 pp.

LÁZARO, I., and NICOL, M.J. (2003) The mechanism of the dissolution and passivation of chalcopyrite: an electrochemical study, In: Proceedings of Hydrometallurgy 2003 – Fifth International Conference in Honor of Professor Ian Ritchie, Young, C.A., Alfantazi, A.M., Anderson, C.G., Dreisinger, D.B., Harris, B., and James, A. (Eds.), TMS, U.S.A.: pp. 405-417.

LÁZARO, I., and NICOL, M.J. (2006) A rotating ring-disk study of the initial stages of the anodic dissolution of chalcopyrite in acidic solutions, Journal of Applied Electrochemistry 36: pp. 425-431.

LEVINE, J.R., COHEN, J.B., CHUNG, Y.W., and GEORGOPOULOS, P. (1989) Grazing-incidence small-angle X-ray scattering: new tool for studying thin film growth, Journal of Applied Crystallography 22: pp. 528-532.

LEYSSENS, K., ADRIAENS, A., DOWSETT, M.G., SCHOTTE, B., OLOFF, I., PANTOS, E., BELL, A.M.T., and THOMPSON, S.P. (2005) Simultaneous in situ time resolved SR-XRD and corrosion potential analyses to monitor the corrosion on copper, Electrochemistry Communications 7: pp. 1265-1270.

LI, D., BANCROFT, G.M., KASRAI, M., FLEET, M.E., YANG, B.X., FENG, X.H., TAN, K., and PENG, M. (1994) Sulfur K- and L-edge X-ray absorption spectroscopy of sphalerite, chalcopyrite and stannite, Physics and Chemistry of Minerals 20: pp. 489-499.

LIANG, C-L., XIA, J-L., ZHAO, X-J., YANG, Y., GONG, S-Q., NIE, Z-Y., MA, C-Y., ZHENG, L., ZHAO, Y-D., and QIU, G-Z. (2010) Effect of activated carbon on chalcopyrite bioleaching with extreme thermophile *Acidianus manzaensis*, Hydrometallurgy 105 (1-2): p. 179-185.

LIDDICOAT, J., and DREISINGER, D. (2007) Chloride leaching of chalcopyrite, Hydrometallurgy 89: pp. 323-331.

LINGE, H.G. (1976) A study of chalcopyrite dissolution in acidic ferric nitrate by potentiometric titration, Hydrometallurgy 2: pp. 51-64.

LITTLEJOHN, P.O.L., and DIXON, D. (2008) The enhancing effect of pyrite on ferrous oxidation by dissolved oxygen, In: Hydrometallurgy 2008 – Sixth International Symposium, Young, C.A., Taylor, P.R., Anderson, C.G., and Choi, Y. (Eds), Society for Mining, Metallurgy and Exploration, Inc., Littleton, U.S.A.: pp. 1098-1109.

LME - London Metal Exchange (2010) Copper price, available at http//:www.co.lme.uk. Accessed in 9, 2010.

LOAN, M., LOUGHLIN, B., HAINES, J., CROKER, D., FENNELL, M., and HODNETT, B.K. (2005) In-situ time resolved synchrotron diffraction studies of high temperature Bayer digestion, Proceedings of the 7th International Alumina Quality Workshop, AQW Inc. Perth, Australia: pp. 117-122.

LOH, J.S.C., FOGG, A.M., WATLING, H.R., PARKINSON, G.M., and O'HARE, D. (2000) A kinetic investigation of gibbsite precipitation using *in situ* time resolved energy dispersive X-ray diffraction, Physical Chemistry Chemical Physics 2: pp. 3597-3604.

LORENZEN, L., and van DENVENTER, J.S.J. (1992) Electrochemical interactions between gold and its associated minerals using cyanidation, Hydrometallurgy 30: pp. 177-194.

LU, Z.Y., JEFFREY, M.I., and LAWSON, F. (2000) An electrochemical study of the effect of chloride ions on the dissolution of chalcopyrite in acidic solutions, Hydrometallurgy 56: pp. 145-155.

MADHUCHHANDA, M., DEVI, N.B., RAO, K.S., RATH, P.C., and PARAMGURU, R.K. (2000) Galvanic interaction between sulfide minerals and pyrolusite, Journal of Solid State Electrochemistry 4: pp. 189-198.

MAJIMA, H., AWAKURA, Y., HIRATO, T., and TANAKA, T. (1985) The leaching of chalcopyrite in ferric chloride and ferric sulfate solutions, Canadian Metallurgical Quarterly 24: pp. 283-291.

MAJUSTE, D., DANTAS, M.S.S, and CIMINELLI, V.S.T. (2009) Identificação de impurezas em eletrodos de calcopirita por técnicas espectroscópicas, In: Anais do XXIII Encontro Nacional de Tratamento de Minérios e Metalurgia Extrativa, Gramado, Brazil: pp. 73-80.

MAJUSTE, D., CIMINELLI, V.S.T., OSSEO-ASARE, K., PANIAGO, R.M., and DANTAS, M.S.S. (2012a) Electrochemical dissolution of chalcopyrite: Detection of bornite by synchrotron small angle X-ray diffraction and its correlation with the hindered dissolution process, Hydrometallurgy 111-112: pp. 114-123.

MAJUSTE, D., CIMINELLI, V.S.T., OSSEO-ASARE, K., and DANTAS, M.S.S. (2012b) Quantitative assessment of the effect of pyrite inclusions on chalcopyrite electrochemistry under oxidizing conditions, Hydrometallurgy 113-114: pp. 167-176.

MANSFELD, F. (2005) Tafel slopes and corrosion rates obtained in the pre-Tafel region of polarization curves, Corrosion Science 47: pp. 3178-3186.

MATEOS, F.B., PÉREZ, I.P., and MORA, F.C. (1987) The passivation of chalcopyrite subjected to ferric sulfate leaching and its reactivation with metal sulfides, Hydrometallurgy 19: pp. 159-167.

MAURICE, D. and HAWK, J.A. (1998) Ferric chloride leaching of mechanically activated chalcopyrite, Hydrometallurgy 49: pp. 103-123.

MCDONALD, R.G., and MUIR, D.M. (2007a) Pressure oxidation leaching of chalcopyrite. Part I: Comparison of high and low temperature reaction kinetics and products, Hydrometallurgy 86: pp. 191-205.

MCDONALD, R.G., and MUIR, D.M. (2007b) Pressure oxidation leaching of chalcopyrite. Part II: Comparison of medium temperature kinetics and products and effect of chloride ion, Hydrometallurgy 86: pp. 206-220.

MCMILLAN, R.S., MACKINNON, D.J., and DUTRIZAC, J.E. (1982) Anodic dissolution of n-type and p-type chalcopyrite, Journal of Applied Electrochemistry 12: pp. 743-757.

MERNAGH, T.P., and TRUDU, A.G. (1993) A laser Raman microprobe study of some geologically important sulphide minerals, Chemical Geology 103: pp. 113-127.

METHA, A.P., and MURR, L.E. (1983) Fundamental studies of the contribution of galvanic interactions to acid-bacterial leaching of mixed metal sulfides, Hydrometallurgy 9: pp. 235-256.

MICROCAL ORIGIN^{TM}, version 8.0, Microcal Softwares, Inc., MA, USA.

MILLER, J.D., and PORTILLO, H.Q. (1979) Silver catalysis in ferric sulfate leaching of chalcopyrite, In: XIII International Mineral Processing Congress, Warsaw, Poland: pp. 691-742.

MILLER, J.D., MCDONOUGH, P.J., and PORTILLO, H.Q. (1981) Electrochemistry in silver catalyzed ferric sulfate leaching of chalcopyrite, In: Process and Fundamental Considerations of Selected Hydrometallurgical Systems, Kuhn, M.C. (Ed.), AIME-SME, New York, U.S.A.: pp. 327-338.

MILLER, K.J., SYLWESTRZAK, L.A., and BAXTER, K.G. (2008) Treatment of copper sulphide deposits – evaluation of a Galvanox^{TM} versus Sepon circuit configuration, In: Alta 2008 Copper Conference, Alta Metallurgical Services, Perth, Australia: pp. 1-20.

MIKHLIN, Y.L., TOMASHEVICH, Y.V., ASANOV, I.P., OKOTRUB, A.V., VARNEK, V.A., and VYALIKH, D.V. (2004) Spectroscopic and electrochemical characterization of the surface layers of chalcopyrite ($CuFeS_2$) reacted in acidic solutions, Applied Surface Science 225: pp. 395-409.

MIKHLIN, Y., TOMASHEVICH, Y.V., TAUSON, V., VYALIKH, D.V., MOLODTSOV, S., and SZARGAN, R. (2005) A comparative X-ray absorption near-edge structure

study of bornite, Cu_5FeS_4 and chalcopyrite, $CuFeS_2$, Journal of Electron Spectroscopy and Related Phenomena 142: pp. 83-88.

MISHRA, K.K, and OSSEO-ASARE, K. (1988) Aspects of the interfacial electrochemistry of semiconductor pyrite (FeS_2), Journal of the Electrochemical Society 135 (10): pp. 2502-2509.

MORÓN, M.C. (2000) Dynamic neutron and synchrotron X-ray powder diffraction methods in the study of chemical processes, Journal of Materials Chemistry 10: pp. 2617-2626.

MUÑOZ, P.B., MILLER, J.D., and WADSWORTH, M.E. (1979) Reaction mechanism for the acid ferric sulfate leaching of chalcopyrite, Metallurgical Transactions B 10: pp. 149-158.

MUNN, J., BARNES, P., HAU-SERMANN, D., AXON, S.A., and KLINOWSKI J. (1992) In-situ studies on the hydrothermal synthesis of zeolites using synchrotron energy-dispersive X-ray diffraction. Phase Transformations 39: pp. 129-34.

MURRAY, J., KIRWAN, L., LOAN, M., and HODNETT, B.K. (2009) In-situ synchrotron diffraction study of the hydrothermal transformation of goethite to hematite in sodium aluminate solutions, Hydrometallurgy 95: pp. 239-246.

NAKAZAWA, H., FUJISAWA, H., and SATO, H. (1998) Effect of activated carbon on the bioleaching of chalcopyrite concentrate, International Journal of Mineral Processing 55: pp. 87-94.

NAVA, D., and GONZÁLEZ, I. (2006) Electrochemical characterization of chemical species formed during the electrochemical treatment of chalcopyrite in sulfuric acid, Electrochimica Acta 51: pp. 5295-5303.

NAVA, D., GONZÁLEZ, I., LEINEN, D., and RAMOS-BARRADO, J.R. (2008) Surface characterization by X-ray photoelectron spectroscopy and cyclic voltammetry of products formed during the potentiostatic reduction of chalcopyrite, Electrochimica Acta 53: pp. 4889-4899.

NICOL, M.J., and LÁZARO, I. (2002) The role of EH measurements in the interpretation of the kinetics and mechanisms of the oxidation and leaching of sulphide minerals, Hydrometallurgy 63: pp. 15-22.

NICOL, M., MIKI, H., and VELÁSQUEZ-YÉVENES, L. (2010) The dissolution of chalcopyrite in chloride solutions: Part 3. Mechanisms, Hydrometallurgy 103 (1-4): pp. 86-95.

NORBY, P. (1996) In-situ time resolved synchrotron powder diffraction studies of syntheses and chemical reactions, Materials Science Forum 228-231: pp. 147-152.

NORBY, P. (1997) Hydrothermal conversion of zeolites: an in situ synchrotron X-ray powder diffraction study, Journal of the American Chemical Society 119: pp. 5215-5221.

NORBY, P. (2006) In-situ XRD as a tool to understanding zeolite crystallization, Current Opinion in Colloid & Interface Science 11: pp. 118-125.

NOWAK, P., KRAUSS, E., and POMIANOWSKI, A. (1984) The electrochemical characteristics of the galvanic corrosion of sulphide minerals in short-circuited model galvanic cells, Hydrometallurgy 12: pp. 95-110.

OLIVEIRA, C., and DUARTE, H.A. (2010) Disulphide and metal sulphide formation on the reconstructed (0 0 1) surface of chalcopyrite: a DFT study, Applied Surface Science 257: pp. 1319-1324.

OSSEO-ASARE, K. (1992) Semiconductor electrochemistry and hydrometallurgical dissolution processes. In: Hydrometallurgy, Theory and Practice. Proceedings of the Ernest Peters International Symposium, Cooper, W.C., and Dreisinger D.B. (Eds.), Hydrometallurgy 29: pp. 61-90.

OSSEO-ASARE, K (1993a) Oxidants and catalysts in the aqueous dissolution of metal sulfides: influence of electronic structure on reactivity, In: Proceedings of the 4th International Symposium in Hydrometallurgy, Hiskey, J.B., and Warren, G.W. (Eds.), SME, Littleton, CO, United States of America: pp. 173-187.

OSSEO-ASARE, K. (1993b) The dissolution of metal sulfides: insights from semiconductor electrochemistry, In: Proceedings of the Fall Meeting of the Mining and Materials Processing Institute of Japan (MMIJ), Fukuoka, Japan: pp. 41-45.

PALMER, B.R., NEBO, C.O., RAU, M.F., and FUERSTENAU, M.C. (1981) Rate phenomena involved in the dissolution of chalcopyrite in chloride-bearing lixiviants, Metallurgical Transactions B 12: pp. 595-601.

PARISE, J.B**.** (2000) Synchrotron studies of phase transformations**,** Transformation Processes in Minerals Reviews in Mineralogy & Geochemistry 39: pp. 285-318.

PARKER, A., KLAUBER, C., KOUGIANOS, A., WATLING, H.R., and VAN BRONSWIJK, W. (2003) An X-ray photoelectron spectroscopy study of the mechanism of oxidative dissolution of chalcopyrite, Hydrometallurgy 71: pp. 265-276.

PARKER, A.J., PAUL, R.L., and POWER, G.P. (1981) Electrochemistry of the oxidative leaching of copper from chalcopyrite, Journal of Electroanalytical Chemistry and Interfacial Electrochemistry 118: pp. 305-316.

PARKER, G.K., WOODS, R., and HOPE, G.A. (2008) Raman investigation of chalcopyrite oxidation, Colloids and Surfaces A: Physicochemical and Engineering Aspects 318: pp. 160-168.

PEARCE, C.I., PATTRICK, R.A.D., VAUGHAN, D.J., HENDERSON, C.M.B., and VAN DER LAAN, G. (2006) Copper oxidation state in chalcopyrite: mixed Cu *d*9 and *d*10 characteristics, Geochimica *et* Cosmochimica Acta 70: pp. 4635-4642.

PETERS, E. (1976) The electrochemistry of sulphide minerals, In: Trends in Electrochemistry, Bockris, J.O.M., Rand, D.A.J. and Welch B.J. (Eds.), Plenum Press, Inc., South Australia, Australia: pp. 267-290.

PESIC, B., and OLSON, F.A. (1984) Dissolution of bornite in sulfuric acid using oxygen as oxidant, Hydrometallurgy 12: pp. 195-215.

PICKERING, H.W., and BYRNE, P.J. (1971) On preferential anodic dissolution of alloys in the low-current region and the nature of the critical potential, Journal of the Electrochemical Society 118 (2): pp. 209-215.

PICKERING, H.W., and WAGNER, C. (1967) Electrolytic dissolution of binary alloys containing a noble metal, Journal of the Electrochemical Society 114 (7): pp. 698-706.

PRADHAN, N., NATHSARMA, K.C., RAO, K.S., SUKLA, L.B., and MISHRA, B.K. (2008) Heap bioleaching of chalcopyrite: a review, Minerals Engineering 21: pp. 355-365.

PRASAD, S., and PANDEY, B.D. (1998) Alternative processes for treatment of chalcopyrite – a review, Minerals Engineering 11 (8): pp. 763-781.

PRICE, D.W., and WARREN, G.W. (1986) The influence of silver ion on the electrochemical response of chalcopyrite and other mineral sulfide electrodes in sulfuric acid, Hydrometallurgy 15: pp. 303-324.

RAO, S.R., and FINCH, J.A. (1988) Galvanic interaction studies on sulphide minerals, Canadian Metallurgical Quarterly 27 (4): pp. 253-259.

RALSTON, J. (1991) Eh and its consequences in sulphide mineral flotation, Minerals Engineering 4: pp. 859-878.

RICHET, P., MYSEN, B.O., and INGRIN, J. (1998) High-temperature X-ray diffraction and Raman spectroscopy of diopside and pseudowollastonite, Physics and Chemistry of Minerals 25: pp. 401-414.

ROBINSON, J., and WALSH, F.C. (1993) *In situ* synchrotron radiation X-ray techniques for studies of corrosion and protection, Corrosion Science 35 (1-4): pp. 791-800.

RODRÍGUEZ, Y., BALLESTER, A., BLÁZQUEZ, M.L., GONZÁLEZ, F., and MUÑOZ, J.A. (2003) New information on the chalcopyrite bioleaching mechanism at low and high temperature, Hydrometallurgy 71: pp. 47-56.

RODGERS, K.A., and HAMPTON, W.A. (2003) Laser Raman identification of silica phases comprising microtextural components of sinters, Mineralogical Magazine 67 (1): pp. 1-13.

ROMERO, R., MAZUELOS, A., PALENCIA, I., and CARRANZA, F. (2003) Copper recovery from chalcopyrite concentrates by the BRISA process, Hydrometallurgy 70: pp. 205-215.

ROSSO, K.M., and VAUGHAN, D.J. (2006) Sulfide mineral surfaces, Reviews in Mineralogy & Geochemistry 61: pp. 505-556.

RRUFF PROJECT (2010) Integrated data base of Raman spectra, X-ray diffraction and chemistry data for minerals. RRUFF ID: aschamalmite (R060690), chalcopyrite (R050559), covellite (R060129), diopside (X050060), elemental sulfur (R040135), galenobismutite (R060988), pyrite (R050190), and wurtzite (R060181). Available at http://rruff.info. Acessed on 4, 2011.

SASAKI, K., NAKAMUTA, Y., HIRAJIMA, T., and TUOVINEN, O.H. (2009) Raman characterization of secondary minerals formed during chalcopyrite leaching with Acidithiobacillus ferrooxidans, Hydrometallurgy 95: pp. 153-158.

SATHIYANARAYANAN, S., SAHRE, M., and KAUTEK, W. (1999) In-situ grazing incidence X-ray diffractometry observation of pitting corrosion of copper in chloride solutions, Corrosion Science 41: pp. 1899-1909.

SCAINI, M.J., BANCROFT, G.M., LORIMER, J.W., and MADDOX, L.M. (1995) The interaction of aqueous silver species with sulfur-containing minerals as studied by XPS, AES, SEM, and electrochemistry, Geochimica *et* Cosmochimica Acta 59 (13): pp. 2733-2747.

SCARLETT, N.V.Y., MADSEN, I.C., and WHITTINGTON, B.I. (2008) Time-resolved diffraction studies into the pressure acid leaching of nickel laterites ores: a comparison of laboratory and synchrotron X-ray experiments, Journal of Applied Crystallography 41: pp. 572-583.

SENANAYAKE, G., and MUIR, D.M. (2003) Chloride processing of metals sulphides: review of fundamentals and applications, In: Hydrometallurgy 2003 – Fifth International Conference in Honor of Professor Ian Ritchie, Young, C.A., Alfantazi, A.M., Anderson, C.G., Dreisinger, D.B., Harris, B., and James, A. (Eds.), TMS, Vancouver, Canada: pp. 517-531.

SEQUEIRA, C.A.C., and SANTOS, D.M.F. (2010) Transient film formation on chalcopyrite in acidic solutions, Journal of Applied Electrochemistry 40: pp. 123-131.

SHACKELFORD, J.F., and ALEXANDER, W. (2001) Materials Science and Engineering Handbook, 3rd ed., CRC Press LLC, Florida, U.S.A.

SHEN, X.F., DING, Y.S., HANSON, J.C., AINDOW, M., SUIB, S.L. (2006) In Situ synthesis of mixed-valent manganese oxide nanocrystals: An in situ synchrotron X-ray diffraction study, Journal of the American Chemical Society128: pp. 4570-4571.

SHUEY, R.T. (1975) Semiconducting ore minerals, Elsevier Scientific Publishing Co., New York, U.S.A.: pp. 242-253.

SMITH, B. (1999) Infrared spectral interpretation: a systematic approach, CRC Press LLC, New York, U.S.A.: 287 pp.

STEPANOV, S., and KOHLER, R. (1994) A dynamical theory of extremely asymmetric X-ray diffraction taking account of normal lattice strain, Journal of Applied Physics 27: pp. 1922-1928.

STUMM, E., and MORGAN, J.J. (1981) Aquatic chemistry, 2nd ed., John Wiley & Sons, Inc., New York, U.S.A.: 780 pp.

SURYANARAYANA, C., and NORTON, M.G. (1998) X-ray diffraction. A practical approach, Plenun Press, New York, U.S.A.: 273 pp.

SUZUKI, S., MATSUBARA, E., KOMATSU, T., OKAMOTO, Y., KANIE, K., MURAMATSU, A., KONISHI, H., MIZUKI, J., and WASEDA, Y. (2007) *Ex-situ* and *in-situ* X-ray diffractions of corrosion products formed on the surface of an iron-silicon alloy, Corrosion Science 49: pp. 1081-1096.

SYLWESTRZAK, L., BAXTER, K., TURNEY, J. and DIXON, D. (2009) Galvanox™ – an opportunity for existing copper flotation concentrators to improve overall project economics, In: Hydrocopper 2009 – V International Copper Hydrometallurgy Workshop, Domic, E., and Casas, J. (Eds.), Gecamin, Antofagasta, Chile: pp. 17-25.

THIRD, K.A., CORD-RUWISCH, R., and WATLING, H.R. (2000) The role of iron-oxidizing bacteria in stimulation or inhibition of chalcopyrite bioleaching, Hydrometallurgy 57: pp. 225-233.

THRALL, M., FREER, R., MARTIN, C., AZOUGH, F., PATTERSON, B., and CERNIK, R.J. (2008) An in situ study of the formation of multiferroic bismuth ferrite using high resolution synchrotron X-ray powder diffraction, Journal of the European Ceramic Society 28: pp. 2567-2572.

TODD, E.C., SHERMAN, D.M., and PURTON, J.A. (2003) Surface oxidation of chalcopyrite ($CuFeS_2$) under ambient atmospheric and aqueous (pH 2-10) conditions: Cu, Fe L- and O K-edge X-ray spectroscopy, Geochimica *et* Cosmochimica Acta 67 (12): pp. 2137-2146.

TOSSELL, J.A., URCH, D.S., VAUGHAN, D.J., and WIECH, G. (1982) The electronic structure of $CuFeS_2$, chalcopyrite, from X-ray emission and X-ray photoelectron spectroscopy and X-α calculations. Journal of Chemical and Physics 77: pp. 77-82.

URBANO, G., MELÉNDEZ, A.M., REYES, V.E., VELOZ, M.A., and GONZÁLEZ, I. (2007) Galvanic interactions between galena-sphalerite and their reactivity, International Journal of Mineral Processing 82: pp. 148-155.

USGS - U.S. Geological Survey (2010) Copper, In: Mineral Commodity Summaries, available at http//:www.usgs.gov. Accessed on August, 2010.

VAN DER LAAN, G., PATTRICK, R.A.D., HENDERSON, C.M.B., and VAUGHAN, D.J. (1992) Oxidation state variations in copper minerals studied with Cu 2*p* X-ray absorption spectroscopy, Journal of Physics and Chemistry of Solids: pp. 53-63.

VAUGHAN, D.J., and CRAIG, J.R. (1978) Mineral chemistry of metal sulfides, Cambridge, New York, U.S.A.: 492 pp.

VAUGHAN, D.J., and ROSSO, K.M. (2006) Chemical bonding in sulfide minerals, Reviews in Mineralogy & Geochemistry 61: pp. 231-264.

VAUGHAN, D.J., and TOSSEL, J.A. (1983) Electronic-structures of sulfide minerals – theory and experiment, Physics and Chemistry of Minerals 9 (6): pp. 253-262.

VENKATACHALAM, S. (1991) Treatment of chalcopyrite concentrates by hydrometallurgical techniques, Minerals Engineering 4 (7-11): pp. 1115-1126.

VELÁSQUEZ-YÉVENES, L., NICOL, M., and MIKI, H. (2010) The dissolution of chalcopyrite in chloride solutions. Part 1. The effect of solution potential, Hydrometallurgy 103: pp. 108-113.

VILCÁEZ, J., SUTO, K., and INOUE, C. (2008) Response of thermophiles to the simultaneous addition of sulfur and ferric ion to enhance the bioleaching of chalcopyrite, Minerals Engineering 21: pp. 1063-1074.

VIRAMONTES-GAMBOA, G., VASQUEZ, B.F.R., and DIXON, D.G. (2007) The active-passive behavior of chalcopyrite: comparative study between electrochemical and leaching responses, Journal of The Electrochemical Society, 154 (6): pp. C299-C311.

YIN, Q., KELSALL, G.H., VAUGHAN, D.J., and ENGLAND, K.E.R. (1995) Atmospheric and electrochemical oxidation of the surface of chalcopyrite ($CuFeS_2$), Geochimica *et* Cosmochimica Acta 59 (6): pp. 1091-1100.

YOU, L.Q., HEPING, L., and LI, Z. (2007) Study of galvanic interactions between pyrite and chalcopyrite in a flowing system: implications for the environment, Environmental Geology 52: pp. 11-18.

WALL, A.J., MATHUR, R., POST, J.E., and HEANEY, P.J. (2011a) Cu isotope fractionation during bornite dissolution: An *in situ* X-ray diffraction analysis, Ore Geology Reviews 42 (1): pp. 62-70.

WALL, A.J., HEANEY, P.J., MATHUR, R., POST, J.E., HANSON, J.C., and ENG, P.J. (2011b) A flow-through reaction cell that couples time-resolved X-ray diffraction with stable isotope analysis, Journal of Applied Crystallography 44: pp. 429-432.

WALTON, R.I., and O'HARE, D. (2001) An in situ energy dispersive X-ray diffraction study of the hydrothermal crystallization of zeolite A. 2: Effect of deuteration on crystallization kinetics, Journal of Physical Chemistry B 105: pp. 91-96.

WALTON, R.I., MILANGE, F., O'HARE, D., DAVIES, A.T., SANKAR, G., and CATLOW, C.R.A. (2001) An in situ energy dispersive X-ray diffraction study of the hydrothermal crystallization of zeolite A. 1: Influence of reaction conditions and transformation into sodalite, Journal of Physical Chemistry B 105: pp. 83-90.

WAN, R.Y., MILLER, J.D., FOLEY, J., and PON, S. (1984) Electrochemical features of the ferric sulfate leaching of $CuFeS_2$/C aggregates, In: Electrochemistry in mineral

and metal processing, Richardson, P.E., Srinivasan, S., and Woods, R. (Eds.), Electrochemical Society, Pennington, NJ, United States of America: pp. 391-416.

WANG, S. (2005) Copper leaching from chalcopyrite concentrates, JOM (July): pp. 48-51.

WANG, G.X., GUO, Z.P., YANG, X.Q., MCBREEN, J., LIU, H.K., and DOU, S.X. (2004) Electrochemical and in situ synchrotron X-ray diffraction studies of $Li[Li_{0.3}Cr_{0.1}Mn_{0.6}]O_2$ cathode materials, Solid State Ionics 167: pp. 183-189.

WANG, M., ZHANG, Y., DENG, T., and WANG, K. (2004) Kinetic modeling for the bacterial leaching of chalcopyrite catalyzed by silver ions, Minerals Engineering 17: pp. 943-947.

WARREN, G.W., WADSWORTH, M.E., and EL-RAGHY, S.M. (1982) Passive and transpassive anodic behavior of chalcopyrite in acid solutions, Metallurgical Transactions B 13: pp. 571-579.

WATLING, H.R. (2006) The bioleaching of sulphide minerals with emphasis on copper sulphides – a review, Hydrometallurgy 84: pp. 81-108.

WEAST, R.C., and SELBY, S.M. (1968) Handbook of chemistry and physics, 48th ed., The Chemical Rubber Co., Cleveland, Ohio, United States of America.

WEB MINERAL (2010) Mineralogy database, Chalcopyrite mineral data. Available at http://www.webmineral.com. Accessed in January, 2010.

WEBSTER, N.A.S., MADSEN, I.C., LOAN, M.J., SCARLETT, N.V.Y., and WALLWORK, K.S. (2009) A flow cell for in situ synchrotron x-ray diffraction studies of scale formation under Bayer processing conditions, Review of Scientific Instruments 80: 084102-1.

WEBSTER, N.A.S., LOAN, M.J., MADSEN, I.C., KNOTT, R.B., and KIMPTON, J.A. (2011) An investigation of the mechanisms of goethite, hematite and magnetite-seeded Al(OH)3 precipitation from synthetic Bayer liquor, Hydrometallurgy 109: pp. 72-79.

WEBSTER, N.A.S., LOAN, M.J., MADSEN, I.C., KNOTT, R.B., BRODIE, G.M., and KIMPTON, J.A. (2012) An in situ synchrotron X-ray diffraction investigation of

lepidocrocite and ferrihydrite-seeded Al(OH)3 crystallisation from supersaturated sodium aluminate liquor, Journal of Crystal Growth 340: pp. 112-117.

WEI, D., and OSSEO-ASARE, K. (1997) Semiconductor electrochemistry of particulate pyrite. Mechanisms and products of dissolution, Journal of the Electrochemical Society 144 (2): pp. 546-553.

WINAND, R. (1991) Chloride hydrometallurgy, Hydrometallurgy 27: pp. 285-316.